Aix*Marseille université
Socialement engagée

NNT/NL : 2020AIXM0001/001ED000

THÈSE DE DOCTORAT

Soutenue à Aix-Marseille Université
le 22 février 2023 par

Eléonore Geulin

Contribution à la modélisation de l'injection de glaçon : de l'injecteur à l'ablation dans le plasma

Contribution to the modeling of pellet injection : from the injector to ablation in the plasma

Discipline
Physique et Science de la Matière

Spécialité
Energie, Rayonnement et Plasma

École doctorale
ED 352 Physique et Science de la Matière

Laboratoire/Partenaires de recherche
- CEA-Cadarache - Institut de Recherche sur la Fusion par confinement Magnétique, Saint-Paul-lez-Durance, France

- Physique des Interactions Ioniques et Moléculaire - Aix-Marseille Université, Marseille, France

Composition du jury

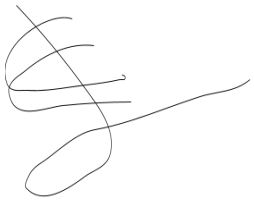
Luca Garzotti UKAEA Culham	Rapporteur
Peter Lang IPP Garching	Rapporteur
Larry Baylor ORNL Oak Ridge	Examinateur
Clarisse Bourdelle CEA/IRFM	Examinatrice
Pascale Hennequin CNRS/LPP	Examinatrice
Ryuichi Sakamoto NIFS Toki	Examinateur
Pascale Hennequin CNRS/LPP	Présidente du jury
Bernard Pégourié CEA/IRFM	Directeur de thèse
Mohammed Koubiti PIIM/AMU	Co-Directeur de thèse

Affidavit

Je soussignée, Eléonore Geulin, déclare par la présente que le travail présenté dans ce manuscrit est mon propre travail, réalisé sous la direction scientifique de Bernard Pégourié et Mohammed Koubiti, dans le respect des principes d'honnêteté, d'intégrité et de responsabilité inhérents à la mission de recherche. Les travaux de recherche et la rédaction de ce manuscrit ont été réalisés dans le respect à la fois de la charte nationale de déontologie des métiers de la recherche et de la charte d'Aix-Marseille Université relative à la lutte contre le plagiat.

Ce travail n'a pas été précédemment soumis en France ou à l'étranger dans une version identique ou similaire à un organisme examinateur.

Fait à Cadarache le 01/12/2022



Cette œuvre est mise à disposition selon les termes de la Licence Creative Commons Attribution - Pas d'Utilisation Commerciale - Pas de Modification 4.0 International.

Liste de publications et participation aux conférences

Liste des publications réalisées dans le cadre du projet de thèse :

1. E. Geulin et. al., Link between ablation and line emission for hydrogen fuelling pellet in LHD - 47th EPS ECA VOL. 45A (2021) P2.1045
2. E. Geulin & B. Pégourié, Pellet Core Fueling in Tokamaks, Stellarators and Reversed Field Pinches - Plasma and Fusion Research, 17 (2022) P.2102101

Participation aux conférences et écoles d'été au cours de la période de thèse :

Présentations & Poster

1. Poster session - at 47th conference on Plasma Physics, European Physical Society (2021)
2. **Invited talk** - at 30th International Toki Conference (2021)
3. talk - at Réunion Scientifique et Technique IRFM/CEA (2021)
4. talk - at LHD Physics Meeting (2021)
5. talk - at Tritium Fueling and Vacuum Workshop Karlsruhe (2022)
6. **Topical plenary talk** - at the International Conference of the Association of Asia Pacific Physical Societies - Division of Plasma Physics (2022)
7. talk - at Réunion Scientifique et Technique IRFM/CEA (2022)

Ecole d'été

1. Fusion pour tous - IRFM (2022).

Résumé

La méthode la plus prometteuse d'alimentation des machines à fusion est d'utiliser des billes millimétriques de glace de deutérium et/ou tritium injectées dans le plasma entre ~ 300 m.s^{-1} et ~ 2 km.s^{-1} : les glaçons. Cette technique a démontré ses capacités dans les machines actuelles, mais les résultats ne sont pas extrapolables aux futures machines de plus grande taille pour lesquelles le design du système d'injection et la construction de scénarios seront essentiellement basés sur les simulations. II est donc important de combler les vides dans la chaîne de modèles allant de la fabrication des glaçons au dépôt de matière dans le plasma. Deux manques apparaissent : la modélisation du transport du glaçon de la sortie de l'injecteur jusqu'à la chambre à vide et la validation détaillée du processus d'ablation. Ce travail vise à contribuer à combler ces vides et comporte trois parties.
La première décrit d'abord la physique du dépôt de matière. Sont ensuite rappelés les principaux résultats obtenus sur les machines actuelles. On décrit enfin les systèmes d'injection de glaçons prévus pour les prochaines machines devant entrer en service ou en projet.
La deuxième partie traite du transport du glaçon entre l'injecteur et la chambre à vide. Les effets pris en compte dans le modèle sont la fragilisation de la glace lors des rebonds, l'augmentation de la température de celle-ci et l'érosion du glaçon. Les principaux résultats sont le ralentissement et la perte de masse du glaçon au cours du trajet, ainsi que l'énergie élastique stockée qui permet de vérifier l'intégrité du glaçon au sortir du tube.
La troisième partie est une contribution à la validation détaillée du code d'ablation HPI2, en comparant ses prédictions aux images et au spectre émis localement par les nuages d'ablation. Les comparaisons simulation-expérience sont menées de deux manières différentes. La première en essayant d'extraire les densité et température des nuages des images et du spectre et en les comparant aux simulations, la seconde en calculant des spectres et images synthétiques à partir des simulations et en les comparant aux mesures. Cette méthode a permis de montrer un accord raisonnable entre les mesures et les simulations validant par la même, les hypothèses et approximations de base du modèle d'ablation sus-cité.
Mots clés : Fusion thermonucléaire par confinement magnétique, Alimentation en deutérium-tritium, Injection de glaçon, Tube guide, Ablation

Abstract

The most promising method for fueling fusion devices is to use millimeter ice pieces of deuterium and/or tritium injected into the plasma between ~ 300 m$\cdot$s^{-1} and ~ 2 km.s^{-1} : the pellets. This technique has demonstrated its capabilities in present machines, but the results cannot be extrapolated to future larger devices where the fueling system design and scenario building will rely essentially on simulations. It is therefore important to fill the gaps in the chain of models from the manufacturing of pellets to the matter deposition in the plasma. Two gaps appear: the modelling of the transport of the pellet from the outlet of the injector to the vacuum chamber, and the detailed validation of ablation process. This work aims at helping to fill up these gaps and is composed of three parts.

The first begins by describing the physics of material deposition. The main results obtained on current machines are then recalled. Finally, one describes the pellet injection systems planned for the next devices to be operated in the next decade or in project.

The second part deals with the transport of the pellet between the injector and the vacuum chamber. Physical processes taken into account in the model are the ice embrittlement during bounces, the increase in its temperature and the erosion of the pellet. Main results are the slowing down and loss of mass of the pellet, as well as the stored elastic energy, which helps at checking the pellet integrity at the exit of the guide tube.

The third part is a contribution to the validation in detail the ablation module of the code HPI2, by comparing its predictions to the images and spectrum emitted locally by the ablation clouds. Simulation experiment comparisons are conducted in two different ways. The first by trying to determine the density and temperature of the clouds from the images and the spectrum then comparing them to the simulations, the second by calculating synthetic spectra and images and comparing them to the measurements. This second method showed a reasonable agreement between the measurements and the simulations which validates the main assumptions and approximations at the basis of the above mentioned ablation model.

Keywords: Thermonuclear fusion by magnetic confinement, Deuterium-Tritium fueling, Pellet injection, Guide tube, Ablation

Remerciements

First of all, I want to thank each Jury member.
Dear Members of my Jury,
I would like to express my heartfelt gratitude to each and everyone of you for your valuable contributions to my thesis.
First, I would like to extend my sincere appreciation to my two rapporteurs, Dr. Luca Garzotti and Dr. Peter Lang, whose insightful questions and remarks have significantly contributed to the quality of my work.
I would also like to express my gratitude to my Jury president Dr. Pascale Hennequin, for her dedication in writing my defense report, as well as for her presence, availability, and thought questions during the defense.
I would like to extend my special thanks to Dr. Ryuichi Sakamoto, who traveled all the way from Japan to attend my defense and for the engaging discussions, we had during my thesis work. Your presence has made my defense even more meaningful and memorable.
Last but not least, I would like to express my appreciation to Dr. Clarisse Bourdelle and Dr. Larry Baylor for their time and effort in examining my work. Your constructive feedback and suggestions have been of great help in improving my thesis.
Thank you all for your unwavering support, guidance, and encouragement throughout my thesis journey. I am truly grateful for your presence and contributions.
For the next I will continue in French.
Je tiens à exprimer mes remerciements les plus chaleureux à mes deux directeurs de thèse, le Dr. Mohammed Koubiti et le Dr. Bernard Pégourié pour leur temps, leur disponibilité, leurs conseils, leur patience et leurs encouragements. Je suis profondément reconnaissante pour tout ce que vous avez fait pour moi. Votre soutien indéfectible et vos conseils avisés ont été la clé de la réussite de ma thèse. Je suis fière d'avoir eu l'opportunité de travailler avec vous et j'espère que cette collaboration se poursuivra à l'avenir.
Je voudrais tout particulièrement remercier le Dr. Pégourié, qui a gagné sa place au paradis à mes côtés, comme il me l'a souvent répété. Merci pour tout, pour avoir été si humain, compréhensif, soutenant et d'une patience extrême. Merci pour tout ce que tu m'as appris. Merci pour l'encadrant que tu as été et pour l'ami que tu es devenu. Merci également de m'avoir fait découvrir de superbes spots d'escalade, de nouvelles recettes et d'avoir ri à mes blagues. Et surtout pour le temps que tu m'as accordé, des fois bien au-delà des horaires de travail. Ce qui m'amène à penser à Claire.
Je voulais te remercier très sincèrement de m'avoir accueillie chez vous et à votre table. Merci d'avoir accepté que nous travaillions si tard. C'était vraiment très agréable de passer du temps chez vous et de discuter ensemble. Merci pour ton sourire accueillant

et ta gentillesse chaque fois que je suis venue.
Je tenais ensuite à remercier ma famille, à vous exprimer ma profonde gratitude pour tout le soutien que vous m'avez apporté ces derniers temps. Votre compréhension face à mon stress et votre patience ont été très importantes pour moi.
Et puis, mes amis... Que dire Merci pour tout.. Vraiment.
Je commencerai par vous remercier les amis du labo ! Plus Particulièrement Dr. Emilie Bourne, Mathieu Carole, Dr Peter Donnel, Raffael Eller-Düll, Dr Kévin Obrejan, Olivier Panico, Dr. Mathieu Peret, Virginia Quadri, Dr. Nicolas Rivals, Dr. Robin Varennes (mais toi on y reviendra plus tard), Dr. Hao Yang, Yann Munschy. Merci pour l'ambiance géniale qu'il y avait au labo grâce à vous. Pour ces repas ensemble, pour ces PhD meetings, pour ces soirées. Un clin d'œil particulier à Raffael et Robin qui ont souvent accepté que je sois leur co-bureau pour pas que je ne me retrouve seule dans le mien. Une pensée spécifique à Emilie, pour nos repas et discussions. Promis, je ne critiquerai plus jamais la cuisine anglaise. Un remerciement particulier aussi à Mathieu, pour nos pauses thé dans le 508, qui je crois, n'ont jamais été sans éclats de rire.
Ensuite je voudrais m'adresser à vous, les filles, Isabeau Bertrix, Dr. Camille Bergez (héhé), Marie-Elodie Placé et Léa Fournasson. Merci d'être là depuis tout ce temps, merci pour votre bienveillance à chaque instant, et surtout pour tous ces moments de fous rires partagés qui ont très largement contribué à réduire mon stress...
Ensuite je voudrai remercier mes colocataires Rémi Duthu et Dr. Robin Varennes (toi aussi héhé). Merci d'avoir toujours été là, merci pour cette vie ensemble, pour votre humour, votre écoute, nos soirées jeux et films, vos allers-retours à la gare et pour le chocolat quand je sombrais dans le stress. Merci aussi d'avoir accepté que je squatte le salon pendant toute la partie rédaction de ce manuscrit. Un énorme merci à toi Robin, qui devait non seulement me supporter à la maison mais également au travail et à l'escalade. Merci aussi pour toutes ces parties d'échecs et toutes ces discussions. Et un énorme merci à toi Rémi, pour toutes nos séances de sport peu motivantes mais toujours marrantes ! Vous êtes les meilleurs.
Et puis il y a Lucie Aragon, la meilleure de toutes les amies qu'on peut rêver d'avoir, qui depuis maintenant 10 ans est toujours là pour rajouter du rose dans ma vie, pour me venir en aide n'importe quand et n'importe où (quel que soit le continent), pour me fournir en tisane déstressante, en huile essentielle focalisante ainsi qu'en chocolat. Merci d'être là et d'être une si bonne amie.
Et enfin il y a Dr. Pierre Forestier-Colleoni, mon mari... merci d'être mon pilier, mon "rock" à chaque moment de ma vie. Je pense qu'à force de m'avoir entendue t'en parler tu serais capable de présenter cette thèse et tout mon travail aussi bien que moi... Tu es toujours là, à l'écoute, attentif, compréhensif et en soutien à chacune de mes décisions. Merci de m'avoir encouragée et supportée (dans tous les sens du terme) durant cette thèse. Merci d'avoir pris des vacances uniquement pour venir me soutenir, me faire rire et de me donner du chocolat, durant cette fin de rédaction. Merci d'être à mes côtés et de me rendre plus forte. Merci d'être l'homme que tu es.
Merci à vous tous du plus profond de mon cœur.

Contents

Affidavit 2

Liste de publications et participation aux conférences 3

Résumé 4

Abstract 5

Remerciements 6

Contents 8

List of Figures 11

List of Tables 18

INTRODUCTION 19
- 0.1. Thermonuclear fusion by magnetic confinement . . . 19
- 0.2. Magnetic configurations . . . 20
- 0.3. Heating and current drive . . . 21
- 0.4. Fueling and density control . . . 22
- 0.5. Motivation of the present work . . . 23

1. STATE OF THE ART 26
- 1.1. Introduction . . . 28
- 1.2. Physics of ablation . . . 29
- 1.3. Physics of homogenization . . . 32
- 1.4. Recent results in fueling . . . 36
- 1.5. Fueling systems of future devices . . . 40
- 1.6. Summary . . . 45

2. MODELING OF PELLET TRAJECTORY INSIDE A GUIDE TUBE 47
- 2.1. Introduction . . . 50
- 2.2. Guide tube building and frame definition . . . 51
  - 2.2.1. The laboratory and local frames . . . 51
  - 2.2.2. Geometry of a section in the local frame . . . 51
  - 2.2.3. Building the guide tube in the laboratory frame . . . 52
  - 2.2.4. Correspondence between the local and laboratory coordinates . 55

2.3. Trajectory between two impacts . . . 55
2.3.1. Equation of motion . . . 55
2.3.2. Pellet position and velocity at the impact point . . . 56
2.3.3. Pellet position and velocity at the end of a section . . . 57
2.4. Impact dynamics and condition for slipping or bouncing . . . 57
2.4.1. Input parameters . . . 57
2.4.2. Perpendicular dynamics and condition for slipping or bouncing 58
2.4.3. Parallel dynamics . . . 61
2.4.4. Condition for slipping due to the curvature of the trajectory . . . 62
2.4.5. Outputs of the bounce: erosion, heating, pellet position and velocity 65
2.5. Slipping dynamics . . . 67
2.5.1. Cylindrical section . . . 67
2.5.2. Toric section . . . 68
2.5.3. End of slipping . . . 69
2.6. Example of code results and main trends with input parameters . . . 70
2.6.1. Example of bounce and slip . . . 71
2.6.2. Influence of κ and θ on the bounce dynamics and pellet trajectory 74
2.6.3. Influence of μ on the pellet exit parameters . . . 79
2.6.4. Influence of the pellet input parameters and limitation of the number of bounces on the trajectories and exit parameters . . . 80
2.6.5. Calculations with exact slipping condition . . . 82
2.6.6. Calculations with the $\alpha_{\mathrm{Lim}} = 3^\circ$ approximation . . . 86
2.7. Summary and Future work . . . 88

3. RELATION BETWEEN THE LOCAL ABLATION RATE AND PELLET CLOUD EMISSION 89
3.1. Introduction . . . 91
3.2. Experimental apparatus . . . 92
3.2.1. The Large Helical Device (LHD) . . . 92
3.2.2. Pellet injection and associated diagnostics . . . 95
3.3. Data processing . . . 97
3.3.1. Photodiode calibration . . . 101
3.3.2. Harmonization of time-resolutions . . . 101
3.3.3. Calibration of camera images . . . 103
3.4. Cloud global characteristics . . . 107
3.5. Emission model . . . 109
3.5.1. Line emission . . . 110
3.5.2. Continuum emission . . . 111
3.5.3. Spectrum and image reconstruction . . . 112
3.6. Unicity of fit parameters . . . 113
3.7. Emission pattern from HPI2 simulation . . . 117
3.7.1. HPI2 simulation of pellet in discharge # 126636 . . . 117
3.7.2. Simulated spectra and emission pattern . . . 122
3.7.3. Relation between ablation rate and cloud emission . . . 123

3.8. Comparison with measurement . . . 124
3.8.1. Global cloud characteristics . . . 124
3.8.2. Interpolation on a realistic timing. . . . 126
3.8.3. Building synthetic signals . . . 127
3.8.4. Behavior of surface brightness . . . 130
3.8.5. Relation between ablation rate and cloud emission . . . 133
3.9. Discussion and conclusion . . . 134

SUMMARY **137**

A. APPENDICES - Chapter 2 **140**
A.1. CALCULATION OF THE MATRIX P AND VECTORS C_x, C_y AND C_z . . . 141
A.2. PELLET BREAKING LIMIT AND BOUNCE DYNAMICS FROM THE $[\sigma(T), \varepsilon(T)]$ DIAGRAM . . . 142
A.2.1. Available D_2 ice mechanical and thermal properties . . . 142
A.2.2. Direct use of the $[\sigma(T), \varepsilon(T)]$ diagram . . . 144
A.3. TRANSCIENT CHANGE IN μ IN CASE OF FORCED SLIPPING . . . 147
A.3.1. Braking during a bounce . . . 147
A.3.2. Braking during a slipping . . . 148
A.3.3. Calculation of μ' . . . 148
A.3.4. Calculation of d . . . 148
A.4. SET OF RECORDED PARAMETERS . . . 150

B. APPENDICES - Chapter 3 **151**
B.1. NAMES OF THE QUANTITIES CHARACTERIZING THE RADIATION . . . 152
B.2. INTERPOLATION PROCEDURE OF HPI2 SIMULATION . . . 153

Bibliography **156**

List of Figures

0.1. Typical safety factor profiles q vs. normalized minor radius r/a for the three main types of magnetic confinement devices, from [8]. 21
0.2. Poloidal cross-sections of a medium size present day device (a) and future reactor (b) where the optimal zone of pellet penetration is shadowed. The red lines at the plasma periphery are the possible locations for pellet launching. 24

1.1. Schematic picture of an ablation cloud showing the local distortion of the magnetic field due to the cloud diamagnetism (magnetic shielding), the sheath at the two ends (the cloud is negatively charged, electrostatic shielding), and the electron and ions stopped at various depths inside the cloud (collisional shielding). 29
1.2. Stopping cross-sections for electrons, hydrogenic ions, and Helium ions. Solid curves represent experimental data for stopping in Hydrogen gas, long-dashed curves are fits to the experimental data, and short-dashed curves are theoretical values for Coulomb stopping in a cold electron plasma [31]. 30
1.3. Simple description of cloud acceleration down the field gradient in an inhomogeneous magnetic field. 32
1.4. Simple description of drift braking by Alfvén wave emission (Φ is the parallel direction). 33
1.5. Drift damping by external connection in a tokamak (the situation is essentially the same in a stellarator) [19] 34
1.6. Drift damping by internal connection in a tokamak (a) and in a stellarator (b). Blue and green lines represent two magnetic field lines along which parallel currents flow. Black arrows are the curvature and gradient currents inside the cloud ([46, 47]) 34
1.7. (a) Time evolution of the deposition peak position (squares) and ablation light emission (thin line, shadowed region) during a pellet injection in Tore Supra. (b) Time evolution of the calculated pellet deposition profile ($\rho = r/a$). The arrows denote the position of the deposition peaks whose sum forms the deposition profile [27]. 35
1.8. Magnetic configuration of a RFP. (a) B_∞-field component profiles. (b) The drift damping by external connection is particularly efficient close to the reversal radius, where field lines are nearly poloidal [49]. 36

1.9. (a) The pellet injection locations on DIII-D mapped to a poloidal cross section. (b) Measured net pellet deposition profile from a 1.8 mm pellet injected from the inner wall (HFS-45 location) overlaid with the calculated ablation profile. (c) Measured deposition depth vs calculated pellet penetration depth for 2.7 mm pellets injected from different injection locations (Depths are normalized to the minor radius. The plasma edge is at 0.0 and the plasma center is at 1.0). (d) Fuelling efficiency of pellets injected from the different injection locations plotted as a function of the measured density deposition depth. The dashed curve is a fit to the LFS pellet data [56] 37
1.10. (a) Demonstration of RMP ELM-mitigated operation at densities far beyond the Greenwald density by pellet fueling in ASDEX-Upgrade. After reaching the mitigation regime by B-coil activation and sufficient gas puffing, maximum available pellet fueling is applied. Pellet fueling gradually increases the line-averaged density to about 1.5 times the Greenwald density without significant impact on confinement while maintaining ELM mitigation. (b) Pre- and Post-pellet density profiles (the phases for which profiles taken are indicated by vertical highlighted bars, marked by blue and red rectangles on the upper horizontal axis in a) [21]. 38
1.11. Comparison of the experimental global energy confinement time with the ISS04-scaling [70] for the two similar discharges in terms of average density and heating power. (a) The pellet discharge with the enhanced phase; (b) the gas-fueled discharge. Short spikes between 2 and 5 s in the gas-fueled discharge are caused by diagnostic NBI blips. For completeness, the experimental confinement time is calculated both with and without the time derivative of the diamagnetic energy. Both definitions coincide under stationary conditions. The color legend is the same for the two plots and is given in b); from [69] 39
1.12. Time evolutions of (a) stored energy W_p together with the sequence of NBIs, (b) electron temperature Te in the core region, and (c) central electron density n_{e0} and averaged density ne in the typical IDB-SDC mode. (d) Typical electron density (closed circles) and temperature (open circles) profiles in the IDB-SDC mode from [71]. 40
1.13. Normalized stored energy as a function of line-averaged electron density. The red filled symbols show the pellet shots in Neutral Beam Injection (NBI) + Electron Cyclotron Heating (ECH) plasmas. Stored energy is normalized by the heating power $P_{inj}^{0.39}$. Blue open circles show the pellet shots in NBI-only plasmas. The black filled triangles show the gas puff shots [75] 40
1.14. Guiding-tube geometry installed inside the JT-60SA vessel for pellet inboard injection. Multiple bends of the guiding tube are expected to impose a limit of about 470 m s^{-1} to the maximum injection speed from [86]. 42

1.15. Geometry of the pellet injection guiding tubes on ITER via inner and outer wall guide tubes routed through a divertor port from [89]. 43
1.16. (a) JA-DEMO geometry including the toroidal field coils (TFC), vacuum vessel (VV), back plate (BP), tritium breeding blanket (BLK) and plasma. Spatial relationships between target flux tube and injection point, pellet guide tube curvature radius (R_b) and injection angle (θ) are shown. Pink filled area is closed by TFC [90]. (b) Generic view of subsystem core fueling for EU-DEMO, composed of pellet source, pellet accelerator, and pellet transfer system aiming at the magnetic HFS of the plasma. The speed range is at least 1200 m s^{-1}, hence centrifuge or single-stage gas gun is regarded to be suitable. (c) Alternative variant using a direct-line-of-sight transfer system. High speeds up to 3000 m s^{-1} is required. Only double-stage gas gun technology will be able to reach this speed range [80] 44

2.1. Parameters defining the different guide tube sections and their arrangement in the local frame. a) cylindrical section, b) toric section. 52
2.2. Definition of the entrance and exit sets of unit vectors. a) cylindrical section, b) toric section. 53
2.3. Connection of two sections, labelled j and $j+1$, in the laboratory frame. 54
2.4. Schematic of the plane $\mathscr{P}$ at the end of a cylindrical a) and toric b) sections, with the points pi chosen for its definition and that of the vectors $\vec{u}_{1,2}$. 58
2.5. Sketch of the correction made due to the pellet trajectory curvature. The bounce on the plane corresponds to the calculated one (green cross). The red cross represents the real pellet position. Small blue arrows represents the radial velocity $\vec{v}^r$, and purple ones, the parallel velocity $\vec{v}^{\parallel}$. a) $\alpha > \delta\alpha$, the last pellet trajectory will be a free flight represented by the red arrow. b) $\alpha < \delta\alpha$, the pellet is pushed against the wall. 63
2.6. Example of pellet trajectory in a rectilinear guide tube. 71
2.7. Behavior of the main pellet parameters during the trip in the guide tube. a) perpendicular force; b) zoom on the perpendicular force during the bounce, c) zoom on the perpendicular force during the slip, d) pellet deformation during the bounce, e) pellet perpendicular velocity during the bounce and, during the whole trip, f) pellet total velocity, h) pellet mass, g) ice temperature and i) stored elastic energy per volume unit (V_p is the pellet volume). 73
2.8. a) Time-evolution of the radial force acting on the ice during a bounce for $\theta = 10^{-2}$, 10^{-1}, 1, 5 kg.s^{-1}; b) Integral of the force vs θ. 74
2.9. Behavior of (a) the perpendicular velocity, (b) the parallel velocity, (c) the pellet mass, (d) the ice temperature and (e) the stored elastic energy vs. θ. The red dashed lines are the initial values at the bounce entrance. 75
2.10. Geometry of the simulated guide tube : a) 3D view, b) $(X_{lab} \times Z_{lab})$ plane, c) $(Y_{lab} \times Z_{lab})$ plane. The cylindrical parts are in orange and the torus sections are in blue. 76

2.11. Pellet trajectory depending on θ value 77
2.12. Variation of $\delta E_p / V_p$ along the guide tube for the four values of θ 78
2.13. Variation of the pellet velocity a), mass b) and ice temperature c) along the guide tube for the four values of θ 78
2.14. Variation of the pellet velocity a), mass b) and ice temperature c) along the guide tube for the four values of μ 79
2.15. Injection location and trajectory of the 32 test pellets in the 1st section of the guide tube. The curvature of the trajectories is due to gravity. . . 80
2.16. Variation along the guide tube of (a) the pellet velocity, (b) the pellet mass, (c) the ice temperature and (d) the stored elastic energy. In (d), the black line is the average over the whole sample; the blue, green and purple lines are the elastic, failure outbreak and first impact breaking limits (see Appendix A.2). 83
2.17. Schematic view of the target location with respect to the guide tube exit, showing the laboratory and local frames 84
2.18.: Impacts of the 32 pellets on the target. (a) and (b) General view in the laboratory and local frames; (c) and (d) Zoom on the central part. The black circle is the barycenter of the impacts. The concentric circles correspond to an angular aperture of 1, 2 and 3 °, respectively. 85
2.19. Identical to Figure 2.16 for the $\alpha_{\text{Lim}} = 3°$ approximation. 87
2.20. Identical to Figure 2.18 for the $\alpha_{\text{Lim}} = 3°$ approximation. 87

3.1. (a) Coil configuration of LHD. Superconducting helical coils (blue), poloidal coils (yellow) and normal conducting Resonant Magnetic Perturbation (RMP) coils, together with plasma. (b) LHD torus hall (from [103]). 92
3.2. Heating and fueling systems in LHD. The zoom shows the implementation of the pellet injectors and associated diagnostics discussed in Section 2.2 93
3.3. (a) Operational domain in T_i and T_e in NBI and NBI+ECH discharges (from [109]), (b) T_i, T_e and n_e profiles for a record high- T_i discharge (from [110]) and (c) T_e and n_e profiles in a SDC discharge (from [111]). 94
3.4. (a) time schedule of discharge #126636, showing the waveforms of the NBI-power and the time of pellet-injection. Numbers #1,2,3 correspond to the Neutral Beams Injectors, shown in Fig. 3.2. (b) Pre-injection electron density and temperature profiles and H_β emission of the ablating pellet mapped on the discharge major radius, ... 95
3.5. Zoom of Fig. 3.2 showing the pellet injection port with the pellet injection direction (red arrow) and the arrangement of the three diagnostics with the corresponding fields of view. 96
3.6. (a) Filter transmissions F_λ : $H_{\beta 05} - 5$ nm width (green), $H_{\beta 20} - 20$ nm (magenta), $C_{576\text{nm}}$ (red). (b) Non-zero value of the transmission factor over the whole wavelength domain for $H_{\beta 20}$. 97

3.7. Point-source image (transfer function) of the fast camera. (a) Experiment, (b) best fit, (c) comparison of measured and calculated vertical and horizontal profiles and (d) comparison of measured and calculated contour-plots. 98
3.8. (a) Photodiode measurements vs. time, (b) example of raw spectrum for frame #119 (spectrometer transmission falls off in the shadowed domain) and (c) corresponding fast camera images in the three wavelength domains $H_{\beta 05}$, $H_{\beta 20}$ and $C_{576\,nm}$. 99
3.9. (a) $H_{\beta 20}$ images for the frames # 114 and # 116, the boxes are the zones where cuts are calculated, (b) perpendicular cuts of light distribution at different places in the cloud images. 100
3.10. Photodiode sensitivity D_λ vs. λ. The red curve is Eq. 3.2 101
3.11. (a) Power in spectra and photodiodes (original and convolved signals) as a function of time. (b) Power in deconvolved spectra (shifted in time by $\delta t_{S/d}$) and photodiodes. 102
3.12. (a) Raw and (b) deconvolved spectra at the beginning (frame #115) and end (frame #124) of the pellet lifetime. 103
3.13. Spectra recorded before the pellet injection and at time of frame #109. 104
3.14. Total power (in arbitrary units) in camera images without and with background subtraction (2 assumptions). (a) $H_{\beta 05}$, (b) $H_{\beta 20}$ and (c) $C_{576\,nm}$ 105
3.15. (a) Radiated energy estimated from the camera images, photodiodes and spectra vs. time, (b) Standard deviation around the average. 105
3.16. (a) Raw camera image. (b) Rotated and interpolated image. (c) Profile of maximum emission (along the axis $Y = 0$) and fitting curve. The decrease of intensity close to $Z = 0$ indicates the pellet position. 106
3.17. (a) Striation frequency vs. time, calculated from the local maxima of the diode signals, (b) photo-diodes measurements, the dashed lines are the continuous component and (c) Fourier spectra of the oscillating part of the diode signals, exhibiting a peak at ~ 74kHz. (a) 108
3.18. Time evolution of (a) the cloud half-length $\langle Z_0^{exp} \rangle$, (b) the cloud radius $\langle R_0^{exp} \rangle$, the horizontal line is the HWHM of the Transfer Function, (c) the maximum of radiated power $m^{*I}_{\Delta\lambda}$ and (d) the total radiated power $P^{*I}_{\Delta\lambda}$. 109
3.19. Geometry for the spectrum calculation and image reconstruction. . . . 112
3.20. Modification of the spectrum for different observation angles ϕ. 114
3.21. Example of calculated spectrum $P^{S,sim}(\lambda)$ (black curve) compared to experimental data $P^{S,\,exp}(\lambda)$ (red crosses). 115
3.22. (a) Set of simulations (red points) chosen for fitting the experimental spectrum $S_{Exp}(\lambda)$.(b) Behavior of the two ratios ρ_{330} and ρ_{560} for the considered set of simulations. 116
3.23. (a) The different sets of α^i 's. The black line is the average values, the red dashed line marks the temperature for a fit by a homogenous cloud. (b) Superposition of all the spectra satisfying the criterion 3.21. 116

3.24. (a) Poloidal and (b) toroidal projections of the pellet trajectory on the magnetic surfaces of LHD. The magenta contour is the LCFS extended by a factor 1.1 for accounting for the ergodic layer surrounding the confined plasma. 117
3.25. (a) Bulk plasma temperature T_∞ (b) density n_∞ and fast ion density n_f vs. normalized minor radius. 118
3.26. Ablation profiles for the 3 simulations. 118
3.27. Snapshots of the color contours of $n_0^2 f_i \left(1 - f_i\right)$ vs. distance along the pellet path (the pellet penetrates from the left to the right). (a) (CW, CCW) = (0, 1), (b) (CW, CCW) = (1/3, 2/3) and (c) (CW, CCW) = (1/2, 1/2). 119
3.28. Comparison between the photo-diode H_α signal and HPI2 predictions of the ablation rate for different simulation: $(CW, CCW) = (0, 1)$ (green dotted line), $(CW, CCW) = (1/3, 2/3)$ (blue full line), $(CW, CCW) = (1/2, 1/2)$ (brown dotted line). The black curve is a calculation without fast ions. The red vertical dashed line indicates the cloud whose parameter evolutions is discussed below. 120
3.29. Time evolution of (a) the cloud radius $R_0^{CW/CCW}$, (b) half-length $Z_0^{CW/CCW}$, (c) ionization fraction $f_i^{CW/CCW}$, (d) heavy particle density $n_0^{CW/CCW}$ and (e) temperature $T_0^{CW/CCW}$. The cross on the curves indicates the time $t_{\text{exit}}^{CW/CCW}$ where the pellet and the cloud dissociate. 121
3.30. Evolution along the pellet path of (a) the cloud radius $R_0^{CW/CCW}$, (b) half-length $Z_0^{CW/CCW}$, (c) ionization fraction $f_i^{CW/CCW}$, (d) heavy particle density $n_0^{CW/CCW}$, (e) temperature $T_0^{CW/CCW}$ and (f) ratio $t_{\text{exit}}^{CW/CCW} / t_{\text{end}}^{CW/CCW}$. Full lines are at the time of the pellet exit, dashed lines at the time of full ionization. The vertical dotted-dashed line shows the position of the cloud displayed in Fig. 3.29 122
3.31. (a) Ablation profile vs. time, the analyzed cloud is indicated by the black dashed line. (b) and (c) Cloud spectrum time evolution, the red crosses are at the time t_{exit} where the pellet exits the cloud. 123
3.32. (a) Cloud emission vs. time at $\lambda = 656$ nm (H_α), 486 nm $\left(H_\beta\right)$ and 434 nm $\left(H_\gamma\right)$ and $\lambda = 576$ nm (Continuum), the red dashed line at time $t_{\text{exit.}}$. (b) Time evolution of the surface emission for the same wavelengths. 123
3.33. (a) Cloud emission vs.time for the whole pellet ablation at $\lambda = 656$ nm (H_α), 486 nm $\left(H_\beta\right)$, 434 nm $\left(H_\gamma\right)$, 576 nm (Continuum) and averaged over the whole wavelength range $\lambda = 400 - 700$ nm (Black full line), the black dashed line indicates the cloud analyzed in Figs 3.29 and 3.31. (b) Cloud emission vs. ablation rate. Here, clouds are supposed to be seen perpendicularly to the magnetic field, where the component π of the Zeeman effect is total. 124
3.34. (a) Calculated cloud deposition frequency $\nu_{\text{Str}}^{\text{sim}}$ and experimental ones ($\text{H}_{\beta 20}$, $\text{H}_{\beta 05}$, C_{576nm}) and (b) cloud particle content N_{cl}^{sim} vs. pellet penetration. 125

3.35. Comparison of the simulated and measured cloud dimensions. (a) Half-length $\langle Z_0^{exp} \rangle$ and Z_0, (b) radius $\langle R_0^{exp} \rangle$ and R_0. 126
3.36. (a) Total power emitted by the clouds vs. time, (b) Identical to (a) for $\lambda = 656\,nm\,(H_\alpha)$. In these two figures, the colored thin lines are the individual contributions of the different clouds. 127
3.37. (a) Power in the $H_{\beta 05}$ wavelength band vs. time, (b) and (c) identical to (a) for the $H_{\beta 20}$ and C_{576nm} wavelength bands. In these three figures, the colored thin lines are the individual contributions of the different clouds. 128
3.38. (a) Synthetic signal of photodiodes in the $H_{\beta 05}$, $H_{\beta 20}$ and C_{576nm} wavelength bands, (b) identical to (a) for the power in the spectra. (c) and (d), experimental counterpart of (a) and (b). See Fig. 3.11a 129
3.39. (a) and (b) Identical to Fig. 3.38b and 3.38d, the vertical bars indicate the times where the simulated and measured spectra are compared. (c) to (e) simulated (red line) and measured (blue line) spectra, the colored axes correspond to the times indicated in a and b. 131
3.40. (a) Individual contribution vs. time of the different clouds to the $H_{\beta 20}$ emission, (b) time evolution of the surfaces of the different clouds and (c) time evolution of the surface brightness of the different clouds. . . . 131
3.41. (a) Contributions of fast ions and bulk electrons to the pellet ablation vs. time, (b) ratio between the fast ion and bulk electron contributions to pellet ablation. 133
3.42. Cloud emission vs. ablation rate in the $H_{\beta 05}$, $H_{\beta 20}$ and C_{576nm} wavelength bands. a) in linear scale and b) in log scale. 133

A.1. a) Maxwell-Wiechert element, b) Voigt-Kelvin element. 142
A.2. (a) $[\sigma(T), \varepsilon(T)]$ diagram for 6 temperature values, (b) Hydrogen heat capacity $C(T)$ as a function of the temperature. 143
A.3. Energy density limits for elastic behavior, failure outbreak and first impact breaking vs. temperature. 144
A.4. Stress-strain diagram for D_2 ice at $8K$, showing the general evolution of the ice state during a bounce. The stress and strain at the elastic limit $(\varepsilon_e, \sigma_e)$, necking $(\varepsilon_v, \sigma_v)$, and breaking (ε_m) points are also indicated. Their values are given in Table A.1. 145
A.5. Variation of the friction coefficient after a forced slipping. 149

B.1. Interpolation procedure for calculating the deposition time of the set of sim-clouds. 154
B.2. Interpolation procedure for calculating the characteristics of the set of sim-clouds. 155

List of Tables

1.1. Major (R) and minor (a) radii, elongation (κ), plasma current (I_p), magnetic field (B_∞), plasma volume (V_{plasma}), fusion power (P_{fus}) and average density ($< n_e >$) for the future large devices to be operated in the next decade or in project. 42

2.1. Geometrical characteristics of the simulated guide tube : section number, type of section (R = rectilinear, T = toric), length, major radius and angular extension. 77
2.2. Exit parameters for the set of 32 pellets: Slowing down, Mass loss, Ice heating, Stored elastic energy per unit volume, Impact radius on the target and Pitch angle of the exit trajectory. Noted quantities are the average value, the total standard deviation and the standard deviations for the pellets showing parameters below or above the average, with the corresponding number of pellets. 82
2.3. Identical to Table 2.2 for the $\alpha_{lim} = 3°$ approximation. 86

3.1. Specifications of LHD (from [108]) 92
3.2. Achieved plasma parameters and key-physics studies for the H-operation phase in LHD (from [103]) 94
3.3. Fit parameters of the camera transfer function. 97
3.4. Level energy and statistic weight of the 5 first levels of Hydrogen. 110
3.5. Frequency, wavelength and Einstein's coefficient for spontaneous emission for H_α, H_β and H_γ 111
3.6. Measured and simulated energy radiated during the whole ablation in the full spectrum and $H_{\beta 05}$, $H_{\beta 20}$ and C_{576nm} wavelength bands. 129

A.1. deuterium ice data used for calculation from [[133] [134]]. T is the temperature, E_Y the Young s' modulus, σ_e^M the stress at elastic limit, ε_c the strain at elastic limit (calculated), σ_v the stress at necking point, ε_v strain at necking point and ε_m strain at breaking point * = extrapolated data) 144
A.2. Set of parameters in the laboratory frame recorded at the end of every simulation step. In the first line 1 refers to a toric section & 2 for a cylindrical section. 150

INTRODUCTION

0.1. Thermonuclear fusion by magnetic confinement

The goal of the researches in the field of controlled thermonuclear fusion by magnetic confinement is to build a reactor using the energy released by the exothermic reaction:

$$D + T \rightarrow He + n^0 + 17.6\text{MeV}$$

where D, T and He symbolize the nuclei of Deuterium, Tritium and Helium-4, respectively. The released energy is distributed between the alpha particle for 20 % and the supernumerary neutron n^0 for 80 %. Building a reactor requires then confining a mixture of Deuterium and Tritium of density n^∞ and temperature T^∞ high enough for the proportion of the released energy carried by the alpha particles to be sufficient for maintaining the temperature, the neutron escaping from the configuration. If one characterizes the thermal insulation of the medium by the characteristic time τ_E (defined as the time constant of the fall of the energy content after cutting off the power sources), this self-sustaining condition can be expressed by the Lawson's criterion [1]:

$$n^\infty \tau_E > 3 \times 10^{20}\ \text{m}^{-3}\ \text{s for}\ T^\infty > 10\ \text{keV}$$

Due to the minimum temperature required (linked to the energy dependence of the DT fusion cross section), the medium is totally ionized, it is a plasma, and it must not be in contact with any material wall, hence the need for confining it by a magnetic field. For conditions satisfying the Lawson's criterion, the burning plasma is said "at ignition".
The threshold values of $n^\infty \tau_E$ and T^∞ given above summarize in themselves the difficulties of controlled thermonuclear fusion, from which derive directly main topics of research. The time τ_E is of course linked to the intrinsic characteristics of the plasma (the confinement modes), but also to the quality of the chosen magnetic configuration. The high value of the temperature threshold underlines quite well the need to heat the plasma up to a point where the fusion rate is high enough for the power carried by the alpha particles is sufficient to sustain ignition. Concerning the density, it is those of Deuterium and Tritium that are involved and, these two elements being consumed in the fusion reactions, an equilibrium can only be maintained by exhausting the ashes (the Helium nuclei) and injecting fresh fuel (Deuterium and Tritium). In other

words, it is mandatory to control in real time the fuel cycle in the plasma. The very compact expression of the Lawson's criterion (it is commonly expressed in the form of the triple product $n^{\infty}T^{\infty}\tau_E$) emphasizes quite symbolically the interdependence and necessary integration of all the fields of research related to controlled fusion. The goal is to design a reactor, a machine, where the improvement of the performance of the overall system depends on the combined developments carried out on each of the sub-systems constituting it.
Our work, which focuses for its largest part on estimating the limitation of the most efficient fueling method developed up to now (the injection of frozen DT pellets), does not escape to this fundamental rule. For this reason, it is useful to briefly introduce the principles of magnetic confinement as well as heating, current generation and fueling methods. It is the subject of the three Sections below.

0.2. Magnetic configurations

The simplest idea for confining a plasma in a magnetic field is to use a toric solenoid. The field lines are then circular and centered on the main axis of the torus, the magnetic field decreasing proportionally to $1/R$, where R is the distance to the major axis. In this configuration, the magnetic field gradient and curvature of the field lines cause the electrons and ions to drift vertically in opposite directions. This movement is inhibited by the vertical electric field resulting from charge separation, but then the particles drift outwards, down the magnetic field gradient, under the effect of this electric field. The consequence is a loss of the plasma on the wall within a few milliseconds. The effect of this drift can be cancelled - on average - by winding the field lines helically around the secondary axis of the torus (the magnetic axis). The vertical drift displacement of the particles when they are above the equatorial plane is compensated by this same displacement when they are below: in the absence of collisions, the particles are indefinitely confined to the vicinity of a magnetic surface. This helix structure of the field lines is obtained by adding a poloidal component B_θ to the main magnetic field B_φ. Several types of machines have been designed which have the appropriate configuration. The three main ones are the STELLARATORS where the configuration is entirely generated by external coils, the REVERSED FIELD PINCHES (RFP) and the TOKAMAKS [1] where the poloidal component of the magnetic field is obtained by the circulation of a toroidal current I_p in the ring of plasma. As far as the magnetic configuration is concerned, they differ essentially by the rate of winding of the field lines around the magnetic axis, quantified by the safety factor $q = \frac{\text{Number of toroidal turns}}{\text{1 poloidal turn}}$, see Figure 0.1. Stellarators ([2],[3],[4]) have the advantage of allowing continuous discharges free from the instabilities associated with the current gradient, but at the cost of a magnetic configuration of low flexibility and of a significant complexity of manufacturing. RFP and tokamak discharges are inherently limited in time, since the current is generated - in most cases - by a transformer effect.

1. Acronym of a Russian expression "TOroidal'naja KAmera MAgnetnymi Katushkami" for "Toroidal chamber with magnetic coils".

They differ in the ratio B_θ / B_φ, whose value decreases from ~ 1 in RFPs to about 10% in tokamaks. The RFP configuration [5] is consecutive to the relaxation of the plasma towards a state of minimum energy [6] and is characterized by an inversion of the poloidal field B_θ at the edge of the plasma column. As for the tokamak configuration, it demonstrated its good stability properties [7], mainly due to a high magnetic field. It is in this last configuration, the most studied so far, that the best performances have been obtained.

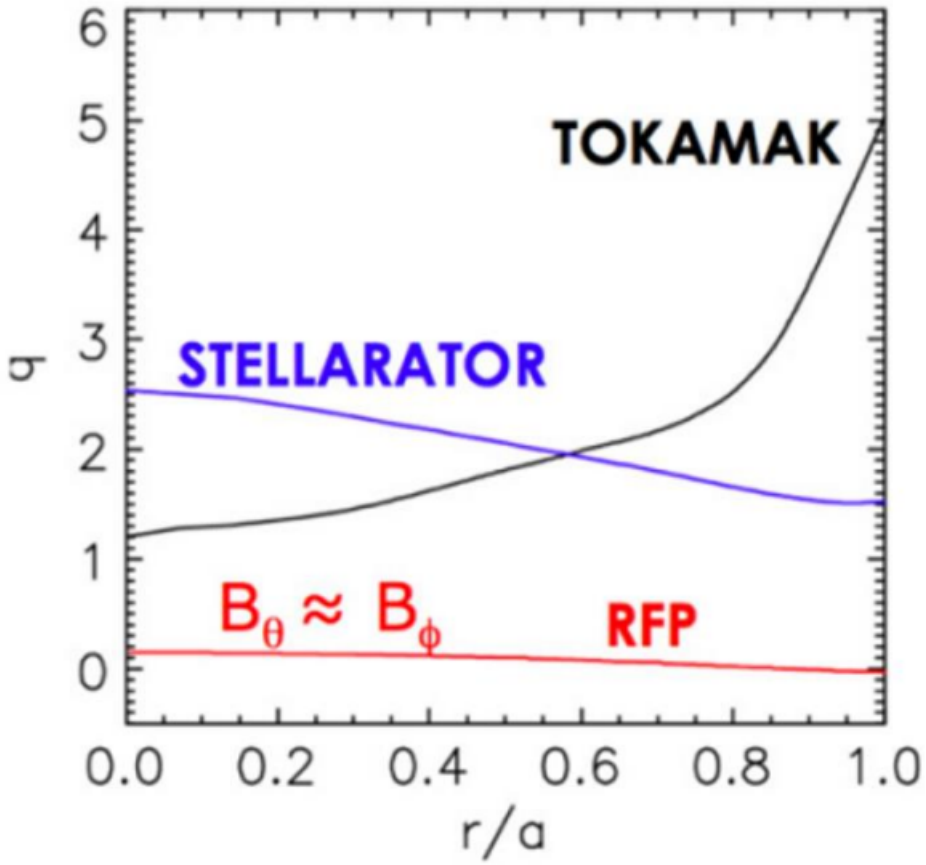


Figure 0.1. – Typical safety factor profiles q vs. normalized minor radius r/a for the three main types of magnetic confinement devices, from [8].

0.3. Heating and current drive

If the three configurations described above are able to confine a plasma for a significant time, they do not allow, without external heating, for reaching a high enough temperature for initiating the fusion reactions (about 10 keV for the Deuterium-Tritium nuclear fusion). Even if the Ohmic heating allows reaching a temperature of a few keV in RFPs and tokamaks, heating the plasma up to thermonuclear temperatures requires significant additional power for all the three types of devices.

A first method is the injection of fast neutral beams [9]. Its principle is simple: since neutral atoms are not deflected by the magnetic field, they propagate in straight line through the plasma and can reach the core of the discharge if their mean free path is large enough, i.e. at high enough injection energy (about 100 keV in present day devices and 1 MeV for a reactor). Once ionized, they remain trapped in the magnetic configuration. The fast ions, which carry most of the beam kinetic energy, thermalize then by transferring their energy to the bulk electrons and ions by Coulomb collisions. The other methods consist in launching an electromagnetic (RF) wave that propagates in the plasma and is absorbed either by ions or by electrons [10]. A superthermal population is thus created which, as in the previous case, thermalize by transferring its energy to the electrons and/or thermal ions by Coulomb collisions. Several frequencies are used that modify the distribution function of the particles they interact with: the electron and ion cyclotron waves, $\nu_{ce} = 100 - 200$ GHz and $\nu_{ci} = 30 - 120$ MHz (and their harmonics), which accelerate the electrons and ions perpendicular to the magnetic field, as well as the lower hybrid wave, $\nu_{LH} = 1 - 8$ GHz, intermediate to the two frequencies mentioned above, which accelerated the electrons parallel to the field [11].
These different heating means can also be used for maintaining the toroidal current in the plasma, increasing by a large factor the discharge duration: by injecting the fast neutral beans tangent to the magnetic field or using antennas radiating an asymmetric spectrum for the methods using RF waves. Both creates superthermal populations whose distribution is asymmetrical parallel to the magnetic field and which therefore carry a significant toroidal current. From a technological point of view, the injection of neutrals has the advantage of requiring no coupling structure close to the plasma, but it is penalized by the difficulty for obtaining, with a good yield, neutrals of sufficient energy for penetrating up to the core of a reactor plasma. As to the systems using RF waves, they are either the antennas which are the weak point, because necessarily close to the plasma (for ν_{ci} and ν_{LH}), or the power generators that are of delicate technology for ν_{ce}.

0.4. Fueling and density control

Ensuring in quasi steady-state a plasma of high enough purity for maintaining burning conditions ($n_{He}/n_e < 8$ %) requires to pump a few % of the edge recycling flux, i.e. to renew the whole plasma particle content within a few seconds [12]. Such a rate of rotation requires an efficient density control [13]. In present day and future devices, extraction is performed by a divertor at the edge of the plasma, see e.g. [14]. As for the fuel supply, it is commonly done by means of a simple valve injecting gas by puffs at the very edge, global transport phenomena ensuring the fuel penetration in the plasma core. If this system has the advantage of simplicity, it has the disadvantage of being of low efficiency, a significant amount of the injected materiel being immediately pumped by the exhaust system [15]. In addition, a too large fuel deposition in the outer part of the discharge can destabilize the local power balance and provoke a

disruption. This limits the maximum reachable density, the so-called Greenwald's limit. The effectiveness of this method of fueling can be increased by using very brief puffs of high intensity (SMBI for Supersonic Molecular Beam Injection), allowing the fuel to be deposited deeper. However, here again, the fuel deposited disturbs the peripheral plasma [16]. Therefore, a more effective means of feeding have been sought, i.e. allowing the material to be deposited deeper in the core of the discharge. The basic idea comes from the fact that, for maintaining a plasma of density n^{∞}, the required source scales as $n^{\infty}(D/\Lambda)$, where D is the effective diffusion coefficient and Λ is the deposition depth of the injected material. Injecting pellet of frozen fuel with a speed between a few hundreds and 1-2 thousands m/s leads to a significant increase in Λ, the dense and cold cloud of gas resulting from the ablation of the pellet protecting it efficiently from the direct heat flux of the plasma. Such a method allows depositing the fuel up to midradius in present day tokamaks (see [17] and [18],[19] for recent reviews). Unfortunately, the demonstration of the drift of the cold material deposited by the pellet down the magnetic field gradient has raised awareness that the effective deposition depth of the source was not only depending on the place where the material was deposited locally, but also on the various drifts that could take place during the homogenization phase [20]. For this reason, in most of present day tokamaks and stellarators and in all future projects, the fueling of the core plasma is planned to be done by pellets injected from the High Field Side (HFS) of the configuration, for taking advantage of the drift down the magnetic field gradient that, in this configuration, favors a deeper fuel penetration.

0.5. Motivation of the present work

In present devices, pellet injection has demonstrated its capacity for depositing matter in the plasma core, allowing to decouple the edge and core densities up to surpass the Greenwald's density (see e.g.[21]. It is therefore the best for future reactor fueling[2]. This deep matter deposition results from two phenomena: the pellet penetration which - for given plasma density and temperature profiles depends on the pellet mass and injection velocity (the ablation phase), then the displacement of the locally deposited material due to its drift down the magnetic field gradient during the homogenization phase. Present day devices and future reactors exhibit very different characteristics with respect to these two phenomena. In today's machines, pellet penetration λ_p is larger than the ∇B-induced displacement $\Delta(\Delta/\lambda_p \sim 0.5)$, while in future reactors the matter penetration will be dominated by the ∇ B-induced displacement, with typical values of $\Delta/\lambda_{\mathrm{p}} \sim 2-3$. It follows that - for an efficient fueling - it is enough that the pellet penetrates inside $r \sim 2a/3$ in present day machines (where a is the plasma minor radius), and mandatory that all the ablation occurs in the High Field Side half of the plasma in future reactors (see Fig. 0.2). For this reason, if present day devices can be fueled by pellet launched from any poloidal position, the fueling of

2. Pellet injection is also envisaged for controlling the Edge Localized Modes frequency [22] and mitigating disruptions [23]

future reactors is mainly considered to be ensured by pellets injected from the HFS, see e.g. [24].

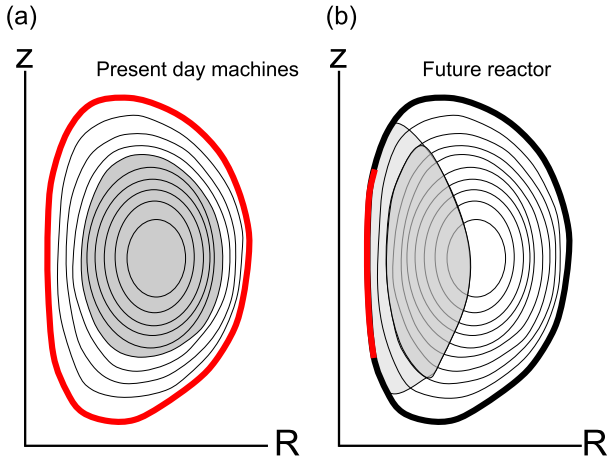


Figure 0.2. – Poloidal cross-sections of a medium size present day device (a) and future reactor (b) where the optimal zone of pellet penetration is shadowed. The red lines at the plasma periphery are the possible locations for pellet launching.

Injecting pellets from the HFS requires that bended guide tubes are used. This reduces the maximum injection velocity, due to the forces exerted on the ice in the curved sections. If this limitation has been documented by a number of experiments in test beds of different geometries [25], it does not exist any tool for predicting, for an arbitrary guide tube geometry and ice mechanical characteristics, the performance of an injection system in terms of reliability (proportion of intact pellets at the guide tube exit) and velocity distribution (magnitude and pitch angle).
The second consequence of the different values of the drift / penetration ratio, Δ/λ_p, in present and future devices is that it is not possible to perform in present machines experiments mimicking the fueling of a reactor. Therefore, every scenario building must be based on simulation only, which underlines the importance of thoroughly validating the physics included in the pellet ablation deposition models. These models calculate sequentially the two steps of matter deposition: the instantaneous ablation, then the drift and homogenization of the locally deposited material. If the physics governing the homogenization phase has been experimentally verified ([26], [27]), this is not the case for the ablation phase. In this latter case, the validation of code predictions was generally done by comparing the measured and calculated total pellet penetrations, which integrates the whole ablation phase, or the calculated ablation profile with that of the Hα or Hβ line emission, assuming a proportionality between the pellet mass loss and the line emission (see [17], [18] and references therein).
Pellet injection is an active field of research and this work aims at taking stock of the present experimental results and, as far as possible, at bridging the gap between our present knowledge and what would be necessary for reliable predictions of pellet

ablation-deposition profiles in next step devices. Chapter 1 is a review of the main results obtained since the last published reviews ([17], [18], [19]), and presents the pellet fueling systems of forthcoming devices. The two following chapters try to strengthen the two weak points mentioned above: Chapter 2 describes a model of pellet propagation in a guide tube for reliable predictions of the performance of a fueling system, and Chapter 3 is an attempt for validating in detail the code predictions of the time evolution of the ablation rate. Last, a summary and discussion of the work to be done before completely validating the predictions concerning the whole pellet injection system and matter deposition profile for future devices is given in the Conclusion.

1. STATE OF THE ART

Sommaire

1.1. Introduction 28
1.2. Physics of ablation 29
1.3. Physics of homogenization 32
1.4. Recent results in fueling 36
1.5. Fueling systems of future devices 40
1.6. Summary 45

Abstract

In a reactor grade device, the role of core fueling is to replace the D and T consumed in the fusion reactions (almost negligible) and to compensate the plasma losses through the separatrix - including the material expelled out by the ELMs. For this purpose, deep material deposition is an advantage and pellet injection the best candidate for fueling the future machines. Once the pellet enter in the plasma, fueling consists in two phases: First, the pellet ablation itself, then the ablated material homogenization and drift in the discharge. The former is a self-regulated process, which depends only of the local plasma characteristics. The second is a global phenomenon, which depends on the whole magnetic configuration. In this presentation, we discuss first the basics of the ablation physics, emphasizing the role of the fast particles – ions and electrons – resulting from NBI or wave heating; then we describe the homogenization process and associated ∇B-induced drift. The drift acceleration and damping processes are described as well as the influence of the magnetic configuration (tokamak, stellarator and reversed field pinch) on the predominance of a given damping process and its consequence on the resulting deposition profile. We finally review the last results relative to pellet fueling in these different kind of devices and present the ongoing projects for future large-scale machines.

1.1. Introduction

In a fusion reactor, the role of core fueling is (1) to replace the DT consumed in fusion reactions, (2) to compensate the gas exhausted with the Helium ashes and (3), to maintain the central density by compensating the particle outflux across the separatrix (which depends on the transport regime and on the density gradient at the edge).
The amount of fuel consumed in fusion reactions is generally negligible: 3.55×10^{20} D and T/GW, i.e. 1.5 Pa m^3 D_2+T_2/GW. The quantity to be injected for replacing the gas exhausted with the ashes depends on the maximum acceptable concentration of Helium in the core for maintaining a high enough reactivity. Considering a conservative value $n_{He}/n_e \sim 8$ %, one should inject 3.7×10^{21} D+T/GW, i.e. 7.8 Pa m^3 D_2+T_2/GW. The most important contribution comes from the conservation of the core density. Taking as an example an ITER-like device, with a major radius of 6 m, a minor radius of 2 m and an elongation 1.7, with a density gradient in the pedestal of $\sim 3 \times 10^{20}$ m^{-4} and using an effective value for the diffusion coefficient of 0.1 m^2/s, one obtains an integrated outflux of $\sim 2.5 \times 10^{22}$ e$_-$/s which requires – to be compensated – an injection of $\sim$ 50 Pa m^3/s of D_2+T_2. It is to be noted that these contributions are not strictly additive (the Helium flux is included in that resulting from the edge density gradient).
Due to the width and density / temperature of the Srape-Off Layer (SOL) in a large-scale device, the screening of the neutrals is important and a simple gas injection from the edge is not efficient enough for feeding the plasma at the required level [28]. Direct fuel injection inside the separatrix, even beyond the top of the pedestal, is mandatory for reaching the required core density. Moreover, this fueling should be ideally done at low energetic cost and without injecting any power or momentum in the discharge. Despite a deep penetration, Neutral Beam Injection (NBI) cannot be used for fueling, on one hand because it couples particle and power injections, on the other hand because the corresponding fluxes ($\sim 6 \times 10^{21}$ at MW/keV, i.e $\sim$ 1 Pa m^3/s for 73 MW injected with 1 MeV neutrals in ITER) are well below the required values. A second option is the injection of cryogenic pellets, a widely documented and mature technique, from both the points of view of the physics ([18], [19]) and of the technical developments [29]. In the future, injection of compact toroids is also envisaged [30], but this technique is not yet developed enough for it to be used in the machines for which beginning of operation is planned during the next decade.
This paper presents the physics of fueling by pellet injection, summarizes the main results obtained in this field during the last decade, and describes the injectors and injection lines presently under manufacturing or planned for the next generation devices. Practically, a simple description of the physics of the pellet ablation and of the homogenization of the deposited material is given in Sections 1.2 and 1.3, explicating the contributions of the different mechanisms at work in tokamaks, stellarators and Reversed Field Pinches (RFPs), and discussing how their respective weight influence the final shape of the matter deposition profile. The main results recently obtained on the tokamaks and stellarators in operation – all of them relative to the compatibility of

pellet injection with high performance scenarios - are reviewed in Section 1.4, and the pellet fueling systems planned in the next step (JT-60SA, ITER) or future (JA/EU-DEMO, FFHR) devices are briefly described in Section 1.5. Finally, the most important points are summarized in Section 1.6.

1.2. Physics of ablation

As soon as a pellet enters into the plasma, the incident ion and electron heat fluxes vaporize its external layers. This ablated material surrounds the pellet and – as long as its ionization degree remains low - stays attached to the pellet in its motion through the plasma. The cold and dense vapor layer absorbs the quasi-totality of the plasma heat flux, protecting the pellet and allowing a deep penetration inside the discharge, much larger than what would be the penetration of gas. In a first approximation, it is a self-regulated process, which only depends on the pellet size and local plasma characteristics (density, temperature and magnetic field): the ablation cloud self-adapts such that the heat flux reaching the pellet is just enough for the newly ablated material to replace the material loss due to the progressive ionization. Three mechanisms participate to the cloud protection, by order of increasing efficiency they are : the cloud diamagnetism, which reduces the effective area of the plasma flux tube intercepted by the cloud, the electrostatic sheath that develops at the plasma cloud interface and repels a part of the incident electrons, and finally the Coulomb collisions inside the cloud (Figure. 1.1). If the electrostatic sheath does not change the total heat flux on the

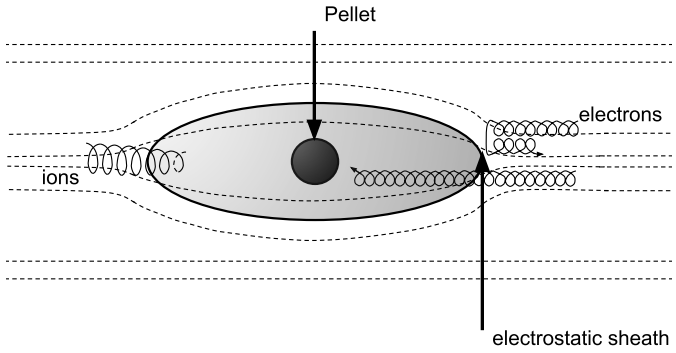


Figure 1.1. – Schematic picture of an ablation cloud showing the local distortion of the magnetic field due to the cloud diamagnetism (magnetic shielding), the sheath at the two ends (the cloud is negatively charged, electrostatic shielding), and the electron and ions stopped at various depths inside the cloud (collisional shielding).

cloud, by repelling the electrons and accelerating the ions, it causes a power transfer from the former to the latter. The stopping cross-section of the ions with the cloud particles being larger than that of the electrons (see Figure 1.2), the ion heat flux is absorbed at the cloud periphery and only a reduced electron heat flux penetrates

deep inside the cloud and ablates the pellet. The most efficient shielding is by far the Coulomb stopping, by which the quasi-totality of the remaining heat flux is absorbed through collisions with the cloud particles, and it is enough to consider this latter shielding for deriving the main dependence of the pellet ablation rate with pellet size and plasma temperature and density.

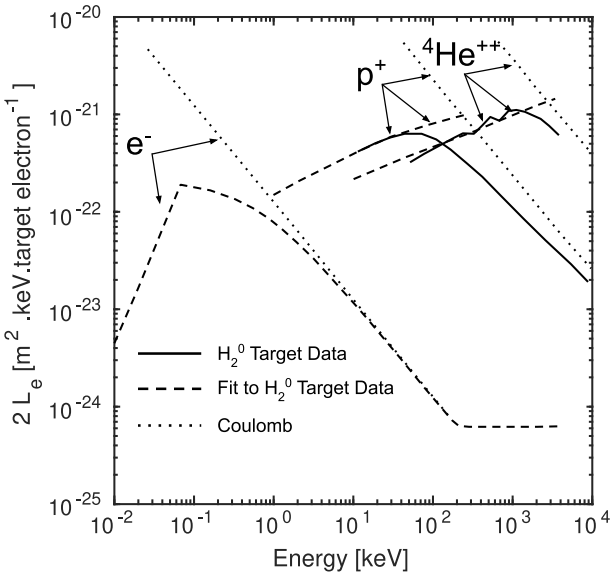


Figure 1.2. – Stopping cross-sections for electrons, hydrogenic ions, and Helium ions. Solid curves represent experimental data for stopping in Hydrogen gas, long-dashed curves are fits to the experimental data, and short-dashed curves are theoretical values for Coulomb stopping in a cold electron plasma [31].

The so-called Neutral Gas Shielding (NGS) scaling [32] is easily deduced from simple consideration.

— The conservation of the power flux across the cloud surface:

$$4\pi R_{cl}^2 n_0 (2T_0)\sqrt{\frac{\gamma T_0}{m_0}} = 2\pi R_{cl}^2 n_\infty (2T_\infty)\sqrt{\frac{\gamma T_\infty}{m_i}}$$

where R_{cl} is the cloud radius, n_0 and T_0 the cloud molecular density and temperature, n_∞ and T_∞ the background plasma density and temperature, m_0 and m_i the cloud molecule mass and plasma ion mass, yielding:

$$n_0 T_0^{3/2} = C_1 n_\infty T_\infty^{3/2} \tag{1.1}$$

— The conservation of the particle flux between the pellet and cloud surfaces:

$$4\pi R_p^2 n_G \frac{dR_p}{dt} = 4\pi R_{cl}^2 n_0 \sqrt{\frac{\gamma T_0}{m_0}}$$

where R_p is the pellet radius and n_p the molecular ice density. Assuming that R_{cl} is proportional to R_p (validated in [[32]]), this yields:

$$\frac{dR_p}{dt} = C_2 n_0 T_0^{1/2} \tag{1.2}$$

— The total dissipation of the incident electron energy in the neutral cloud [32]. Approximating the energy loss function of the electrons in neutral Hydrogen by $\frac{dE}{ds} = -C_{\text{loss}} n_0 E^{-2/3}$, the condition $\int_{2T_\infty}^{0} E^{2/3} dE = -C_{loss} n_0 \int_0^{R_{cl}} ds$ leads to:

$$n_0 = \frac{3(2^{5/3})}{5} \frac{T_\infty^{5/3}}{C_{\text{loss}} R_{cl}} = C_3 \frac{T_\infty^{5/3}}{R_p} \tag{1.3}$$

Combining eq 1.1, 1.2 and 1.3, one obtains:

$$\frac{dR_p}{dt} \propto R_p^{-2/3} n_\infty^{1/3} T_\infty^{29/18}$$

Despite the numerous approximations, this scaling was confirmed for Maxwellian plasmas by more sophisticated models taking into account the other shielding mechanisms and was validated over a large number of experiments in several machines ([18], [19] and references therein, [33], [34]). Reasons for this robustness are detailed in [35]. One observes nevertheless large deviations to this ablation law as soon as the electron or ion distribution functions exhibit significant suprathermal tails. In the presence of fast ions (Ion Cyclotron Resonance Heating (ICRH) or Neutral Beam Injection (NBI)) [1], overablation is due to a geometrical effect. The ion orbit dimensions becoming comparable to those of the cloud, the fast ions can enter laterally and reach the pellet after having only covered a short distance inside the shielding cloud, which increases the residual heat flux at the pellet surface, and thus the ablation rate. Several models were developed for quantifying this overablation ([31], [36], [37]) and their predictions compared with experiments performed in tokamaks or stellarators with ICRH [37] or NBI additional power ([36], [38], [39]). The situation is different in the presence of fast electrons, for which the stopping cross-section becomes weak enough for they can cross the cloud and even the pellet without being stopped (see Figure 1.2). A volume heating of the pellet follows, which entirely vaporizes when the amount of accumulated heat becomes comparable to the sublimation energy of the whole material contained in the pellet. Practically, this situation is met in tokamak discharges where Lower Hybrid Current Drive (LHCD) generates the current in a non-inductive way [37] or in the presence of a beam of runaway electrons. Electron Cyclotron Resonance Heating (ECRH) does not generate a significant suprathermal tail, but this method allows a localized power deposition, which can also lead to a local overablation [40].

1. In a reactor, the α-particles are not expected to have a significant effect because the pellet will be fully ablated in the external part of the plasma

1.3. Physics of homogenization

As the pellet is ablated, it leaves along its path a series of dense and cold clouds (radius ~ 1 cm, length ~ 10 cm, typically 1000× denser and colder than the background plasma). These clouds homogenize in the discharge by expanding along the field lines (see e.g. [41]). Nevertheless, since the parallel energy transport (~ at the thermal electron velocity) is much faster than the density parallel transport (~ at the sound velocity), the temperatures in the cloud and the background plasma equilibrate much faster than the densities, leading to a localized overpressure in the cloud. A charge separation develops then in the cloud, due to the vertical drift of electrons and ions ($v_{\nabla Be/i}$) in the inhomogeneous magnetic field B_∞. The associated current, $\delta j_{\nabla B}$, is compensated by a polarization current, j_{pol}, driven by an electric field E, which induces a $E \times B_\infty$ drift down the magnetic field gradient (Figure 1.3). This drift velocity writes ([42], [43], see a more complete discussion in [18]):

$$\frac{dV_d}{dt} = \left[\frac{dV_d}{dt}\right]_{\nabla B} = \frac{2(n_0 T_0(1 + M_0^2/2) - n_\infty T_\infty)}{R_c n_0 m_0} \tag{1.4}$$

where T_∞ is the temperature of the background plasma and where T_0, m_0 and M_0 are the temperature, the ion / atom mass and the Mach number of parallel expansion in the cloud (the parallel expansion increases the electron and ion vertical curvature drift and thus the cloud polarization). R_c is the curvature radius of the magnetic field lines (~ the major radius in a tokamak). At the beginning of the drift, during the phase

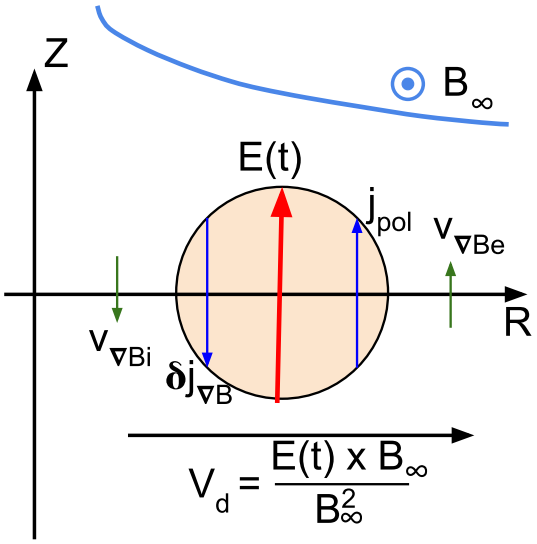


Figure 1.3. – Simple description of cloud acceleration down the field gradient in an inhomogeneous magnetic field.

of ideal MHD, the cloud drags away the magnetic flux tube it intercepts: the potential distribution propagates along the flux tube, from the two ends of the cloud, carried by an Alfvén wave at velocity C_A (Alfvén velocity). This mechanism is schematized

in Figure 1.4, showing that, due to the magnetic tension, the field exerts a force per surface unit, $F_m = B_\infty^2/\mu_0$ that, projected on the direction of the cloud displacement, generates a return force that brakes the drift (see e.g. [44]). The equation for the evolution of the drift velocity writes then:

$$\frac{dV_d}{dt} = \left[\frac{dV_d}{dt}\right]_{\nabla B} - V_d \frac{2B_\infty^2}{\mu_0 C_A n_0 m_0 Z_0} \tag{1.5}$$

where Z_0 is the cloud parallel length. As long as the only two terms of the r.h.s. of Eq.1.5 are considered, the cloud drift stops a short time after pressure equilibration (which implies also that the cloud parallel expansion stops) and the specificities of the different magnetic configurations (tokamak, stellarator or RFP) do not play any role. With increasing time, the cloud electric potential perturbation invades the whole

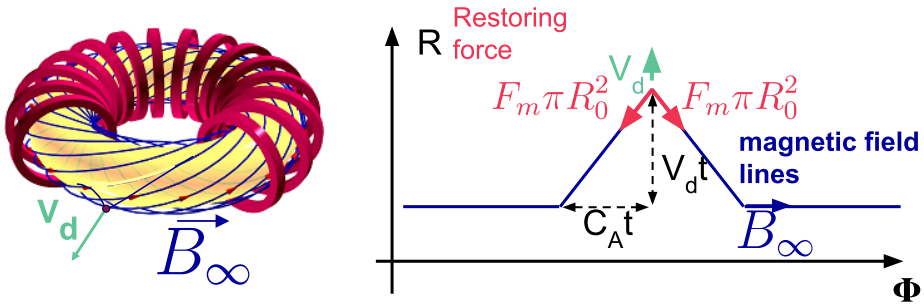


Figure 1.4. – Simple description of drift braking by Alfvén wave emission (Φ is the parallel direction).

magnetic surface and the cloud length, that increases typically at the sound speed, $C_s(T_0)$, becomes large enough for covering significant poloidal and toroidal angular sectors. This situation is the source of two processes that contribute simultaneously to the damping of the cloud drift, more efficently than the Alfvén damping.
The former (External Connection, EC) results from the connection along the same flux tube of two regions oppositely charged (Figure 1.5). The circuit is then closed by a resistive parallel current, $j_{//}$, along this flux tube, the cloud acting as a current generator. In this regime, the damping term due to the Alfven wave emission vanishes progressively, and the equation of evolution of the drift velocity writes ([45]):

$$\frac{dV_d}{dt} = \left[\frac{dV_d}{dt}\right]_{\nabla B} - V_d \frac{\sigma_\infty B_\infty^2 \pi R_0^2}{2 n_0 m_0 Z_0 Z_\infty} \tag{1.6}$$

where σ_∞ is the plasma parallel conductivity and Z_∞ the length of the flux tube connecting the two ends of the cloud. On the major part of the discharge, Z_∞ is bounded by $2\pi^2 Ra/R_0$, where R and a are the major and minor radii of the plasma, but it decreases down to $2\pi qR$, where q is the safety factor, close to the integer rational surfaces that play a preponderant role in the stopping of the drift.
The second (Internal Connection, IC) results from the progressive misalignment of

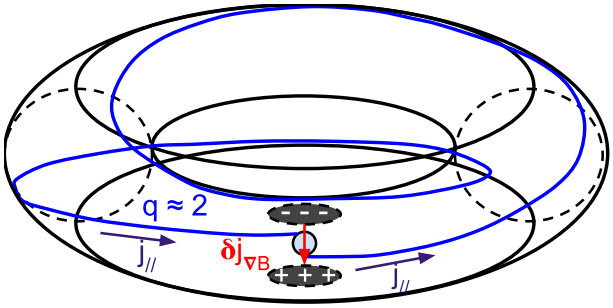


Figure 1.5. – Drift damping by external connection in a tokamak (the situation is essentially the same in a stellarator) [19]

the current $\delta j_{\nabla B}$ as the cloud, whose parallel length increases continuously, covers wider and wider poloidal and toroidal angular sectors [46]. Beyond a critical length Z_c, the relative directions of the current $\delta j_{\nabla B}$ are inverted at the two cloud ends (w.r.t. the field lines), and the circuit is closed by a parallel current inside the cloud, Figure 1.6. This second phenomenon does not brake the drift, but decreases drastically its driving term. Its integration in the equation of evolution of the drift velocity leads to (see e.g. [47]):

$$\frac{dV_d}{dt} = \left[\frac{dV_d}{dt}\right]_{\nabla B} \frac{Z_c}{\pi Z_0} \sin\left(\frac{\pi Z_0}{Z_c}\right) \tag{1.7}$$

It is the fact that these two last mechanisms depend on the magnetic configuration

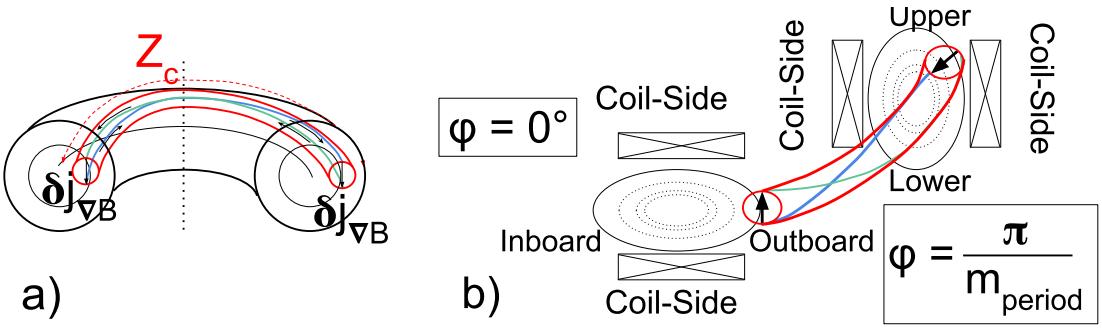


Figure 1.6. – Drift damping by internal connection in a tokamak (a) and in a stellarator (b). Blue and green lines represent two magnetic field lines along which parallel currents flow. Black arrows are the curvature and gradient currents inside the cloud ([46, 47])

that determines the drift dynamics in the different kinds of devices (tokamak, stellarator or RFP) and thus the resulting matter deposition profile. See also [48] for MHD simulations.
In tokamaks, the time after which the EC becomes efficient scales as $\tau_{EC} \sim \frac{2\pi R}{C_A}$ close to the strongly rational surfaces (Figure 1.5), shorter than that after which the IC becomes efficient $\tau_{IC} \sim \frac{\pi q R}{C_s(T_0)}$, Figure 1.6a. It is therefore this former process that is

dominant in the stopping of the drift and the matter deposition profile exhibits a stair-like shape (the deposition peak progresses step by step with pellet ablation), every integer or half-integer surface acting as a drift barrier (Figure 1.7, [27]). Conversely,

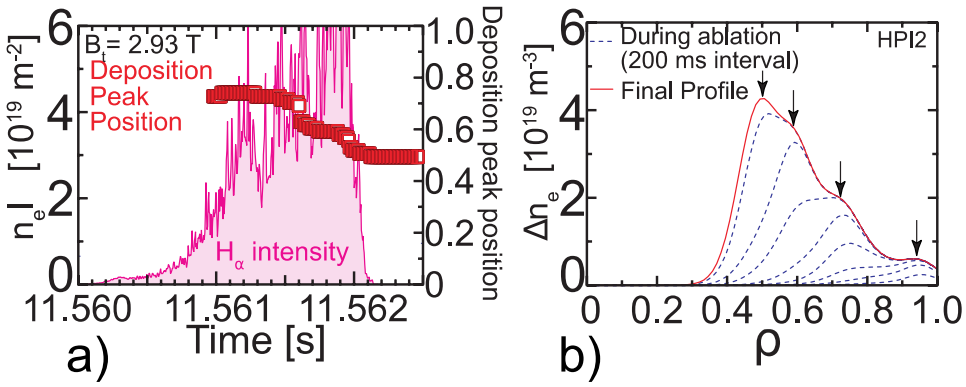


Figure 1.7. – (a) Time evolution of the deposition peak position (squares) and ablation light emission (thin line, shadowed region) during a pellet injection in Tore Supra. (b) Time evolution of the calculated pellet deposition profile ($\rho = r/a$). The arrows denote the position of the deposition peaks whose sum forms the deposition profile [27].

in stellarators, if the time τ_{EC} is of the same order of magnitude as in tokamaks, the length Z_c beyond which the IC becomes efficient is only half the toroidal period of the configuration, $Z_C \sim \frac{\pi R}{m_{\text{period}}}$, where m_{period} is the number of periods [47], Fig 1.6b. Consequently, $\tau_{IC} < \tau_{EC}$, and the drift stopping in stellarators is dominated by the IC. In helical devices, the ∇B induced displacement is – for machines of similar size and plasma conditions – smaller than in tokamaks.
In RFPs, the poloidal magnetic field is larger than the toroidal magnetic field in the external half of the plasma, where the major part of ablation occurs, Figure 1.8. The drift is then essentially directed outwards, along the minor radius. The cloud homogenization time (pressure equilibration) is short, because of the large magnetic shear that strongly stretches the clouds during their parallel expansion, increasing their cross-field surface, and of the large transport coefficients in these devices [49]. At the reversal radius, where the toroidal field vanishes and changes direction, the connection length Z_∞ is very short, $\sim 2\pi a$. Locally, the damping of the drift is very efficient and the material deposited at this place takes the shape of an overdense poloidal ring that expands in the toroidal direction more slowly than the matter deposited deeper in the discharge [49]. The model described above was implemented in different codes adapted to the tokamak configuration [2] or to the stellarators ([47, 52]) and checked against experiments over a significant number of devices ([18, 19] and references therein, [26, 47, 53–55]).

2. A pure MHD description of the drift and of the resulting modification of the deposition profile is found in [50, 51]

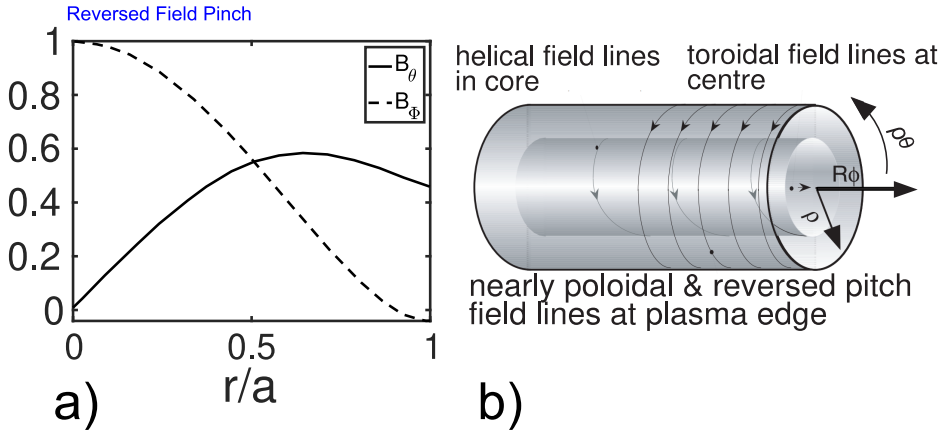


Figure 1.8. – Magnetic configuration of a RFP. (a) B_∞-field component profiles. (b) The drift damping by external connection is particularly efficient close to the reversal radius, where field lines are nearly poloidal [49].

1.4. Recent results in fueling

The deep matter penetration in a discharge fueled by pellet injection has two main advantages: a higher fueling efficiency (ϵ_f, defined as the proportion of injected particles present in the plasma at the end of injection) and a wider operational domain in density, because of a better decoupling between the core and edge plasma densities. These two facts are documented for a long time in the literature (see [18] and references therein) and only the most salient points and recent results are listed below.
In tokamaks, if one excepts the injection of energetic neutrals – which couples a significant power injection to a modest fueling, and the injection of compact toroids – for which technology is not mature enough, the injection of cryogenic pellets is the fueling method exhibiting the highest efficiency (with $\epsilon_f(GP) < 10$ % for a gas puffing, $\epsilon_f(SMBI) \sim 30$ to 60 % for Supersonic Molecular Beam Injection [16] and $\epsilon_f(PI) \sim 30$ to 90 % for pellet injection). In the case of pellet injection, the wide range in ϵ_f and deposition depth comes from the variable contribution of the ∇B-induced drift to the matter penetration ([18], [56], see Figure 1.9). This is the reason why, in most experiments, pellets are injected from the High Field Side (HFS) of the machine, and not from its Low Field Side (LFS).
Nevertheless, the good instantaneous fueling properties demonstrated by pellet injection must be tempered by the presence of a subsequent phase of density decrease and by its contribution to the global discharge fueling. In large-scale devices (ITER, DEMO), the role of pellet injection in the fueling of the core is dominant because of the opacity of the SOL to the neutrals. But in present day mid-scale devices, the core fueling is yet dominated by the recycling flux. For this reason, in Tore Supra, two macroscopically similar L-mode discharges, the former fueled by gas puff, the latter by pellet injection, demonstrated identical particle balance despite very different fueling efficiencies: $\epsilon_f(GP) = 5$ %, $\epsilon_f(PI) \sim 60$ %, [57].
During this last decade, in tokamaks, most of the experimental activities implying pel-

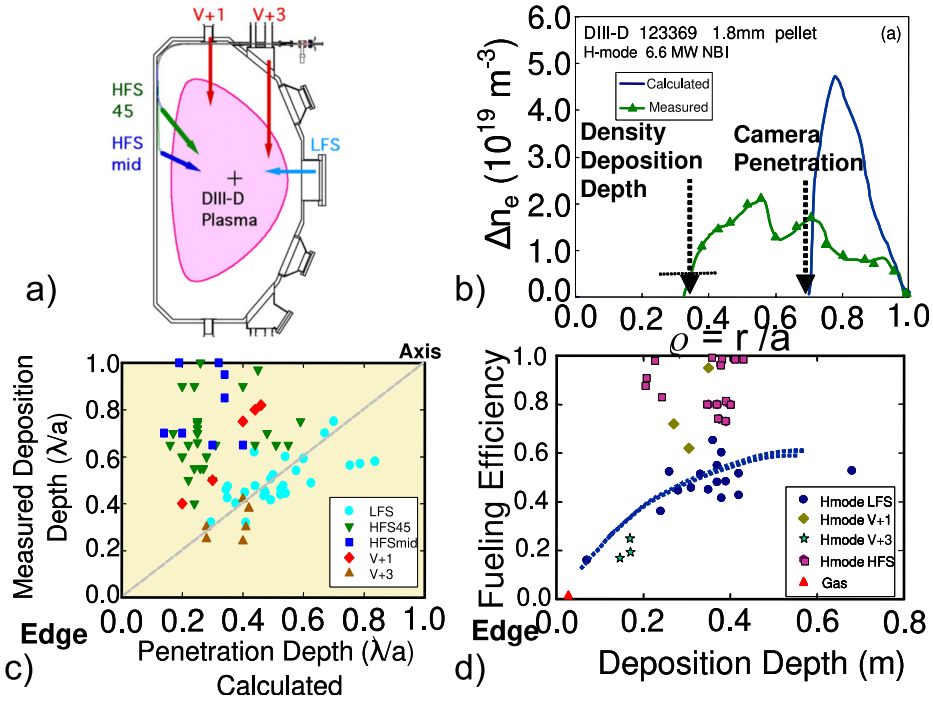


Figure 1.9. – (a) The pellet injection locations on DIII-D mapped to a poloidal cross section. (b) Measured net pellet deposition profile from a 1.8 mm pellet injected from the inner wall (HFS-45 location) overlaid with the calculated ablation profile. (c) Measured deposition depth vs calculated pellet penetration depth for 2.7 mm pellets injected from different injection locations (Depths are normalized to the minor radius. The plasma edge is at 0.0 and the plasma center is at 1.0). (d) Fuelling efficiency of pellets injected from the different injection locations plotted as a function of the measured density deposition depth. The dashed curve is a fit to the LFS pellet data [56]

let injection were devoted to the mitigation of disruptions using shattered pellets (like in DIII-D, KSTAR and JET), and to the demonstration of the compatibility of pellet fueling with ELM pacing by Resonant Magnetic Perturbation (RMP) in high performance scenarios (mainly in MAST and ASDEX Upgrade). This manuscript concentrates on core fueling, and thus on the second of these two domains of research. The corresponding studies documented that pellet fueling was not only compatible with, but could also favor the access to H-mode ([18], see [58] for recent results), allowing to operate above the Greenwald density and to simultaneously control the ELMs by RMP ([18] and references therein, [59–62], see an example of one of the most spectacular results in this field in Figure 1.10) or by shallow pellet injection [63]. As in tokamaks,

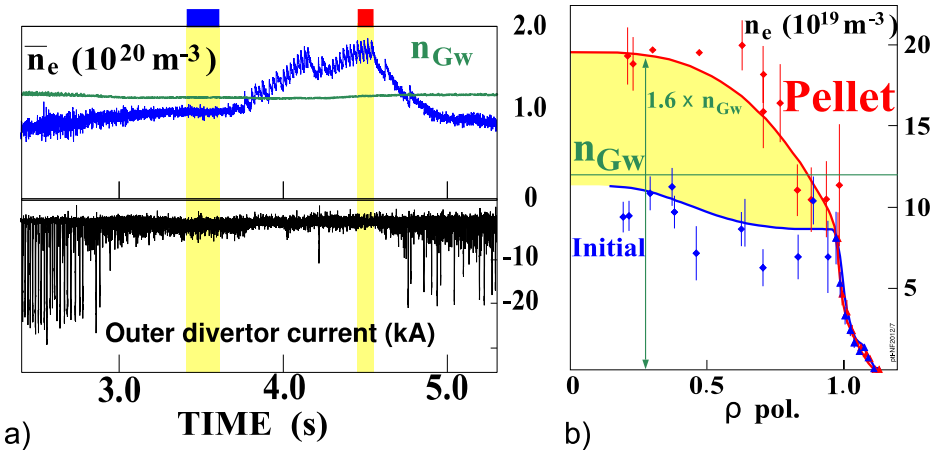


Figure 1.10. – (a) Demonstration of RMP ELM-mitigated operation at densities far beyond the Greenwald density by pellet fueling in ASDEX-Upgrade. After reaching the mitigation regime by B-coil activation and sufficient gas puffing, maximum available pellet fueling is applied. Pellet fueling gradually increases the line-averaged density to about 1.5 times the Greenwald density without significant impact on confinement while maintaining ELM mitigation. (b) Pre- and Post-pellet density profiles (the phases for which profiles taken are indicated by vertical highlighted bars, marked by blue and red rectangles on the upper horizontal axis in a) [21].

it was observed in LHD an increase in the accessible density at fixed injected power in pellet-fueled discharges [64]. However, one of the intrinsic difficulties of density control in helical devices is that, as long as the neoclassical transport dominates as expected in high performance discharges, the density profiles will be hollow in absence of deep core fueling [65]. Using pellet injection for overcoming this difficulty was extensively investigated in LHD [66] and W7-X [67]. In both cases, series of pellets (from a few to a few tens) were injected in the plasma with a high frequency (from a few tens to a few hundreds of Hz). Peaked density profiles were obtained with this technique, with a transient increase in the confinement in W7-X ([68, 69]), Figure 1.11, up to ~ 30 % larger than the predictions of the empirical scaling ISS04 [70]. Experiments

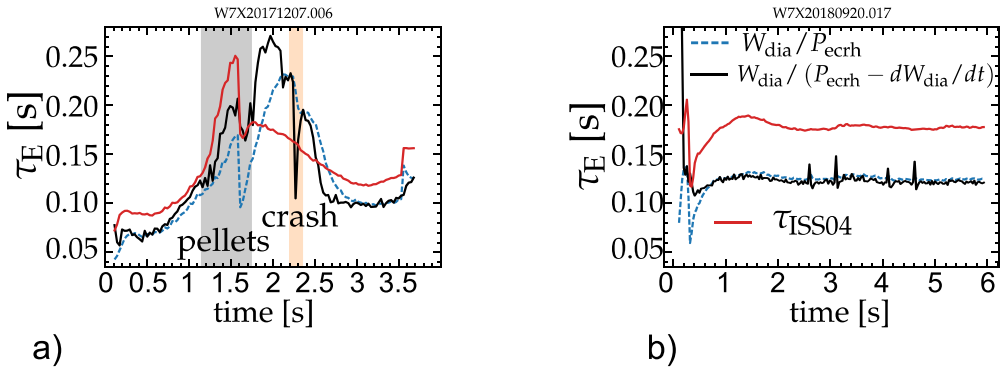


Figure 1.11. – Comparison of the experimental global energy confinement time with the ISS04-scaling [70] for the two similar discharges in terms of average density and heating power. (a) The pellet discharge with the enhanced phase; (b) the gas-fueled discharge. Short spikes between 2 and 5 s in the gas-fueled discharge are caused by diagnostic NBI blips. For completeness, the experimental confinement time is calculated both with and without the time derivative of the diamagnetic energy. Both definitions coincide under stationary conditions. The color legend is the same for the two plots and is given in b); from [69]

in the superdense core mode (SDC see, e.g. [71]) were continued in LHD. This mode, which is triggered by a series of pellets in a low recycling regime, is characterized by a central core of high density and high pressure (5×10^{20} m^{-3}, 0.85 keV, $\beta \sim 4\%$), stable, and maintained by an Internal Diffusion Barrier (IDB), Figure 1.12. Significant MHD activity or impurity accumulation are not observed in this regime, for which end is caused by a new type of ballooning mode, localized in space, and destabilized by the 3D nature of the Heliotron configuration [72]. Pellet fueling experiments were also performed in TJ-II and Heliotron J. In TJ-II, they demonstrated the presence of a ∇B-induced drift that lowers the fueling efficiency when the pellets are injected from the LFS, and showed that the post-pellet injection behavior was in agreement with the predictions of neoclassical theory ([73], [74]). It was also confirmed in Heliotron J that, at equivalent density, the stored energy was larger in the discharges fueled by pellets than in those fueled by gas puff [75], Figure 1.13.
Last, post-pellet injection transport studies were performed in the reversed field pinch RFX [76] and completed in the Madison Symmetric Torus (MST), where the Greenwald limit was overcome in a high confinement pellet-fueled discharge. In MST, the density was increased by up to a factor of 4 in discharges combining pellet fueling with pulsed poloidal current drive (PPCD), with a record in the beta value ($\beta \sim 26$ %) [77].

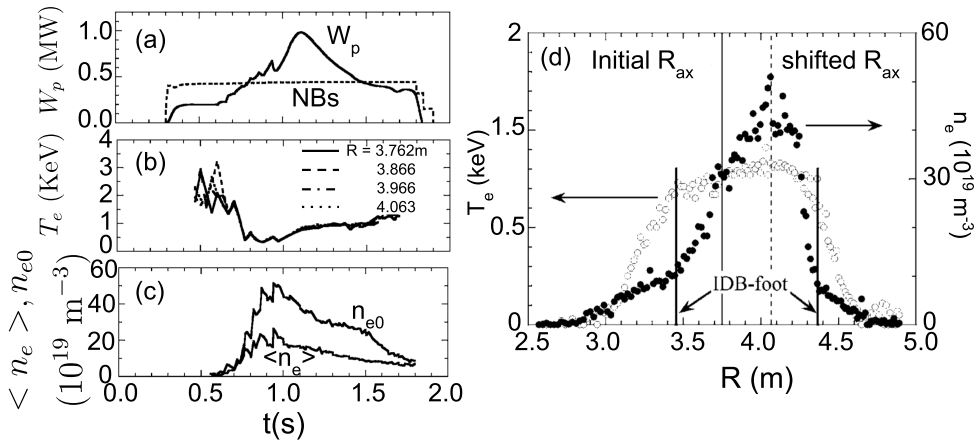


Figure 1.12. – Time evolutions of (a) stored energy W_p together with the sequence of NBIs, (b) electron temperature Te in the core region, and (c) central electron density n_{e0} and averaged density ne in the typical IDB-SDC mode. (d) Typical electron density (closed circles) and temperature (open circles) profiles in the IDB-SDC mode from [71].

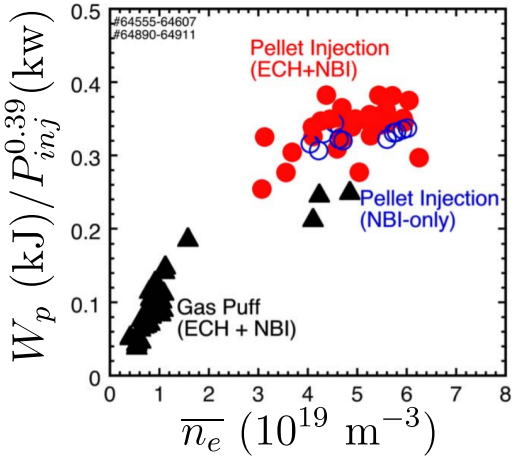


Figure 1.13. – Normalized stored energy as a function of line-averaged electron density. The red filled symbols show the pellet shots in Neutral Beam Injection (NBI) + Electron Cyclotron Heating (ECH) plasmas. Stored energy is normalized by the heating power $P_{inj}^{0.39}$. Blue open circles show the pellet shots in NBI-only plasmas. The black filled triangles show the gas puff shots [75]

.

1.5. Fueling systems of future devices

If the experiments summarized in the previous section demonstrate that pellet injection has the capacity for fueling efficiently today's machines, the situation will

be different in the future – reactor grade – devices, and the results obtained up to now are hardly extrapolated. This comes essentially from the larger plasma size and from the higher temperature and density expected at the edge of the plasma. This would result in a smaller pellet penetration (typically up to a normalized radius $\rho = r/a \sim 0.95$ to 0.90, compared to $\rho \sim 0.7$ to 0.5 in present day machines). That is why drift displacement is essential to the matter penetration. Consequently, HFS pellet injection will be mandatory in both large-scale tokamaks and stellarators [78]. In fact, HFS injection is hampered by the necessity to use bended guide tubes between the pellet injector and the exit point in the vacuum chamber. This limits the injection speed because of the erosion and constraints experienced by the pellets when they slip – or bounce – along the wall of the guide tube. The maximum speed can be estimated by balancing the yield strength of the Hydrogen ice by the pressure exerted by the centrifuge force on the pellet during its path in the guide tube [25]. The resulting expression, calibrated on laboratory experiments, is $V_p^{Max} = 36.4$ [m.s^{-1}] $\sqrt{R_C/2R_p}$, where R_C is the bending radius of the guide tube. One cannot compensate this speed limitation by an increase in the pellet size, because the perturbation that results from this instantaneous density increment (pellet injection being adiabatic, the plasma is cooled in the same proportion) can induce important plasma control difficulties ([79, 80]). This is also the case when the arrival time of the pellets in the plasma is not well controlled, due e.g. to a small dispersion of the injection velocity with pneumatic injectors (gas guns). Fueling a reactor by pellet injection results therefore from a compromise between the requirement that the matter penetrates deep enough and the limitations in the pellet speed and mass mentioned above.

Presently, pellet injection systems for three large tokamaks are under manufacturing or design. By order of size and planned date of commissioning, they are those of JT-60SA, ITER and DEMO. Typical values relevant for the fueling of these machines (they can slightly change depending on the publication), with those of the FFHR project, are listed in Table 1.1 ([81–85]) [3]. For JT-60SA, the required fueling rate is ≤ 30 Pa.m^3.s^{-1} (1.5×10^{22} at s^{-1}) in Hydrogen and Deuterium. Pellets are continuously extruded from a reservoir where the ice is formed. They have a particle content of (0.3 to 1.3)$\times 10^{21}$ at. and are accelerated by a centrifuge injector, with a frequency up to 50 Hz [86]. The HFS injection line enters the vacuum chamber by and equatorial port, in the outer midplane, and exhibits several bends up to its end slightly above the inner midplane (Figure 1.14). For reliable injection, this limits the allowed pellet speed to $V_p^{Max} = 0.47$ km.s^{-1}. Simulations demonstrating the possibilities of density control with this system can be found in [81].

Concerning ITER, the expected core fueling rate is up to 85 Pa.m^3.s^{-1} ($\sim 4.25 \times 10^{22}$ at.s^{-1}) [12], this value being confirmed by the simulations of the different scenarios ITER will be operated in ([87, 88]). The pellets (H_2, D_2, 10 % D_2 - 90 % T_2) are also continuously extruded and have a particle content of 6×10^{21} at. (the plasma density increment is $\delta n/n \sim 7$ %). The final system of ITER will consist in 3 pairs of

3. From the author's knowledge, no pellet fueling evaluation is available for the Chinese project CFETR.

	JT-60SA	ITER	JA-DEMO	EU-DEMO	FFHR-d1
R [m]	2.96	6.2	8.5	9	14.4
a [m]/κ	1.18/193	2/1.7	2.42/1.65	2.9/1.6	2.54
I_p [MA]	5.5	15	12.3	18	-
B_∞ [T]	2.25	5.3	5.94	5.9	4.7
V_{plasma} [m^3]	133	830	~ 1600	~ 2400	1878
P_{fus} [GW]	-	0.5	1.42	2	3
$< n_e >$ [10^{19} m^{-3}]	2 to 10	8 tot 10	6.6	7.3	$n_e(0)$ 25

Table 1.1. – Major (R) and minor (a) radii, elongation (κ), plasma current (I_p), magnetic field (B_∞), plasma volume (V_{plasma}), fusion power (P_{fus}) and average density ($< n_e >$) for the future large devices to be operated in the next decade or in project.

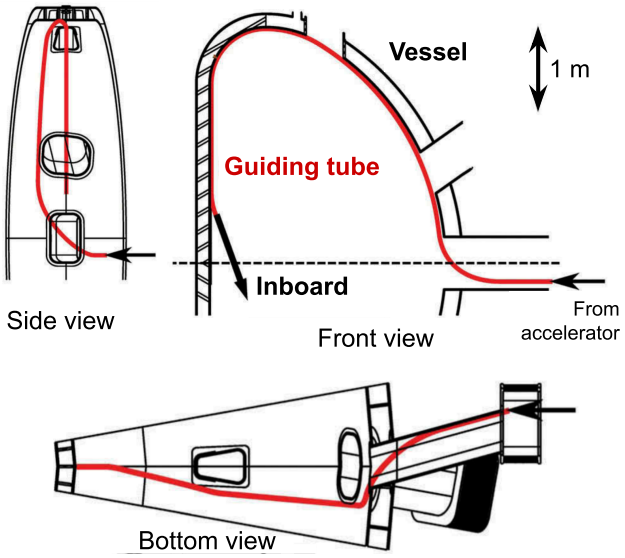


Figure 1.14. – Guiding-tube geometry installed inside the JT-60SA vessel for pellet inboard injection. Multiple bends of the guiding tube are expected to impose a limit of about 470 m s^{-1} to the maximum injection speed from [86].

injectors, each of them able to inject pellets at a maximum frequency of 16 Hz. Each pair of injectors will be equipped with 3 guide tubes (2 HFS for fueling, 1 LFS for ELM pacing, Figure 1.15). In this geometry, the maximum injection speed was measured to be $V_p^{Max} \sim 0.3$ km.s^{-1}, the pellets being pneumatically accelerated by a single-stage gas gun [89].

Two versions of DEMO are being developed: one in Japon (JA-DEMO [83]), the other in Europe (EU-DEMO [84]). For JA-DEMO, a rather complete study of the needs in terms of fueling is given in [90], the imposed constraint being that the maximum of deposition should be at $r/a \sim 0.85$. For the set of performed simulations, it is

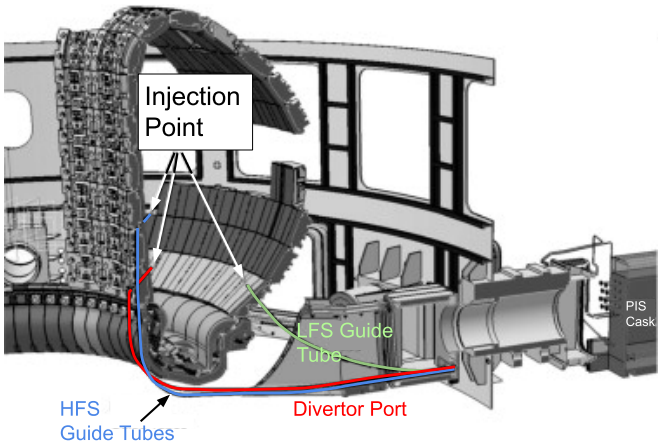


Figure 1.15. – Geometry of the pellet injection guiding tubes on ITER via inner and outer wall guide tubes routed through a divertor port from [89].

found that the best configuration for core fueling: ~ 25 Pa.m^3.s^{-1} ($\sim 1.2 \times 10^{22}$ at.s^{-1}), would be to inject pellets of a particle content of 4×10^{21} at., from HFS, with a velocity $V_p \geq 2$ km.s^{-1}. Such a velocity requires to use a double-stage gas gun, the pellet being condensed *in situ* in the gun (with a condensation time ~ 30 s), and large curvature radii are required for the guide tube $R_C \sim 10$ m, Fig 1.16a. With these parameters, an injection frequency of 3 Hz would require to install 90 guns around the torus.
The first design of the pellet fueling system of EU-DEMO used the same pellet size as that planned for ITER (6×10^{21} at.), and the first calculations of penetration / deposition profiles done in this frame [91]. However, for minimizing the difficulties in the plasma control that were resulting from a too large density increment [79], the pellet particle content was reduced down to 2×10^{21} at. in the pre-conceptual design [80]. The required injection frequency would be then in the range 5 to 7 Hz for an injected flux of ~ 20 to 30 Pa m^3 s^{-1} (~ 1.0 to 1.4×10^{22} at s^{-1}). Two alternative configurations are yet considered for the injection geometry, the injector being in both cases placed above the cryostat, Figures 1.16b and 1.16c. The first uses a curved guide tube ($R_b \sim 10$ m), allowing an injection speed of $V_p \sim 1.7$ km s^{-1}, for which a single-stage gas gun is sufficient. The second uses straight-line injection for minimizing the erosion in the guide tube. Pellets are then injected at high velocity ($V_p \geq 3$ km.s^{-1}) with a double-stage gas gun [92]. Presently, there is no reactor grade project of Heliotron planned to be manufactured in the next decade. Nevertheless, several studies were conducted for evaluating the fueling needs in a device of characteristics close to those of FFHR-d1 (see Table 1.1), of 3 GW of fusion power and of the same configuration as LHD but 4 times larger (i.e. ~ 60 times in volume). Simulations were performed for evaluating the required characteristics of a fueling system (pellet size, injection speed and frequency) for satisfying the power balance in the plasma, using transport properties measured in LHD extrapolated to a thermonuclear plasma ([93, 94]). They showed that :

— a deep core fueling is mandatory for carrying by diffusion the matter at the center

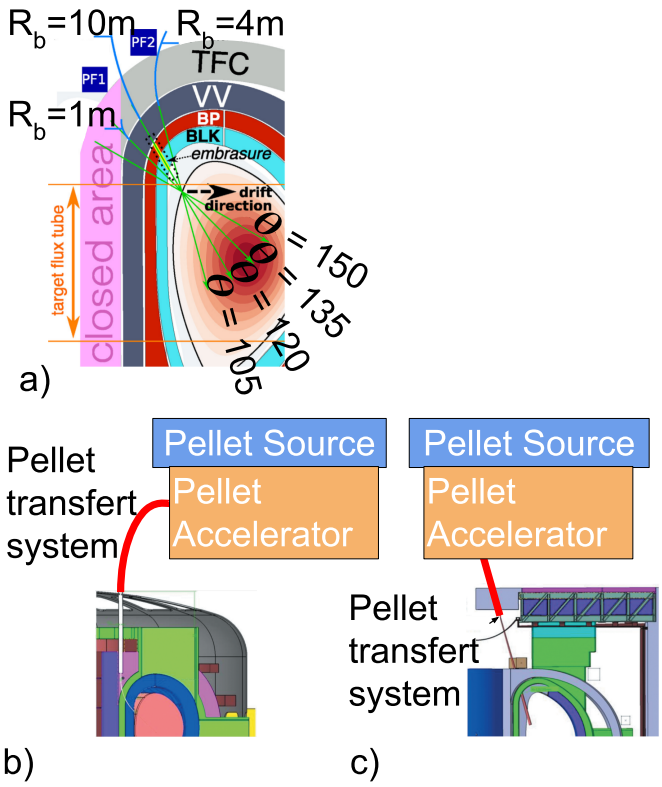


Figure 1.16. – (a) JA-DEMO geometry including the toroidal field coils (TFC), vacuum vessel (VV), back plate (BP), tritium breeding blanket (BLK) and plasma. Spatial relationships between target flux tube and injection point, pellet guide tube curvature radius (R_b) and injection angle (θ) are shown. Pink filled area is closed by TFC [90]. (b) Generic view of subsystem core fueling for EU-DEMO, composed of pellet source, pellet accelerator, and pellet transfer system aiming at the magnetic HFS of the plasma. The speed range is at least 1200 m s^{-1}, hence centrifuge or single-stage gas gun is regarded to be suitable. (c) Alternative variant using a direct-line-of-sight transfer system. High speeds up to 3000 m s^{-1} is required. Only double-stage gas gun technology will be able to reach this speed range [80]

.

of the discharge,
— the performance of present day injectors are sufficient for the required fueling (particle content 2×10^{22} at, velocity $V_p \sim 1$ km s^{-1}, injection frequency 10 Hz), but at the price of a large particle throughput, of the order of ~ 320 Pa m^3 s^{-1} (1.6×10^{23} at s^{-1}),
— it is possible to decrease this throughput by using a higher pellet speed (decrease by a factor of 3 for $V_p \sim 10$ km s^{-1}, requiring an injection frequency of $\sim$ 3Hz), but these velocities are out of the performance of today's technology,
— it is not possible to decrease this throughput by using larger pellets, the variation of the fusion power at every injection leading to unacceptable heat loads on the divertor,
— finally, preliminary estimations seem to show that the SDC regime, demonstrated in LHD [71], would be only accessible in a reactor if major progresses are done in the techniques of matter injection (pellet velocity larger than 10 km s^{-1} or injection of compact toroids). In this case, the fueling requirement is the same than that estimated for extrapolated LHD discharge (point 2) [95].

1.6. Summary

Up to now, pellet injection is the most mature method for a direct fueling of the plasma core in next generation devices. But the physics of the homogenization in the discharge of the matter locally deposited, under the form of cold and dense clouds, leads to a difference in performance depending on the type of device considered (tokamak, stellarator or reversed field pinch). A simple description of the main phenomena that – in the state of our current understanding – govern the acceleration and damping of the drift of the deposited material down the magnetic field gradient allows to explain these differences. Particularly, one shows that, under the same conditions, the material radial displacement during its homogenization is larger in a tokamak than in a stellarator, and that its drift is mainly damped close to the reversal radius in a reversed field pinch.
The two main advantages of pellet injection w.r.t. the other usual fueling methods (Gas Puff and Supersonic Molecular Beam Injection), namely a higher fueling efficiency and a better decoupling between the core and edge densities, are documented for a long time. Consequently, activity during this last decade was more concentrated on the compatibility of pellet fueling with the high performance plasma scenarios envisaged in the future machines. In tokamaks, in addition to the experiments on the mitigation of disruptions with shattered pellets, the main progress was, in ASDEX-Upgrade, the demonstration that pellet fueling could be compatible with the suppression of ELMs by Resonant Magnetic Perturbation in discharges of density larger than the Greenwald limit. In helical devices, the density profile tends to be hollow when the neoclassical transport is dominant. This difficulty was overcome in LHD and W7-X by the injection of trains of pellets at high frequency, the cooling of the plasma by the first pellets allowing the others to penetrate deeper in the discharge. This technique made possible not

only to obtain peaked density profiles, but also led to an energy confinement larger than that predicted by the empirical scaling ISS04. A better confinement was also measured in Heliotron J in pellet fueled discharges. These good results are nevertheless difficult to extrapolate to the next generation devices, of larger size, where the pellet material deposition will be shallow.
In these future machines, where the plasma pressure will be higher, the presence of the ∇B-induced drift will impose to inject pellets from the High Field Side. If high velocity injection from the top of the device – which requires a rectilinear guide tube – remains an option for EU-DEMO, the other projects (JA-DEMO, ITER, JT-60SA) privilege pure High Field Side injection with bended guide tubes, even if the latter strongly limit the injection velocity. This point underlines how important it is to integrate the pellet injection system from the beginning of the design of a device for minimizing the speed limitation. If in future tokamaks a deep enough deposition depth can be obtained with present injector technology, this is not the case in reactor-grade stellarators, where the first simulations tend to indicate that the required velocities are of the order or higher than 10 km.s^{-1}. A last point to be noted is – and this is the case for all the pulsed techniques of matter injection – that every pellet induces a variation of the instantaneous fusion power and of the heat load on the divertor. The pellet particle content must consequently be small in front of that of the plasma for this perturbation does not lead to difficulties in the plasma control and to preserve the integrity of the most exposed Plasma Facing Components.

2. MODELING OF PELLET TRAJECTORY INSIDE A GUIDE TUBE

Sommaire

2.1. Introduction 50
2.2. Guide tube building and frame definition 51
2.2.1. The laboratory and local frames 51
2.2.2. Geometry of a section in the local frame 51
2.2.3. Building the guide tube in the laboratory frame 52
2.2.4. Correspondence between the local and laboratory coordinates . 55
2.3. Trajectory between two impacts 55
2.3.1. Equation of motion 55
2.3.2. Pellet position and velocity at the impact point 56
2.3.3. Pellet position and velocity at the end of a section 57
2.4. Impact dynamics and condition for slipping or bouncing 57
2.4.1. Input parameters 57
2.4.2. Perpendicular dynamics and condition for slipping or bouncing 58
2.4.3. Parallel dynamics 61
2.4.4. Condition for slipping due to the curvature of the trajectory . . . 62
2.4.4.1. First order calculation 62
2.4.4.2. Limitation of the number of bounces by forcing the pellet to slip 64
2.4.5. Outputs of the bounce: erosion, heating, pellet position and velocity 65
2.5. Slipping dynamics 67
2.5.1. Cylindrical section 67
2.5.2. Toric section 68
2.5.3. End of slipping 69
2.6. Example of code results and main trends with input parameters 70
2.6.1. Example of bounce and slip 71
2.6.2. Influence of κ and θ on the bounce dynamics and pellet trajectory 74
2.6.2.1. Influence of κ and θ on the bounce dynamics 74
2.6.2.2. Influence of κ and θ on the whole trajectory 75
2.6.3. Influence of μ on the pellet exit parameters 79

2.6.4. Influence of the pellet input parameters and limitation of the number of bounces on the trajectories and exit parameters . . . 80
2.6.5. Calculations with exact slipping condition 82
2.6.6. Calculations with the $\alpha_{\mathrm{Lim}} = 3^{\circ}$ approximation 86
2.7. Summary and Future work 88

Abstract

High Field Side pellet injection will be used for fueling rector grade future devices. This technique requires the use of bended guide tubes, which limits the maximum velocity for reliable pellet injection, due to the forces exerted on the pellet when it bounces or slips on the guide tube wall, up to destroy the pellet when the induced constraint becomes larger than the ice yield strength. The forces experienced by a pellet are (1) that resultant from the pellet deformation during a bounce, (2) the centrifugal and Coriolis forces, (3) the slipping friction force, (4) the gravitation force and (5) the viscous friction with the residual gas filling up the guide tube. This report describes a code that aims at estimating quantitatively the time evolution of the mass, temperature, velocity and forces experienced by a pellet along its path in a guide tube, between the injector and its release in the vacuum chamber. Results are the evolution of the pellet mass, velocity, temperature, stored energy and forces applied to the ice along the pellet path. The probability that the pellet remains intact at its exit of the guide tube is calculated from the time history of the perpendicular forces applied to the pellet and from the stored elastic energy in the ice.

2.1. Introduction

Pellet injection is the most promising technique for fueling future large fusion devices. In such machines, the sharp increase of the plasma density and temperature inside the separatrix prevents pellets to penetrate far beyond the pedestal, and one must take advantage of the ∇B-induced drift, directed down the magnetic field gradient, for obtaining a deep matter deposition and an efficient core fueling ([96],[24]). This requires injecting pellets from the High Field Side of the device, either from the top at velocities up to several kilometers per second, e.g. ([97], [92]), or closer to the inner midplane at a smaller speed - from a few hundreds to $1-1.5$ kms^{-1} - more in the capability of present day injectors [29]. This second configuration, which is presently preferred, requires the use of a bended guide tube, which limits the maximum velocity allowing reliable pellet injection [80]. This limitation originates from the force exerted on the pellet when it bounces or slips on the guide tube wall, destroying the pellet when the induced constraint becomes larger than the Hydrogen ice yield strength.
The forces experienced by a pellet during its path in a bended guide tube are:

- The force associated to the pellet deformation during a bounce : $\sim R_p E_y \delta R_p$, where R_p is the pellet radius, E_y the Hydrogen ice Young modulus, and δR_p the contraction of the pellet radius at the time of the impact.
- The centrifugal force : $mv^2/\langle R\rangle$, where m and v are the pellet mass and velocity, and $\langle R\rangle$ the curvature radius of the trajectory of the pellet slipping along the wall of the guide tube.
- The Coriolis force: $\sim -2mv\langle\dot{R}\rangle/\langle R\rangle$.
- The friction force when the pellet slips along the tube: $\sim -\mu mv^2/\langle R\rangle$, where the value of μ, which depends on the roughness of the tube inner surface, on the ice properties and eventually, on the thickness and density of the tinny gas cloud around the pellet, should be determined experimentally.
- The gravitation : mg, where $g = 9.81$ m.s^{-2} is the gravitational acceleration. This force is essential for avoiding that a pellet launched in the middle of a rectilinear guide tube can be calculated to fly without touching the walls during an indefinite time.
- The viscous friction : $-\beta v^2$, proportional to the square of the pellet velocity in the range of Reynolds number relevant for pellet injection $\left(10^3 < \mathscr{R} < 10^5\right)$. It is directly linked to the pellet erosion and / or to the remaining of the propellant gas in case of gas gun injector. This force cannot be completely neglected, particularly in case of a pumping failure or if the previous pellet completely vaporizes in a section of the guide tube not efficiently pumped.

This report describes a code that aims at estimating quantitatively the time evolution of the erosion, temperature, velocity and force experienced by a pellet along its path in a guide tube between the injector and its release in the vacuum chamber. If coupled with a pumping calculation of the guide tube, it can also calculate the unavoidable gas source associated with pellet injection. Main approximation is that of a spherical - and not cylindrical - pellet, for limiting the number of degrees of freedom. The pellet can only bounce on or slip along the wall of the guide tube, without the possibility of

rolling, and rotation of the pellet is not considered. Consequently, the reflection at the time of a bounce is quasi-specular, even if there is the possibility for introducing a random perturbation of the direction of reflection for simulating the effect of the non-sphericity of the pellet. The calculation follows the center of mass of the pellet, i.e. the trajectory of a point in a tube of effective radius $R_\delta = R_G - R_p$, where R_G is the radius of the guide tube. It is noticeable that, since the pellet can be eroded during its path in the guide tube, R_δ is likely to continuously increase, even if R_G remains constant. Two reference frames are alternatively used: that of the laboratory (identified by the subscript L) where the global parameters of the pellet trajectory are reconstructed, and that dedicated to the calculation of the pellet bounce or slip, slowing down, erosion, heating and force exerted on the ice.
The structure of the code is explicated in the following. The guide tube building and coordinate transformation between the two reference frames are detailed in section 2.2 . The calculation of the trajectory between two impacts, impact dynamics, quasi-specular reflection (with the possible introduction of a random perturbation), and trajectory if the pellet slips along the guide tube wall are described in sections 2.3 to 2.5 . At every step, the slowing down, erosion and heating of the pellet are calculated. Finally, section 2.6 presents an example of the whole code results, followed by a discussion and a conclusion in Section 2.7.

2.2. Guide tube building and frame definition

2.2.1. The laboratory and local frames

Both the laboratory $\left(\overrightarrow{x_L}, \overrightarrow{y_L}, \overrightarrow{z_L}\right)$ and local $\left(\vec{x}, \vec{y}, \vec{z}\right)$ frames are Cartesian, with the vertical direction along the $\vec{z}$ axis in the laboratory frame ($\vec{g} = -9.81\ \vec{z}$). In the local frame, the entrance aperture of every guide tube section is centered at the origin and oriented in the $\vec{z}$ direction. Toric sections are located in the $\vec{x} \times \vec{y}$ plane, with the toroidal angle φ turning in the trigonometric sense. Parameters of cylindrical sections are their length L, and tube radius R_G, those of toric sections are their toroidal angular extension φ_M, and major and minor radii, R_0 and R_G (eventually complemented by the superscript j when necessary). See Figure 2.1 for the details of the geometry.

2.2.2. Geometry of a section in the local frame

Sections are identified by two sets of unit vectors, the first located at the entrance of the section, of coordinates $O_b(0,0,0)$, $X_b(1,0,0)$, $Y_b(0,1,0)$ and $Z_b(0,0,1)$, the second at the exit of the section, of coordinates $O_e\left(x_e^0, y_e^0, z_e^0\right)$, $X_e\left(x_e^x, y_e^x, z_e^x\right)$, $Y_e\left(x_e^y, y_e^y, z_e^y\right)$ and $Z_e\left(x_e^z, y_e^z, z_e^z\right)$.

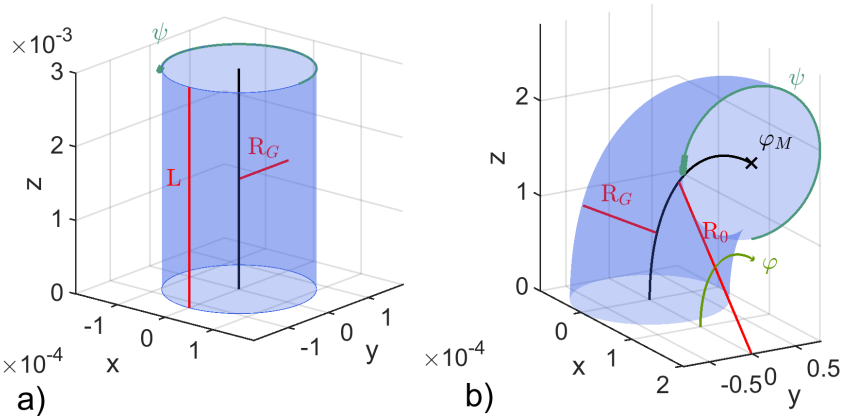


Figure 2.1. – Parameters defining the different guide tube sections and their arrangement in the local frame. a) cylindrical section, b) toric section.

For a cylindrical section (Figure 2.2a):

$$\begin{array}{rcl}
\left(x_e^0, y_e^0, z_e^0\right) & = & (0, \quad 0, \quad L \quad) \\
\left(x_e^x, y_e^x, z_e^x\right) & = & (1, \quad 0, \quad L \quad) \\
\left(x_e^y, y_e^y, z_e^y\right) & = & (0, \quad 1, \quad L \quad) \\
\left(x_e^z, y_e^z, z_e^z\right) & = & (0, \quad 0, \quad 1+L \quad)
\end{array}$$

For a toric section (Figure 2.2b):

$$\begin{array}{rcl}
\left(x_e^0, y_e^0, z_e^0\right) & = & (\quad R_0\left(1-\cos(\varphi_M)\right), \quad 0, \quad R_0\sin(\varphi_M) \quad) \\
\left(x_e^x, y_e^x, z_e^x\right) & = & (\quad x_e^0+\cos(\varphi_M), \quad 0, \quad z_e^0-\sin(\varphi_M) \quad) \\
\left(x_e^y, y_e^y, z_e^y\right) & = & (\quad x_e^0, \quad 1, \quad z_e^0 \quad) \\
\left(x_e^z, y_e^z, z_e^z\right) & = & (\quad x_e^0+\sin(\varphi_M), \quad 0, \quad z_e^0+\cos(\varphi_M) \quad)
\end{array}$$

2.2.3. Building the guide tube in the laboratory frame

Transfer in the laboratory frame is made in four steps, with intermediate frames $\left(\vec{x'}, \vec{y'}, \vec{z'}\right)$ and $\left(\vec{x''}, \vec{y''}, \vec{z''}\right)$. They are:

— From $(\vec{x}, \vec{y}, \vec{z})$ to $\left(\vec{x'}, \vec{y'}, \vec{z'}\right)$, a rotation of angle $\alpha_x(\in]0, \pi])$ around axis $\vec{x}$.

— From $\left(\vec{x'}, \vec{y'}, \vec{z'}\right)$ to $\left(\vec{x''}, \vec{y''}, \vec{z''}\right)$, a rotation of angle $\alpha_y(\in]0, 2\pi])$ around axis $\vec{y'}$.

— From $\left(\vec{x''}, \vec{y''}, \vec{z''}\right)$ to $\left(\vec{x}_L, \vec{y}_L, \vec{z}_L\right)$, a rotation of angle $\alpha_z(\in]0, 2\pi])$ around axis $\vec{z''}$.

— And finally a translation of vector $\left(x_L^0, y_L^0, z_L^0\right)$.

This writes:

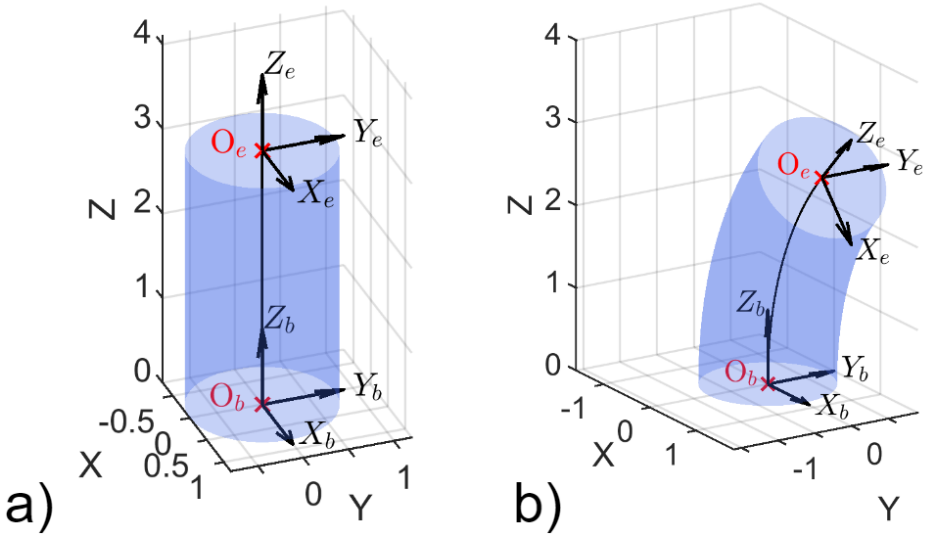


Figure 2.2. – Definition of the entrance and exit sets of unit vectors. a) cylindrical section, b) toric section.

$$\begin{pmatrix} x_L \\ y_L \\ z_L \end{pmatrix} = [M] \begin{pmatrix} x \\ y \\ z \end{pmatrix} + \begin{pmatrix} x_L^0 \\ y_L^0 \\ z_L^0 \end{pmatrix} \tag{2.1}$$

with

$$[M](\alpha_x, \alpha_y, \alpha_z) =$$
$$\begin{bmatrix} \cos\alpha_y \cos\alpha_z & -\cos\alpha_y \sin\alpha_z & \sin\alpha_y \\ \sin\alpha_x \sin\alpha_y \cos\alpha_z + \cos\alpha_x \sin\alpha_z & -\sin\alpha_x \sin\alpha_y \sin\alpha_z + \cos\alpha_x \cos\alpha_z & -\sin\alpha_x \cos\alpha_y \\ -\cos\alpha_x \sin\alpha_y \cos\alpha_z + \sin\alpha_x \sin\alpha_z & \cos\alpha_x \sin\alpha_y \sin\alpha_z + \sin\alpha_x \cos\alpha_z & \cos\alpha_x \cos\alpha_y \end{bmatrix}$$

In the laboratory frame, O_b, X_b, Y_b, Z_b and O_e, X_e, Y_e, Z_e are transformed in O_{Lb}, X_{Lb}, Y_{Lb}, Z_{Lb} and O_{Leb}, X_{Le}, Y_{Le}, Z_{Le} by eq. 2.1. The connection between two sections labelled j and $j+1$ is then done by requiring that the vector $\overrightarrow{O_{Lb}^{j+1} Z_{Lb}^{J+1}}$ is superimposed to that defined by $\overrightarrow{O_{Le}^{J} Z_{Le}^{J}}$, when those defined by $\overrightarrow{O_{Lb}^{J+1} X_{Lb}^{J+1}}$ and $\overrightarrow{O_{Lb}^{J+1} Y_{Lb}^{J+1}}$ can rotate by an angle $\delta\alpha_z^{j+1}$ around the direction defined by $\overrightarrow{O_{Le}^{J} Z_{Le}^{J}} = \overrightarrow{O_{Lb}^{J+1} Z_{Lb}^{J+1}}$ with respect to $\overrightarrow{O_{Le}^{J} X_{Le}^{J}}$ and $\overrightarrow{O_{Le}^{J} Y_{Le}^{J}}$. See Figure 2.3 .
This leads to:

$$
\begin{aligned}
O_{Lb}^{j+1} &= & O_{Le}^{j} \\
X_{Lb}^{j+1} &= & O_{Le}^{j} + [M]\left(\alpha_x^{j+1}, \alpha_y^{j+1}, \alpha_z^{j+1} + \delta\alpha_z^{j+1}\right) X_{Le}^{j} \\
Y_{Lb}^{j+1} &= & O_{Le}^{j} + [M]\left(\alpha_x^{j+1}, \alpha_y^{j+1}, \alpha_z^{j+1} + \delta\alpha_z^{j+1}\right) Y_{Le}^{j} \\
Z_{Lb}^{j+1} = Z_{Le}^{j} &= & O_{Le}^{j} + [M]\left(\alpha_x^{j+1}, \alpha_y^{j+1}, \alpha_z^{j+1} + \delta\alpha_z^{j+1}\right) Z_{Le}^{j}
\end{aligned}
$$

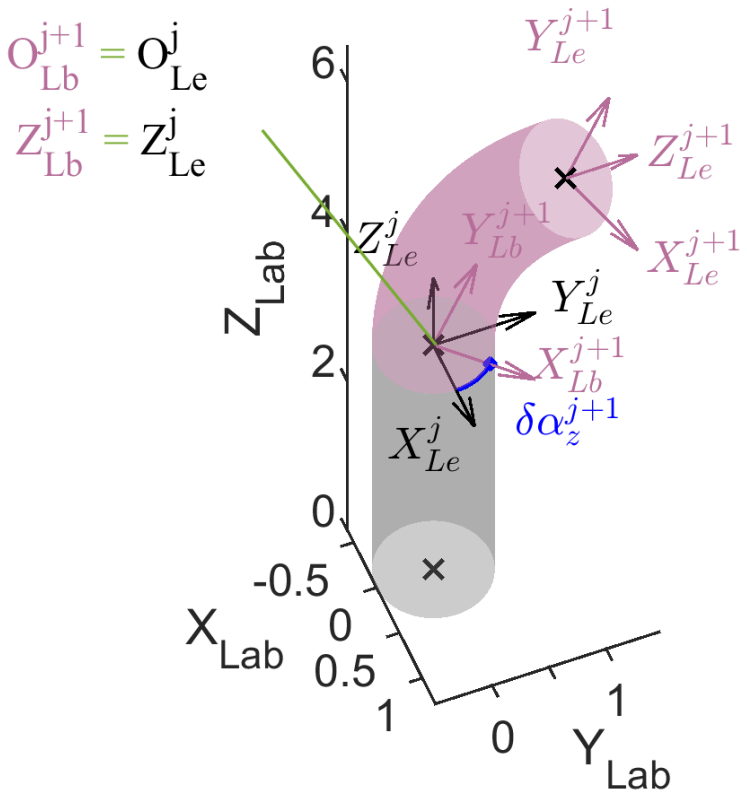


Figure 2.3. – Connection of two sections, labelled j and $j+1$, in the laboratory frame.

2.2.4. Correspondence between the local and laboratory coordinates

For calculating the different characteristics of the pellet trajectory, it is necessary to transfer a guide tube section from the laboratory frame to the local frame. Knowing the coordinates $O_L\left(x_L^0, y_L^0, z_L^0\right)$, $X_L\left(x_L^x, y_L^x, z_L^x\right)$, $Y_L\left(x_L^y, y_L^y, z_L^y\right)$ and $Z_L\left(x_L^z, y_L^z, z_L^z\right)$ defining the set of unit vectors at the entrance of the considered section, the angles α_x, α_y and α_z are determined by the relations:

$$\alpha_x = -\tan^{-1}\left[\left(y_L^z - y_L^0\right)/\left(z_L^z - z_L^0\right)\right] + \pi C_x(i) \tag{2.2a}$$

$$\alpha_y = \tan^{-1}\left[\left(x_L^z - x_L^0\right)\cos\alpha_x/\left(z_L^z - z_L^0\right)\right] + \pi C_y(i) \tag{2.2b}$$

$$\alpha_z = -\tan^{-1}\left[\left(y_L^x - y_L^0\right)/\left(x_L^x - x_L^0\right)\right] + \pi C_z(i) \tag{2.2c}$$

where i is defined by requiring that the i^{th} line of the matrix P equals :

$$\left[\text{sign}\left(x_L^x - x_L^0\right), \text{sign}\left(y_L^x - y_L^0\right), \text{sign}\left(x_L^z - x_L^0\right), \text{sign}\left(y_L^z - y_L^0\right), \text{sign}\left(z_L^z - z_L^0\right)\right].$$

The matrix P and vectors C_x, C_y and C_z are explicated in Appendix A.1. The inverse transfer, from $\left(\vec{x_L}, \vec{y_L}, \vec{z_L}\right)$ to $(\vec{x}, \vec{y}, \vec{z})$, writes then:

$$\begin{pmatrix} x \\ y \\ z \end{pmatrix} = [M'] \begin{pmatrix} x_L - x_L^0 \\ y_L - y_L^0 \\ z_L - z_L^0 \end{pmatrix} \tag{2.3}$$

with

$$[M']\left(-\alpha_z, -\alpha_y, -\alpha_x\right) =$$

$$\begin{bmatrix} \cos\alpha_y\cos\alpha_z & \cos\alpha_x\sin\alpha_z + \sin\alpha_x\sin\alpha_y\cos\alpha_z & \sin\alpha_x\sin\alpha_z - \cos\alpha_x\sin\alpha_y\cos\alpha_z \\ -\cos\alpha_y\sin\alpha_z & \cos\alpha_x\cos\alpha_z - \sin\alpha_x\sin\alpha_y\sin\alpha_z & \sin\alpha_x\cos\alpha_z + \cos\alpha_x\sin\alpha_y\sin\alpha_z \\ \sin\alpha_y & -\sin\alpha_x\cos\alpha_y & \cos\alpha_x\cos\alpha_y \end{bmatrix}$$

2.3. Trajectory between two impacts

2.3.1. Equation of motion

During its flight between two successive impacts, the pellet experiences two forces: the gravity and the fluid friction with the remaining gas filling up the guide tube. The latter writes $\vec{F}_f = -\beta v^2(\vec{v}/|v|)$, with $\beta = \frac{\pi}{2}R_p^2\rho C_D$, where ρ is the mass density of the remaining gas and the drag coefficient $C_D \sim 0.4 - 0.5$ for a sphere in the range of Reynolds number $2\ 10^3 < \mathscr{R} < 3\ 10^5$ [98]. The differential equation governing the

pellet velocity is then:

$$\dot{v}^s + \frac{\beta}{m_1} v^2 \left(v^s/|v|\right) = \vec{g}\cdot\vec{s} = g^s$$

where m_1 is the initial pellet mass and where $s = x, y$ or z in the local reference frame (note that if $\vec{g}$ has only a z-component in the laboratory frame, it can have 3 non-zero components in the local frame, depending on the orientation of the considered section). In this whole section, subscript "1" refers to the origin of the pellet flight and subscript "2" to its end.
The solution of the above equation (with its first order development, valid for $\Delta t \ll \frac{\beta|v_1|}{m_1}$) is, in terms of velocity v and position s:

$$\begin{array}{lll} v^s(t) & = \frac{m_1 g^s}{\beta|v_1|} + \left(v_1^s - \frac{m_1 g^s}{\beta|v_1|}\right) e^{-\frac{\beta|v_1|}{m_1}t} & \rightarrow \quad v_1^s + \left(g^s - \frac{\beta|v_1|v_1^s}{m_1}\right) t \\ s(t) & = s_1 + \frac{m_1 g^s}{\beta|v_1|}t + \left(\frac{m_1(\beta|v_1|v_1^s - m_1 g^s)}{\beta^2 v_1^2}\right) & \rightarrow \quad s_1 + v_1^s t + \left(g^s - \frac{\beta|v_1|v_1^s}{m_1}\right)\frac{t^2}{2} \end{array} \tag{2.4}$$

where v_1 is the initial pellet velocity and where s_1 and v_1^s are the s-component of the initial position and velocity of the pellet.

2.3.2. Pellet position and velocity at the impact point

The coordinates of the successive impact points are calculated by following the motion of the center of the pellet in cylindrical or toric sections of radius $R_{\delta 1} = R_G - R_{p1}$, where R_{p1} is the pellet radius at the beginning of the considered flight. In the local reference frame, the parametric equations describing the shape of the wall of the guide tube are, for a cylinder:

$$\begin{array}{ll} x_c = & R_{\delta 1}\cos\psi \\ y_c = & R_{\delta 1}\sin\psi \\ z_c = & z \end{array} \tag{2.5}$$

where ψ is the poloidal angle (Figure 2.1b), and for a torus:

$$\begin{array}{ll} x_t = & R_0(1-\cos\varphi) + R_{\delta 1}\cos\varphi\cos\psi \\ y_t = & R_{\delta 1}\sin\psi \\ z_t = & R_0\sin\varphi - R_{\delta 1}\sin\varphi\cos\psi \end{array} \tag{2.6}$$

Where φ is the toroidal angle (Figure 2.1b). The pellet trajectory is followed from its initial position (x_1, y_1, z_1) and velocity (v_1^x, v_1^y, v_1^z) up to the point where it matches the equations defining the wall of the guide tube.
This yields, for a cylinder:

$$\left[x_c\left(\psi_2, z_2\right), y_c\left(\psi_2, z_2\right), z_c\left(\psi_2, z_2\right)\right] = [x(t), y(t), z(t)]$$

where the unknowns are z_2, ψ_2 and the time t.
And for a torus :

$$\left[x_t\left(\psi_2,\varphi_2\right), y_t\left(\psi_2,\varphi_2\right), z_t\left(\psi_2,\varphi_2\right)\right] = [x(t), y(t), z(t)]$$

where the unknowns are φ_2, ψ_2 and t.
In both cases, the coordinates of the impact point $\left(x_2, y_2, z_2\right)$ and the different components of the pellet velocity $\left(v_2^x, v_2^y, v_2^z\right)$ are calculated by equations (2.4), (2.5) and (2.6).

2.3.3. Pellet position and velocity at the end of a section

In the last part of its path in a guide tube section, the pellet does not hit the wall, but escapes the section through the aperture at the end of the latter. The coordinates and velocity of the pellet at its exit are then determined by calculating the intersection of the pellet trajectory with the plane $\mathscr{P}$ defining the end aperture of the section. The later can be defined by 3 points : $p1$ ($\psi = \pi/2$), $p2$ ($\psi = \pi$) and $p3$ (the end of the central line). Writing their coordinates as $\left[x_{pi}, y_{pi}, z_{pi}\right]$, where $i = [1,2,3]$, one can define 2 noncollinear vectors ($\vec{u}_1$ and $\vec{u}_2$) (see Figure 2.4) leading to the parametric equation of $\mathscr{P}$:

$$\mathscr{P} = \left[x_{\mathscr{P}}, y_{\mathscr{P}}, z_{\mathscr{P}}\right] = \left[x_{pi}, y_{pi}, z_{pi}\right] + \chi_1\left[u_{1x}, u_{1y}, u_{1z}\right] + \chi_2\left[u_{2x}, u_{2y}, u_{2z}\right] \quad (2.7)$$

Where χ_1 and χ_2 ($\in \mathbb{R}$) are the plane parameters. The coordinates of the exit point $\left(x_2, y_2, z_2\right)$ are given for a cylindrical or toric section by the set of equations:

$$\left[x_{\mathscr{P}}\left(\chi_1,\chi_2\right), y_{\mathscr{P}}\left(\chi_1,\chi_2\right), z_{\mathscr{P}}\left(\chi_1,\chi_2\right)\right] = [x(t), y(t), z(t)]$$

In both cases, the unknowns are χ_1, χ_2 and t, and the different components of the pellet velocity $\left(v_2^x, v_2^y, v_2^z\right)$ are calculated by eq. 2.4.

2.4. Impact dynamics and condition for slipping or bouncing

2.4.1. Input parameters

When arriving at the impact point (hereafter indicated by the subscript “2”), the effective radius of the guide tube is $R_{\delta 2}$, the pellet mass and temperature are m_2 and T_2, respectively, and its incident velocity v_2.

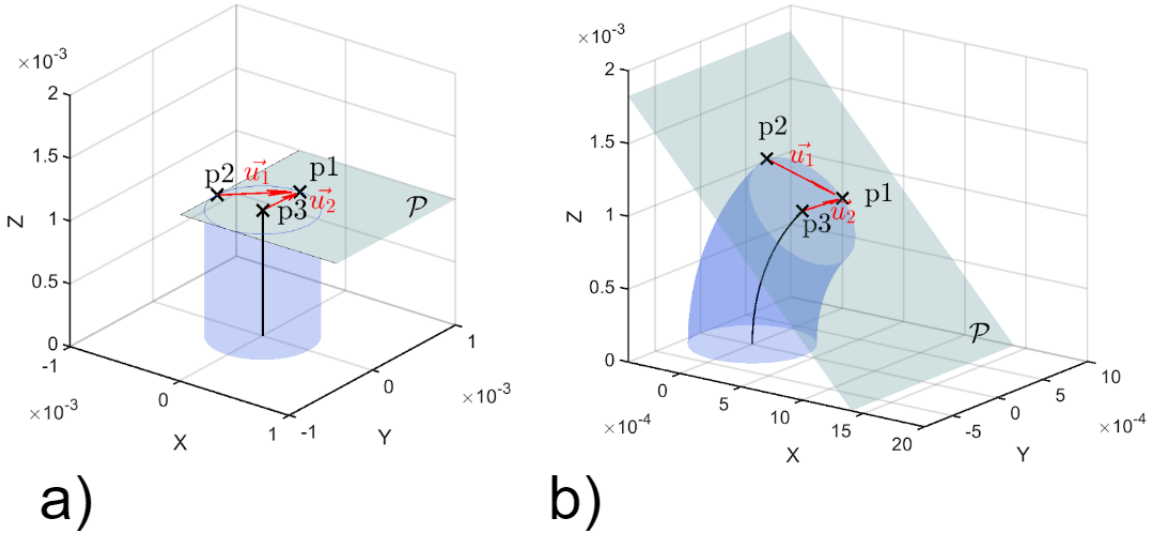


Figure 2.4. – Schematic of the plane $\mathscr{P}$ at the end of a cylindrical a) and toric b) sections, with the points pi chosen for its definition and that of the vectors $\vec{u}_{1,2}$.

2.4.2. Perpendicular dynamics and condition for slipping or bouncing

The impact dynamics is described by a Kelvin-Voigt viscoelastic model (see, e.g. [99] and Appendix A.2). At the impact point, the pellet mass is m_2 and its initial velocity v_2. For a cylindrical section, it is convenient to use the frame:

$$\begin{pmatrix} u_r \\ u_\psi \\ u_z \end{pmatrix} = \begin{pmatrix} \cos\psi_2 & \sin\psi_2 & 0 \\ -\sin\psi_2 & \cos\psi_2 & 0 \\ 0 & 0 & 1 \end{pmatrix} \begin{pmatrix} u^x \\ u^y \\ u^z \end{pmatrix} \tag{2.8}$$

with the inverse transformation:

$$\begin{pmatrix} u_x \\ u_y \\ u_z \end{pmatrix} = \begin{pmatrix} \cos\psi_2 & -\sin\psi_2 & 0 \\ \sin\psi_2 & \cos\psi_2 & 0 \\ 0 & 0 & 1 \end{pmatrix} \begin{pmatrix} u^r \\ u^\psi \\ u^z \end{pmatrix} \tag{2.9}$$

and for a toric section:

$$\begin{pmatrix} u_r \\ u_\psi \\ u_\varphi \end{pmatrix} = \begin{pmatrix} \cos\varphi_2\cos\psi_2 & \sin\psi_2 & -\sin\varphi_2\cos\psi_2 \\ -\cos\varphi_2\sin\psi_2 & \cos\psi_2 & \sin\varphi_2\sin\psi_2 \\ \sin\varphi_2 & 0 & \cos\varphi_2 \end{pmatrix} \begin{pmatrix} u^x \\ u^y \\ u^z \end{pmatrix} \tag{2.10}$$

with the inverse transformation:

$$\begin{pmatrix} u_x \\ u_y \\ u_z \end{pmatrix} = \begin{pmatrix} \cos\varphi_2\cos\psi_2 & -\cos\varphi_2\sin\psi_2 & \sin\varphi_2 \\ \sin\psi_2 & \cos\psi_2 & 0 \\ -\sin\varphi_2\cos\psi_2 & \sin\varphi_2\sin\psi_2 & \cos\varphi_2 \end{pmatrix} \begin{pmatrix} u^r \\ u^\psi \\ u^\varphi \end{pmatrix} \tag{2.11}$$

where the pellet coordinates are known from Section 2.3. The two forces acting on the ice as long as the pellet is in contact with the wall are the gravity $\left(m_2\vec{g}\cdot\vec{u}_\perp\right)\vec{u}_\perp$ and the centrifugal force $\left(\vec{F}_C\cdot\vec{u}_\perp\right)\vec{u}_\perp$.
In a cylindrical section, the latter writes:

$$F^r_{c_2} = \frac{m_2 v_2^{\psi^2}}{R_{\delta 2}} \tag{2.12}$$

In a toric section:

$$F^r_{C_2} = m_2\left(-\frac{v_2^{\varphi^2}\cos\psi_2}{R_0 - R_{\delta 2}\cos\psi_2} + \frac{v_2^{\psi^2}}{R_{\delta 2}}\right) \tag{2.13}$$

Writing the centrifugal force as $F^r_{C_2} = \frac{m_2 v_2^{\parallel 2}}{<R>}$, one obtains the expression of the curvature radius $< R >$ which is, for a cylinder:

$$< R >= \frac{v_2^{\psi 2} + v_2^{z2}}{\frac{v_2^{\psi^2}}{R_{\delta 2}}} \tag{2.14}$$

and for a torus:

$$< R >= \frac{v_2^{\psi 2} + v_2^{\varphi 2}}{-\frac{v_2^{\varphi^2}\cos\psi_2}{R_0 - R_{\delta 2}\cos\psi_2} + \frac{v_2^{\psi^2}}{R_{\delta 2}}} \tag{2.15}$$

Stricto sensu, the magnitude of F^r_c varies during the impact, since the slipping friction reduces both v_2^φ and v_2^ψ. However, this variation is small enough for being neglected in this calculation. In the frame of a Kelvin-Voigt model (an elastic spring and a viscous damper connected in parallel), two parameters characterize the behavior of the pellet during the impact: κ, in $\left[kg.s^{-2}\right]$, and θ, in $[kg.s^{-1}]$. These parameters integrate not only the ice properties but also the characteristics of the gas cloud surrounding the pellet, and they can change significantly with the incidence angle of the pellet trajectory. As long as v_2^r is large enough, they are dominated by the ice Young's modulus E_Y and viscosity η. One has then $\kappa \to R_p E_Y$ and $\theta \to R_p\eta$, and the pellet/cloud system behaves as a weakly damped oscillator. But at grazing incidence, the gas characteristics can dominate, and the pellet/cloud system behaves as a strongly damped oscillator. It is assumed in the following that κ is a constant for any deformation r of the pellet surface, which is not necessarily true in the general case. Analogously, the parameter

θ, which integrates not only the ice properties but also the characteristics of the gas cloud surrounding the pellet and/or those of the liquid film at the pellet tube interface, should be determined experimentally. This approximation can be partially removed by introducing an *a priori* dependence of κ & θ on v_2^r. Then, the differential equation that governs the pellet deformation is:

$$\ddot{r} + \frac{\theta}{m_2}\dot{r} + \frac{\kappa}{m_2} r = \left(\frac{F_{c_2}^r}{m_2} + g_2^r\right) \tag{2.16}$$

Giving the force exerted on the pellet as:

$$F^r(t) = F_{\text{ext}} - \theta \dot{r}(t) - \kappa r(t) \tag{2.17}$$

with

$$F_{\text{ext}} = F_{c_2}^r + m_2 g_2^r$$

The solution of eq.2.16 depends on whether θ is smaller or larger than $2\sqrt{\kappa m_2}$.

If $\theta < 2\sqrt{\kappa m_2}$:

$$r(t) = \frac{F_{c_2}^r + m_2 g^r}{\kappa}\left\{1 - e^{-t/\tau}\left[\cos(\omega t) + B\sin(\omega t)\right]\right\} \tag{2.18a}$$

$$v^r(t) = \dot{r}(t) = \frac{F_{c_2}^r + m_2 g^r}{\kappa} e^{-t/\tau}\left\{\left[\frac{1}{\tau} - \omega B\right]\cos(\omega t) + \left[\frac{B}{\tau} + \omega\right]\sin(\omega t)\right\} \tag{2.18b}$$

where

$$\omega = \sqrt{\frac{\kappa}{m_2} - \frac{\theta^2}{4m_2^2}},\ \tau = 2m_2/\theta,\ \text{and}\ B = \frac{1}{\omega}\left(\frac{1}{\tau} - \frac{\kappa v_2^r}{F_{c_2}^r + m_2 g^r}\right)$$

The contact between the pellet and the wall stops for $r(t) = 0$, i.e. for the bounce time t_B such that :

$$e^{t_B/\tau} = \cos(\omega t_B) + B\sin(\omega t_B) \tag{2.19}$$

The pellet does not bounce, but slips along the wall of the guide tube if eq.2.19 has no solution.

If $\theta > 2\sqrt{\kappa m_2}$ (the critical solution $\theta = 2\sqrt{\kappa m_2}$ is of no practical interest):

$$r(t) = \frac{F_{c_2}^r + m_2 g^r}{\kappa}\left\{1 - \frac{1}{r_E - r_F}\left[\begin{array}{l}\left(\frac{\kappa v_2^r}{F_{c_2}^r + m_2 g^r} - r_F\right)e^{-r_E t} + \\ \left(-\frac{\kappa v_2^r}{F_{c_2}^r + m_2 g^r} + r_E\right)e^{-r_F t}\end{array}\right]\right\} \tag{2.20a}$$

$$v^r(t) = \dot{r}(t) = \frac{F_{c_2}^r + m_2 g^r}{\kappa}\frac{1}{r_E - r_F}\left[\begin{array}{l}\left(\frac{\kappa v_2^r}{F_{c_2}^r + m_2 g^r} - r_F\right)r_E e^{-r_E t} + \\ \left(-\frac{\kappa v_2^r}{F_{c_2}^r + m_2 g^r} + r_E\right)r_F e^{-r_F t}\end{array}\right] \tag{2.20b}$$

where :

$$r_{E/F} = \sqrt{\frac{\kappa}{m_2}}\left[\frac{\theta}{2\sqrt{\kappa m_2}} + / - \left(\frac{\theta^2}{4\kappa m_2} - 1\right)^{1/2}\right]$$

In these conditions,

$$\lim_{t\to\infty} r(t) = \frac{F_{c_2}^r + m_2 g^r}{\kappa}$$

and there is no solution for $r(t) = 0$. Consequently, the pellet systematically slips along the wall of the guide tube after the impact.

2.4.3. Parallel dynamics

During the time where the pellet is in contact with the wall, its parallel velocity, $v^{\parallel} = \sqrt{v^{\psi^2} + v^{z|\varphi^2}}$, is essentially reduced by the slipping friction of intensity $\mu F^r(t)$ since the braking by the fluid friction is negligible. The differential equation $v^{\parallel}$ obeys to is:

$$\dot{v}^{\parallel} = \mu F^r / m_2$$

From eqs 2.17 and 2.18, for $\theta < 2\sqrt{\kappa m_2}$, it comes:

$$v^{\parallel}(t) = v_2^{\parallel} + \frac{\mu}{m} F_{\text{ext}}\left[-\alpha_{1s} + e^{-t/\tau}\left\{\alpha_{1s}\cos(\omega t) + \alpha_{s2}\sin(\omega t)\right\}\right] \tag{2.21}$$

with:

$$\begin{cases} \alpha_{1s} = \frac{\theta}{\kappa} - \frac{\tau + B\tau^2\omega}{(1+\omega^2\tau^2)} \\ \alpha_{2s} = \frac{B\theta}{\kappa} + \frac{\omega\tau^2 - \tau B}{(1+\omega^2\tau^2)} \end{cases} \tag{2.22}$$

From eqs 2.17 and 2.20, for $\theta > 2\sqrt{\kappa m_2}$, one obtains:

$$\begin{aligned} v^{\parallel}(t) = &\left[v_2^{\parallel} + \frac{\mu F_{\text{ext}}}{m}\left(\frac{1}{(r_E - r_F)}\left(\frac{\alpha_{1L}}{r_E} + \frac{\alpha_{2_L}}{r_F}\right) - \frac{\theta}{\kappa}\right)\right] \\ &+ \frac{\mu F_{\text{ext}}}{m}\frac{1}{(r_E - r_F)}\left[\left(\frac{\theta}{\kappa} - \frac{1}{r_E}\right)\alpha_{1L}e^{-r_E t} + \left(\frac{\theta}{\kappa} - \frac{1}{r_F}\right)\alpha_{2L}e^{-r_F t}\right] \end{aligned} \tag{2.23}$$

with:

$$\begin{cases} \alpha_{1L} = \left(\frac{\kappa v_2^r}{F_{c_2}^r + m_2 g^r} - r_F\right) \\ \alpha_{2L} = \left(-\frac{\kappa v_2^r}{F_{c_2}^r + m_2 g^r} + r_E\right) \end{cases} \tag{2.24}$$

The components of the pellet velocity at the end of the bounce, $v_2'^r = v^r(t_B)$, $v_2'^{\psi} = \frac{v^{\parallel}(t_B)v_2^{\psi}}{\sqrt{v_2^{\psi^2} + v_2^{z|\varphi^2}}}$ and $v_2'^{z|\varphi} = \frac{v^{\parallel}(t_B)v_2^{z|\varphi}}{\sqrt{v_2^{\psi^2} + v_2^{z|\varphi^2}}}$ can be calculated by eqs. 2.18b, 2.20b, 2.21 and (2.23). At this stage, for mimicking the effect of the non-sphericity of the pellet, it is possible to introduce a random perturbation on the velocity components: δv^r, δv^{ψ}

and $\delta v^{z|\varphi}$. The latter must satisfy:

$$\left(v^{\psi}+\delta v^{\psi}\right)^2+\left(v^{r}+\delta v^{r}\right)^2+\left(v^{z|\varphi}+\delta v^{z|\varphi}\right)^2=v^{\psi^2}+v^{r^2}+v^{z|\varphi^2}$$

The parallel distance covered during the time t_B writes, for $\theta<2\sqrt{\kappa m_2}$:

$$s^{\parallel}(t_B)=\left[v_2^{\parallel}-\frac{\mu}{m}F_{\text{ext}}\alpha_{1s}\right]t_B+\frac{\mu F_{\text{ext}}}{m}\frac{\tau}{\left(\tau^2\omega^2+1\right)}\left[\lambda_{1s}+e^{-t/\tau}\left[-\lambda_{1s}\cos\left(\omega t_B\right)+\lambda_{2s}\sin\left(\omega t_B\right)\right]\right] \tag{2.25}$$

with:

$$\begin{cases}\lambda_{1s}=\alpha_{1s}+\alpha_{2s}\omega\tau\\ \lambda_{2s}=-\alpha_{2s}+\alpha_{1s}\omega\tau\end{cases} \tag{2.26}$$

and α_{1s} & α_{2s} given in eq 2.22.
And for $\theta>2\sqrt{\kappa m_2}$:

$$\begin{aligned}s^{\parallel}(t_B)=&\left[v_2^{\parallel}+\frac{\mu F_{\text{ext}}}{m}\left[\frac{1}{(r_E-r_F)}\left(\frac{\alpha_{1L}}{r_E}+\frac{\alpha_{2L}}{r_F}\right)-\frac{\theta}{\kappa}\right]\right]t_B+\\ &\frac{\mu F_{\text{ext}}}{m}\frac{1}{(r_E-r_F)}\left[\left(\frac{1}{{r_E}^2}-\frac{\theta}{\kappa r_E}\right)\alpha_{1L}e^{-r_E t_B}+\left(\frac{1}{{r_F}^2}-\frac{\theta}{\kappa r_F}\right)\alpha_{2L}e^{-r_F t_B}\right]+\\ &\frac{\mu F_{\text{ext}}}{m}\frac{1}{(r_E-r_F)}\left[\left(-\frac{1}{{r_E}^2}+\frac{\theta}{\kappa r_E}\right)\alpha_{1L}+\left(-\frac{1}{{r_F}^2}+\frac{\theta}{\kappa r_F}\right)\alpha_{2L}\right]\end{aligned} \tag{2.27}$$

with α_{1L} & α_{2L} expressed in eq 2.24.

2.4.4. Condition for slipping due to the curvature of the trajectory

2.4.4.1. First order calculation

For simplicity, the calculation of section 2.4.2 is performed for a bounce on a flat surface, which is generally not the case in a guide tube. This can make the pellet to slip along the wall surface at the bounce exit even if, *stricto sensu*, its whole perpendicular kinetic energy is not absorbed during the bounce. This effect can be taken into account by a first order correction of the direction of the pellet velocity w.r.t. the wall, the principle of which is displayed in Figure 2.5. At the exit of the bounce, the velocity components w.r.t. the flat reference surface are ${v'_2}^r$ and ${v'_2}^{\parallel}=v^{\parallel}(t_B)$. The angle between the pellet velocity and this reference surface is therefore $\alpha=\arcsin\left(\frac{{v'_2}^r}{\sqrt{{v'_2}^{r2}+{v'_2}^{\parallel^2}}}\right)=\arcsin\left(\frac{{v'_2}^r}{v'_2}\right)$.
But due to the curvature of the pellet trajectory at the bounce location (of radius $\langle R\rangle$) and to the parallel distance $s_{\parallel}(t_B)$ covered during the bounce, the wall direction w.r.t. the reference flat surface has changed by an angle $\delta\alpha=\frac{s_{\parallel}(t_B)}{\langle R\rangle}$ between the beginning and the end of the bounce. This does not change the magnitude of the pellet velocity, but its angle w.r.t. the wall surface.

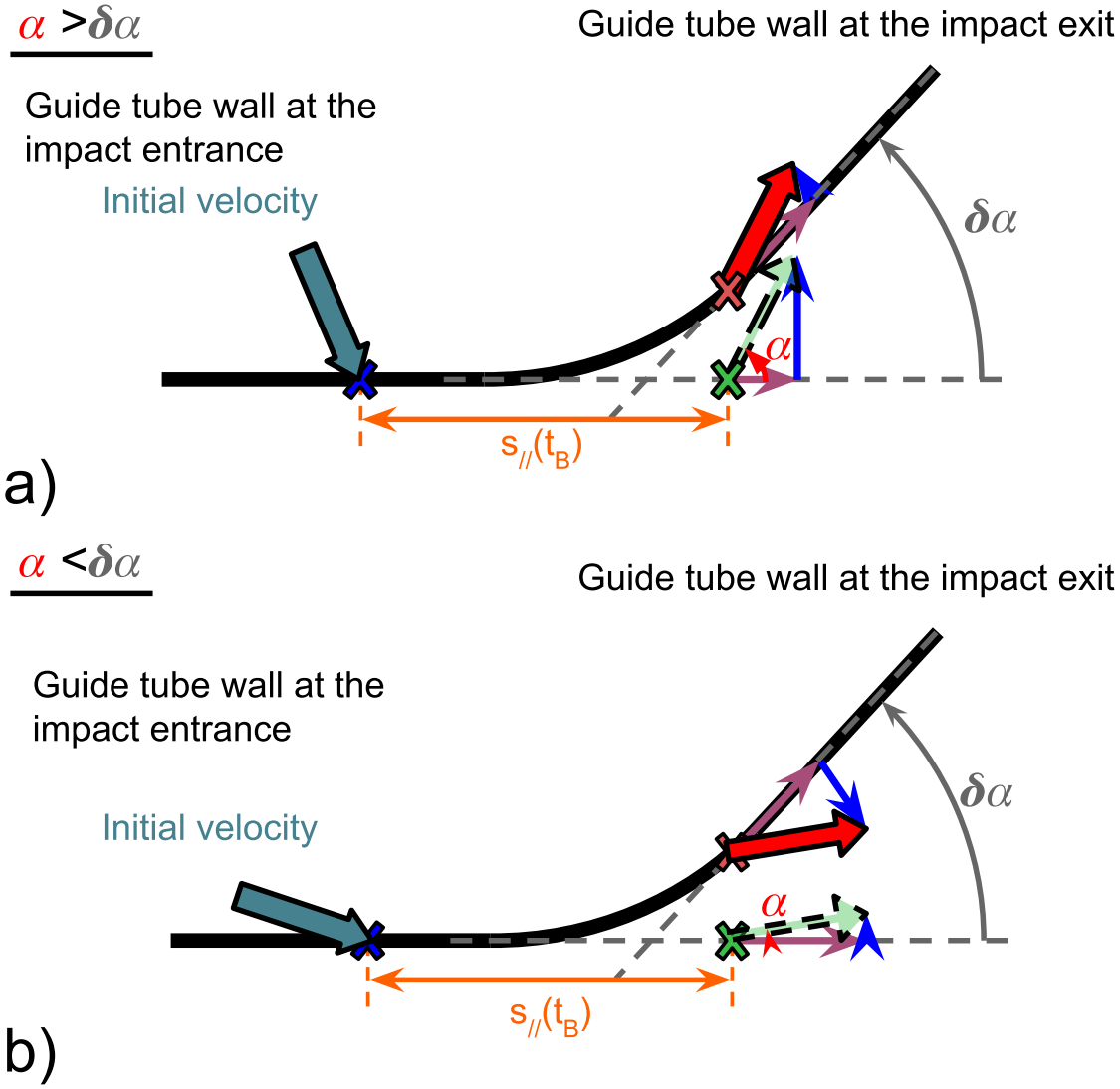


Figure 2.5. – Sketch of the correction made due to the pellet trajectory curvature. The bounce on the plane corresponds to the calculated one (green cross). The red cross represents the real pellet position. Small blue arrows represents the radial velocity $\vec{v}^r$, and purple ones, the parallel velocity $\vec{v}^{\parallel}$. a) $\alpha > \delta\alpha$, the last pellet trajectory will be a free flight represented by the red arrow. b) $\alpha < \delta\alpha$, the pellet is pushed against the wall.

For $\alpha > \delta\alpha$,the angle of the pellet velocity w.r.t. the wall at the end of the bounce is simply reduced, becoming $\alpha - \delta\alpha$, and the new components of the velocity write:

$$\begin{aligned} v_2''^r &= \sqrt{v_2^{\parallel 2}(t_B) + v_2'^{r2}} \times \sin\{\alpha - \delta\alpha\} \\ &= \sqrt{v_2^{\parallel 2}(t_B) + v_2'^{r2}} \times \sin\left\{\arcsin\left[\frac{v_2'^r}{\sqrt{v_2'^{\parallel 2}(t_B) + v_2'^{r2}}}\right] - \frac{s_\parallel(t_B)}{\langle R\rangle}\right\} \end{aligned} \tag{2.28a}$$

$$v_2''^{\parallel} = \sqrt{v_2^{\parallel 2}(t_B) + v_2'^{r2} - v_2''^{r2}} \tag{2.28b}$$

For $\alpha \leq \delta\alpha$, the pellet remains stuck to the wall, and one has:

$$v_2''^r = 0 \tag{2.29a}$$

$$v_2''^{\parallel} = \sqrt{v_2'^{\parallel 2} + v_2'^{r2}} \tag{2.29b}$$

In all cases, the new components of the parallel velocity are given by:

$$v_2''^{\psi,z|\varphi} = v_2'^{\psi,z|\varphi}\frac{v_2''^{\parallel}}{v_2'^{\parallel}} \tag{2.30}$$

2.4.4.2. Limitation of the number of bounces by forcing the pellet to slip

For any realistic values of κ, θ and μ, the decrease in v^r is larger than that in $v^{\parallel}$ during a bounce (in the opposite case, the pellet leaves in free flight). This has for consequence that, along a trajectory of constant curvature, the distance covered between two successive bounces, d, decreases continuously. This can lead to a huge accumulation of bounces on a very short distance before the condition $\alpha < \delta\alpha$ is verified, allowing the pellet to slip. This accumulation of bounces has no physical significance and leads to an unacceptable calculation time. Solution is to impose that the pellet slips as soon as the angle of the velocity with the wall at the end of the bounce, $(\alpha - \delta\alpha)$, is smaller than a critical value $\delta\alpha_{\text{Lim}}$ chosen by the user (this procedure does not prevent from an accumulation of bounces for $(\alpha - \delta\alpha) \geq \delta\alpha_{\text{Lim}}$ but it allows controlling the distance δ covered between two successive bounces). With this approximation, it comes:

$$v_2''^r = \sqrt{v_2'^{r2} + v_2'^{\parallel 2}} \qquad \text{for } \alpha - \delta\alpha > \delta\alpha_{\text{Lim}} \tag{2.31a}$$

$$v_2''^r = 0 \qquad \text{for } \alpha - \alpha \leq \delta\alpha_{\text{Lim}} \tag{2.31b}$$

the eqs. 2.28b, 2.29b and 2.30 being unchanged.
The phase of forced slipping that follows is only an approximation for a series of bounces and the value of μ must be adapted for ensuring that the braking of the pellet

due to the friction with the wall during this phase is equal to that resulting from the bounces. This value, μ', can thus be different to that used during the other phases of slipping and, for consistency, it must be applied on a distance d about that which would be covered by the succession of bounds until the condition $\alpha < \delta\alpha$ is verified. (This approximation is nevertheless not perfect because the series of bounce can lead to an accumulation of energy in the ice if the elastic limit is exceeded, which will not be the case for an equivalent slipping.) The calculation of μ' (not included in the present state of the model) is detailed in Appendix A.3.

2.4.5. Outputs of the bounce: erosion, heating, pellet position and velocity

Although the pellet parameters are considered as constant during the bounce, its mass and temperature change due to erosion and heating, and its parallel velocity is reduced due to the slipping friction. These effects are taken into account in the following corrections.

The pellet is braked during the impact, with $v_2'' < v_2(0)$, leading to a loss in kinetic energy:

$$\begin{aligned}\delta E^{kin} &= \delta E_r^{kin} + \delta E_{\parallel}^{\text{kin}} \\ &= \tfrac{1}{2} m_2 \left({v_2''^r}^2 - {v_2^r}^2(0) \right) + \tfrac{1}{2} m_2 \left({v_2''^{\parallel}}^2 - {v_2^{\parallel}}^2(0) \right)\end{aligned}$$

In the most general case, the sum of $-\delta E^{kin}$ and of the heat carried by conduction as long as the pellet touches the wall, $f(F^r)(T_G - T_2)\,t_B$, is used for:

— creating defaults,
— eroding the pellet,
— heating the ice.

Two coefficients γ_1 & γ_2 govern the balance between these different effects. Default creation results from the dissipation of a proportion γ_1 of the loss of perpendicular kinetic energy:

$$\delta E_p = -\gamma_1 \delta E_r^{kin} \tag{2.32}$$

The remaining available energy $-\delta E_{\parallel}^{kin} - \delta E_p + f(F^r)(T_G - T_2)$ is used for eroding the pellet in proportion γ_2 and heating the ice in proportion $(1-\gamma_2)$.
The reduction of the pellet radius writes:

$$\delta R_p'' = R_{p2} - R_{p2}'' = \frac{\gamma_2 \left[\frac{1}{2} m_2 \left({v_2}^2 - {v_2'}^2 \right) - \delta E_p + f\left(F^r\right)\left(T_G - T_2\right) t_B \right]}{4\pi n_S \left(\varepsilon_S - \frac{3}{2} k_B T_2 \right) R_{p2}^2} \tag{2.33}$$

where n_s and ϵ_s are the molecular ice density and sublimation energy. k_B is the

Boltzmann's constant. The remaining pellet mass is then:

$$m_2'' = m_2 \left(\frac{R_{p2}''}{R_{p2}} \right)^3 \tag{2.34}$$

In the case where the pellet slips at the end of the bounce ($r(t_B) \neq 0$), $\delta R_p''$ must be corrected from the remaining pellet deformation, yielding:

$$\delta R_p'' \rightarrow \delta R_p'' + r(t_B)$$

Finally the increase in the average temperature of the ice is:

$$T_2'' = T_2 + \frac{(1-\gamma_2)\left[\frac{1}{2} m_2 \left({v_2}^2 - {v_2'}^2 \right) - \delta E_p + f\left(F^r\right)\left(T_G - T_2\right) t_B\right]}{C_p m_2} \tag{2.35}$$

where C_p is the specific heat of the Hydrogen ice.

The knowledge of $R_{\delta 2}''$ (meaning R_δ at the end of the bounce) allows to calculate the components of the pellet position and velocity at the end of the bounce.
For a cylindrical section, the distance covered along z and the variation of the angle ψ are:

$$\begin{cases} \psi_2'' - \psi_2 &= \frac{s''^{\parallel} v_2''^{\psi}}{R_{\delta 2}'' v_2''^{\parallel}} \\ z_2'' - z_2 &= \frac{s''^{\parallel} v_2''^{z}}{v_2''^{\parallel}} \end{cases}$$

From eq. (2.9) the coordinates of the pellet at time t_B are therefore:

$$\begin{array}{ll} x_2'' = & R_{\delta 2}'' \cos\psi_2'' \\ y_2'' = & R_{\delta 2}'' \sin\psi_2'' \\ z_2'' = & z_2'' \end{array} \tag{2.36}$$

and the components of the pellet velocity at the end of the bounce are:

$$\begin{pmatrix} v_2''^{x} \\ v_2''^{y} \\ v_2''^{z} \end{pmatrix} = \begin{bmatrix} \cos\psi_2'' & -\sin\psi_2'' & 0 \\ \sin\psi_2'' & \cos\psi_2'' & 0 \\ 0 & 0 & 1 \end{bmatrix} \begin{pmatrix} v_2''^{r} \\ v_2''^{\psi} \\ v_2''^{z} \end{pmatrix} \tag{2.37}$$

The same calculation but with eq. (2.11) for a toric section yields:

$$\begin{cases} \psi_2'' - \psi_2 &= \frac{s''^{\parallel} v_2''^{\psi}}{R_{\delta 2}'' v_2''^{\parallel}} \\ \varphi_2'' - \varphi_2 &= \frac{s''^{\parallel} v_2''^{\varphi}}{\left(R_0 + R_{\delta 2}'' \cos\psi_2''\right) v_2''^{\parallel}} \end{cases}$$

$$\begin{aligned} x_2'' &= R_0\left(1-\cos\varphi_2''\right)+R_{\delta 2}''\cos\varphi_2''\cos\psi_2'' \\ y_2'' &= R_{\delta 2}''\sin\psi_2'' \\ z_2'' &= R_0\sin\varphi_2''-R_{\delta 2}''\sin\varphi_2''\cos\psi_2'' \end{aligned} \tag{2.38}$$

$$\begin{pmatrix} v_2''^x \\ v_2''^y \\ v_2''^z \end{pmatrix} = \begin{bmatrix} \cos\varphi_2''\cos\psi_2'' & -\cos\varphi_2''\sin\psi_2'' & \sin\varphi_2'' \\ \sin\psi_2'' & \cos\psi_2'' & 0 \\ -\sin\varphi_2''\cos\psi_2'' & \sin\varphi_2''\sin\psi_2'' & \cos\varphi_2'' \end{bmatrix} \begin{pmatrix} v_2''^r \\ v_2''^\psi \\ v_2''^\varphi \end{pmatrix} \tag{2.39}$$

Outputs are the post-impact guide tube effective radius, $R_{\delta 2}'' = R_{\delta 2} + \delta R_p''$, the pellet mass, temperature and increment of stored elastic energy, m_2'', T_2'' and δE_p, and, in the local frame, the pellet position and velocity at the end of the bounce (or calculation time if the pellet slips). These values are the input for calculating the following impact on the guide tube wall if the pellet bounces (Section 2.3) or its trajectory along the wall if it slips (Section 2.5).

2.5. Slipping dynamics

If the duration of a bounce is short ($\sim 10^{-5}$ s) with respect to the evolution time of the different forces and pellet characteristics, this is not the case for the slipping phases, which can last up to the whole time of the pellet trip in the guide tube. In these conditions, the approximations made in the previous sections are no longer valid, and the equations of motion must be solved exactly. Along the pellet trajectory, the three external forces to be considered are (the centrifugal and Coriolis forces are pseudo-forces that appear naturally in the expression of the acceleration):

— the slipping friction force: F_s,
— the gravity: F_g,
— the fluid friction force: F_f.

Simultaneously, the pellet mass m (and consequently radius R_p and effective radius of the guide tube $R_\delta = R_G - R_p$) and temperature T evolve thanks to the ice erosion and heating.

2.5.1. Cylindrical section

In the $(\vec{u}_r, \vec{u}_\psi, \vec{u}_z)$ frame, the components of the three forces listed above are :

$$\left[F_s^r, F_s^\psi, F_s^z\right] = -\mu m\left(\frac{v^{\psi 2}}{R_\delta}+g^r\right)\left[0, \frac{v^\psi}{\sqrt{v^{\psi 2}+v^{z2}}}, \frac{v^z}{\sqrt{v^{\psi 2}+v^{z2}}}\right] \tag{2.40a}$$

$$\left[F_g^r, F_g^\psi, F_g^z\right] = m\left[g^r, g^\psi, g^z\right] \tag{2.40b}$$

$$\left[F_f^r, F_f^\psi, F_f^z\right] = -\beta\left(v^{\psi 2} + v^{z^2}\right)\left[0, \frac{v^\psi}{\sqrt{v^{\psi^2} + v^{z^2}}}, \frac{v^z}{\sqrt{v^{\psi^2} + v^{z^2}}}\right] \tag{2.40c}$$

with acceleration expression:

$$\frac{d^2\vec{\rho}}{dt^2} = \left[\ddot{R}_\delta - R_\delta\dot{\psi}^2\right]\vec{e_r} + \left[2\dot{R}_\delta\dot{\psi} + R_\delta\ddot{\psi}\right]\vec{e_\psi} + \ddot{z}\vec{e_z} \tag{2.41}$$

where ρ is the vector radius defining the pellet position. Writing $\dot{R}_\delta = -R\dot{m}$ with $R = \left(\frac{1}{36Mn_s}\right)^{1/3} m^{-2/3}$, and where M is the mass of a molecule, one obtains for the equation of motion in the $\vec{e_\psi}$ direction:

$$\ddot{\psi} = \frac{2R\dot{\psi}}{R_\delta}\dot{m} + \frac{1}{R_\delta m}\left(F_s^\psi + F_g^\psi + F_f^\psi\right) \tag{2.42}$$

and, in the $\vec{e_z}$ direction:

$$\ddot{z} = \frac{1}{m}\left(F_s^z + F_g^z + F_f^z\right) \tag{2.43}$$

The equations that govern the behavior of m, and T are :

$$\dot{m} \quad = -\frac{\gamma_2 M}{\epsilon_s - \frac{3}{2}k_B T}\left[f(F^r)(T_G - T) + \sqrt{F_s^{\psi^2} + F_s^{z^2}}\, v_\parallel\right] \tag{2.44}$$

with $v_\parallel = \sqrt{v_\psi^2 + v_z^2}$
and:

$$\dot{T} = -\left(1 - \gamma_2\right)\frac{\left(\epsilon_s - \frac{3}{2}k_B T\right)}{C_p\gamma_2 M}\frac{\dot{m}}{m} \tag{2.45}$$

The condition for stopping the slip is $\sum F^r \leq 0$, i.e.:

$$R_\delta\dot{\psi}^2 + g^r \leq 0 \tag{2.46}$$

2.5.2. Toric section

Similarly, for a toric section the components of the three forces in the $(\vec{u_r}, \vec{u_\psi}, \vec{u_\varphi})$ frame are:

$$\left[F_s^r, F_s^\psi, F_s^\varphi\right] = -\mu m\left(\frac{v^{\psi^2}}{R_\delta} - \frac{v^{\varphi^2}\cos\psi}{R_0 - R_\delta\cos\psi} + g^r\right)\left[0, \frac{v^\psi}{\sqrt{v^{\psi^2} + v^{\varphi^2}}}, \frac{v^\varphi}{\sqrt{v^{\psi^2} + v^{\varphi^2}}}\right] \tag{2.47a}$$

$$\left[F_g^r, F_g^\psi, F_g^\varphi\right] = m\left[g^r, g^\psi, g^\varphi\right] \tag{2.47b}$$

$$\left[F_f^r, F_f^\psi, F_f^\varphi\right] = -\beta\left(v^{\psi^2} + v^{\varphi^2}\right)\left[0, \frac{v^\psi}{\sqrt{v^{\psi^2}+v^{\varphi^2}}}, \frac{v^\varphi}{\sqrt{v^{\psi^2}+v^{\varphi^2}}}\right] \tag{2.47c}$$

with acceleration expression :

$$\begin{aligned}\frac{d^2\vec{\rho}}{dt^2} =& \left[\ddot{R}_\delta + \dot{\varphi}^2\left(R_0 - R_\delta\cos(\psi)\right)\cos(\psi) - R_\delta\dot{\psi}^2\right]\vec{e_r} + \\ & \left[R_\delta\ddot{\psi} + 2\dot{R}_\delta\dot{\psi} - \dot{\varphi}^2\left(R_0 - R_\delta\cos(\psi)\right)\sin(\psi)\right]\vec{e_\psi} + \\ & \left[\ddot{\varphi}\left(R_0 - R_\delta\cos(\psi)\right) + 2\dot{\varphi}\left(R_\delta\dot{\psi}\sin(\psi) - \dot{R}_\delta\cos(\psi)\right)\right]\vec{e_\varphi}\end{aligned}$$

This leads, for the equation of motion in the $\vec{e_\psi}$ direction (the coefficient R is defined in the previous section):

$$\ddot{\psi} = \frac{2R\dot{\psi}}{R_\delta}\dot{m} + \frac{1}{R_\delta}\left(\frac{F_s^\psi + F_g^\psi + F_f^\psi}{m} + \frac{v^{\varphi^2}\sin(\psi)}{\left(R_0 - R_\delta\cos(\psi)\right)}\right)$$

with $v^\varphi = \dot{\varphi}\left(R_0 - R_\delta\cos(\psi)\right)$.
And, in the $\vec{e_\varphi}$ direction:

$$\ddot{\varphi} = -\frac{2R\dot{\varphi}\cos(\psi)}{\left(R_0 - R_\delta\cos(\psi)\right)}\dot{m} + \frac{1}{\left(R_0 - R_\delta\cos(\psi)\right)}\left[\frac{F_s^\varphi + F_g^\varphi + F_f^\varphi}{m} - 2v^\psi\dot{\varphi}\sin(\psi)\right] \tag{2.48}$$

with $v^\psi = \dot{\psi}R_\delta$.
The equations for m and T are:

$$\dot{m} = -\frac{\gamma_2 M}{\epsilon_s - \frac{3}{2}k_B T}\left[f(F^r)(T_G - T) + \mu m\left(\frac{v^{\psi^2}}{R_\delta} - \frac{v^{\varphi^2}\cos(\psi)}{R_0 - R_\delta\cos(\psi)} + g^r\right)v_\parallel\right] \tag{2.49}$$

$$\dot{T} = -\left(1-\gamma_2\right)\frac{\left(\epsilon_s - \frac{3}{2}k_B T\right)}{C_p\gamma_2 M}\frac{\dot{m}}{m} \tag{2.50}$$

Identically, the condition for stopping the slip is $\sum F^r \leq 0$, i.e.:

$$\frac{v^{\psi^2}}{R_\delta} - \frac{v^{\varphi^2}\cos\psi}{R_0 - R_\delta\cos\psi} + g^r \leq 0 \tag{2.51}$$

2.5.3. End of slipping

The calculation stops either when the pellet exits the considered section or when one of the conditions (2.46) or (2.51) is verified, at time t_s. Equations (2.36),(2.37) and (2.38),(2.39) allow to transfer pellet position and velocity in the laboratory frame.

2.6. Example of code results and main trends with input parameters

If the model described in the previous Sections takes into account most of the effects that can affect the pellet trajectory and characteristics during its path through a guide tube, their quantification is not easy because the value of most of the coefficients involved in the calculations are not accurately known.

- The ice characteristics (κ and θ) could be in principle be estimated from Appendix A.2, but only the static strain-stress variation is known, and this variation varies with the ice temperature, which changes with the pellet manufacturing method (extrusion or in-situ condensation) and pellet contact with the wall of the guide tube.
- The branching coefficients γ_1 and γ_2 are unknown.
- The fluid friction coefficient β can be calculated provided the background gas pressure in the guide tube is known.
- The slipping friction coefficient μ is expected to vary not only with the surface smoothness of the guide tube wall, but also with the ice temperature and presence or not of a cloud of gas surrounding the pellet and protecting it from a direct contact with the wall (Leidenfrost effect).
- The coefficient f quantifying the heat transfer when the pellet is in contact with the guide tube wall is not known and is also expected to vary depending on the presence of a cloud of gas.

Because these different coefficients evolve simultaneously during the pellet path in the guide tube due to the interplay between the different processes, it is not possible to perform a consistent and comprehensive analysis of the consequences of the different physical processes at work. For this reason, only the trends associated to the most influencing parameters are investigated below, using just "reasonable guess" for the values of the different coefficients because of the lack of knowledge of accurate ones. Consequently, the calculations presented in the following subsections are more to be taken as a demonstration of the code capabilities and sensitivity to the different parameters than to realistic simulations.
Practically, four analyses are presented:

- The comparison of the dynamics of a bounce and a slip (Subsection 2.6.1),
- The influence of θ and μ on the pellet trajectory and exit characteristics (Subsections 2.6.2 and 2.6.3),
- The influence of the dispersion of the pellet input parameters (in position and velocity direction at the entrance of the guide tube) on the exit characteristics and the characterization of the consequence of limiting the number of bounces by forcing the pellet to slip if the angle of rebound is below a critical value α_{Lim} (Subsection 2.6.4).

Coefficients γ_1 and γ_2, β and f are not systematically varied.

2.6.1. Example of bounce and slip

An example of the evolution of the pellet parameters during a sequence comprising a free flight and a bounce followed by a slip is presented in Figures 2.6 and 2.7.

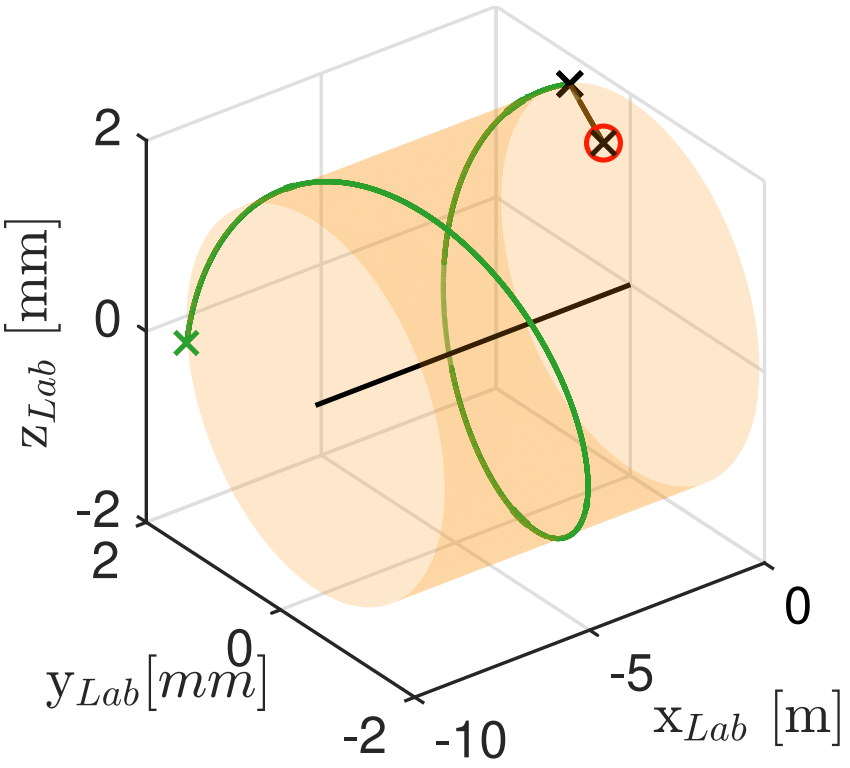


Figure 2.6. – Example of pellet trajectory in a rectilinear guide tube.

The simulation parameters are:
Guide tube radius and length: $R_G = 3$ mm and $L = 9$ m.
Initial pellet mass : $m(0) = 1$mg (radius $R_p(0) = 1.1$ mm).
Pellet launching point at 1.4 mm from the center of the guide tube.
Initial velocity $V \sim V^{\parallel} = 580$ m.s^{-1}, with a perpendicular component $V^r = 2.8$ m.s^{-1}.

The model coefficients are chosen for the main processes introduced above are visible. They can have consequently unrealistic values. They are:
The heat conduction and viscous braking coefficients: $f = \beta = 0$.
The spring rate and attenuator damping coefficient: $\kappa = 10^7$ kg.s^{-2} and $\theta = 0.05$ kg·s^{-1}.
The slipping coefficient: $\mu = 0.9$ (strongly oversized).
The branching ratios between the storing of elastic energy, erosion and heating are: $\gamma_1 = 0.3$ and $\gamma_2 = 0.9$

The behavior of the main parameters are displayed in Figure 2.7. The total duration of the pellet trip in the guide tube is ~ 15.5 ms.

Figure 2.7a shows the force applied to the pellet for the two first millisecond of the trip. The bounce corresponds to the negative spike at $t \sim 0.2$ ms, between the free flight on the left and slipping phase on the right. Figures. 2.7b and 2.7c are a zoom on the force exerted on the pellet during the bounce and slip phases (red and green rectangles in Fig. 2.7a). In Fig. 2.7b, one sees that the bounce duration is $\sim 10^{-3}$ ms, with a maximum force $F^r \sim -8$ N, much larger than that experienced by the pellet during the slipping phase $F^r \sim -4 \times 10^{-4} N$ (Fig. 2.7c). During this latter phase, the modulation of F^r is due to the gravity. The vertical spike on the left of the figure corresponds to the bounce.
Figures 2.7d and 2.7e show the evolution of the pellet compression r (up to a few μm with the used values of κ and θ) and perpendicular velocity v^r. The bounce stops for $r = 0, v^r \sim -2.5$ m. s^{-1}. This velocity being negative (directed toward the inner of the guide tube) and with a non-zero value, the pellet should leave in free flight, and not slip. The fact that the pellet slips is due to the curvature of the guide tube surface that is large enough for sticking the pellet on the wall at the end of the bounce, see section 2.4.4. Stricto sensu, the short time interval during which $v^r < 0$ in Fig. 2.7d is therefore not physical. A rigorous calculation would show v^r tending smoothly to zero, with no discontinuity, and would suppress the spike where $F^r > -4 \times 10^{-4} N$ on the left of 2.7c.
Last, Figures 2.7f to 2.7i show the evolution of the pellet total velocity and mass, ice temperature and stored elastic energy during the different phases of its trip in the guide tube. During the free flight, no force is applied. The velocity, mass of the pellet, ice temperature and stored energy remain all constant. At the time of the bounce, the dissipated energy (due to the damping coefficient θ) causes an abrupt decrease in the pellet velocity and mass and an increase in the ice temperature and stored elastic energy. Last, during the phase of slipping, the dissipated energy (due to the slipping coefficient μ) causes a small pellet erosion and slowing down and a moderate increase in the ice temperature, but no change in the stored elastic energy, as explained is Sections 2.4.5 and 2.5.

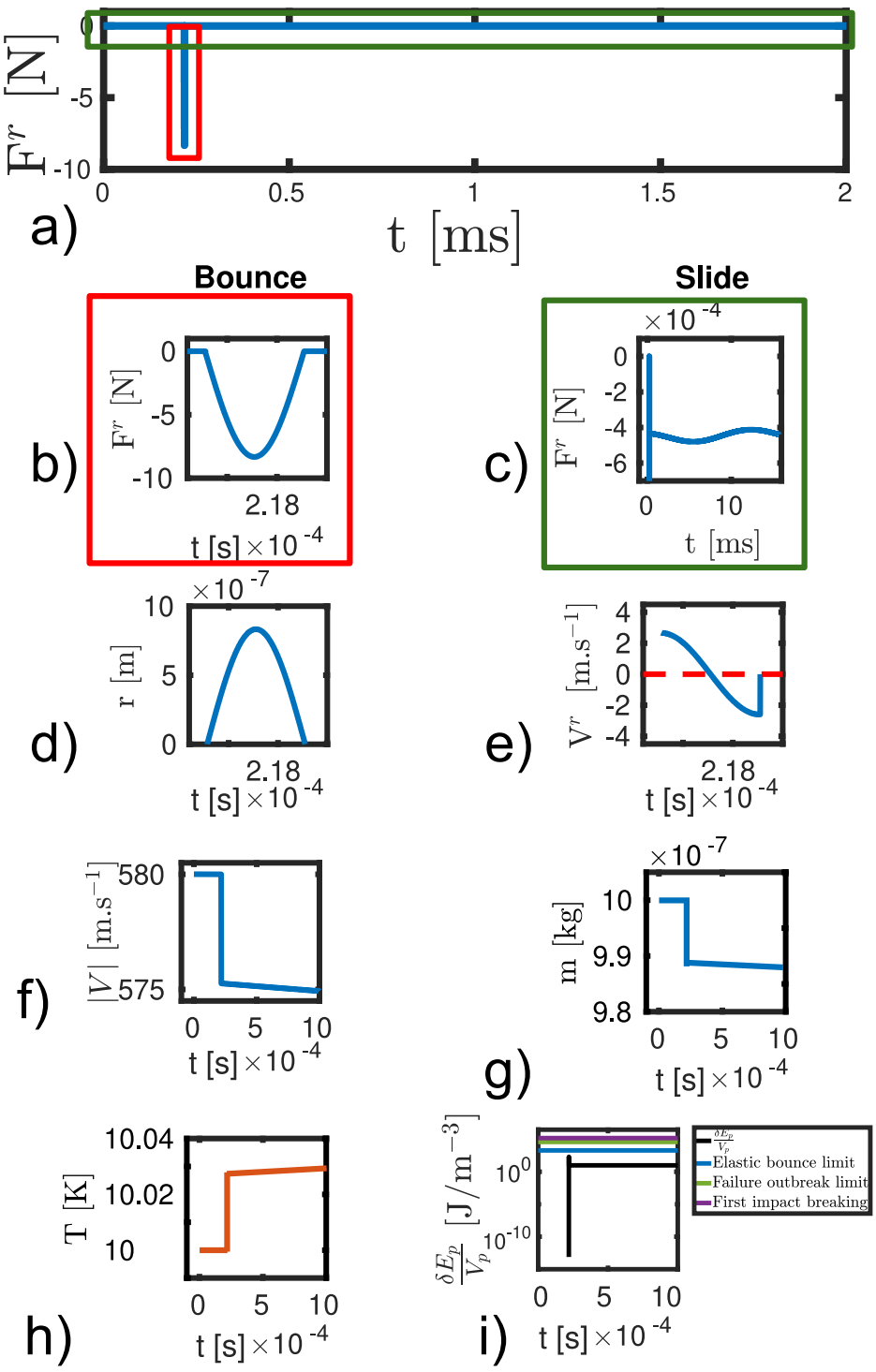


Figure 2.7. – Behavior of the main pellet parameters during the trip in the guide tube. a) perpendicular force; b) zoom on the perpendicular force during the bounce, c) zoom on the perpendicular force during the slip, d) pellet deformation during the bounce, e) pellet perpendicular velocity during the bounce and, during the whole trip, f) pellet total velocity, h) pellet mass, g) ice temperature and i) stored elastic energy per volume unit (V_p is the pellet volume).

2.6.2. Influence of κ and θ on the bounce dynamics and pellet trajectory

2.6.2.1. Influence of κ and θ on the bounce dynamics

The parameters κ and θ, which characterize the ice mechanical properties, influence strongly the consequences of a bounce in terms of slipping probability, slowing down, erosion, heating and ice embrittlement. The main trends in the change in a bounce dynamics observed when varying the ratio θ/κ are summarized below, through four simulations with input parameters:
Initial pellet mass : $m(0) = 1$mg (radius $R_p(0) = 1.1$ mm).
Initial velocity $V^{\parallel} = 599.7$ m.s^{-1}, with a perpendicular component $V^r = 1.6$ m.s^{-1}.
Contact heat transfer and viscous braking coefficients: $f = 0$ and $\beta = 5\times10^{-11}$ kg^{-1} m^{-1}.
Slipping coefficient: $\mu = 3\times10^{-2}$.
Branching ratios between the storing of elastic energy, erosion and heating: $\gamma_1 = 0.3$ and $\gamma_2 = 0.9$. The spring rate and attenuator damping coefficient chosen for this scan are: $\kappa = 10^7$ kg$\cdot$s^{-2} and $\theta = 10^{-2}, 10^{-1}, 1$ and 5 kg$\cdot$s^{-1}.

The evolution of the radial force exerted on the ice during a bounce is displayed in Figure 2.8. Due to the stronger energy dissipation with increasing θ, the initial value of the force increases with θ, but the total duration of the bounce decreases (Fig. 2.8a), as well as the integral of the force (Fig.2.8b). This last point is of importance since it controls the braking of the parallel velocity during the bounce.

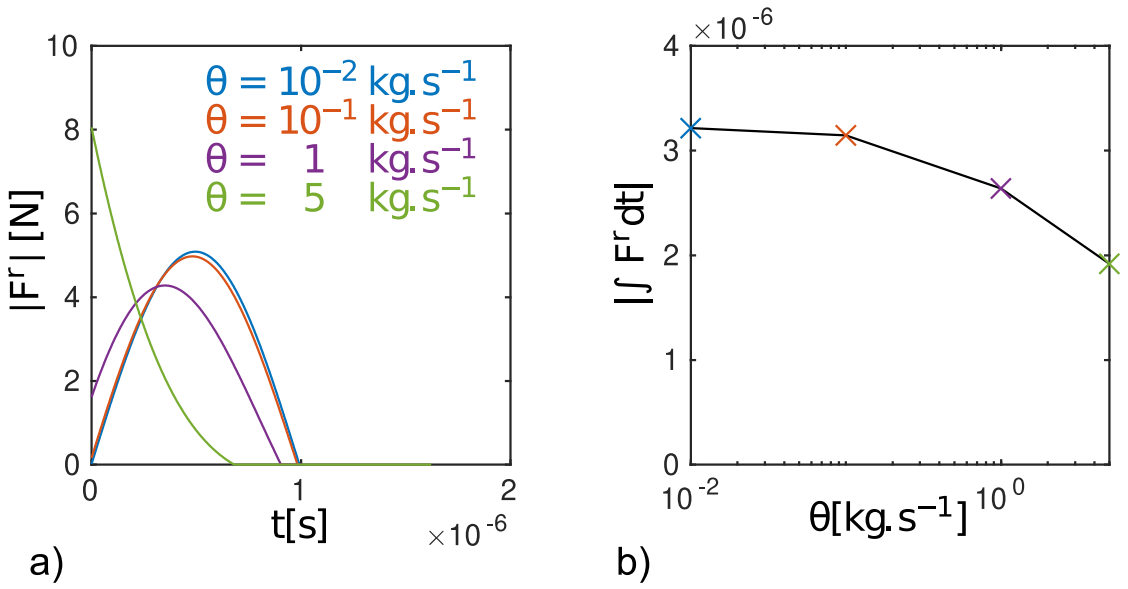


Figure 2.8. – a) Time-evolution of the radial force acting on the ice during a bounce for $\theta = 10^{-2}$, 10^{-1}, 1, 5 kg.s^{-1}; b) Integral of the force vs θ.

Then, the variation with θ of the main parameters of the pellet during the bounce are

displayed in Figure 2.9. Figs. 2.9a and 2.9b show that the velocity slowing down in the perpendicular and parallel directions evolve in opposite senses. If the observed trend seems natural for V^r, it is rather counterintuitive for $V^{\parallel r}$, even if it is clear that it comes from the decrease in $\left|\int F^r dt\right|$ with θ. This implies that, depending on the ratio θ/μ, one can observe situations where the angle of the velocity with respect to the wall at the exit of a bounce is larger than at its entrance. The behavior of the pellet intrinsic parameters (m, T and $\delta E_p/V_p$, , where V_p is the pellet volume, Figs. 2.9c to 2.9e) follow that of the kinetic energy, with the mass loss and ice heating decreasing and with the stored energy increasing with θ.

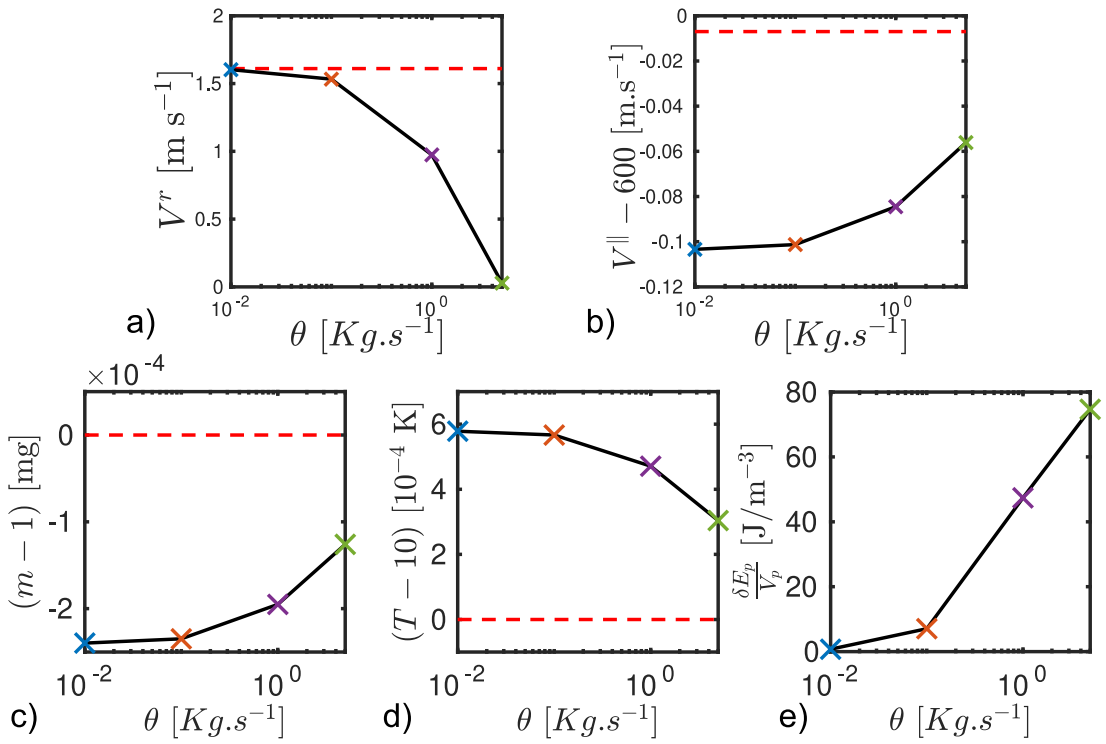


Figure 2.9. – Behavior of (a) the perpendicular velocity, (b) the parallel velocity, (c) the pellet mass, (d) the ice temperature and (e) the stored elastic energy vs. θ. The red dashed lines are the initial values at the bounce entrance.

2.6.2.2. Influence of κ and θ on the whole trajectory

The fact that the choice κ and θ has an impact on the exit angle of bounces influences the whole pellet trajectory in the guide tube. This is exemplified by launching the pellets corresponding to the four cases discussed above in a guide tube of geometry close to that of the JT-60SA tokamak (characteristics given in Table 2.1, [100],[86]), see Figure 2.10. This guide tube has an inner radius $R_G = 3$ mm (i.e. $R_\delta = R_G - R_p = 2$ mm) and a total length $L_G = 17.3$ m. It is composed of a succession of rectilinear and toric

sections, the characteristics of which are listed in Table 2.1. The launching point of the pellets, at the entrance of the first section, is located at $r^{in} = 1.3$ mm at the bottom of the guide tube (see Figure 2.11). The most visible effect is the reduction of the number

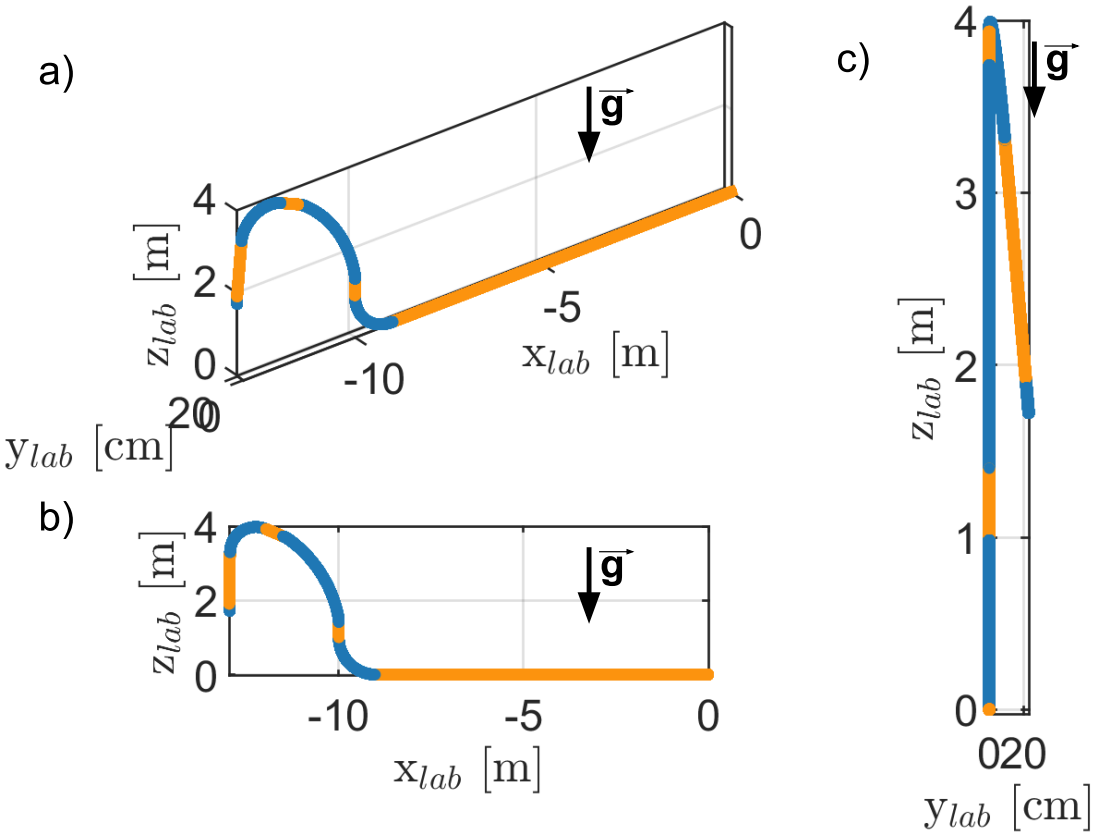


Figure 2.10. – Geometry of the simulated guide tube : a) 3D view, b) ($X_{lab} \times Z_{lab}$) plane, c) ($Y_{lab} \times Z_{lab}$) plane. The cylindrical parts are in orange and the torus sections are in blue.

of bounces with increasing θ, as shown in Figure 2.12. The effect is particularly clear in section 1($s < 9$ m), where the length of the free flights between the bounces (horizontal segments between vertical lines) increases regularly with θ. It is noticeable that, due to the decrease of the total number of bounces, the stored elastic energy at the guide tube exit does not increase with θ, but remains almost constant or decreases for $\theta = 5$ even if, individually, the stored energy per bounce increases when θ increases (see Fig. 2.9e).

The consequences on the evolution of the slowing down, mass and ice temperature are shown in Figure 2.13. Here also, no regular variation is observed with the value of θ, but the dispersion of the final values remains small (between 5 and 12%) in front of the range of θ-values investigated (from 0.01 to 5). This is because, as far as the whole trajectories are considered, the importance of the slipping phases, and not only that of the bounces, is significant in the evolution of the different parameters.

Section #	Type	L[m]	R_0[m]	$\Delta\Phi$ [°]
1	R	9.0	–	–
2	T	–	1.0	90
3	R	0.4	–	–
4	T	–	1.0	12
5	T	–	3.4	41
6	T	–	1.0	14
7	R	0.5	–	–
8	T	–	0.7	112
9	R	1.4	–	–
10	T	–	1.0	11

Table 2.1. – Geometrical characteristics of the simulated guide tube : section number, type of section (R = rectilinear, T = toric), length, major radius and angular extension.

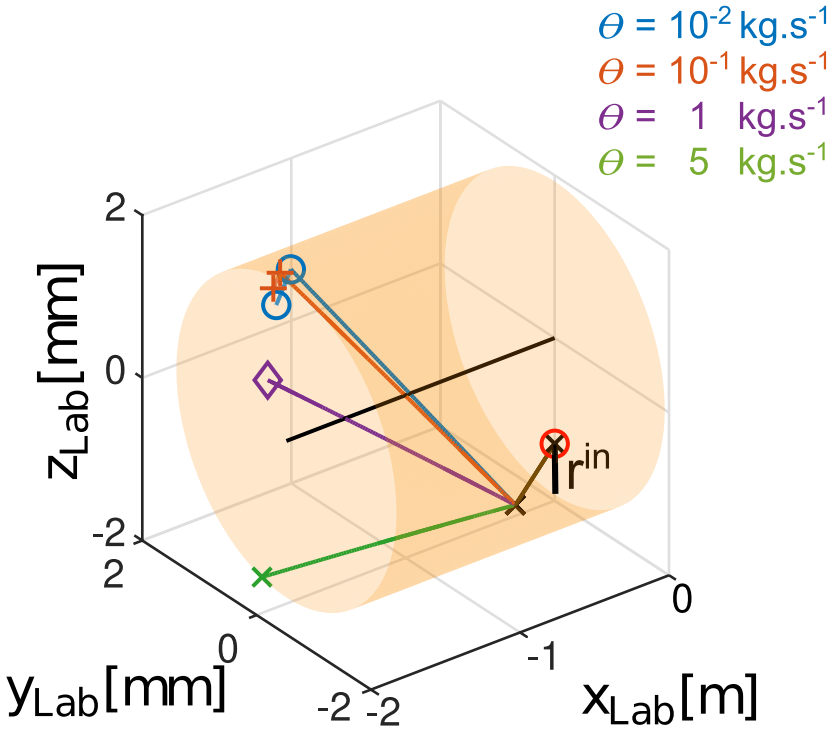


Figure 2.11. – Pellet trajectory depending on θ value

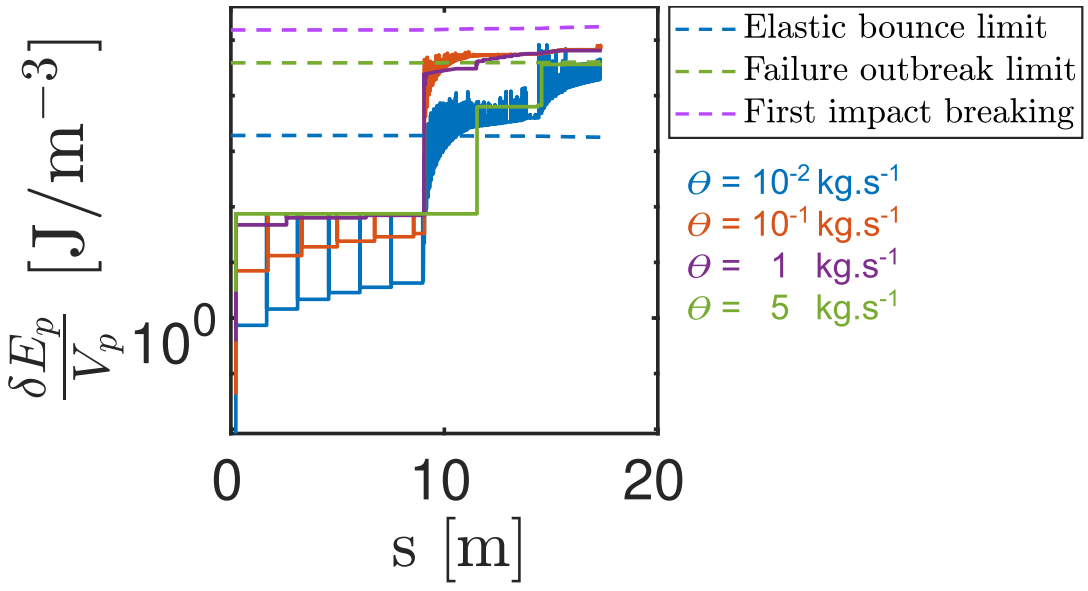


Figure 2.12. – Variation of $\delta E_p / V_p$ along the guide tube for the four values of θ

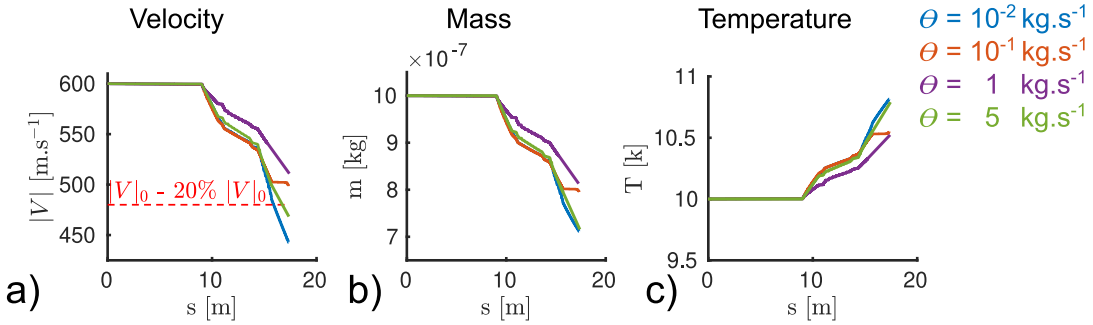


Figure 2.13. – Variation of the pellet velocity a), mass b) and ice temperature c) along the guide tube for the four values of θ

2.6.3. Influence of μ on the pellet exit parameters

In addition to braking the pellets and changing their trajectory by modifying the velocity angle with respect to the wall at the bounce exit, the slipping friction coefficient μ influences also the intrinsic pellet parameters, mass and ice temperature, by changing the balance between what happens during the bounces and what happens during the slipping phases. This effect is investigated by launching 10 pellets in the guide tube described in the previous subsection, with different injection conditions and μ-values. Common inputs are:
$\kappa = 10^8$ kg·s^{-2}, $\theta = 1.5$ kg·s^{-1},
$f = 0$ and $\beta = 5\times10^{-11}$ kg·m^{-1},
$\gamma_1 = 0.3, \gamma_2 = 0.9$
and $V^{\|I} = 600$ m·s^{-1}.
The parameters that are varied are:
$V^r = 0, 0.14, 0.2$ m·s^{-1},
$r^{in} = 0.36, 0.5$ mm
and $\mu = 10^{-3}, 10^{-2}, 3\times10^{-2}, 6\times10^{-2}$.

The results are displayed in Figure 2.14 showing, as could be expected, a regular increase of all the different effects and dispersion in the final values of the velocity, mass and ice temperature with increasing value of μ. However, the variation is not linear, since an increase by a factor 60 in μ leads to an increase by a factor of only about 30 in the slowing down and mass loss (from ~ 1.3% to 40% of the initial value). The change in the ice temperature is negligible for $\mu = 10^{-3}$ and is up to 10% for $\mu = 6\times10^{-2}$.

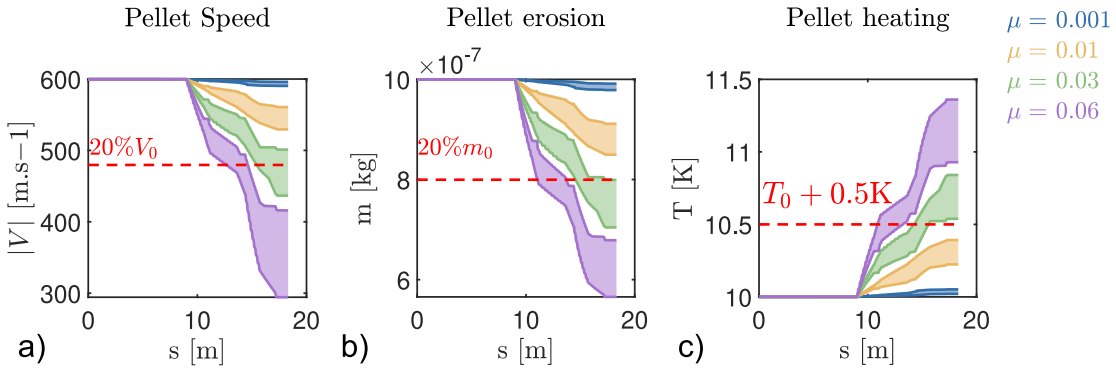


Figure 2.14. – Variation of the pellet velocity a), mass b) and ice temperature c) along the guide tube for the four values of μ

2.6.4. Influence of the pellet input parameters and limitation of the number of bounces on the trajectories and exit parameters

The simulation of a single pellet trajectory cannot give a reliable estimation of the capability of a given guide tube geometry for delivering intact pellets with limited mass loss and velocity dispersion in the plasma. This can only be done by launching a number of pellets with dispersion in initial parameters equal to what is expected at the injector exit and to perform a statistical analysis of their characteristics at the exit of the guide tube. This is what is done in this subsection where 32 pellets of initial mass $m(0) = 1$mg are launched in the guide tube introduced in the subsection 2.6.2. Pellets are launched at the entrance of the guide tube with a space distribution centered on the axis of the guide tube, with a dispersion $\sigma_G^{in} = 1.1 \times 10^{-1}$ mm and with a velocity $V = 600$ m.s^{-1}, with an angular dispersion $\sigma_V^{in} = 1.2 \times 10^{-2\circ}$, see Figure 2.15. Two series of simulations are performed: the first uses the exact condition for slipping

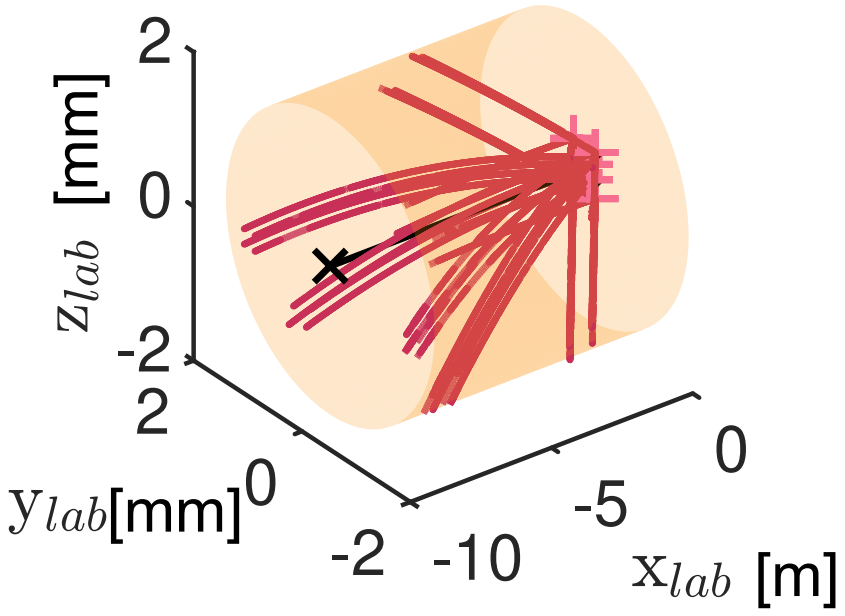


Figure 2.15. – Injection location and trajectory of the 32 test pellets in the 1st section of the guide tube. The curvature of the trajectories is due to gravity.

at the exit of a bounce, the 2nd the approximation for a faster calculation [1] allowing to slip if the exit angle of the bounce is smaller than $\alpha_{\text{Lim}} = 3°$. Model parameters are:
$f = 0$,
$\beta = 5 \times 10^{-11}$ kg·m^{-1},
$\kappa = 10^{7}$ kg·s^{-2},

1. With the parameters used in this set of simulations (weak σ_v^{in} and relatively large α_{Lim}), the gain in calculation time and required memory is about an order of magnitude when using the α_{Lim} approximation.

$\theta = 10^{-2}$ kg·s^{-1},
$\mu = 3 \times 10^{-2}$,
$\gamma_1 = 0.3$ and $\gamma_2 = 0.9$.

	$\langle X \rangle$	σ_X	σ_X^-(nb. of pellets)	σ_X^+(nb. of pellets)
Slowing down [%]	40.18	19.11	10.95(21)	27.30(11)
Mass loss [%]	36.02	8.14	7.87(16)	8.15(16)
Temperature increase [%]	10.87	3.10	3.61(16)	3.52(16)
Stored energy $\left[10^3\ \mathrm{J.m^{-3}}\right]$	39.7	27.0	14.5(21)	39.0(11)
Impact radius on target [cm]	4.66	14.7		
Pitch angle of exit trajectory [°]	2.67	6.96		

Table 2.2. – Exit parameters for the set of 32 pellets: Slowing down, Mass loss, Ice heating, Stored elastic energy per unit volume, Impact radius on the target and Pitch angle of the exit trajectory. Noted quantities are the average value, the total standard deviation and the standard deviations for the pellets showing parameters below or above the average, with the corresponding number of pellets.

2.6.5. Calculations with exact slipping condition

The behaviors of the velocity, mass, temperature, and stored energy along the guide tube are displayed in Figure 2.16 and the final values characterized quantitatively in Table 2.2. A fictive target, located at 1 m from the tube exit perpendicularly to the axis of the last section (see the geometry in Figure 2.17), visualizes the velocity dispersion of the pellet beam at the exit of the guide tube. Last, Figure 2.18 displays the impacts corresponding to the set of pellets.
As it could be expected, there is only negligible effect on the pellets in the first rectilinear section of the guide tube. For the pellets which fly freely all over the section, the very limited slowing down is due to fluid friction; for those which bounce once or twice, it is the decrease of the perpendicular velocity during the bounce that is the main cause. The effects are much larger and the dispersion becomes significant as soon as the pellets penetrate the bended sections. As can be seen from Table 2.2, the exit parameter distribution is slightly asymmetric, the pellets that exhibit the larger deviation with respect to the mean value being those launched toward the top of the pipe in Figure 2.15. The evolution along the guide tube of the stored energy per unit volume (Figure 2.16d) exhibits a large dispersion from pellet to pellet, with no clear trend. However, the average value (black curve), shows a smooth increase in the second part of the tube, indicating that no section is particularly deleterious for the pellet integrity. Nevertheless, all pellets exceed the failure outbreak limit at the end of their path (see Appendix A.2; these limits depend on the ice temperature, which explains why they vary differently for every pellet in the second part of the guide tube).

Figure 2.18 displays the impact distribution of the set of 32 pellets on the fictive target. Most of them show an angular deviation of their exit velocity smaller than 6°, but two of them impact the target at a large distance from its center (marked by a purple cross and black triangle outside the zoomed region in Figure 2.18b). For understanding

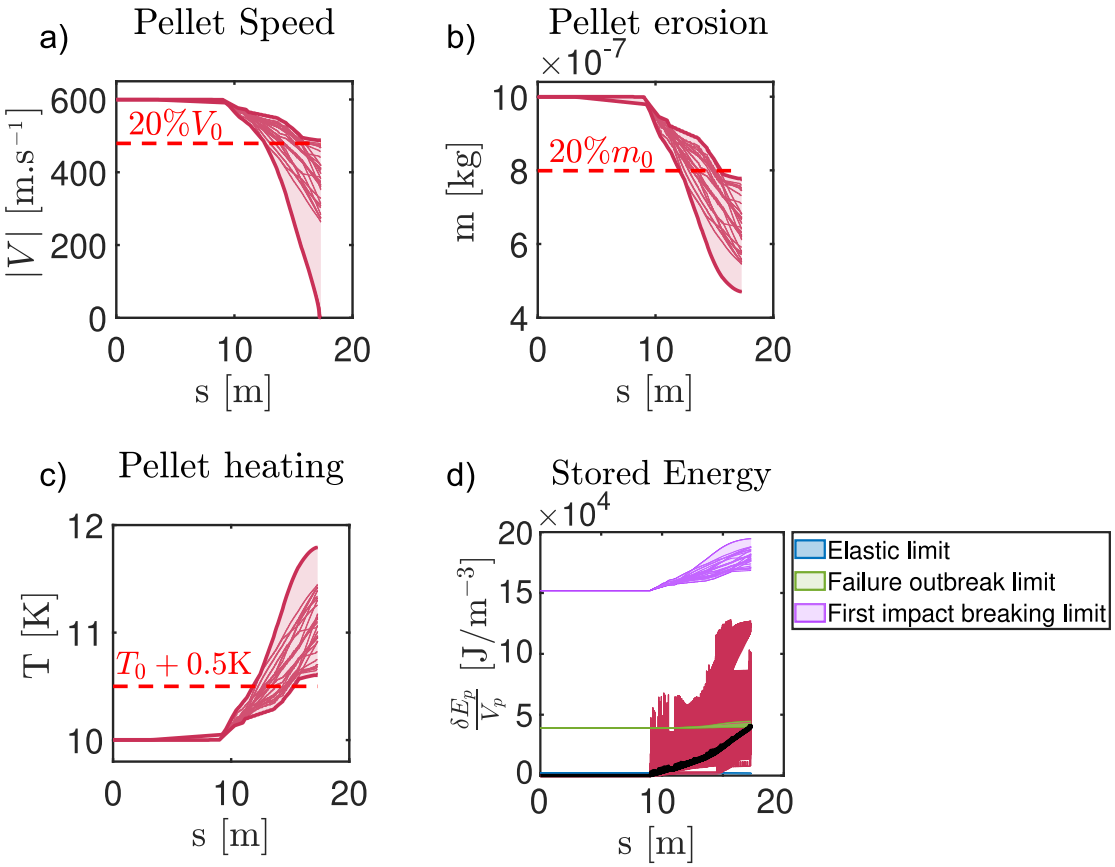


Figure 2.16. – Variation along the guide tube of (a) the pellet velocity, (b) the pellet mass, (c) the ice temperature and (d) the stored elastic energy. In (d), the black line is the average over the whole sample; the blue, green and purple lines are the elastic, failure outbreak and first impact breaking limits (see Appendix A.2).

better the reason of these large deviations, three pellets are more specifically followed, marked by colored triangles in Figures. 2.18b and 2.18d. A detailed analysis of their trajectory shows that their deviation at the guide tube exit is correlated to the number of bounces they experience during their path (from 590 for the pellet marked by a black triangle to 150 and 89 for those marked by the red and purple ones). This comes from the relative values chosen for θ and μ. In the present case, at every bounce, the perpendicular velocity decreases less than the parallel velocity, which increases the pitch angle of the pellet velocity with respect to the axis of the guide tube section. This behavior can be generalized: the increase or decrease of the velocity aperture of a set of pellets at the guide tube exit with respect to what it is at its entrance depends of the ratio θ/μ. For large values of θ, the perpendicular velocity decreases more than the parallel velocity during a bounce, which decreases the pitch angle of the pellet velocity with respect to the axis of the guide tube section and tends to reduce the aperture of the velocity distribution at the guide tube exit. Conversely, for small values of θ w.r.t.

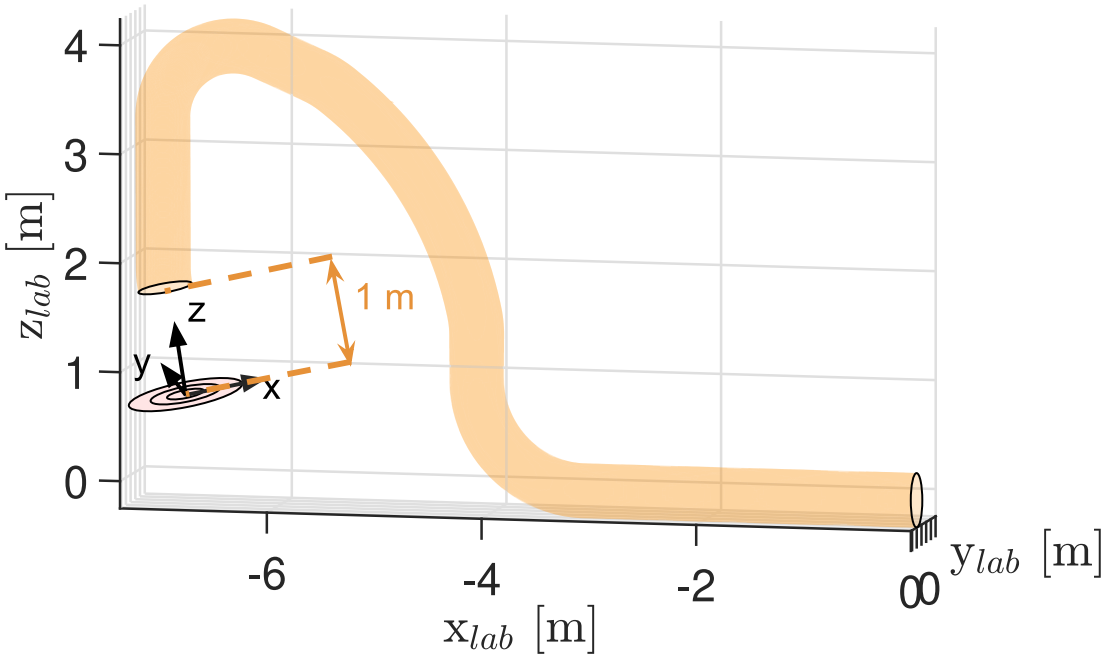


Figure 2.17. – Schematic view of the target location with respect to the guide tube exit, showing the laboratory and local frames

μ as in the present simulation, the trend is an increase of the aperture of the velocity distribution.

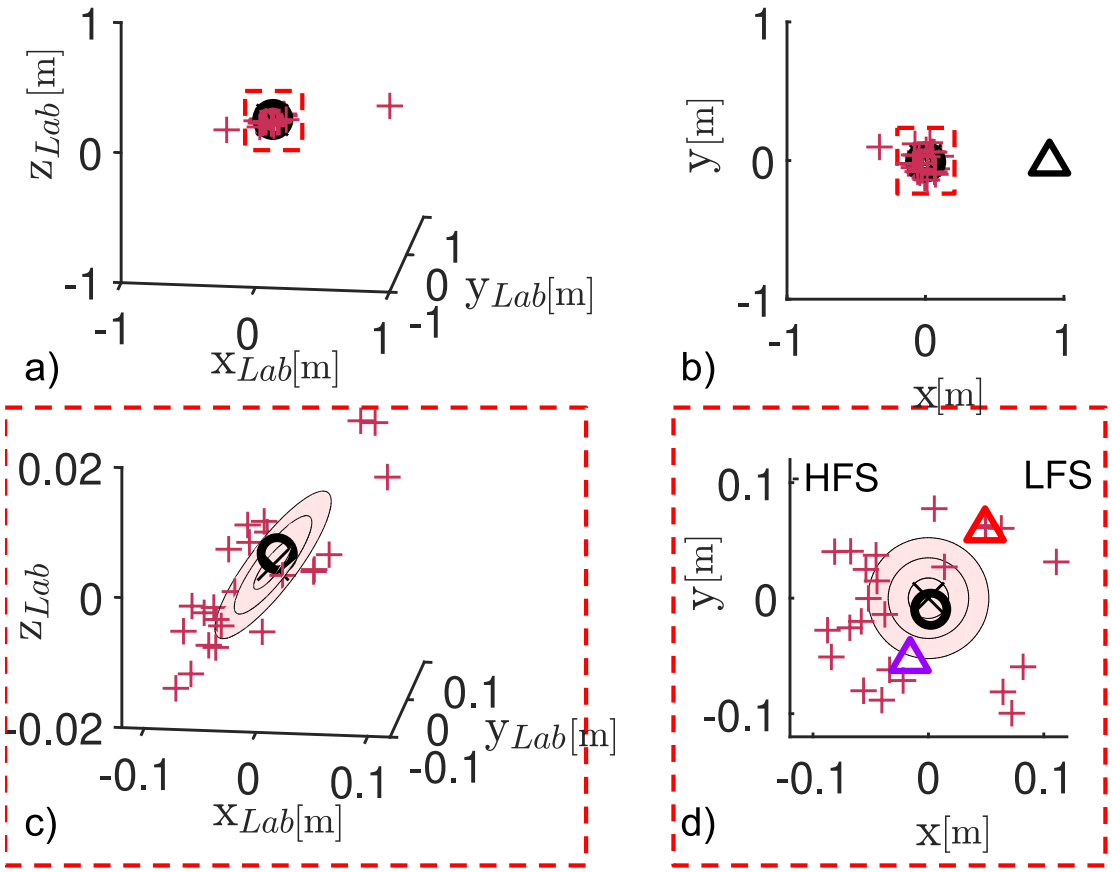


Figure 2.18. – : Impacts of the 32 pellets on the target. (a) and (b) General view in the laboratory and local frames; (c) and (d) Zoom on the central part. The black circle is the barycenter of the impacts. The concentric circles correspond to an angular aperture of 1, 2 and 3 °, respectively.

2.6.6. Calculations with the $\alpha_{\mathrm{Lim}} = 3°$ approximation

As it can be seen from Table 2.3 and Figures 2.19 and 2.20 (which correspond to Table 2.2 and Figures 2.16 and 2.18 of the previous section), trends are identical when using the $\alpha_{\mathrm{Lim}} = 3°$ approximation, although less pronounced and with a somewhat smaller dispersion, even if with more asymmetric distributions. It must be noted that the value $\alpha_{\mathrm{Lim}} = 3°$, used for this calculation, is chosen for demonstrating the gain it brings in computer time and memory, and can be too large with respect to the guide tube geometry. Particularly, since the approximation consists in forcing the pellets to slip and not to bounce when the elastic energy in the ice increases only during the bounces, this quantity can be significantly underestimated if the choice of α_{Lim} is not adapted. This is clearly seen in Table 2.3, where the average value of $\delta E_p / V_p$ at the guide tube exit is smaller by more than an order of magnitude with respect to what it is using exact calculation; and in Figure 2.19d, where its average value exceeds the elastic limit, but not the failure outbreak limit (individually, only 12/32 pellets exceed this limit, when it was the case for all of them with the exact calculation). The choice of the value for α_{Lim} can therefore be delicate, and depends on what one is interested in, the slowing down and mass loss or the pellet integrity. When considering the mean value of $\delta E_p / V_p$ in the zoom of Figure. 2.19d, one distinguishes two steps, the first at $s \approx 12$ m, the second at $s \approx 15$ m. They are associated to the exit of sections 3 and 7 , at the junction between rectilinear and toric sections (the same feature is possibly seen at the junction of sections 9 and 10).
The distribution on the impacts on the target is displayed in Figure 2.20, showing an aperture smaller than for the exact calculation (Figure 2.18), consistently with the discussion at the end of the previous subsection, since the number of bounces is significantly reduced when using this approximation.

	$\langle X \rangle$	σ_X	σ_X^-(nb. of pellets)	σ_X^+(nb. of pellets)
Slowing down [%]	28.59	14.41	8.32(23)	23.73(9)
Mass loss [%]	29.02	8.90	5.90(22)	12.83(10)
Temperature increase [%]	8.41	3.22	2.06(22)	4.71(10)
Stored energy $\left[10^3 \mathrm{J.m}^{-3}\right]$	1.93	2.67	1.48(22)	4.10(10)
Impact radius on target [cm]	1.29	3.29		
Pitch angle of exit trajectory [°]	0.74	1.88		

Table 2.3. – Identical to Table 2.2 for the $\alpha_{lim} = 3°$ approximation.

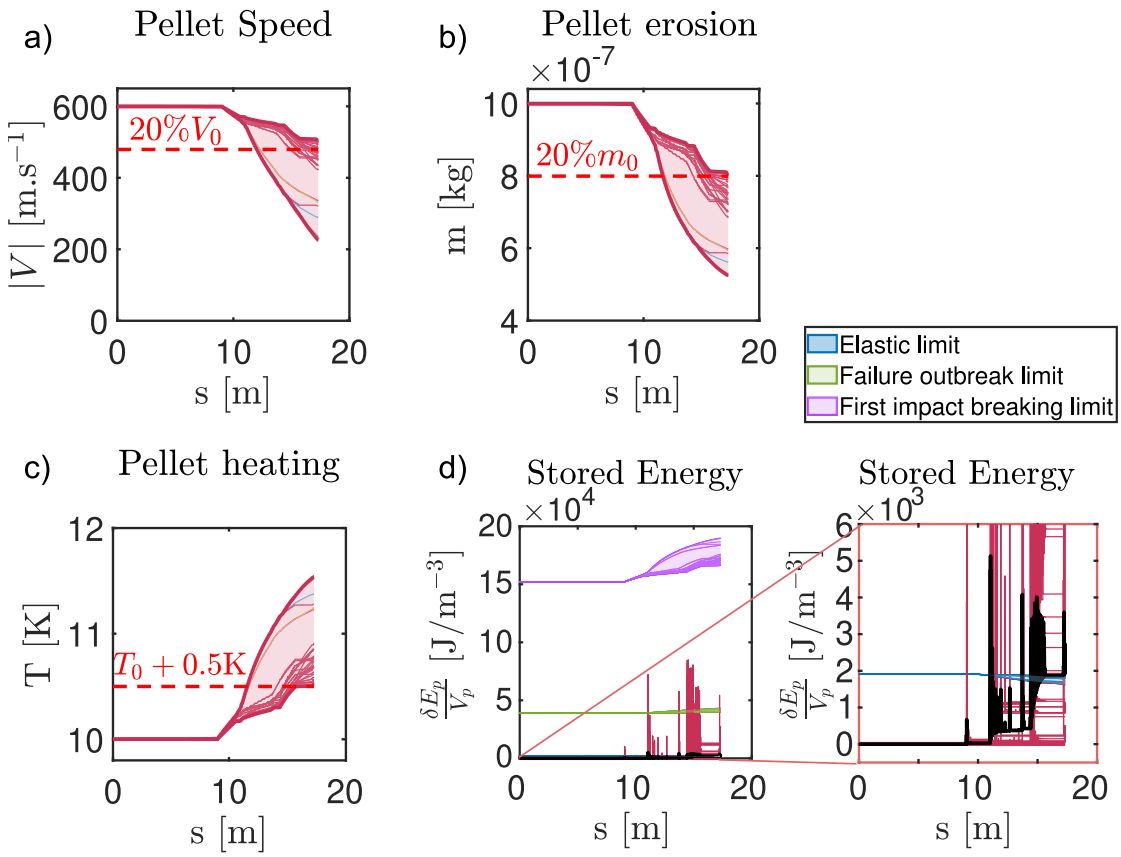


Figure 2.19. – Identical to Figure 2.16 for the $\alpha_{\text{Lim}} = 3°$ approximation.

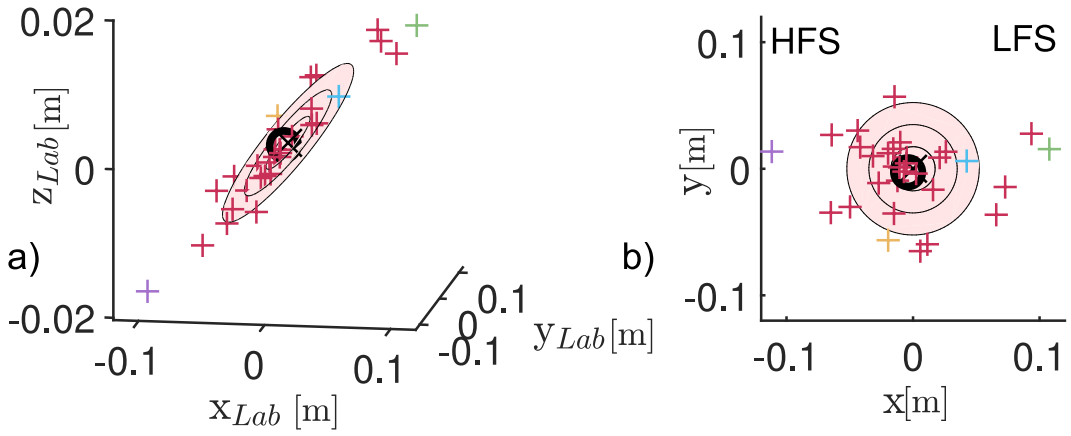


Figure 2.20. – Identical to Figure 2.18 for the $\alpha_{\text{Lim}} = 3°$ approximation.

2.7. Summary and Future work

This report describes a code aiming at calculating the path of a pellet inside a guide tube. The tube model consists in an arbitrary number of cylindrical rectilinear or toric sections arranged in an arbitrary geometry. Pellets are assumed spherical. They can bounce on or slip along the wall of the guide tube, but not roll. In addition to the centrifugal and Coriolis pseudo-forces, the external forces considered are that due to the ice deformation during a bounce, the slipping friction when the pellet touches the wall, the fluid friction due to the residual gas present in the guide tube and the gravity. The loss of kinetic energy resulting from the work of these forces is used for eroding the pellet, increasing the ice temperature and storing elastic energy in the pellet. In addition to the evolution of the pellet velocity, mass and ice temperature all along the trajectory, code output is the angular deviation of the pellet velocity at its exit of the guide tube with respect of the central axis of the last section. Reliable predictions require the statistical analysis of the results for a large number of pellets launched with a dispersion in initial position, mass and velocity magnitude and direction corresponding to what is expected at the exit of the type of injector considered. In a close future, the model should be complemented by considering the possibility of a curvature varying continuously in the toric sections (clothoid curves) and, at a longer term, by introducing the possibility of guide tubes of rectangular cross-section. The model uses a number of coefficients governing the magnitude of the different effects and forces (the contact heat transfer, the fluid and friction braking) or the ice reaction to the efforts (elasticity, dissipation, heat capacity, branching ratios between erosion, heating and storing of elastic energy). Most of these coefficients are not accurately known, which prevents the model from yielding reliable predictions in its present state. Only the behavior with temperature of the static strain-stress curve and heat capacity for Deuterium ice are known from literature, which cannot be used in confidence because the visco-elastic properties of a medium depend generally on the speed of deformation. Even if the fit of measurements already obtained on guide tube models in different laboratories will be an essential step in the code validation, it cannot be used for determining the values of the above mentioned coefficients because of the interplay between the different physical processes. Dedicated experiments will be therefore mandatory, using test beds with guide tubes of e.g. constant curvature and varying length and pipe diameter, or different ice quality by manufacturing the pellets by in-situ condensation or extrusion.

3. RELATION BETWEEN THE LOCAL ABLATION RATE AND PELLET CLOUD EMISSION

Sommaire

3.1. Introduction 91
3.2. Experimental apparatus 92
3.2.1. The Large Helical Device (LHD) 92
3.2.2. Pellet injection and associated diagnostics 95
3.3. Data processing 97
3.3.1. Photodiode calibration 101
3.3.2. Harmonization of time-resolutions 101
3.3.3. Calibration of camera images 103
3.4. Cloud global characteristics 107
3.5. Emission model 109
3.5.1. Line emission 110
3.5.2. Continuum emission 111
3.5.3. Spectrum and image reconstruction 112
3.6. Unicity of fit parameters 113
3.7. Emission pattern from HPI2 simulation 117
3.7.1. HPI2 simulation of pellet in discharge # 126636 117
3.7.2. Simulated spectra and emission pattern 122
3.7.3. Relation between ablation rate and cloud emission 123
3.8. Comparison with measurement 124
3.8.1. Global cloud characteristics 124
3.8.2. Interpolation on a realistic timing. 126
3.8.3. Building synthetic signals 127
3.8.4. Behavior of surface brightness 130
3.8.5. Relation between ablation rate and cloud emission 133
3.9. Discussion and conclusion 134

Abstract

The experimental reproduction of the conditions of pellet injection expected in future large devices being not possible in present day machines, it is mandatory to validate as thoroughly as possible the available ablation models. Among the different points yet in discussion, there is the relation between the spectroscopic measurement of the ablation clouds and the local ablation rate. This relation is investigated by coupling an emission model to the time-dependent simulation of ablation clouds with the HPI2 pellet ablation/deposition code. The simulated quantities are the time-evolution of the cloud visible spectrum ($\lambda = 400 - 700$ nm) and images in different wavelength domains (e.g. H_α, H_β or the continuum around $\lambda = 576$ nm). It is found that the cloud emission is anisotropic, this is particularly the case of H_α and H_β lines, and that the relation between the cloud emission and the ablation rate depends not only on the conditions of pellet injection, but also on the direction of observation. It follows that it is in general not possible to estimate the ablation profile from that of an emission line (H_α or H_β). The code predictions are compared with corresponding measurements for a well-documented pellet injected in LHD, showing a good agreement for global values and main trends. The reasons of observed discrepancies are discussed.

3.1. Introduction

Pellet injection is necessary for the fueling of ITER and DEMO. However, the experimental reproduction of the conditions expected in these machines is not possible in present day devices, and predictions rely exclusively on modeling. It is thus mandatory to validate the available ablation/deposition codes as thoroughly as possible. Fueling by pellets consists in two phases: the ablation phase, which is a selfregulated process, during which clouds much denser and colder than the background plasma (typically by a factor 10^3) are deposited along the pellet trajectory; then the homogenization phase, during which the deposited material expands along the magnetic field lines and simultaneously drifts down to the magnetic field gradient (see Chapter 1, Section 1.3 for more details). If the physics involved in the homogenization phase is well characterized experimentally ([26, 27]), this is not the case for the former ablation phase. Up to now, ablation code validation relies only on the comparison between the calculated and measured values of the total penetration depth of the pellets into the plasma (see e.g. [31, 101, 102], and refs. in Chapter 1). Such a procedure integrates the entire path of the pellet, and the experimental estimation of the local ablation rate is based on the assumption that the latter is proportional to the intensity of radiation emitted by the ablation clouds. In this perspective, the cloud characteristics (particle content, dimensions, density and temperature, which are the initial conditions of the drift phase) and the relation between line emission and ablation rate are of particular interest. From the point of view of simulation, a number of cloud characteristics are estimated from ablation codes (e.g. the ablation module of HPI2 [37, 38]), but the link between the calculated ablation rate and line emission is not known. In this chapter, an emission model is used to compute the emission spectra of the ablation clouds all along the pellet lifetime. Synthetic spectra and cloud images are built and compared with measurements of a well documented pellet [1] injected in the Large Helical Device (LHD): stellarator at the National Institute for Fusion Science - NIFS, Toki, Japan [103] (it is noticeable that the characteristics of ablation clouds, which are only function of the local plasma properties, do not depend on the magnetic configuration). The first part of this chapter - Sections 3.2 and 3.3- introduces shortly the Large Helical Device, describes the diagnostics used in this study and the procedure for cross calibrating the data. Section 3.4 presents the available measurements. A second part -Sections 3.5 and 3.7 - describes the emission model and discusses the different quantities of interest which can be simulated when applying this model to the predictions of an ablation code. In the following part - Section 3.8 - these predictions are compared to the available measurements. Last, in Section 3.9, the observed discrepancies between the simulation and measurements and the difficulties associated to the inverse approach (extracting the cloud parameters from the measurements) are discussed in detail. Applying the same procedure to other ablation codes (e.g. [31, 34, 44, 104]) would help in discriminating them for more accurate predictions.

1. This pellet is well representative of a significant number of quasi-identical experiments recorded in the LHD database.

3.2. Experimental apparatus

3.2.1. The Large Helical Device (LHD)

The Large Helical Device is a stellarator operated by the National Institute for Fusion Science (NIFS, Gifu, Japan) and one of the main pieces of the research program on Nuclear Fusion in Japan [105]. It has a Heliotron magnetic configuration, where the magnetic field is produced by the electric current in a series of pair coils wound around the vacuum chamber with regular intervals (the current in each coil of the pair differs in both intensity and direction) [106]. As far as the design of a fusion reactor is concerned, the main advantageous features of this type of machine are (1) a current-free plasma, which leads to steady, high-Q, and disruption-free reactors and (2) a high-density operation, which largely reduces the divertor heat loads [107]. A picture of the coil system and plasma shape in LHD are displayed in Fig. 3.1, and its main nominal parameters are summarized in Table 3.1 [108]. For heating the

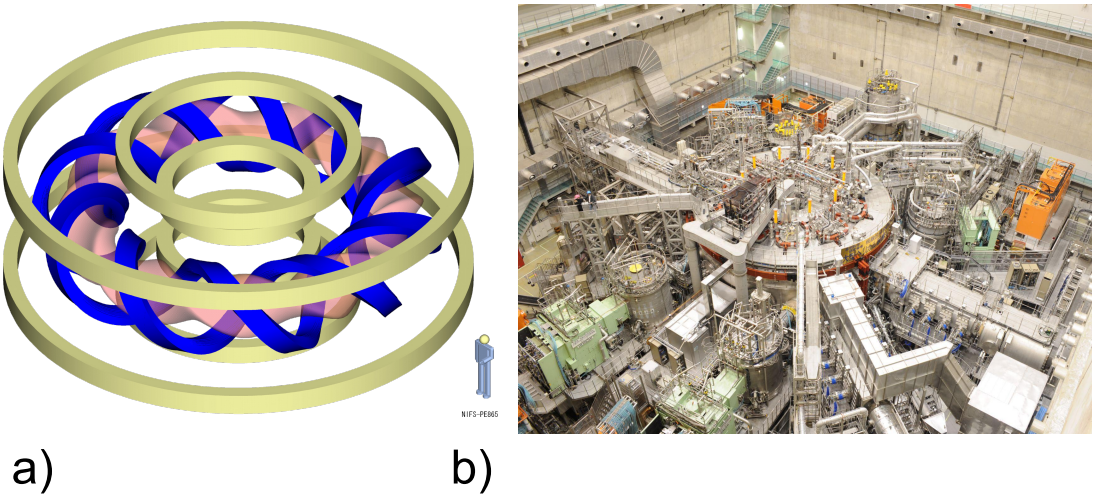


Figure 3.1. – (a) Coil configuration of LHD. Superconducting helical coils (blue), poloidal coils (yellow) and normal conducting Resonant Magnetic Perturbation (RMP) coils, together with plasma. (b) LHD torus hall (from [103]).

	Phase I (II)
Major radius R	3.9 m
Minor radius a	0.65 m
Plasma volume V_p	30 m^3
Coil minor radius a_c	0.975 m
Magnetic field B_t	3(4)T
Magnetic energy	0.9(1.6) GJ

Table 3.1. – Specifications of LHD (from [108])

plasma, three negative-ion-based 180-190 keV neutral beams (NBI) with total power of $8-16$ MW are injected tangentially to the plasma, and two positive-ion-based $40-80$ keV neutral beams with total power of $6-18$ MW are injected perpendicularly. In addition, electron cyclotron resonance heating (ECH) with total power of 5.5 MW is also available. For fueling, LHD is equipped with four gas puff valves and two pellet injectors [103], see Figure 3.2. During its first phase of operation (from 1998 to 2017),

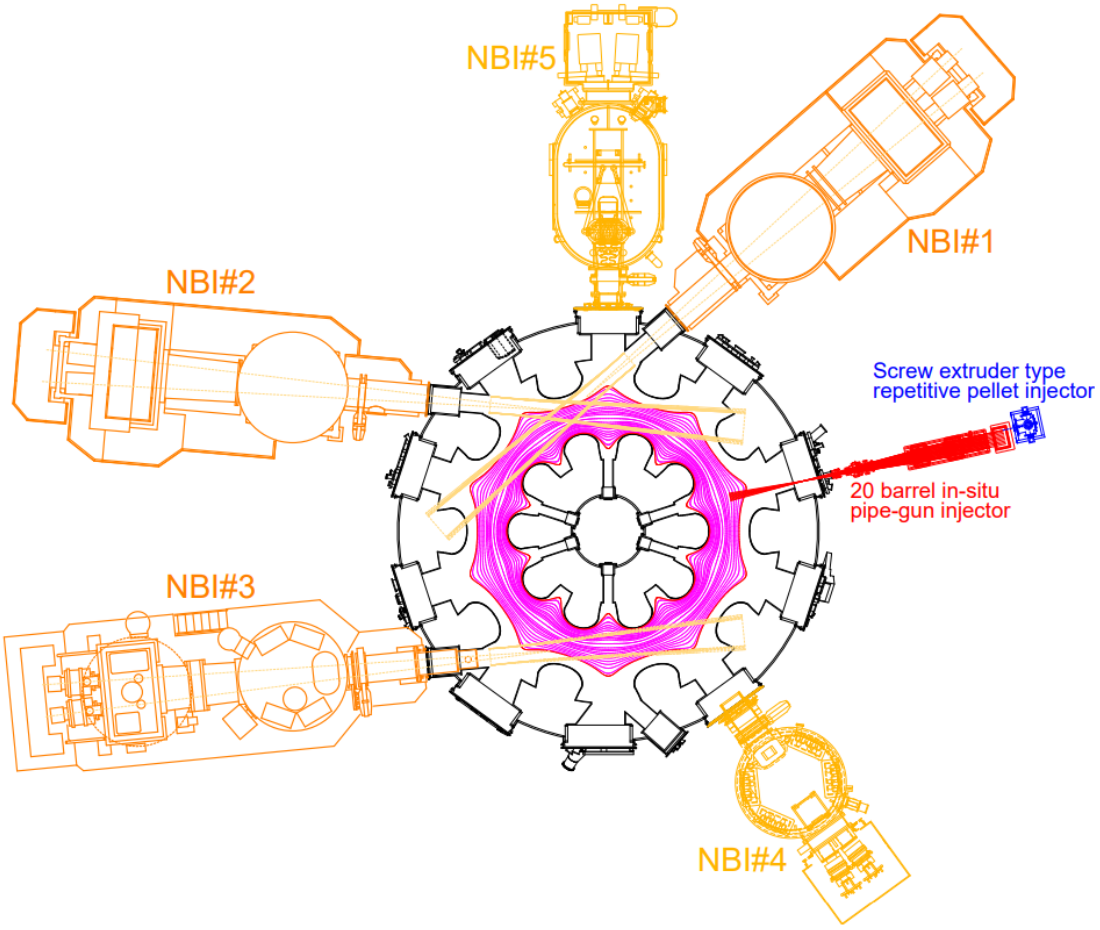


Figure 3.2. – Heating and fueling systems in LHD. The zoom shows the implementation of the pellet injectors and associated diagnostics discussed in Section 2.2

LHD was operated with Hydrogen as working gas. Main achievements are summarized in Table 3.2 [103] and illustrated in Fig. 3.3, which displays the operational domain of the electron and ion temperatures covered by discharges with NBI and NBI + ECH [109], the ion and electron temperatures and density profiles for the record high-T_i discharge [110] and the density and electron temperature profiles for a super-dense core (SDC) discharge [111]. Since February 2017, LHD is operated by using Deuterium as working gas, performing studies devoted for a large part to the change in confinement performance depending of the dominant working gas, the socalled

"isotope effect".

Parameters	Achieved	Key physics	Target
Ion temperature T_i	10 keV ($n_e = 1.2 \times 10^{19}$ m^{-3})	Ion ITB Impurity hole	10 keV ($n_e = 1.2 \times 10^{19}$ m^{-3})
Electron temperature T_e	20 keV ($n_e = 2 \times 10^{19}$ m^{-3}) 10 keV ($n_e = 1.6 \times 10^{19}$ m^{-3})	Electron ITB	10 keV ($n_e = 2 \times 10^{19}$ m^{-3})
Electron density n_e	1.2×10^{21} m^{-3} ($T_e = 0.25$ KeV)	Super dense core	4×10^{20}m^{-3} ($T_e = 1.3$ KeV)
Beta	5.1 % ($B_T = 0.425$ T) 4.1 % ($B_T = 1$ T)	MHD in current-free plasmas	5% ($B_T = 1-2$ T)
Duration time	54 min. 28 sec (0.5 MW, 1 keV,$n_e = 4 \times 10^{18}$ m^{-3}) 47 min. 39 sec (1.2 MW, 2 keV,$n_e = 1 \times 10^{19}$ m^{-3})	Dynamic Wall retention	1 hour (3 MW)

Table 3.2. – Achieved plasma parameters and key-physics studies for the H-operation phase in LHD (from [103])

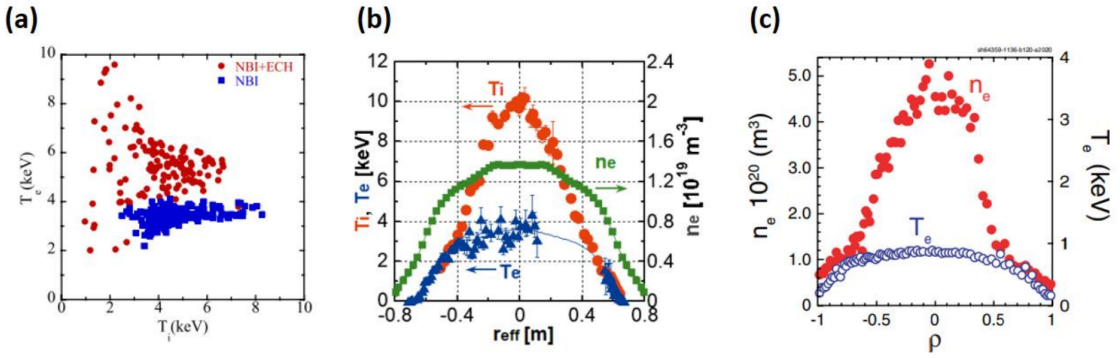


Figure 3.3. – (a) Operational domain in T_i and T_e in NBI and NBI+ECH discharges (from [109]), (b) T_i, T_e and n_e profiles for a record high- T_i discharge (from [110]) and (c) T_e and n_e profiles in a SDC discharge (from [111]).

3.2.2. Pellet injection and associated diagnostics

LHD is equipped with two pellet injectors. The first is a pneumatic injector for periodic injection of extruded pellets for long times (pellet size $l_p = 2-2.5$ mm, injection frequency up to $\nu_{inj} = 11$ Hz, injection velocity $V_{inj} = 150-550$ m.s^{-1}) [112]. The second is a 20-barrel gas gun injector launching in-situ condensed pellets $\left(l_p = 3-3.8\right.$ mm, $\left.V_{inj} \leq 1200\ \mathrm{m\cdot s^{-1}}\right)$ [113], see Fig. 3.2. For this analysis, a well-documented pellet $\left(l_p \sim 3\right.$ mm, particle content $N_p \sim 10^{21}$ at. $\left.\right)$ is chosen, injected at $V_{\mathrm{inj}} \sim 1000$ m.s^{-1} in a 7 MW NBI-heated discharge (#126636). Fig. 3.4 shows the conditions of the experiment: the injected NBI-power and the background plasma density and temperature profiles at the time of pellet-injection.

The images, line-emission and spectra of the ablation clouds are measured by a set of

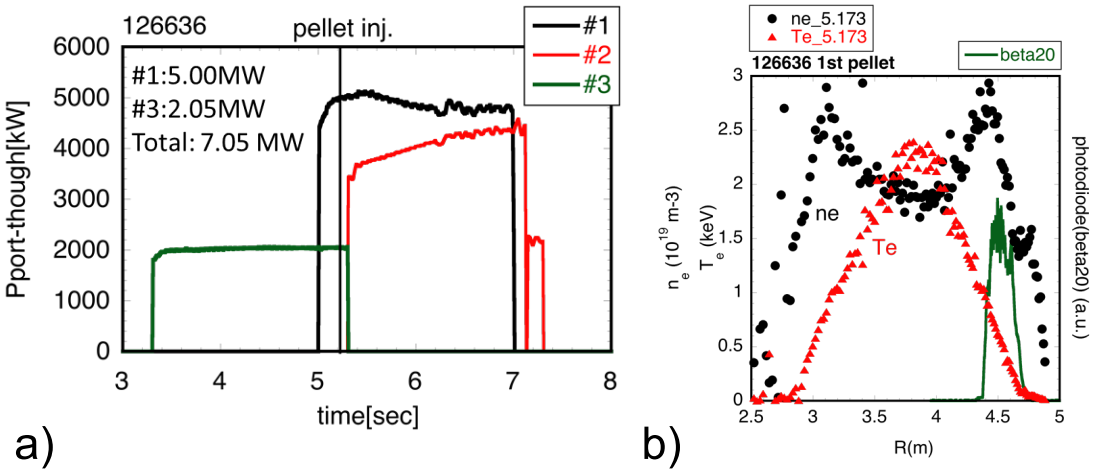


Figure 3.4. – (a) time schedule of discharge #126636, showing the waveforms of the NBI-power and the time of pellet-injection. Numbers #1,2,3 correspond to the Neutral Beams Injectors, shown in Fig. 3.2. (b) Pre-injection electron density and temperature profiles and H_β emission of the ablating pellet mapped on the discharge major radius,

three diagnostics arranged around the injectors as shown in Fig. 3.5:

— A high-speed imagining spectroscopie system. It consists on a multibranch fiberscope and a fast camera (one image every 20 μs, exposure time 2 μs). Each objective lens is equipped with a band filter $\left(H_\beta\right.$ with two filter widths: 5 and 20 nm, and the continuum close to the wavelength $\lambda = 576$ nm, see Fig. 3.6) [114]. A set of ≈ 20 frames are registered per pellet injection, among them about 10 are of accuracy high enough for being analyzed.

— A set of 3 fast diodes [2] (same filters, time resolution $\delta t_D = 2$ μs).

2. Diode measurements of total emission (hereafter referred to as $ND10$), and in the H_α and H_y lines are also available, but only used for the determination of the striation frequency $\nu_{\mathrm{Str}}^{\mathrm{exp}}$ in Section 3.4.

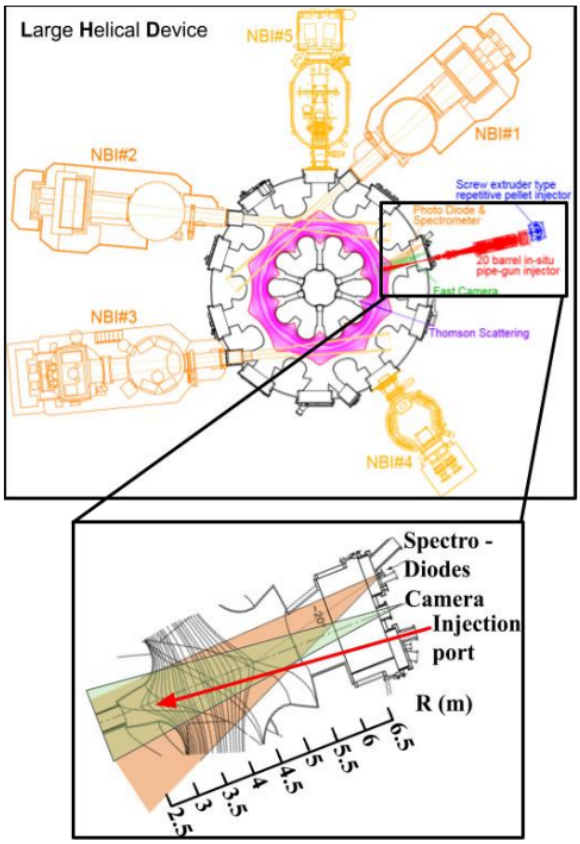


Figure 3.5. – Zoom of Fig. 3.2 showing the pellet injection port with the pellet injection direction (red arrow) and the arrangement of the three diagnostics with the corresponding fields of view.

— A high-resolution spectrometer, absolutely calibrated, in the domain $\lambda = 370 - 710$ nm (one spectrum every 16μs, but the signal integration time δt_S is longer) [115].

In the cross-field direction, the size of the Transfer Function of the imaging system (TF, point-source image, displayed in Fig. 3.7a) is comparable to that of a cloud image. For calculation purpose, it is fitted by a combination of two 2D-Gaussians, the parameters of which are listed in Table 3.3:

$$TF(Y,Z) = \frac{1}{\pi}\sum_{i=1}^{2}\frac{\varpi_i}{\sigma_i^Y\sigma_i^Z}\exp-\left[\left(\frac{Y-\delta_i^Y}{\sigma_i^Y}\right)^2+\left(\frac{Z-\delta_i^Z}{\sigma_i^Z}\right)^2\right]$$

where $\sigma_i^Y = b_i\cos\zeta_i + a_i\sin\zeta_i$ and $\sigma_i^Z = b_i\sin\zeta_i + a_i\cos\zeta_i$, and ζ_i is the angle between the major axis of the Transfer Function with respect to the vertical Y axis, see Fig. 3.7. In this expression, ϖ_1 and ϖ_2 are the weight of the two Gaussians.

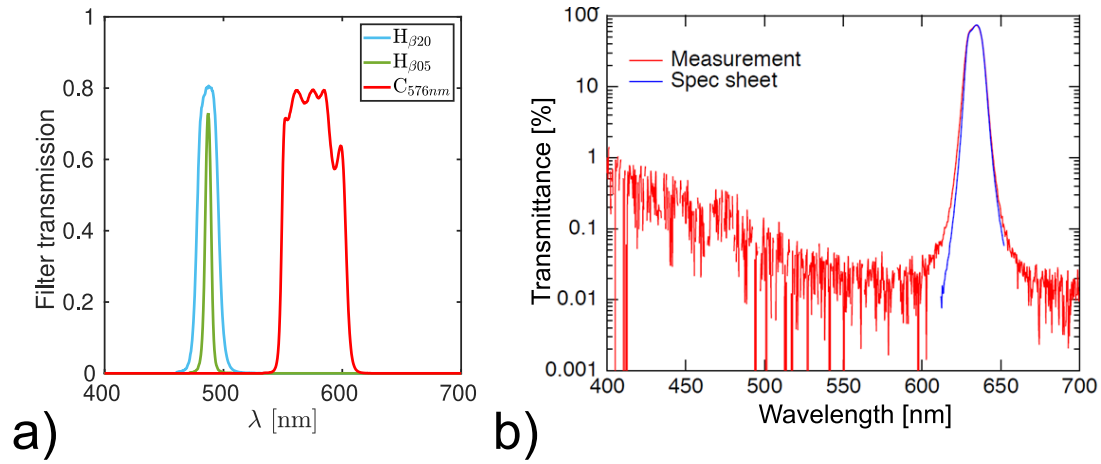


Figure 3.6. – (a) Filter transmissions F_λ : $H_{\beta 05}$ – 5 nm width (green), $H_{\beta 20}$ – 20 nm (magenta), $C_{576\text{nm}}$ (red). (b) Non-zero value of the transmission factor over the whole wavelength domain for $H_{\beta 20}$.

	Gaussian #1	Gaussian #2
ϖ_i : Relative magnitude	0.74	0.16
b_i : major half-axis [m]	7.2×10^{-3}	2.43×10^{-2}
a_i : minor half-axis [m]	6.3×10^{-3}	1.95×10^{-2}
ζ_i : b_i angle w.r.t. vertical Y [°]	40	55
δ_i^Y Y off-centering [m]	0	-1.8×10^{-4}
δ_i^Z Z off-centering [m]	0	-3.3×10^{-3}

Table 3.3. – Fit parameters of the camera transfer function.

3.3. Data processing

The available measurements for the pellet in discharge #126636 are displayed in Fig. 3.8, showing the photodiode signals, an example of spectrum (the spectrometer transmission falls off below $\lambda \sim 400$ nm) and of the set of the 3 camera images (their space resolution, i.e. the size of a pixel, varies with the exact distance between the pellet and the camera, its average value is ~ 6 mm).

At the beginning of the pellet lifetime, a few frames (#114, #116, marginally #112 with a time interval $\Delta t = 40$ μs between frames #112 – #114 and #114 – #116) [3] show two clouds emitting simultaneously, see an example in Figure 3.9. The secondary cloud appears as a shoulder on the side of the main cloud and cannot be clearly separated when determining the cloud dimensions. This superimposition of clouds emitting simultaneously is consistent with the picture where a part of the ablation cloud is periodically dissociated from the pellet, eventually before to be fully ionized. However,

3. One must note two successive frames do not correspond to two successive clouds. In other words, the secondary clouds in frame #116 do not correspond to the primary clouds in frames #114 or #115.

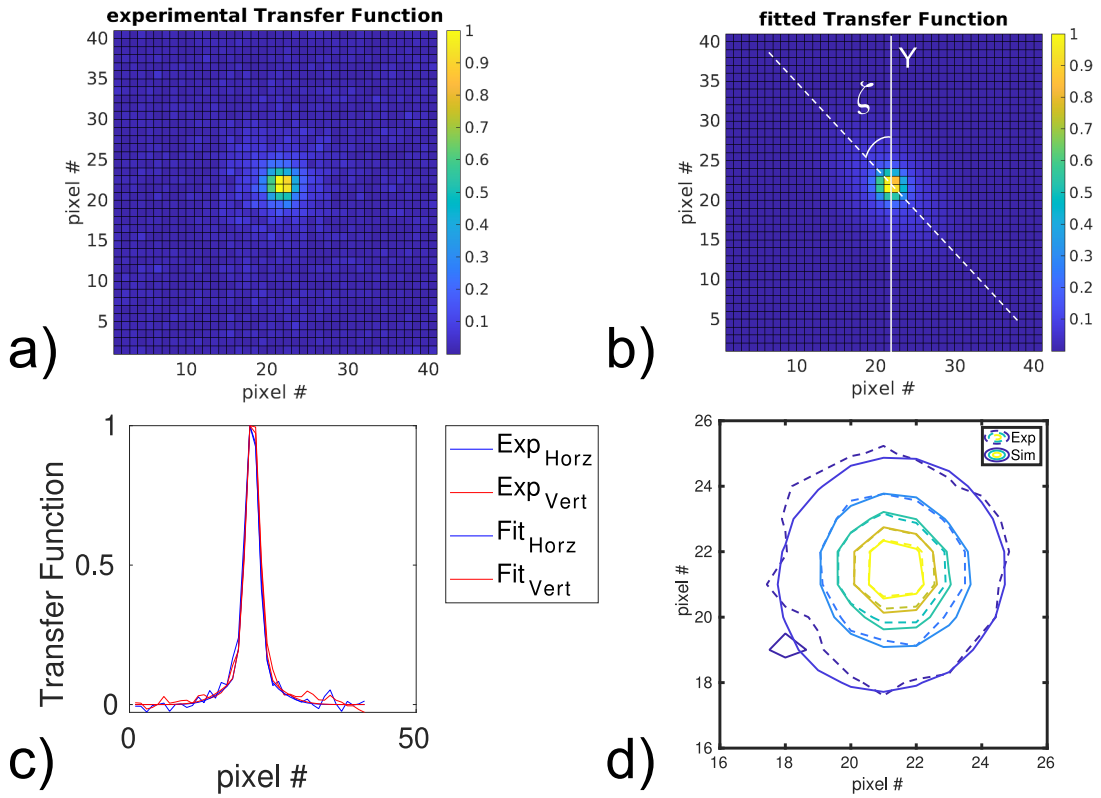


Figure 3.7. – Point-source image (transfer function) of the fast camera. (a) Experiment, (b) best fit, (c) comparison of measured and calculated vertical and horizontal profiles and (d) comparison of measured and calculated contour-plots.

the fact that two clouds can emit at the same time complicates the interpretation of the images and spectra (it was shown in [116] that cloud are detectable during a period of 5 to 10 μs after they begin to emit light).

The spectrometer being the only calibrated diagnostic, the photodiode signals and camera images must be cross-calibrated for corresponding the best to the measured spectrum power in the different wavelength domains. Knowing the filter transmissions $F_{\Delta\lambda}$ (Fig. 3.6a), the total energy emitted by the pellet in a given wavelength domain is:

$$E^{*S}_{\Delta\lambda} = \int P^{*S}_{\Delta\lambda} dt, \text{ where } P^{*S}_{\Delta\lambda} = \int F_{\Delta\lambda} P^{*S}_{\lambda} \cdot d\lambda \tag{3.1}$$

where P^{*S}_{λ} is the measured power in the spectrum ([W.nm^{-1}]), assuming isotropic emission (for the sake of clarity, the way the symbols for the different radiation quantities is explicated in Appendix B.1).

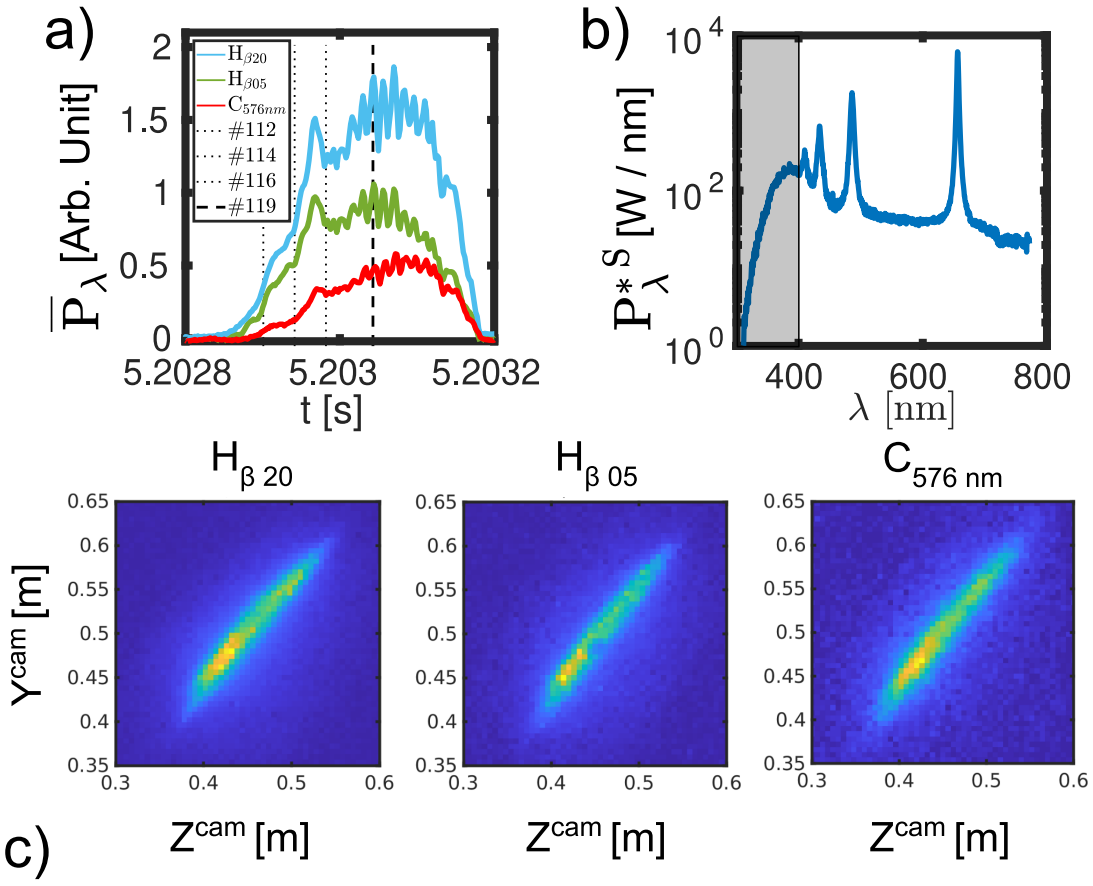


Figure 3.8. – (a) Photodiode measurements vs. time, (b) example of raw spectrum for frame #119 (spectrometer transmission falls off in the shadowed domain) and (c) corresponding fast camera images in the three wavelength domains $H_{\beta 05}$, $H_{\beta 20}$ and $C_{576\ nm}$.

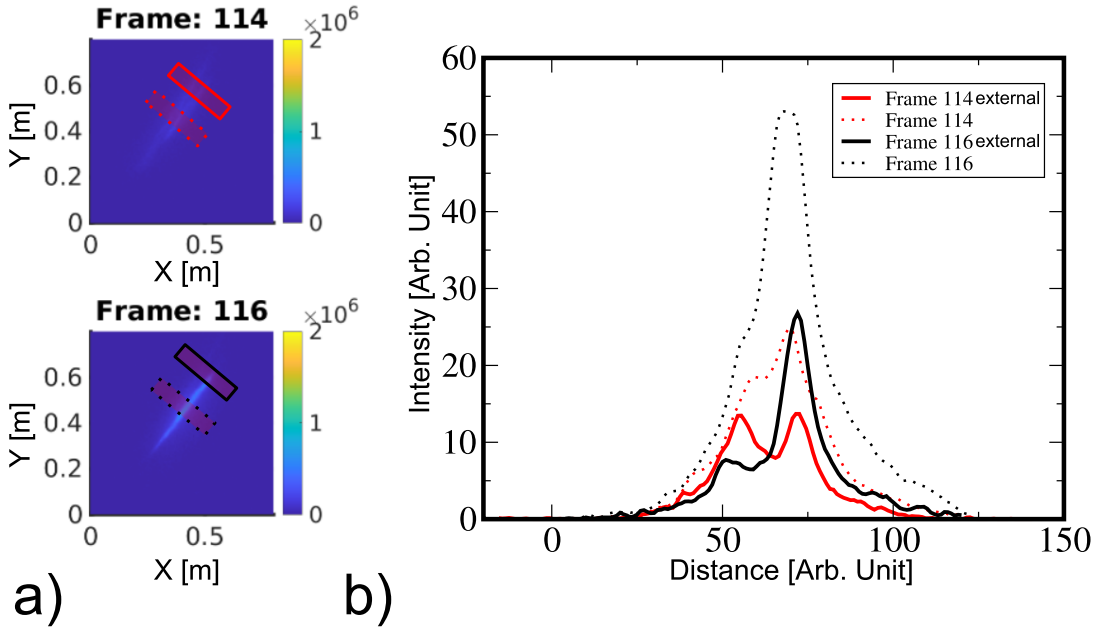


Figure 3.9. – (a) $H_{\beta 20}$ images for the frames # 114 and # 116, the boxes are the zones where cuts are calculated, (b) perpendicular cuts of light distribution at different places in the cloud images.

3.3.1. Photodiode calibration

If the diode signals are only available in arbitrary units, one knows from the manufacturer's documentation that - in the range of wavelength of interest - the diode sensitivity, D_λ, can be approximated by (see Fig. 3.10):

$$D_\lambda[\mathrm{A.W^{-1}}] = 0.0012 \times \lambda[\,\mathrm{nm}] - 0.34 \tag{3.2}$$

The effective filter transmission is therefore: $F^e_{\Delta\lambda} = F_{\Delta\lambda} D_\lambda$ and the signal measured

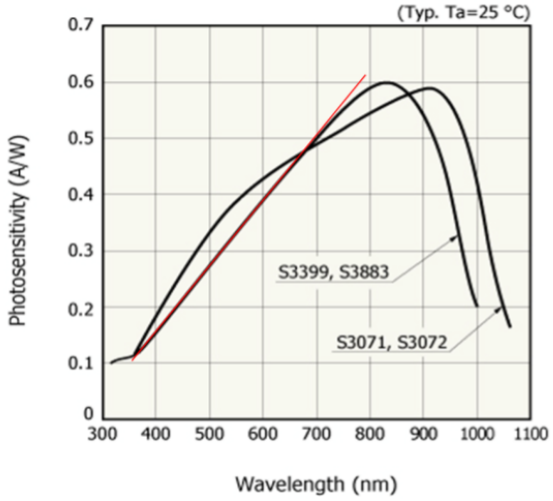


Figure 3.10. – Photodiode sensitivity D_λ vs. λ. The red curve is Eq. 3.2

by the diode: $\bar{P}^D_{\Delta\lambda} = \frac{P^{*D}_{\Delta\lambda}}{X_{\Delta\lambda}} = \frac{\int F^e_{\Delta\lambda} P^{*D}_\lambda d\lambda}{X_{\Delta\lambda}}$, where $X_{\Delta\lambda}$ is the calibration factor. Correcting $\bar{P}^D_{\Delta\lambda}$ from the diode sensitivity and imposing the equality of the radiated energy in the considered range of wavelength, on obtains:

$$X_{\Delta\lambda} = \frac{E^{*S}_{\Delta\lambda}}{\int \bar{P}^D_{\Delta\lambda} dt} \frac{\int F^e_{\Delta\lambda} d\lambda}{\int F_{\Delta\lambda} d\lambda} \tag{3.3}$$

Practically, on obtains $\mathrm{X_{576\ nm}} = 1.4922 \times 10^3$ W/(Arb. Unit),
$\mathrm{X_{H\beta\ 05}} = 1.4391 \times 10^3$ W/(Arb. Unit),
$\mathrm{X_{H\beta\ 20}} = 1.5531 \times 10^3$ W/(Arb. Unit),

Average value, used for calibrating the data, is $\langle X_{\Delta\lambda} \rangle = 1.4948 \times 10^3$ W/(Arb. Unit).

3.3.2. Harmonization of time-resolutions

The photodiodes and fast camera have the same integration time (2 μs), but that of the spectrometer, $\delta \mathrm{t_S}$, is not given in [115], where it is only specified that it is longer than the period of the measurement, i.e. 16 μs. Consequently, $\delta \mathrm{t_S}$ is determined by convolving the photodiode signals $P^{*D}_{\Delta\lambda} = X_\lambda \bar{P}^D_{\Delta\lambda}$ by a door function of adapted width

up to best fitting the time dependence of the spectra properly integrated over the three wavelength domains. The required width of the door function is 84 μs which, taking into account the integration time δt_D of the photodiodes, leads to $\delta t_S = 86$ μs. Then, the time vectors of the photodiode calibrated signals P^{*D}_{C576nm}, $P^{*D}_{H\beta 05}$ and $P^{*D}_{H\beta 20}$ and spectra P^{*S}_{C576nm}, $P^{*S}_{H\beta 05}$ and $P^{*S}_{H\beta 20}$ are adapted by calculating the shift in time $\delta t_{S/D}$ that minimizes the quantity $\int \sum_{\Delta\lambda} \left| P^{*D}_{\Delta\lambda} - P^{*S}_{\Delta\lambda} \right| dt$.
The best agreement is obtained for a time delay of the spectra w.r.t. the photodiodes $\delta t_{S/D} = -4$ μs. Final results are displayed in Fig. 3.11. Deconvolving the spectra by a

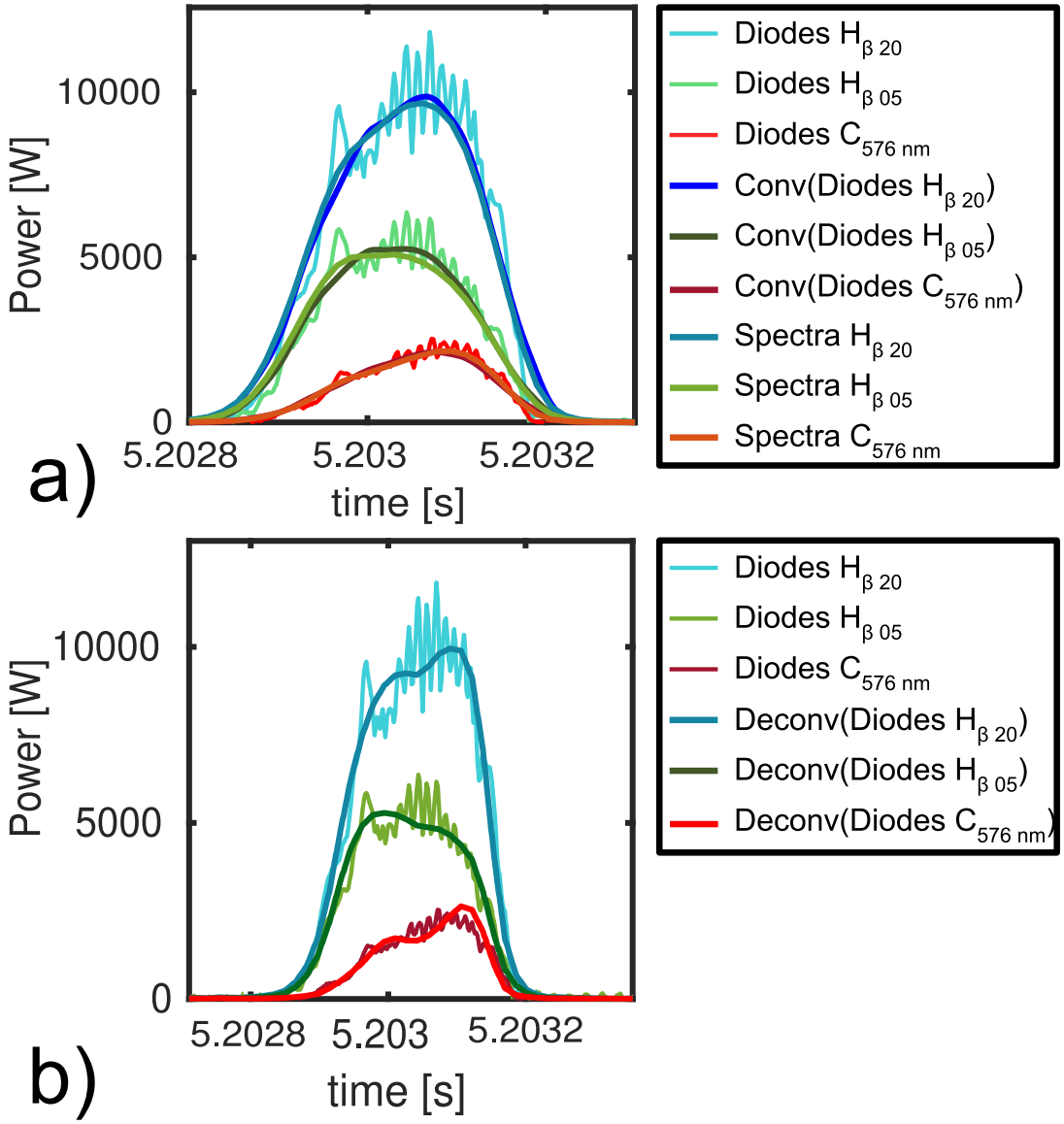


Figure 3.11. – (a) Power in spectra and photodiodes (original and convolved signals) as a function of time. (b) Power in deconvolved spectra (shifted in time by $\delta t_{S/d}$) and photodiodes.

door function of 84 μs yields spectra with the same time resolution as the photodiode signals and camera images. Practically, one observes only significant changes in the line and continuum intensities at the beginning and end of the ablation, where the spectra evolution is fast. An example is displayed in Fig. 3.12, for frames #115 (beginning of visible ablation, $t-5.2\ \mathrm{s} = 2.96\times10^{-3}$ s) and #124 (end of ablation, $t-5.2\ \mathrm{s} = 3.14\times10^{3}$ s).

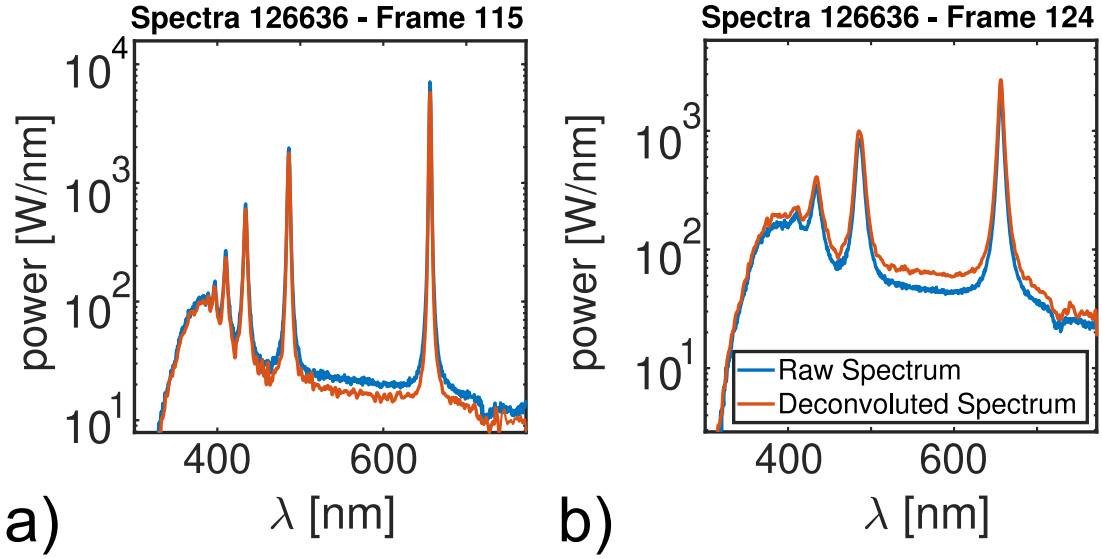


Figure 3.12. – (a) Raw and (b) deconvolved spectra at the beginning (frame #115) and end (frame #124) of the pellet lifetime.

3.3.3. Calibration of camera images

For a reliable analysis, it is mandatory to subtract from the camera images the contributions other than that of the cloud emission. They are 1) the background plasma emission and 2) the camera obscurity current. The first is estimated from the two spectra displayed in Fig. 3.13, the one recorded a long time before the pellet injection, the second at the time of frame #109 ($t-5.2\ \mathrm{s} = 2.84\times10^{-3}$ s) where the pellet just enters the plasma. Both are $\sim 10^2-10^3$ lower than the measurements during the ablation itself. Consequently, the images corresponding to frame #109 are taken as the sum of the background plasma emission and obscurity current contributions. The procedure for eliminating this background depends on the ratio between these two components:

— If the background plasma emission is larger than the obscurity current, the average value of the signal of frame #109 must be subtracted from the other images.

— In the opposite case, the images must remain unchanged where the value of the local signal is larger than this average value and must be put to zero where it is lower.

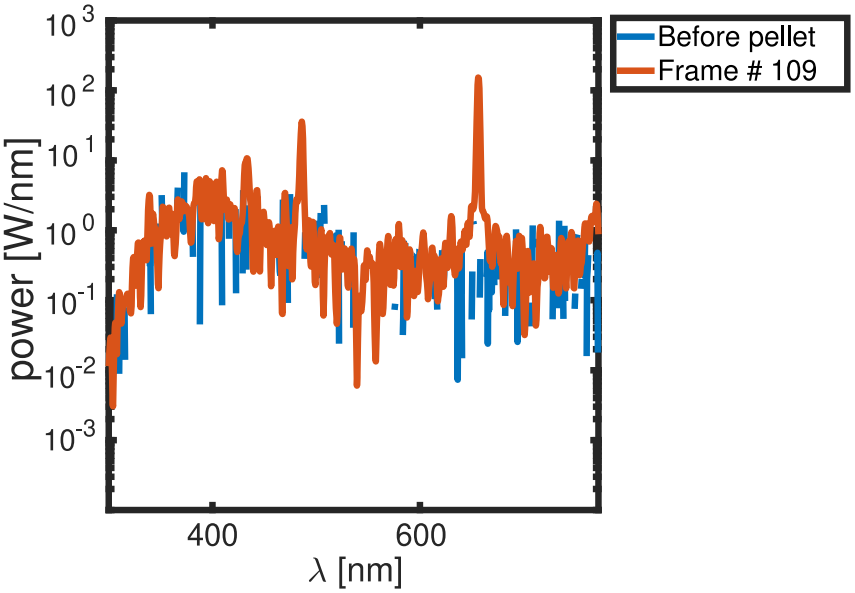


Figure 3.13. – Spectra recorded before the pellet injection and at time of frame #109.

Figure 3.14 shows, for the three wavelength domains ($H_{\beta 05}$, $H_{\beta 20}$ and C_{576nm}), the power integrated over the whole image, $\bar{P}^{I}_{\Delta\lambda}$, with no background subtraction (square marker), when putting the signal to zero where it is lower than the average of frame #109 (star marker) and with the average of frame #109 subtracted from the whole image (circle marker). The first procedure (star marker) does not reproduce the very low values of the integrated power at the beginning and end of ablation, as observed in Fig. 3.11b. It is therefore the second procedure, i.e. the background subtraction over the whole image, which is used for this study. Identically to what is done for the photodiode signals, the camera images are calibrated in energy by imposing that the total energy radiated in the three wavelength domains and summed over all the frames is equal to the corresponding value calculated from the spectra: $\sum_{\Delta\lambda} Y_{\Delta\lambda} \bar{P}^{I}_{\Delta\lambda} = \sum_{\Delta\lambda} P^{*S}_{\Delta\lambda}$. One obtains then:

$$Y_{\Delta\lambda} = \frac{\sum_{\Delta\lambda} P^{*S}_{\Delta\lambda}}{\sum_{\Delta\lambda} \bar{P}^{I}_{\Delta\lambda}} \tag{3.4}$$

with calibration factors,

$$\begin{aligned} Y_{576\ \mathrm{nm}} &= 328.199\ \mathrm{W/(Arb.\ Unit)}, \\ Y_{H\beta 05} &= 628.187\ \mathrm{W/(Arb.\ Unit)}, \\ Y_{H\beta 20} &= 608.538\ \mathrm{W/(Arb.\ Unit)}. \end{aligned}$$

The average value for the H_β-line is $\langle Y_{H\beta} \rangle = 618.363$ W./(Abr. Unit), the difference with $Y_{576\ \mathrm{nm}}$ results from the wavelength dependence of the camera sensitivity and fibers transmission. A global comparison is displayed in Fig. 3.15, showing a good agreement between the different signals. The fact that the global shape of $P^{*I}_{\Delta\lambda}$ fits well

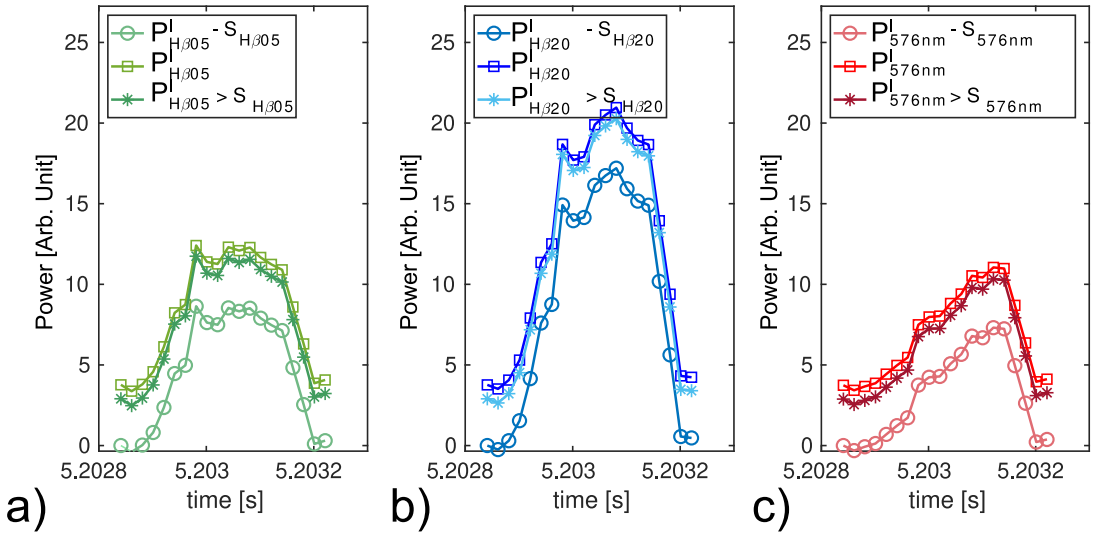


Figure 3.14. – Total power (in arbitrary units) in camera images without and with background subtraction (2 assumptions). (a) $H_{\beta 05}$, (b) $H_{\beta 20}$ and (c) $C_{576\ nm}$

those of $P^D_{\Delta\lambda}$ and $P^S_{\Delta\lambda}$ validates the procedure for the background subtraction used previously. The standard deviation around the average is ~ 10 % for the ~ 10 central frames where the radiated energy is large enough. Last, after background subtraction,

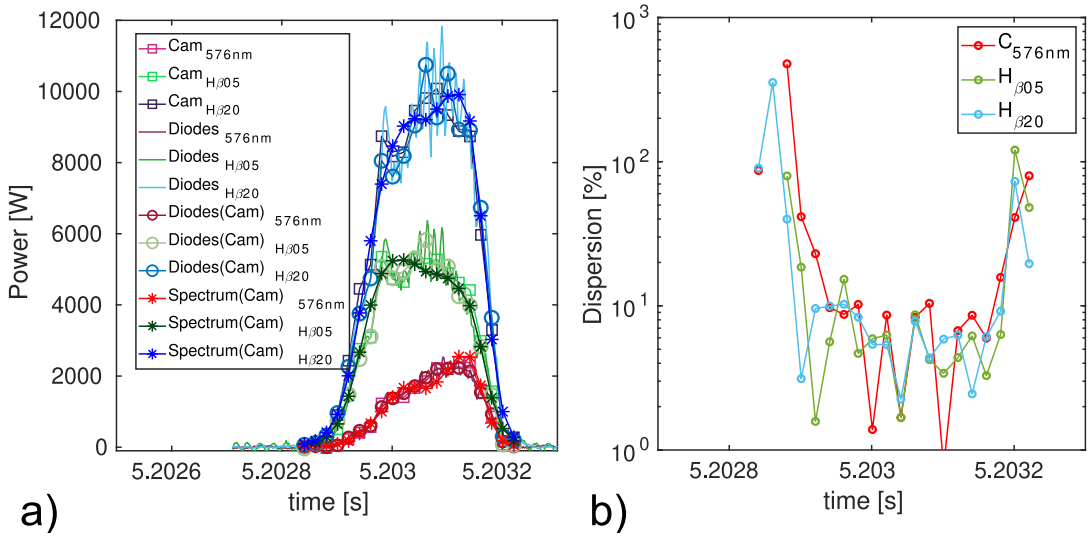


Figure 3.15. – (a) Radiated energy estimated from the camera images, photodiodes and spectra vs. time, (b) Standard deviation around the average.

raw camera images are rotated for aligning the cloud's major axis (its inclination changes from frame to frame due to the variation in the direction of the magnetic field) along the horizontal Z-direction and interpolated for easier comparison with

simulations. An example is shown in Figure 3.16, for the $H_{\beta\ 20}$-image of frame #118 ($t - 5.2\ \mathrm{s} = 3.02 \times 10^{-3}$ s). The whole procedure is expected to make available, for all the frames, a spectrum and set of three images in the $H_{\beta\ 05}$, $H_{\beta\ 20}$ and $C_{576\ \mathrm{nm}}$ bands, consistent in energy content and integration time.

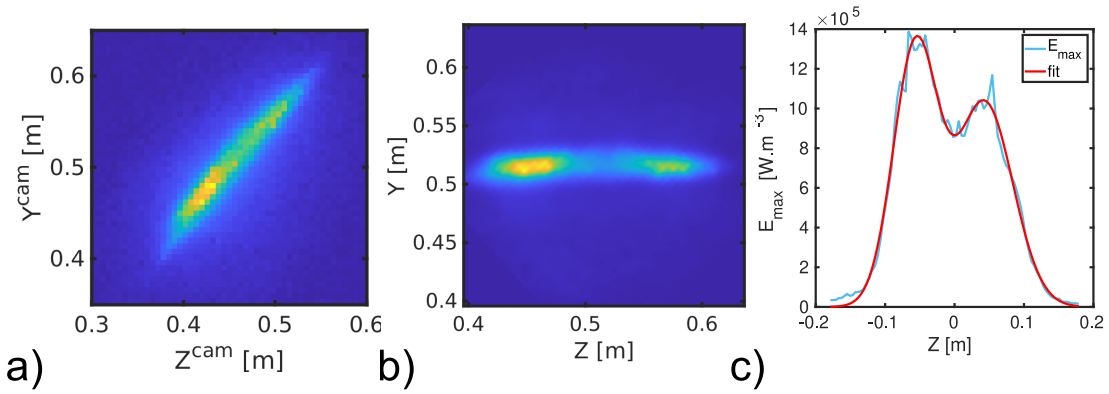


Figure 3.16. – (a) Raw camera image. (b) Rotated and interpolated image. (c) Profile of maximum emission (along the axis $Y = 0$) and fitting curve. The decrease of intensity close to $Z = 0$ indicates the pellet position.

3.4. Cloud global characteristics

In addition to the frame-by-frame data detailed in the previous section, some global characteristics of the clouds can be extracted from the above-presented measurements. They are the striation frequency and cloud dimensions along the pellet path.
As seen in e.g. Fig. 3.11, the light emission is modulated due to the quasi-periodic detachment of the ionizing part of the ablation clouds. This modulation appears as striations on the time-integrated ablation patterns ([20, 117]). The striation frequency can be determined either by calculating the frequency from the times of emission of the local maxima for the different diode signals (Fig. 3.17a), or by performing a Fourier analysis of the latter after having subtracted the continuous component (Figs. 3.17b and 3.17c). With both methods, one obtains $\langle \nu_{\mathrm{Str}}^{\mathrm{exp}} \rangle \sim 74 \pm 10$ kHz, with a trend of increasing frequency with pellet penetration.
Knowing the pellet initial particle content N_p, the total duration of pellet ablation τ_p and the striation mean frequency $\langle \nu_{\mathrm{Str}}^{\mathrm{exp}} \rangle$, one can obtain an average value for the cloud content $\langle N_{\mathrm{cl}}^{\mathrm{exp}} \rangle$, from the condition $\sum N_{\mathrm{cl}}^{\mathrm{exp}} = N_p$, yielding: $\langle N_{\mathrm{cl}}^{\mathrm{exp}} \rangle = N_p / \left(\tau_p \nu_{\mathrm{Str}}^{\mathrm{exp}} \right) \sim (3.5 - 4.5) \times 10^{19}$ atoms.
The characteristic dimensions of the clouds, half-length $\langle Z_0^{\mathrm{exp}} \rangle$ and radius $\langle R_0^{\mathrm{exp}} \rangle$, are taken as the HWHM of the images in the different wavelength bands. Because discharge #126636 (Figure 3.4a) is heated by parallel NBI injecting both fast neutrals in the same direction (Beams # 1 and 3 , see Fig. 3.2), the cloud incoming energy, and thus characteristics, can be asymmetric whether ones considers the co(CW)- or counter (CCW)-beam direction. In most cases, the pellet position in the cloud appears as a darker region close to its center, allowing identification of the two sides. The behavior of $\langle Z_0^{\mathrm{exp}} \rangle$ and $\langle R_0^{\mathrm{exp}} \rangle$ with time is shown if Figure 3.18a and 3.18 b. At each time, the dispersion results from the variation with the wavelength band. Cloud dimensions compare well with measurements in other machines, e.g. T-10 [118]. The general trend is a net decrease of the cloud length and radius with increasing penetration, with no clear difference between the co- and counter-beam sides. The maximum power in the half-images $m_{\Delta\lambda}^{*I}$ and integrated values $P_{\Delta\lambda}^{*I}$ are shown in Figures 3.18c and 3.18 d. In this case, a small asymmetry is detected on the maximum emitted power $m_{\Delta\lambda}^{*I}$, but the dispersion is too large on $P_{\Delta\lambda}^{*I}$ for a clear trend to be seen.

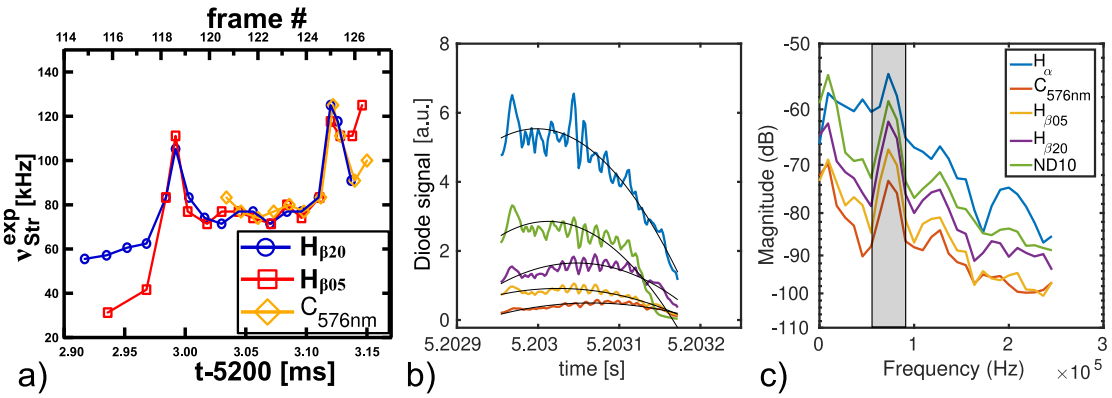


Figure 3.17. – (a) Striation frequency vs. time, calculated from the local maxima of the diode signals, (b) photo-diodes measurements, the dashed lines are the continuous component and (c) Fourier spectra of the oscillating part of the diode signals, exhibiting a peak at ~ 74kHz. (a)

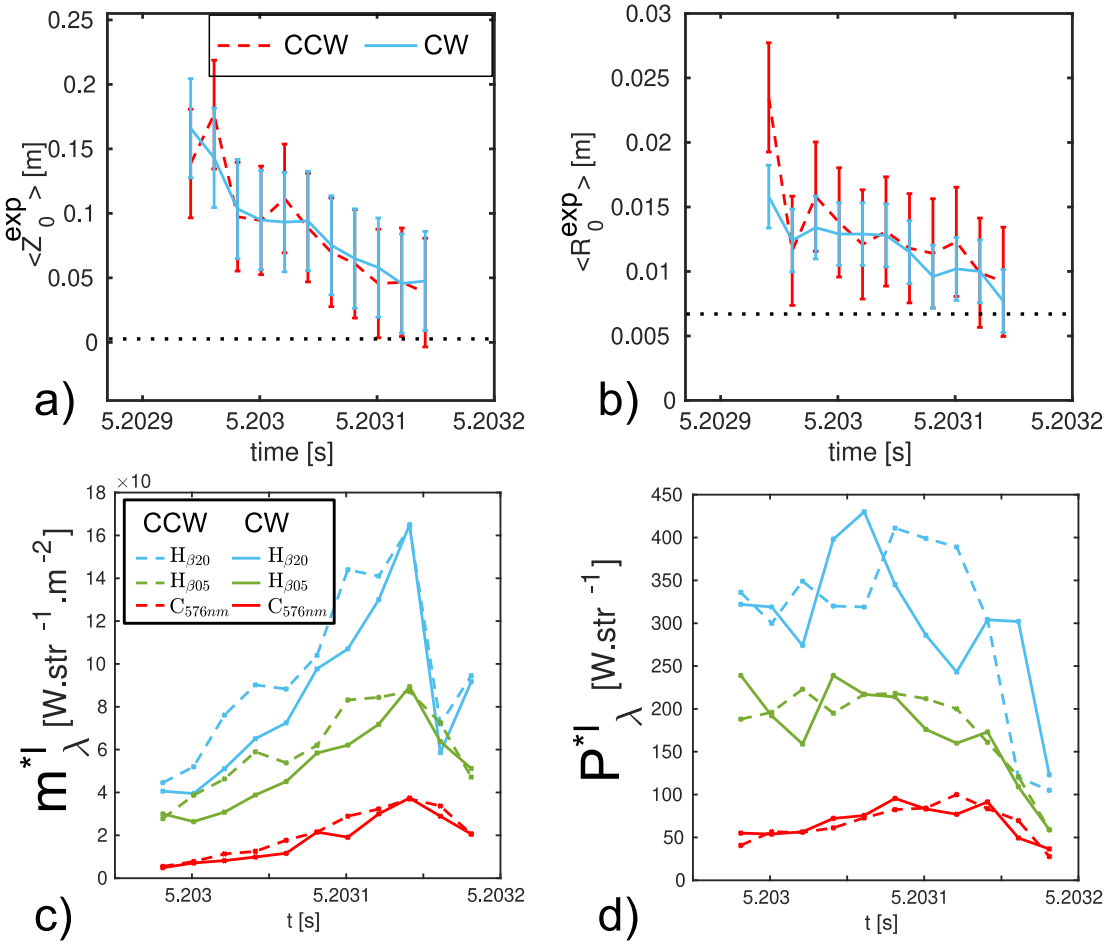


Figure 3.18. – Time evolution of (a) the cloud half-length $\langle Z_0^{exp} \rangle$, (b) the cloud radius $\langle R_0^{exp} \rangle$, the horizontal line is the HWHM of the Transfer Function, (c) the maximum of radiated power $m^{*I}_{\Delta\lambda}$ and (d) the total radiated power $P^{*I}_{\Delta\lambda}$.

3.5. Emission model

The spectrum calculation follows the lines drawn in ref [115]. Initially, this model was built for interpreting the spectrum of the ablation cloud of a pellet injected in the LHD (shown in Fig 3.21). Starting from the fact that the emission lines of neutral hydrogen exhibit Stark broadening profiles, the electron density was evaluated through comparison with theoretical data, with a high enough value for justifying complete Local Thermodynamic Equilibrium (LTE) in the cloud. It is also demonstrated that the continuum radiation is dominated by two components, which correspond to radiative recombination and radiative electron attachment, respectively. The whole model is composed of the calculation of:

— The line emission assuming LTE, the line profile taking into account both Doppler

and Stark broadenings [4],
— The continuum emission due to radiative recombination, radiative electron attachment and Bremsstrahlung of the incident plasma electrons in the cloud.
— A radiative transfer calculation assuming a cylindrical cloud, where the angle between the cloud axis and the observation direction is explicitly taken into account.

3.5.1. Line emission

One considers a cloud of heavy particle density (atom and ion) and temperature distributions $[n_0(X,Y,Z); T_0(X,Y,Z)]$ embedded in a plasma of local density and temperature $[n_\infty, T_\infty]$. Local thermodynamic equilibrium (LTE) is assumed in the cloud. In these conditions, the ionized fraction, f_i, writes: $f_i = \frac{1}{2}\left[\sqrt{(\psi^2+4\psi)}-\psi\right]$ with

$$\psi = \left(\frac{2\pi m_e}{h^2}\right)^{3/2} \frac{(k_B T_0)^{3/2}}{n_0} \exp\left(\frac{E_i}{k_B T_0}\right) \tag{3.5}$$

and $E_i = -13.6$eV. m_e is the electron mass, h and k_B the Planck's and Boltzmann's constants, respectively.
The densities of the excited states (noted by the subscripts " p "), are given by:

$$n_0^p = (1-f_i)\, n_0 \frac{g_p}{g_1} \exp\left(\frac{-(E_p - E_i)}{k_B T_0}\right) \tag{3.6}$$

where the energies E_p and statistic weights g_p of the excited levels are given in Table 3.4.
Only three emission lines of the Balmer's series are considered: $H_\alpha(3\rightarrow 2), H_\beta(4\rightarrow 2)$

	p = 1 (ground)	p = 2	p = 3	p = 4	p = 5
E_p (eV)	$-13.6\,(=E_i)$	−3.4	−1.51	−0.85	−0.54
$g_p = 2p^2$	2	8	18	32	50

Table 3.4. – Level energy and statistic weight of the 5 first levels of Hydrogen.

and $H_\gamma(5\rightarrow 2)$. The fact that the lines of higher order are not considered explains why the simulation does not fit the measured spectrum in the range $\lambda \sim 350-400$ nm, see Fig. 3.21. The frequency, wavelength, and Einstein's coefficient for spontaneous emission for these three lines are given in Table 3.5. The shape of the emission line, which displays a Voigt profile V_λ, results from the convolution of a Doppler (Gaussian)

4. Zeeman effect is not considered due to the quasi-perpendicular observation of the clouds (average angle > 80°), which would modify the line intensity by ≈ 0.5%, and to the weak wavelength separation between π and σ components (0.88 nm for H_α, 0.48 nm for H_β and 0.38 nm for H_γ), much smaller than the Stark broadenning.

	$\nu_0\,(10^{14}\ \mathrm{Hz})$	$\lambda_0\,(10^{-9}\ \mathrm{m})$	$A_{p\to 2 \text{ with p} \geq 3}\,(10^6\ \mathrm{s}^{-1})$
H_α	4.574	656	44.11
H_β	6.173	486	8.421
H_γ	6.912	434	2.531

Table 3.5. – Frequency, wavelength and Einstein's coefficient for spontaneous emission for H_α, H_β and H_γ

and of a Stark (Lorentzian) broadening. The Doppler component is given by:

$$\varphi_D(\lambda) = \frac{1}{\sqrt{\pi}\Delta\lambda_0} \exp\left[-\left(\frac{\lambda-\lambda_0}{\Delta\lambda_0}\right)^2\right] \tag{3.7}$$

where $\Delta\lambda_0 = \frac{\lambda_0}{c}\sqrt{\frac{2k_BT_0}{m_H}}$, c being the light velocity and m_H the proton mass, and the Stark component by:

$$\varphi_S(\lambda) = \frac{2/\pi L_F}{1+\left(\frac{\lambda-\lambda_0}{L_{F/2}}\right)^2} \tag{3.8}$$

where $L_F = 2F$, with the HWHM $F = \lambda\Delta_{\text{Stark}}$ is taken from [119]. The line intensity $\rho^L(\lambda)$ and absorption coefficient κ_λ write:

$$\rho^L(\lambda) = \frac{hc}{4\pi\lambda}\left[\sum_{m=3}^{5} A_{m2}n_0^m\right] V_\lambda(\lambda) \tag{3.9}$$

$$\kappa_\lambda = \frac{\lambda^4}{8\pi c}\left[\sum_{m=3}^{5} A_{m2}\left(n_0^2\frac{g_m}{8} - n_0^m\right)\right] V_\lambda(\lambda) \tag{3.10}$$

3.5.2. Continuum emission

Three physical processes are considered to participate to the continuum emission. They are the radiative attachment, the radiative recombination and the Bremsstrahlung, the two former being the most important. Details of the calculation are explicated in [115]. For the radiative attachment, $H + e \to H^- + h\nu$, the radiated power per unit of volume and per unit of frequency writes:

$$\rho_A(\nu) = \frac{1}{2}\sqrt{\frac{2}{\pi}}\frac{h^4}{m_H^{3/2}c^2}\left(\frac{1}{k_BT_0}\right)^{3/2}\exp\left(-\frac{h\nu - E_{H^-}}{k_BT_0}\right)\nu^3\sigma_{\text{det}}\,n_0^2 f_i\left(1-f_i\right) \tag{3.11}$$

where ν is the frequency, $E_{H^-} = 0.7542$eV and the cross-section σ_{det} is taken from [120]. Per unit of wavelength, this yields: $P^A(\lambda) = \rho_A(\nu)\frac{\nu^2}{c}$. Identically, for the radiative

recombination, $H^+ + e \rightarrow H(p) + h\nu$, one has:

$$\rho_p(\nu) = 2\sqrt{\frac{2}{\pi}}\frac{h^4}{m_e^{3/2}c^2}p^2\left(\frac{1}{k_B T_e}\right)^{3/2}\exp\left(-\frac{h\nu - \chi_H(p)}{k_B T_e}\right)\sigma_{ion}(p,\nu)\nu^3 n_0^2 f_i^2 \qquad (3.12)$$

with $\chi_H(p) = -E_p = \frac{13.6}{p^2}$eV is the ionization potential of level "p" and where the photo-ionization cross-section $\sigma_{\text{ion}}(p,\nu)$ is calculated following ([115, 121]). In this calculation, terminating levels up to $p = 10$ are taken into account, yielding: $P^R(\lambda) = \sum_{p=2}^{10}\rho_p(\nu)\frac{\nu^2}{c}$. And for the Bremsstrahlung:

$$\rho_B(\nu) = \frac{1}{6\pi}\sqrt{\frac{2}{3\pi}}\frac{e^6}{m_e^{3/2}c^3\varepsilon_0^3}\left(\frac{1}{k_B T_e}\right)^{1/2}\exp\left(-\frac{h\nu}{k_B T_e}\right)g_{ff}n_0^2 f_i^2 n_e \qquad (3.13)$$

i.e.: $P^B(\lambda) = \rho_B(\nu)\frac{\nu^2}{c}$ with the electron density $n_e = n_0 f_i$ and $T_e = T_0$ for the cloud contribution, $n_e = n_e^\infty$ and $T_e = T_e^\infty$ for the plasma contribution (negligible). g_{ff} is the Gaunt's factor.

3.5.3. Spectrum and image reconstruction

The cloud is embedded in a box of dimensions $2X_{\max} \times 2Y_{\max} \times 2Z_{\max}$ and it is seen along the X direction, which - in Fig. 3.19 - makes an angle ϕ with one of the symmetry axis of the cloud. The radiative transfer calculation is performed in the x-direction,

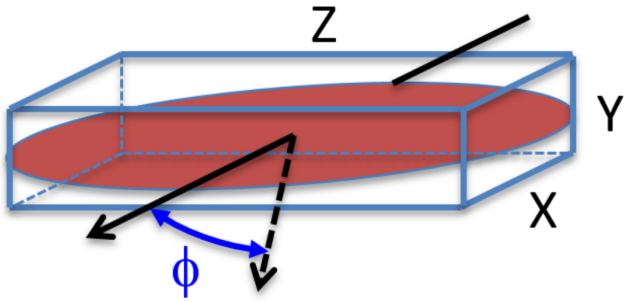


Figure 3.19. – Geometry for the spectrum calculation and image reconstruction.

from $-X_{\max}$ to $X_{\max}$, along all the lines $x = C^{st}, z = C^{st}$, following: $\frac{dI_\lambda}{dx} = -\kappa_\lambda I_\lambda + \sum\rho_\lambda$ The radiative transfer calculation is performed in the x-direction, from $-X_{\max}$ to $X_{\max}$, along all the lines $x = C^{st}, z = C^{st}$, following:

$$\frac{dI_\lambda}{dx} = -\kappa_\lambda I_\lambda + \sum\rho_\lambda \qquad (3.14)$$

where I_λ is the light intensity at wavelength λ and κ_λ and $\sum\rho_\lambda$ the corresponding absorption coefficient and emitted power contributions detailed in the previous Section.

The spectrum is then calculated as:

$$P^S(\lambda) = \int_{-Y_{\max}}^{Y_{\max}} \int_{-Z_{\max}}^{Z_{\max}} I_\lambda \left(X_{\max}, y, z\right) dy dz \tag{3.15}$$

and the images for the different filters, as:

$$P^I_{\Delta\lambda}(y,z) = \int I_\lambda \left(X_{\max}, y, z\right) F_{\Delta\lambda} d\lambda \tag{3.16}$$

For direct comparison with measurement, the images are convolved with the camera transfer function, i.e.:

$$P^{\mathrm{I,TF}}_{\Delta\lambda}(y,z) = \left(P^I_{\Delta\lambda}(y,z) * TF(y,z)\right) \tag{3.17}$$

where " $*$ " is the convolution product.
The fact that the absorption coefficient κ_λ is large in the H_α (and H_β) emission lines has for consequence that the clouds are not isotropic emitters and that their spectrum depends strongly on the angle ϕ they are observed under. This is shown in Fig. 3.20 where the spectrum of a cloud of radius $R_0 = 1.2 \times 10^{-2}$ m, total length $2Z_0 = 2 \times 10^{-1}$ m, density $n_0 = 5 \times 10^{24}$ m^{-3} and temperature $T_0 = 1$ eV is displayed for different observation angles [5]. The continuum being optically thin, its intensity does not change with ϕ, but the effect is visible on the emission lines as soon as $\phi \geq 30°$.

3.6. Unicity of fit parameters

Records of ablation cloud spectra for pellets injected in different plasma conditions are analyzed in [115] and [122]. In all cases, the spectra are accurately reproduced, but the corresponding cloud dimensions are unrealistic (see the discussion in [115]). This comes likely from the fact the cloud emission varies strongly with time and space, as demonstrated in [123], and that the spectrometer data are average values integrated over several clouds. Verifying this hypothesis requires checking if a spectrum can be reproduced by a combination of spectra calculated with different input parameters or if the solution is unique.
An example of simulation $\left(P^{\mathrm{S,sim}}(\lambda)\right)$ and comparison with measurement $\left(P^{\mathrm{S,exp}}(\lambda)\right)$ is displayed in Fig. 3.21 (data from Fig. 3 of [115]), showing the line emission and the different continuum components. Simulation parameters are:
$n_0 = 1.85 \times 10^{25}$ m^{-3}
$T_0 = 9.83 \times 10^{-1}$eV
$\left(n_e = 2.32 \times 10^{23}\ \mathrm{m}^{-3}\right)$
Radius $R_0 = 1.33 \times 10^{-3}$ m

5. This figure illustrates the modification of the line profiles due to the increasing optical depth with ϕ. Considering the splitting of the lines due to the Zeeman effect and the associated decrease of the π component, these would decrease the line intensities by 20, 25, and 33 % for $\phi = 60$, 75 and 88°, respectively.

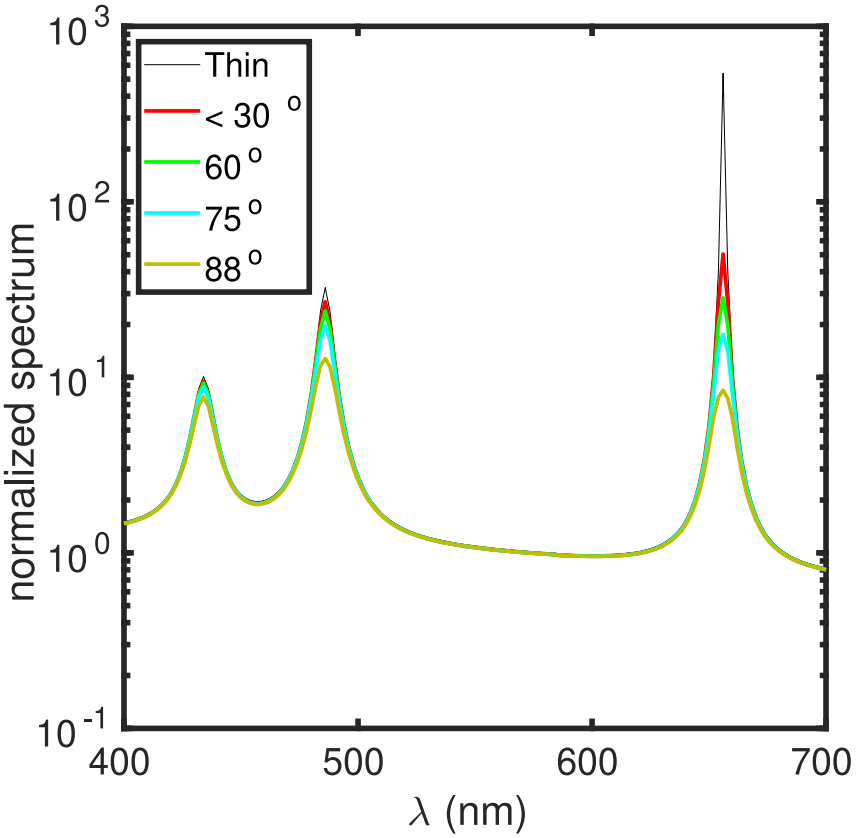


Figure 3.20. – Modification of the spectrum for different observation angles ϕ.

Length $Z_0 = 2.22$ m
If the simulation reproduces well the measurement, the best fit parameters (particularly R_0 and Z_0) are unrealistic for an ablation cloud (see Fig. 3.21) and, in all cases, Z_0 exceeds the field of view of the spectrometer, as noted in [115]. This questions the uniqueness of the solution using a homogenous cloud. Starting from the fact that the most constrained quantity from the spectrum is the electron density n_e through the Stark broadening of the emission lines, a study was performed to see if it is possible to find a combination of spectra along the line $n_e = 2.32 \times 10^{23}$ m^{-3} that reproduces the experimental spectrum $P^{\mathrm{S,exp}}(\lambda)$. Indeed, at constant n_e and adapted radius, all the emission lines display the same profile and only the continuum intensity changes with the chosen couple (n_0, T_0). Using a basis of N_S simulated spectra calculated with the same value of n_e but with different couples $\left(n_0^i, T_0^i\right)$, it should be therefore possible to find a set of N_S coefficients α^i $\left(\sum_i \alpha^i = 1\right)$ such that :

$$P^{\mathrm{S,exp}}(\lambda) = \sum_i \alpha^i P^{\mathrm{S,sim}\,i}(\lambda) \tag{3.18}$$

Ideally, one should use a continuous set of spectra and allow the coefficients of the linear combination to vary also continuously. But the possibilities are limited because the number of cases to test varies as $\sim {N_\alpha}^{N_S}$, where $N_\alpha = 1 + 1/\delta\alpha$ is the number of

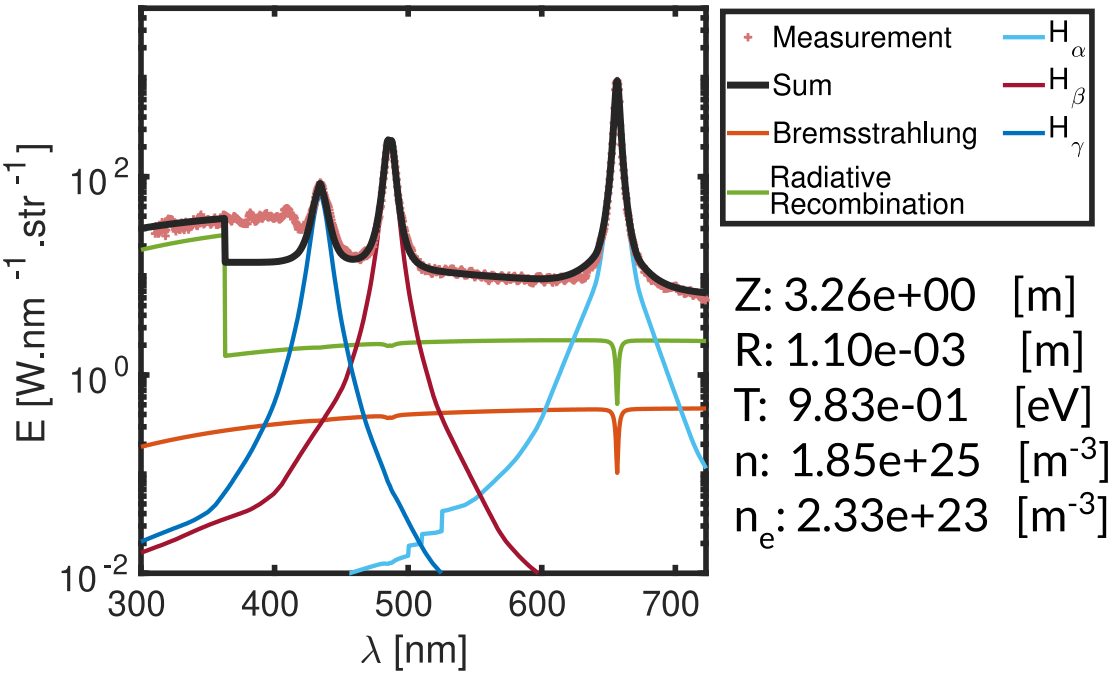


Figure 3.21. – Example of calculated spectrum $P^{\mathrm{S,sim}}(\lambda)$ (black curve) compared to experimental data $P^{\mathrm{S,\,exp}}(\lambda)$ (red crosses).

authorized values for the α^i 's. Here, we use $\delta\alpha = 0.05$ and $N_S = 10$.
For evaluating the quality of a fit, one characterizes the evolution of the continuum by two ratios:

$$\rho_{330} = \frac{\int_{320n\ \mathrm{nm}}^{345\ \mathrm{nm}} P^{\mathrm{S,exp}}(\lambda)d\lambda}{\int_{320\ \mathrm{nm}}^{345\ \mathrm{nm}} P^{\mathrm{S,sim}}(\lambda)d\lambda} \tag{3.19}$$

and

$$\rho_{560} = \frac{\int_{550\ \mathrm{nm}}^{580\ \mathrm{nm}} P^{\mathrm{S,exp}}(\lambda)d\lambda}{\int_{550\ \mathrm{nm}}^{580\ \mathrm{nm}} P^{\mathrm{S,sim}}(\lambda)d\lambda} \tag{3.20}$$

A fit is considered to be acceptable if both ratios verify:

$$\frac{1}{(1+\delta\alpha)} \leq \rho_{330};\ \rho_{560} \leq (1+\delta\alpha) \tag{3.21}$$

The chosen set of $N_S = 10$ simulations and corresponding ratio evolution is shown in Fig. 3.22. The range in temperature is limited by the available data (Stark broadening [119]) towards the low values, and by unrealistic values for the $\left(R_0^i, Z_0^i\right)$ couple towards the high values. The different set α^i 's that satisfy the inequality 3.21 are plotted in Figure 3.23a. More than 2000 combinations satisfy this criterion, and one must note that any linear combination of these different solutions is also a solution. As

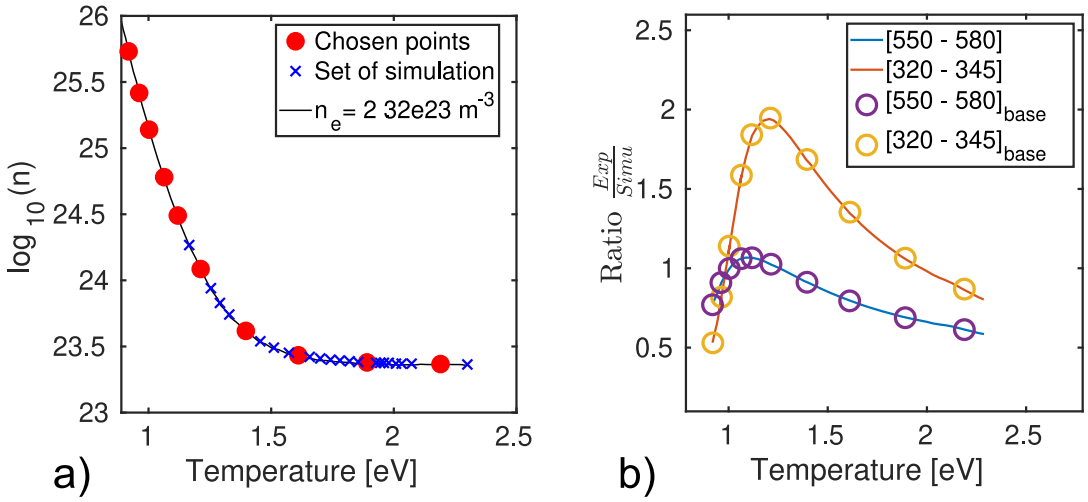


Figure 3.22. – (a) Set of simulations (red points) chosen for fitting the experimental spectrum $S_{\text{Exp}}(\lambda)$.(b) Behavior of the two ratios ρ_{330} and ρ_{560} for the considered set of simulations.

an example, the black line in Fig. 3.23a is just the average value of each α^i over the set of solutions, the comparison between all the synthetic spectra and $P^{\text{S,exp}}(\lambda)$ is displayed in Fig. 3.23b. The same exercise could be done by combining spectra

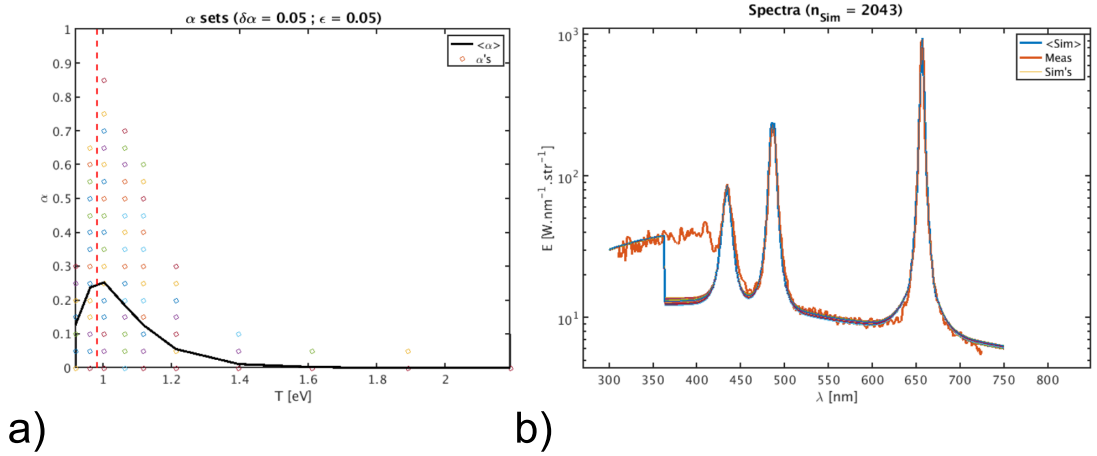


Figure 3.23. – (a) The different sets of α^i 's. The black line is the average values, the red dashed line marks the temperature for a fit by a homogenous cloud. (b) Superposition of all the spectra satisfying the criterion 3.21.

with different Stark broadening but same continuum value... In conclusion, this study demonstrates that a given spectrum can be fitted by numerous density and temperature combinations, underlining the difficulty of extracting without *a priori* assumptions cloud parameters from measurements. For this reason, it was chosen to proceed in the inverse way, i.e. to build synthetic spectra and images for a pellet

ablation simulation, and then to compare them with available measurements.

3.7. Emission pattern from HPI2 simulation

3.7.1. HPI2 simulation of pellet in discharge # 126636

The ablation module of the code HPI2 ([37, 38]) is a Neutral Gas and Plasma Shielding (NGPS) model that takes into account the over-ablation due to the fast ions. Input parameters are:

— The injection geometry (magnetic axis at $R_{\text{axis}} = 3.75$ m, toroidal field $B_{\text{axis}} = 2.64T$ for discharge # 126636), as displayed in Fig. 3.24,
— The pellet initial particle content $N_p = 10^{21}$ at. and injection velocity $V_{\text{inj}} \sim 1.1 \times 10^3$ m.s^{-1},
— The background plasma density (n_∞) and temperature (T_∞) profiles, see Figs. 3.25a and 3.25b,
— The fast ions density (n_f) profile, Fig. 3.25b, mean energy $E_f = 175$ keV and average cosine of pitch angle $\langle \cos\theta \rangle = 0.9$.

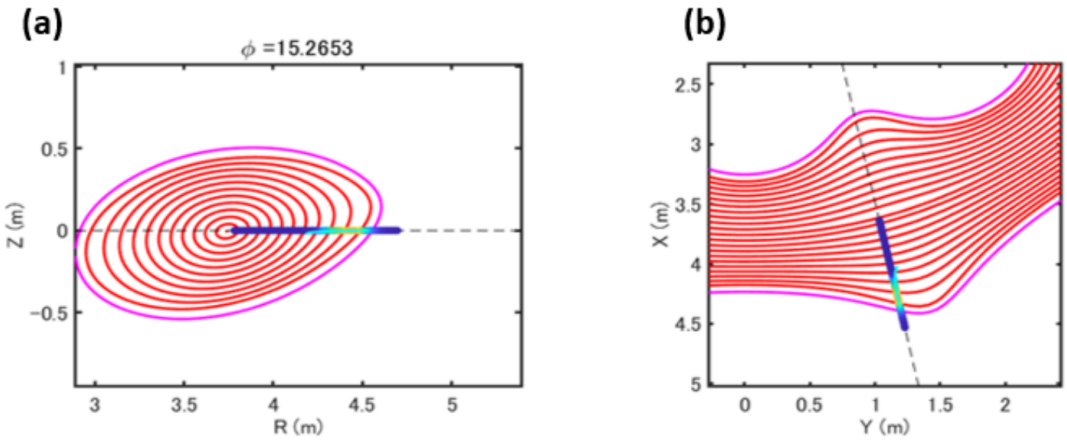


Figure 3.24. – (a) Poloidal and (b) toroidal projections of the pellet trajectory on the magnetic surfaces of LHD. The magenta contour is the LCFS extended by a factor 1.1 for accounting for the ergodic layer surrounding the confined plasma.

Three different cases are simulated [6], which differ by the proportion the fast ions are assumed to heat the CW - and CCW-sides of the cloud. They are: #1 $(CW, CCW) = (0,1)$; #2 $(CW, CCW) = (1/3, 2/3)$ and #3 $(CW, CCW) = (1/2, 1/2)$. Despite the total pellet penetration is rather similar for these three simulations (Fig. 3.26), the time evolution of the CW- and CCW-sides of the clouds differ significantly, depending on the considered asymmetry in the over-ablation due to fast ions. This is shown in

6. HPI2 simulations were performed by A. Matsuyama (National Institutes for Quantum Science and Technology Rokkasho, Japan).

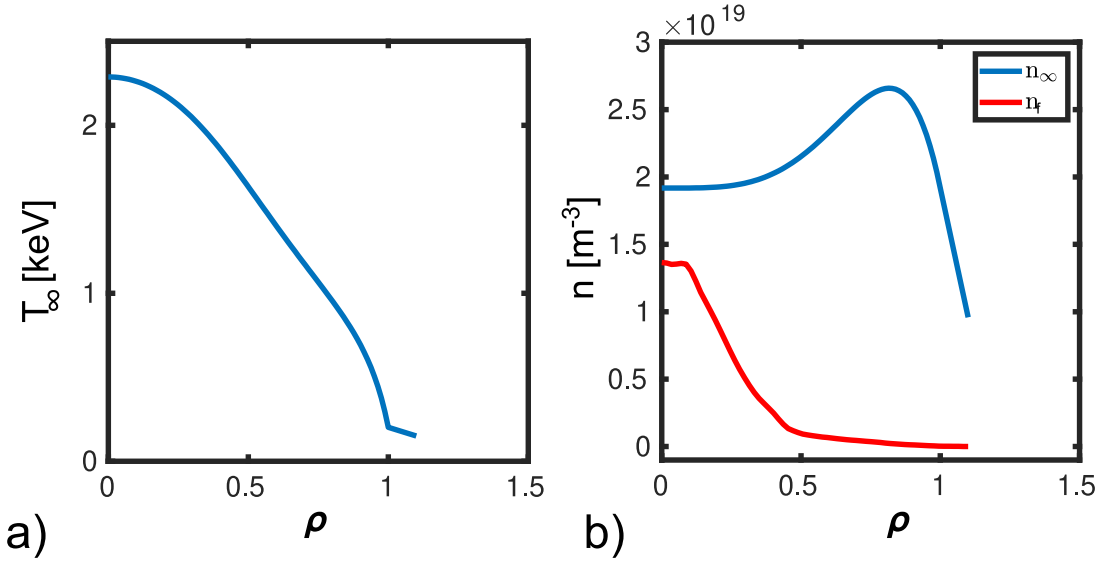


Figure 3.25. – (a) Bulk plasma temperature T_∞ (b) density n_∞ and fast ion density n_f vs. normalized minor radius.

Fig. 3.27 which displays, for a few numbers of clouds, the color contours of $n_0^2 f_i (1 - f_i)$, where f_i is the ionized fraction, taken to be a proxy of the light emission.

A small asymmetry between the left- and right-sides of the measured clouds is

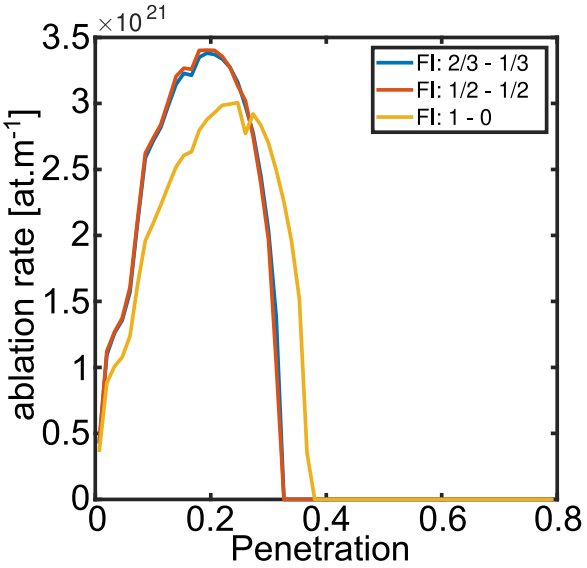


Figure 3.26. – Ablation profiles for the 3 simulations.

evidenced in Fig. 3.18. Although it is not possible to build corresponding figures from the HPI2 predictions presented above, it is the simulation #2, $(CW, CCW) = (1/3, 2/3)$ that reproduces the best the experimental asymmetry. The weak asymmetry observed in Fig. 3.18 can be explicated by comparing the cloud total lengths $\sim 0.2 - 0.3$ m and

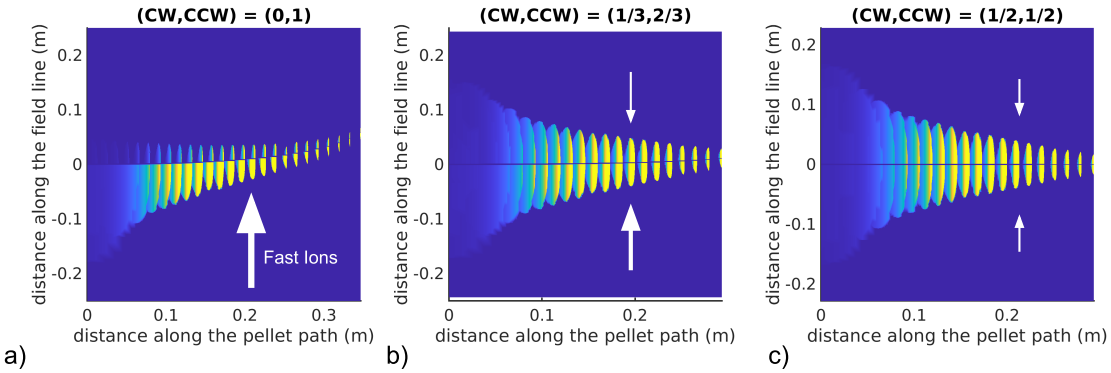


Figure 3.27. – Snapshots of the color contours of $n_0^2 f_i\left(1-f_i\right)$ vs. distance along the pellet path (the pellet penetrates from the left to the right). (a) $(\mathrm{CW},\mathrm{CCW}) = (0,1)$, (b) $(\mathrm{CW},\mathrm{CCW}) = (1/3,2/3)$ and (c) $(\mathrm{CW},\mathrm{CCW}) = (1/2,1/2)$.

radii $\left\langle R_0^{\exp}\right\rangle \sim 10^{-2}$ m with the characteristic dimensions of the fast ion gyro-orbit (pitch of the helix ~ 0.2 m and Larmor radius $\rho_f^L \sim 1.5\times10^{-2}$ m). The cloud cross-field size $\left\langle R_0^{\exp}\right\rangle$ being smaller than the ion gyro-orbit ρ_f^L, the fast ions can impact the cloud by its lateral side, and this over a length typically equal to the pitch of the orbit, which is comparable to the cloud total length. Therefore, even if all the fast ions arrive on only one side of the cloud, their heating is much more evenly distributed over the whole cloud volume, which explains the very weak observed asymmetry.
The comparison of the ablation rate prediction of the different simulations and photodiode H_α signal is displayed in Fig. 3.28. The agreement between the predicted and measured pellet penetrations is satisfactory, showing a slight overestimation for the simulation $(CW,CCW) = (0,1)$, and a slight underestimation for the simulations $(CW,CCW) = (1/3,2/3)$ and $(CW,CCW) = (1/2,1/2)$. For comparison, a calculation without taking into account the over-ablation due to fast ions is also shown. In this case, the pellet penetration is strongly over-estimated, underlining the importance of the latter in the reduction of the pellet penetration. At every location where the ablation rate is calculated, HPI2 simulates the time evolution of the ablation cloud dimensions, density, temperature and ionization fraction. An example is displayed in Figure 3.29, for a cloud emitted close to the maximum of ablation (indicated by the red dashed line in Fig. 3.28). At the beginning of the cloud evolution, expansion is spherically symmetric (Figs. 3.29a and 3.29b). When temperature reaches ~ 1 eV, ionization fraction is high enough for strongly braking the radial expansion, which slows down in the same proportion the density decrease rate (Figs.3.29d to 3.29e). Simultaneously with increasing ionization, the cloud drifts in the cross-field direction, down the magnetic field gradient, up to a time $t_{\text{exit}}^{CW/CCW}$ where the pellet exits from the cloud. At this time, the density source in the cloud stops, visible on Fig. 3.29e by an increase of the ionization rate. The simulation stops at full ionization, at time $t_{end}^{CW/CCW}$.
Fig. 3.30 displays the main cloud parameters at times $t_{\text{exit}}^{CW/CCW}$ and $t_{\text{end}}^{CW/CCW}$ all

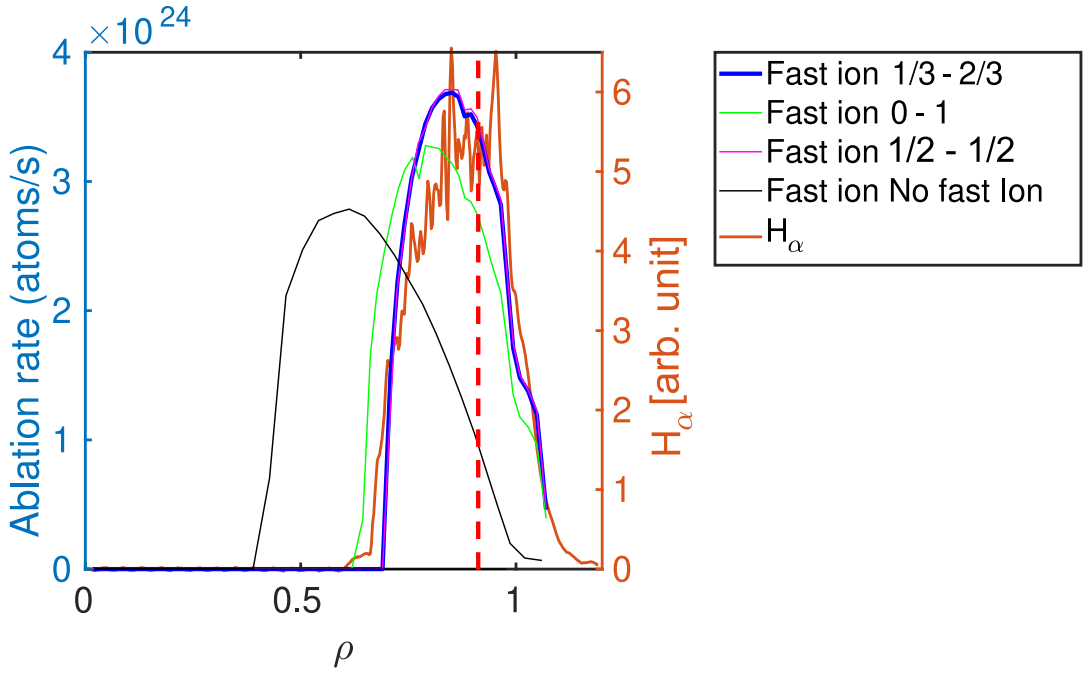


Figure 3.28. – Comparison between the photo-diode H_α signal and HPI2 predictions of the ablation rate for different simulation: $(CW, CCW) = (0,1)$ (green dotted line), $(CW, CCW) = (1/3, 2/3)$ (blue full line), $(CW, CCW) = (1/2, 1/2)$ (brown dotted line). The black curve is a calculation without fast ions. The red vertical dashed line indicates the cloud whose parameter evolutions is discussed below.

along the pellet path. The vertical dotted-dashed line indicates the cloud whose time evolution is shown in Fig. 3.29. Globally, the asymmetry between the two sides remains small. Fig. 3.30f shows that $t_{\text{end}}^{CW/CCW} > t_{\text{exit}}^{CW/CCW}$ along the whole pellet path. This has for consequence that, at a given time, the total emitted light is the sum of the individual emission of several clouds, up to ~ 3 at the plasma edge.

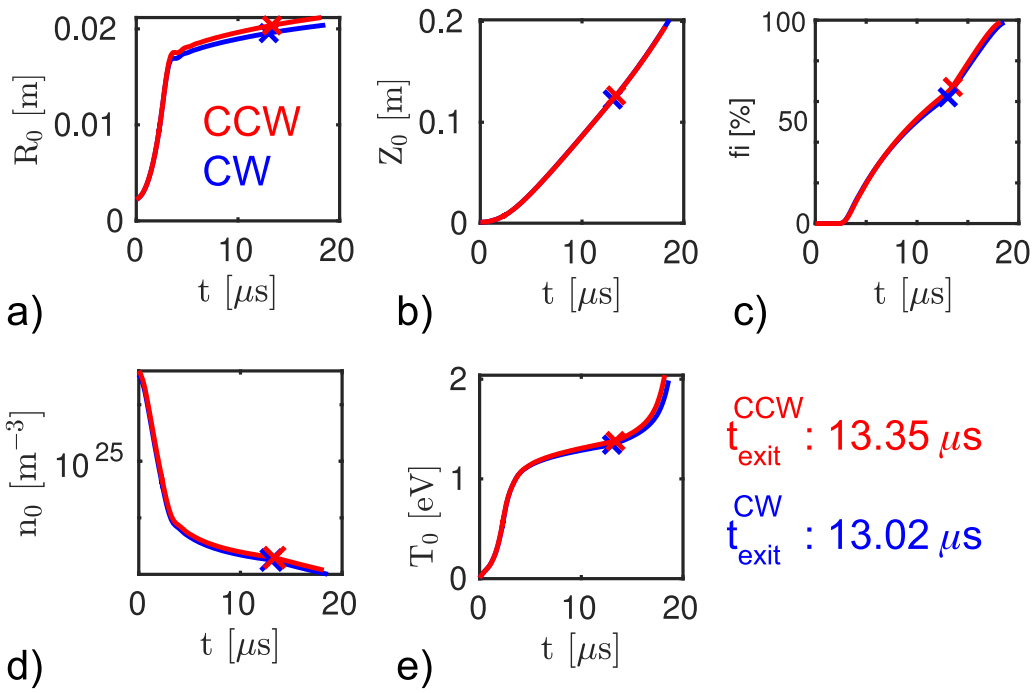


Figure 3.29. – Time evolution of (a) the cloud radius $R_0^{CW/CCW}$, (b) half-length $Z_0^{CW/CCW}$, (c) ionization fraction $f_i^{CW/CCW}$, (d) heavy particle density $n_0^{CW/CCW}$ and (e) temperature $T_0^{CW/CCW}$. The cross on the curves indicates the time $t_{\text{exit}}^{CW/CCW}$ where the pellet and the cloud dissociate.

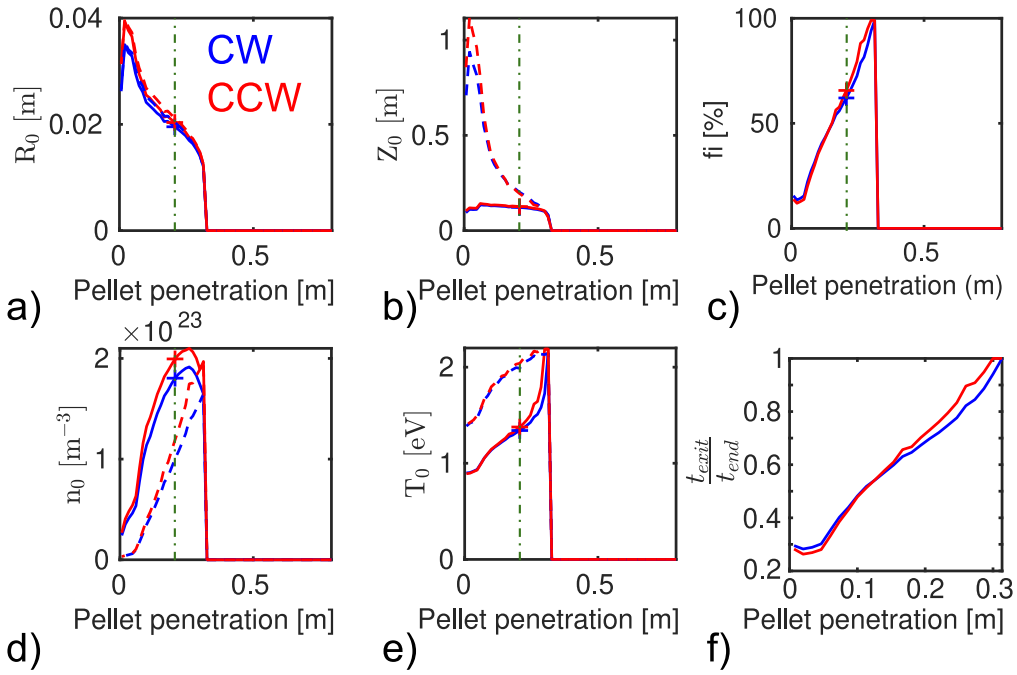


Figure 3.30. – Evolution along the pellet path of (a) the cloud radius $R_0^{CW/CCW}$, (b) half-length $Z_0^{CW/CCW}$, (c) ionization fraction $f_i^{CW/CCW}$, (d) heavy particle density $n_0^{CW/CCW}$, (e) temperature $T_0^{CW/CCW}$ and (f) ratio $t_{\text{exit}}^{CW/CCW}/t_{\text{end}}^{CW/CCW}$. Full lines are at the time of the pellet exit, dashed lines at the time of full ionization. The vertical dotted-dashed line shows the position of the cloud displayed in Fig. 3.29

3.7.2. Simulated spectra and emission pattern

For every cloud, the emission model described in Section 3.5 is applied 19 times, for $f_i = 5$ % to $f_i = 95$ %, by step of 5 %.
An example of spectrum evolution for a cloud deposited at about 1/3 of the pellet path is displayed in Fig. 3.31. The time of cloud deposition with respect to the ablation profile is shown in Fig. 3.31a, and the logarithmic and linear vertical scales in Figs 3.31b and 3.31c allow visualizing better the changes in the continuum and line emissions with increasing ionization rate. Due to the motion of the partly ionized material down the magnetic field gradient, the cloud drifts with respect to the pellet position and both separate at a time $t_{\text{exit}} = 143$ μs, indicated by the line of red crosses in Figs 3.31b and 3.31c. At the location where the cloud is deposited, the plasma heat flux is not high enough for ionizing instantaneously the newly ablated material and the cloud continues to emit about 10 μs after the pellet left the cloud, a value that compares well with the measurements reported in [116]. The time dependence of the peak emission of the cloud in the H_α, H_β and H_γ lines and in the continuum at $\lambda = 576$ nm is displayed in Fig. 3.32a. If the variations in the emission amplitudes remain limited (about a factor of 2 for the lines and 4 for the continuum), the surface emissions

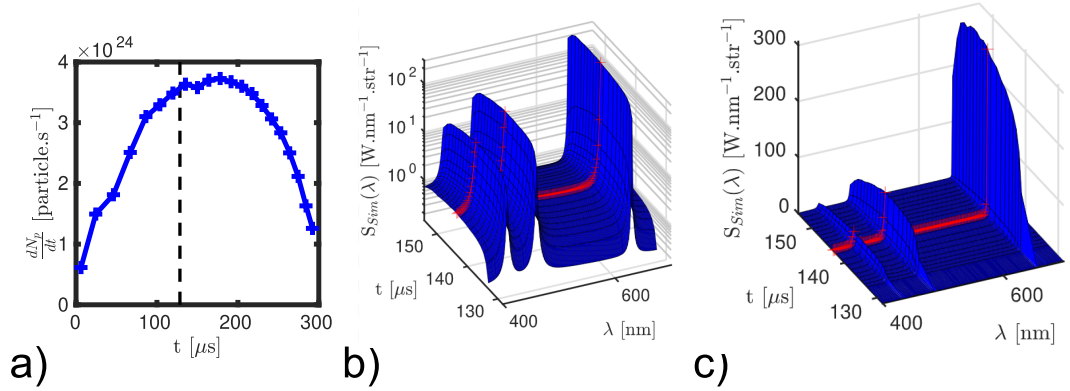


Figure 3.31. – (a) Ablation profile vs. time, the analyzed cloud is indicated by the black dashed line. (b) and (c) Cloud spectrum time evolution, the red crosses are at the time t_{exit} where the pellet exits the cloud.

$\frac{\left(\Sigma\left\langle P_\lambda^{CW/CCW}\right\rangle\right)}{\left(2\Sigma R_0^{CW/CCW} Z_0^{CW/CCW}\right)}$ decrease by a factor between 15 and 20 between the beginning and the end of the cloud lifetime. As discussed in the next subsection, this modulation in the cloud emission and strong decrease in the surface intensity explain the main features of the experimental records of pellet ablation by diodes or fast cameras.

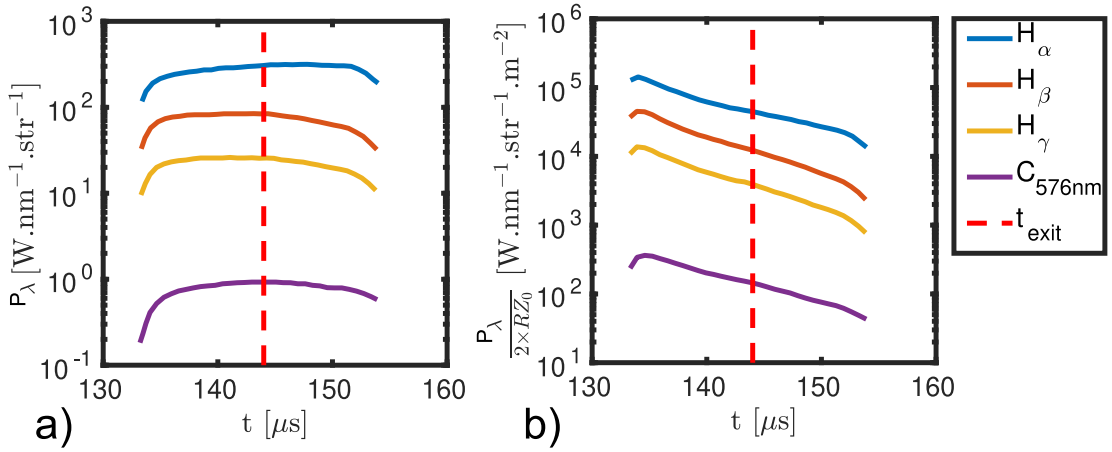


Figure 3.32. – (a) Cloud emission vs. time at $\lambda = 656\,\text{nm}\,(H_\alpha), 486\,\text{nm}\,(H_\beta)$ and $434\,\text{nm}\,(H_\gamma)$ and $\lambda = 576$ nm (Continuum), the red dashed line at time $t_{\text{exit.}}$. (b) Time evolution of the surface emission for the same wavelengths.

3.7.3. Relation between ablation rate and cloud emission

An interesting point to be investigated is the relation between the ablation rate, $\frac{\text{dN}_\text{p}}{\text{dt}}$, and the line or continuum emission intensity. This is done in Fig. 3.33 where the peak emission of the clouds in the H_α, H_β and H_γ lines and in the continuum at $\lambda = 576$ nm are plotted over the whole time of pellet ablation, with the average emission over the

whole wavelength range (400 - 700 nm, black curve). The same quantities are plotted vs. the instantaneous ablation rate in Fig. 3.33b. The behavior is globally the same for the different wavelengths: the emission increases quasi-exponentially up to the maximum of the ablation rate, then remain almost constant during the decreasing phase of $\frac{dN_p}{dt}$, in the second phase of the pellet lifetime, demonstrating that there is no univocal relation between the ablation rate and cloud emission, whatever the range of wavelengths considered. However, and even if that does not change the main conclusion of this study, it must be underlined that these results cannot be directly compared with observations because the fact that several clouds can emit light simultaneously is not taken into account in the present discussion.

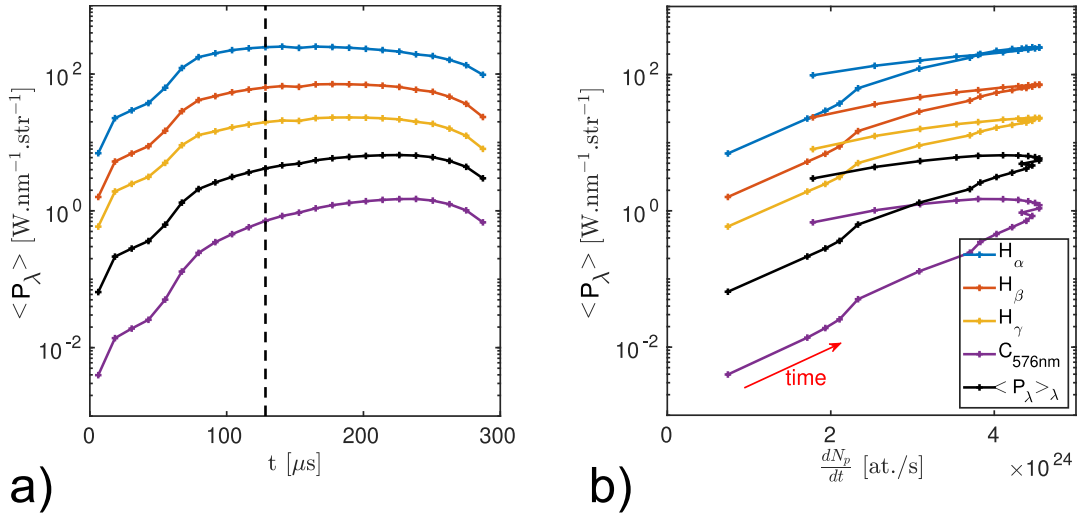


Figure 3.33. – (a) Cloud emission vs.time for the whole pellet ablation at λ = 656 nm (H_α), 486 nm (H_β), 434 nm (H_γ), 576 nm (Continuum) and averaged over the whole wavelength range $\lambda = 400 - 700$ nm (Black full line), the black dashed line indicates the cloud analyzed in Figs 3.29 and 3.31. (b) Cloud emission vs. ablation rate. Here, clouds are supposed to be seen perpendicularly to the magnetic field, where the component π of the Zeeman effect is total.

3.8. Comparison with measurement

3.8.1. Global cloud characteristics

The evolution of some global parameters can be directly obtained from the HPI2 simulation. They are the frequency of cloud deposition, $\nu_{\mathrm{Str}}^{\mathrm{sim}}$ (the simulated counterpart of the striation frequency $\nu_{\mathrm{Str}}^{\mathrm{exp}}$, Fig. 3.17a), and the cloud particle content N_{cl}^{sim}. Both quantities are plotted in Figs 3.34a and 3.34b. The agreement is good between $\nu_{\mathrm{Str}}^{\mathrm{exp}}$ and $\nu_{\mathrm{Str}}^{\mathrm{sim}}$, and the average value $\langle N_{\mathrm{cl}}^{\mathrm{sim}} \rangle = 4 \times 10^{19} at.$ compares also well with the

experimental determination $\langle N_{\mathrm{cl}}^{\mathrm{exp}} \rangle \sim (3.5-4.5)\times 10^{19}$ at.. If the cloud particle content

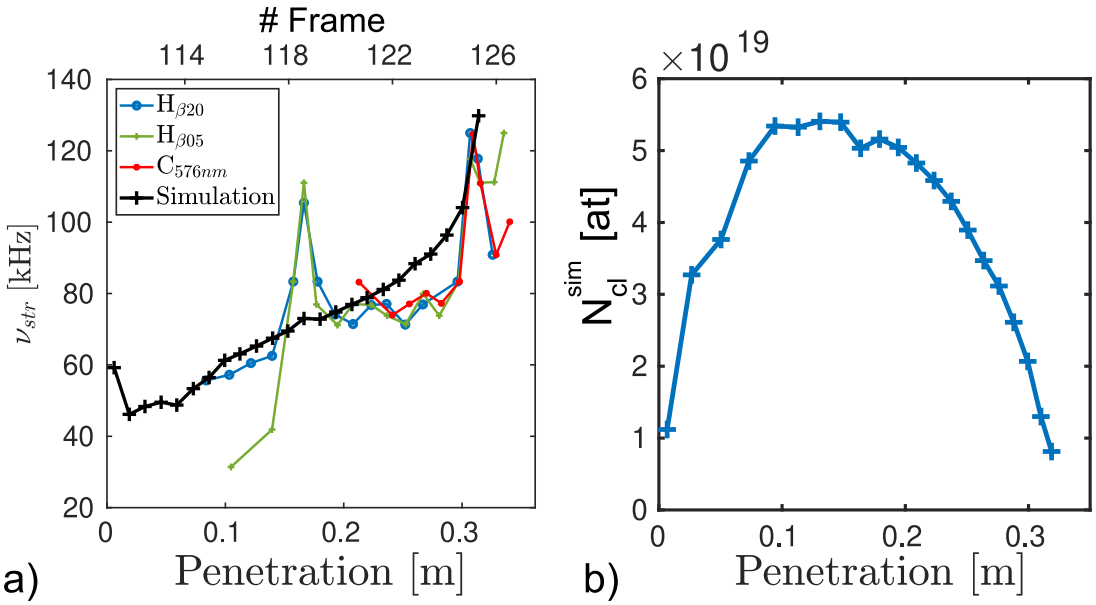


Figure 3.34. – (a) Calculated cloud deposition frequency $\nu_{\mathrm{Str}}^{\mathrm{sim}}$ and experimental ones ($H_{\beta 20}$, $H_{\beta 05}$, C_{576nm}) and (b) cloud particle content N_{cl}^{sim} vs. pellet penetration.

and striation frequency are only function of the pellet position, the radius and length of the cloud evolve continuously with time. Camera images been taken randomly with respect to the cloud deposition times, one cannot make a point-to-point comparison. It follows that only the main trends can be compared, with two constraints:

— The measured cloud radius $\langle R_0^{\mathrm{exp}} \rangle$ must be smaller than the simulated radius R_0 because the the camera detects only the brightest part of the emission pattern.

— The measured cloud half-length $\langle Z_0^{\mathrm{exp}} \rangle$ must be smaller than its simulated counterpart $Z_0\,(t_{\mathrm{end}}\,)$ because of the camera dynamics and because the cloud emission depends on the ionized fraction that is not evenly distributed in the parallel direction.

Such a comparison is displayed in Fig. 3.35. Both $\langle Z_0^{\mathrm{exp}} \rangle$ and $\langle R_0^{\mathrm{exp}} \rangle$ satisfy the above constraints, but the measured values are smaller than the code predictions. If this is explained for a part by the relatively rough method used for determining the cloud dimensions (HWHM of the images), other phenomena can play a role. The fact that cloud emission is weaker at its periphery can lead to an underestimation of $\langle R_0^{\mathrm{exp}} \rangle$, and the rapid decrease of the cloud surface brightness with time is responsible for the fact that the cloud becomes undetectable well before complete ionization.

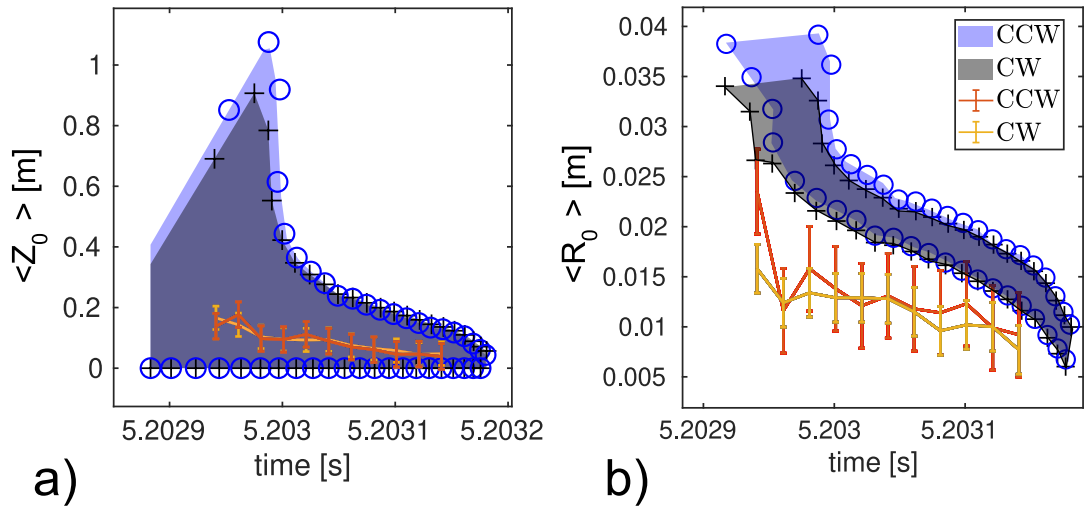


Figure 3.35. – Comparison of the simulated and measured cloud dimensions. (a) Half-length $\langle Z_0^{\text{exp}} \rangle$ and Z_0, (b) radius $\langle R_0^{\text{exp}} \rangle$ and R_0.

3.8.2. Interpolation on a realistic timing.

In the HPI2 simulation, the ablation rate and cloud parameters are calculated at regular time/space intervals. This does not allow a direct comparison with measurements because of the simultaneous emission of different clouds (from ~ 3 at the edge to only 1 at the end of the pellet path, see Fig. 3.30f). For a consistent comparison, one must start from the physical picture behind the ablation model: (1) the pellet penetrates in the plasma, (2) a neutral cloud forms, (3) this neutral cloud begins to ionize and drift with respect to the pellet, (4) at time t_{exit} , the partly ionized cloud dissociates from the neutral cloud but continues to ionize - thus emitting light - until the time t_{end} where it is fully ionized but (5) simultaneously to step (4) at the same time t_{exit} , a new partly ionized cloud begins to form. It follows that both clouds emit simultaneously during a time interval $t_{\text{end}} - t_{\text{exit}}$. This quasi-periodic process repeats until the full consumption of the pellet particles. For mimicking these successive steps and calculating the emission pattern and associated spectra, all the data related to the simulated clouds are first interpolated such that each cloud begins to develop at the exit time of the preceding (see the principle explicated in Appendix B.2). Then, the total spectrum and images are reconstructed by summing up the individual contributions of the different clouds emitting simultaneously. The results are displayed in Fig.3.36a for the total power in the range $\lambda = 400 - 700$ nm and in Fig. 3.36b for the peak of H_α emission at $\lambda = 656$ nm. In both cases, it is observed that, due to the simultaneous emission of the different clouds, the maximum emission occurs at another time than that corresponding to the maximum of emission of the most emitting cloud. Particularly, the quasi double-peak structure that is visible on Fig. 3.36b is reminiscent to that observed on the experimental H_α signal in Fig. 3.28.

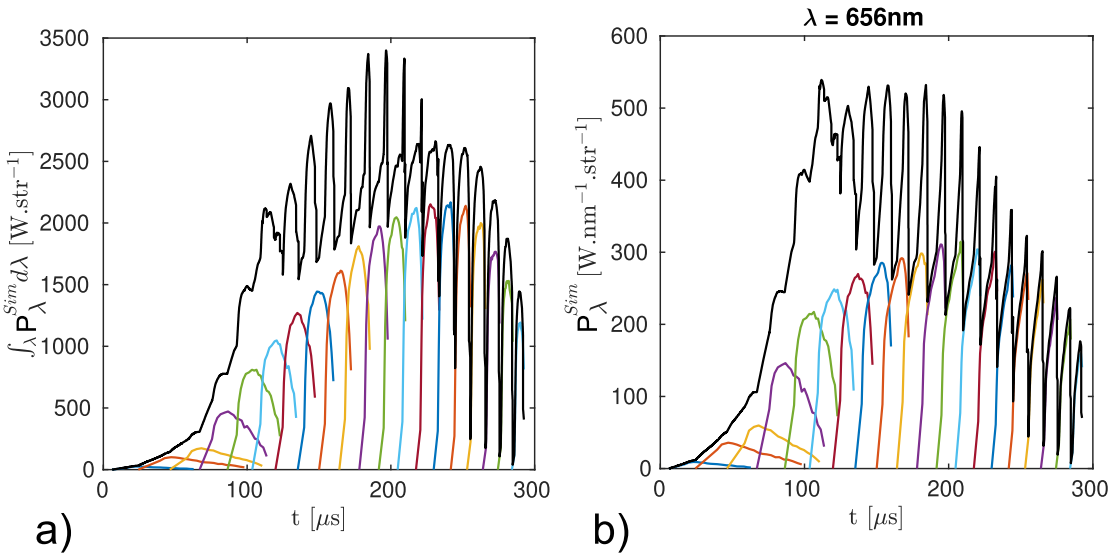


Figure 3.36. – (a) Total power emitted by the clouds vs. time, (b) Identical to (a) for $\lambda = 656$ nm (H_α). In these two figures, the colored thin lines are the individual contributions of the different clouds.

3.8.3. Building synthetic signals

For a more accurate comparison with measurements, synthetic signals are built to be compared with the fast diodes and spectrometer measurements in the $H_{\beta 05}$, $H_{\beta 20}$ and $C_{576\text{nm}}$ wavelength bands [7]. Starting from the knowledge of the spectra at every time for every cloud, the followed procedure is to:

— Sum at every time the spectra of the different clouds emitting simultaneously, yielding $P_\lambda^{\text{sim}} = \sum_i P_\lambda^{\text{sim}\,i}$.

— Multiply the resulting spectra by the different filter transmission factors $F_{\Delta\lambda}$: $P_\lambda^{\text{sim}} F_{\Delta\lambda}$.

— Integrate over the wavelength dimension: $\int P_\lambda^{\text{sim}} F_{\Delta\lambda} d\lambda$. The result is displayed in Figure 3.37 for the three wavelength bands $H_{\beta 05}$, $H_{\beta 20}$ and $C_{576\text{nm}}$.

— Last, convolve $\int P_\lambda^{\text{sim}} F_{\Delta\lambda} d\lambda$ with door functions of total width 2 μs and 86 μs for reconstructing synthetic diodes and spectrometer signals, respectively. The result is displayed in Fig. 3.38a (fast diodes) and 3.38b (spectrometer) and compared to the measurements shown in Figs 3.38c and 3.38d, respectively.

If a point-to-point comparison of the simulated and measured emissions is not possible (the times of striation maxima are not predictable, since their position can be perturbed by fluctuations in the cloud size or the crossing of rational magnetic surfaces [124]), one can compare the general trends and integrated quantities. Three phases can be distinguished in Fig. 3.38c: a smooth emission increase terminated by a well-marked peak at about 1 / 3 of the pellet lifetime, a phase of strong striations for

7. No attempt was done for optimizing the simulation by playing on the uncertainties on the pellet and plasma parameters or magnetic reconstruction: the simulation inputs are just the nominal values.

the second third, then a last phase that begins by an abrupt decrease in the striation intensity that remains smaller until the emission vanishes (these two last phases are particularly visible on the $H_{\beta 05}$ signal). The same structure can be distinguished in Fig. 3.38a, even if the peak at the end of the first phase is smaller and the differences between the two following phases more clearly marked. These three phases are due to the dominant contribution of the ablation by the fast ions for the first one (as demonstrated at the end of this subsection), by a large overlapping of the times during which the clouds emit light for the second, and by an almost complete separation between the cloud emissions for the last one. Due to the long integration time, the simulated and measured powers in the spectra (Figs. 3.38b and 3.38d) exhibit just bell-shaped curves that do not allow a detailed comparison. It can be just remarked that the relative positions of the maxima for the different wavelength domains (marked by a circle on the curves) are in good agreement.

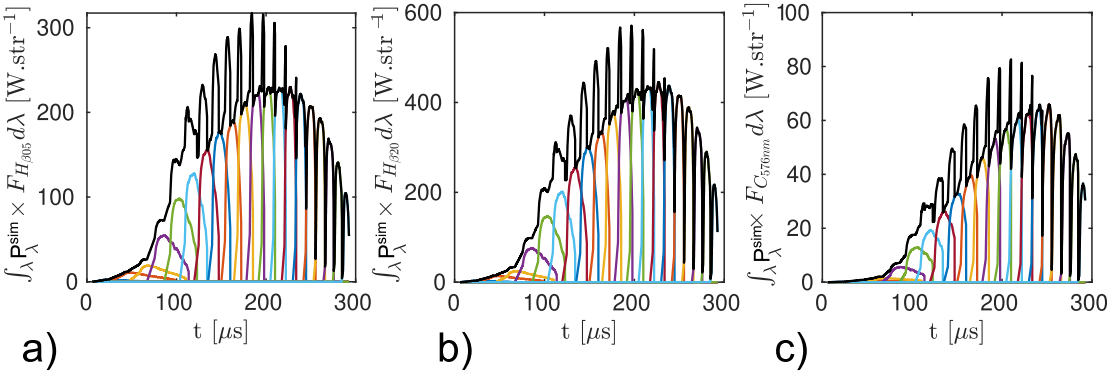


Figure 3.37. – (a) Power in the $H_{\beta 05}$ wavelength band vs. time, (b) and (c) identical to (a) for the $H_{\beta 20}$ and C_{576nm} wavelength bands. In these three figures, the colored thin lines are the individual contributions of the different clouds.

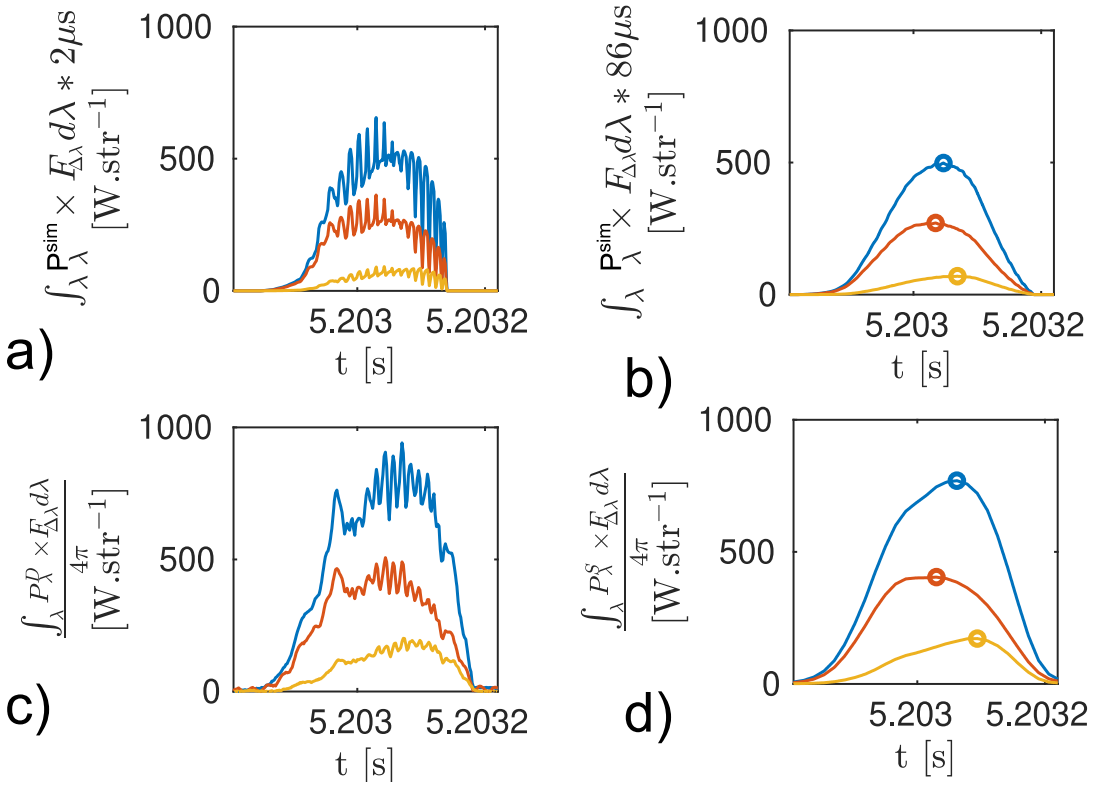


Figure 3.38. – (a) Synthetic signal of photodiodes in the $H_{\beta 05}$, $H_{\beta 20}$ and C_{576nm} wavelength bands, (b) identical to (a) for the power in the spectra. (c) and (d), experimental counterpart of (a) and (b). See Fig. 3.11a

	$\iint P(\lambda)d\lambda dt$	$\int H_{\beta 05}dt$	$\int H_{\beta 20}dt$	$\int C_{576nm}dt$
Measurement $[J.str^{-1}]$	1.062	9.2×10^{-2}	1.69×10^{-1}	3.3×10^{-2}
Simulation[J.str $^{-1}$]	4.42×10^{-1}	4.8×10^{-2}	8.7×10^{-2}	1.1×10^{-2}
Ratio (Sim/Meas)	0.42	0.52	0.51	0.33

Table 3.6. – Measured and simulated energy radiated during the whole ablation in the full spectrum and $H_{\beta 05}$, $H_{\beta 20}$ and C_{576nm} wavelength bands.

The energies radiated in the different wavelength bands are given in Table 3.6. The differences in the simulated and measured values are related to differences between simulated and measured spectra, as exemplified in Fig. 3.39. Three spectra are chosen, spotted with respect to the relative height of the $H_{\beta 20}$ signal at the times of interest (Figs 3.39a and 3.39b). The first is taken during the increasing phase of emission, for $H_{\beta 20}/H_{\beta 20}^{\mathrm{Max}} \sim 1/2$ (Fig. 3.39c), the second close to the maximum of emission, for $H_{\beta 20}/H_{\beta 20}^{\mathrm{Max}} \sim 1$ (Fig. 3.39d), and the last in the decreasing phase, for $H_{\beta 20}/H_{\beta 20}^{\mathrm{Max}} \sim 2/3$ (Fig. 3.39e). In these three figures, the simulated continuum is a factor between 2

and 3 below the measurement [8] and the lines are narrower, but less self-absorbed, which explains for a part the different ratios (from ~ 2 to 3) between the simulated and measured H_β and C_{576nm} energies.
This difference in the self-absorption, and therefore in the optical depth of the emission lines (which scales as the line integrated density along the line of sight), is likely explained by the assumption of a homogeneous density in the clouds. Indeed, at constant number of particles in a cylindrically symmetric cloud with density radial distribution $\propto r^{-\alpha}$, the line integrated density increases when α increases, i.e. when the distribution becomes more peaked.
Analogously, the fact that the simulated total radiated energy is only 40 % of the measurement is likely due to the assumption of a constant source of matter during the whole time that the pellet stays inside the cloud. Indeed, at time t_{exit} , when the pellet exits an existing fully developed cloud and begins to build a new one, it is only shielded by the neutral cloud, less efficient than the ensemble constituted by the neutral plus the partly ionized clouds. Its ablation rate should therefore be large, before to decrease progressively with the building of the new cloud. At constant number of particles in the cloud at t_{exit}, the cloud is bigger sooner when the instantaneous source of matter decreases with time, and thus the emission.
It follows that, although no quantitative estimation can be given with the present version of HPI2, the above discussion shows that the two main simplifications done in the calculation of the time evolution of the cloud characteristics can be responsible for the main differences observed between the simulated and measured spectra.

3.8.4. Behavior of surface brightness

The shape of the time evolution in the different emission lines (Figs. 3.36 and 3.37) comes from the fact that several clouds emit simultaneously, with comparable intensities, particularly at the beginning of ablation. However, except at the very beginning of the pellet path, only one cloud is detected on the camera images. This apparent contradiction is explained by the rapid parallel expansion of the clouds, the consequence of which is a fast decrease of their surface brightness. This is demonstrated in Fig. 3.40, which displays the time evolution of the cloud emission in the $H_{\beta 20}$ band (Fig. 3.40a), the increase with time of the cloud surface (Fig. 3.40b) and the ratio of both, i.e. the surface brightness (Fig. 3.40c). The two peaks on the time evolution of the cloud surface come from the difference of behavior of the CW and CWW half-clouds, which are not identically heated by the fast ions (see Fig. 3.30). The visible surfaces come to zero when the clouds cease to emit, all the material inside being ionized. For all the clouds, the surface brightness decreases rapidly and, at times where several clouds emit simultaneously, their ratio is between a factor of ~ 10 at the beginning of ablation (the simultaneous emission lasting between 20 and 30 μs) and a factor of ~ 3 at the end of the pellet path (but, in this case, the superposition time is extremely short

8. An obvious contribution comes from the choice of the pellet initial particle content, $N_p = 8 \times 10^{20}$ at. for a nominal value of 10^{21} at., which assumes 20 % erosion in the guide tube and can be overestimated.

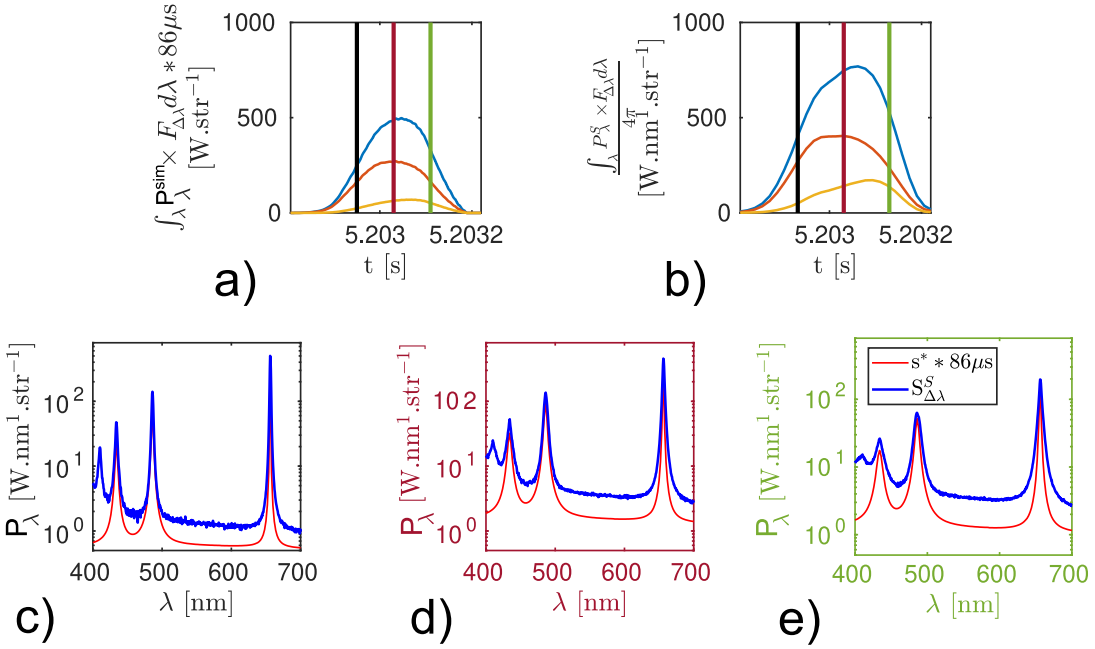


Figure 3.39. – (a) and (b) Identical to Fig. 3.38b and 3.38d, the vertical bars indicate the times where the simulated and measured spectra are compared. (c) to (e) simulated (red line) and measured (blue line) spectra, the colored axes correspond to the times indicated in a and b.

- 1 μs - and the two clouds should be merged on the images). Taking into account the qualitative argument that the brightness distribution is more peaked when the pellet is yet inside the cloud (because of the source of matter at the cloud center) than when it has left, and the limited dynamics of the fast camera, this explains why only one cloud image is generally detected on the camera images. Two phases appear

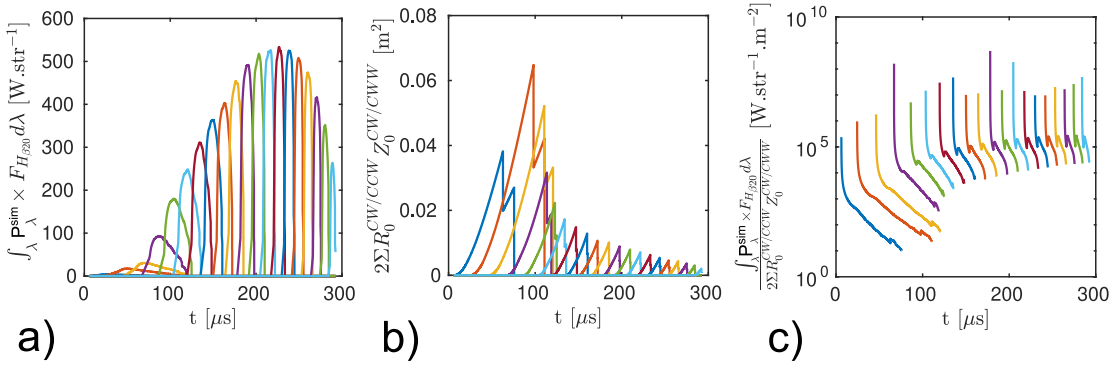


Figure 3.40. – (a) Individual contribution vs. time of the different clouds to the $H_{\beta 20}$ emission, (b) time evolution of the surfaces of the different clouds and (c) time evolution of the surface brightness of the different clouds.

clearly in Fig. 3.40b: the surface of the three first clouds deposited at the beginning of

ablation reach much larger values than that of the other cloud deposited later. This is explained by the ratio of the contributions of the bulk electrons and fast ions to the ablation rate. Indeed, when two populations (subscripts f for the fast ions and ∞ for the background plasma) of different energies and densities ablate simultaneously a pellet of radius R_p, the resultant ablation rate ([38, 124]) writes:

$$\frac{dN_p}{dt} = \left[\left(\frac{dN_p}{dt}\bigg|_f \right)^3 + \left(\frac{dN_p}{dt}\bigg|_\infty \right)^3 \right]^{1/3} \tag{3.22}$$

where $\frac{dN_p}{dt}\Big|_\infty$ and $\frac{dN_p}{dt}\Big|_f$ are what would be the value of the ablation rate in absence of the other population. It is established that, in HPI2, the ablation by a Maxwellian plasma follows the Neutral Gas Shielding (NGS) scaling [125], with a constant ~ 2.5 times larger than that given in the original paper (see [126]):

$$\frac{dN_p}{dt}\bigg|_\infty = 4\pi \left(1.3 \times 10^{-13}\right) n_s R_p[m]^{4/3} n_\infty \left[m^{-3}\right]^{1/3} T_\infty[\mathrm{eV}]^{1.64} \tag{3.23}$$

Knowing the local values of $\frac{dN_p}{dt}$ and R_p from the HPI2 simulation, one can estimate the real contribution of the fast ions and bulk to the ablation rate as:

$$\frac{dN_p}{dt}\bigg|_{f,R} = \frac{dN_p}{dt}\bigg|_f \left(\frac{\frac{dN_p}{dt}}{\frac{dN_p}{dt}\Big|_\infty + \frac{dN_p}{dt}\Big|_f} \right)$$

$$\frac{dN_p}{dt}\bigg|_{\infty,R} = \frac{dN_p}{dt}\bigg|_\infty \left(\frac{\frac{dN_p}{dt}}{\frac{dN_p}{dt}\Big|_\infty + \frac{dN_p}{dt}\Big|_f} \right)$$

The total ablation rate $\frac{dN_p}{dt}$ and the two contributions $\frac{dN_p}{dt}\Big|_{\infty,R}$ and $\frac{dN_p}{dt}\Big|_{f,R}$ are displayed vs. pellet penetration in Fig. 3.41a, the ratio $\frac{dN_p}{dt}\Big|_{f,R} / \frac{dN_p}{dt}\Big|_{\infty,R}$ in Fig. 3.41b. The contribution of fast ions is larger than that of the bulk during the whole ablation, but its contribution dominates particularly during the first 70-80 μs, which is the time interval during which the three first clouds characterized by a larger surface are deposited. One can also remark that the strong emission of these three first clouds is mainly responsible for the double-maximum structure of the H_α emission, visible in both the simulation (Fig. 3.36b) and measurement (Fig. 3.28). This kind of shape is generally not observed when the pellets are injected in Maxwellian plasma [9].

9. If, in the present case, the association between the simulated and measured shapes of the H_α emission is pertinent, one must be cautious when interpreting the details of the time history of the light emitted during pellet ablation, because it can exhibit some variation in shape, even for quasi-identical pellets injected in macroscopically similar plasmas.

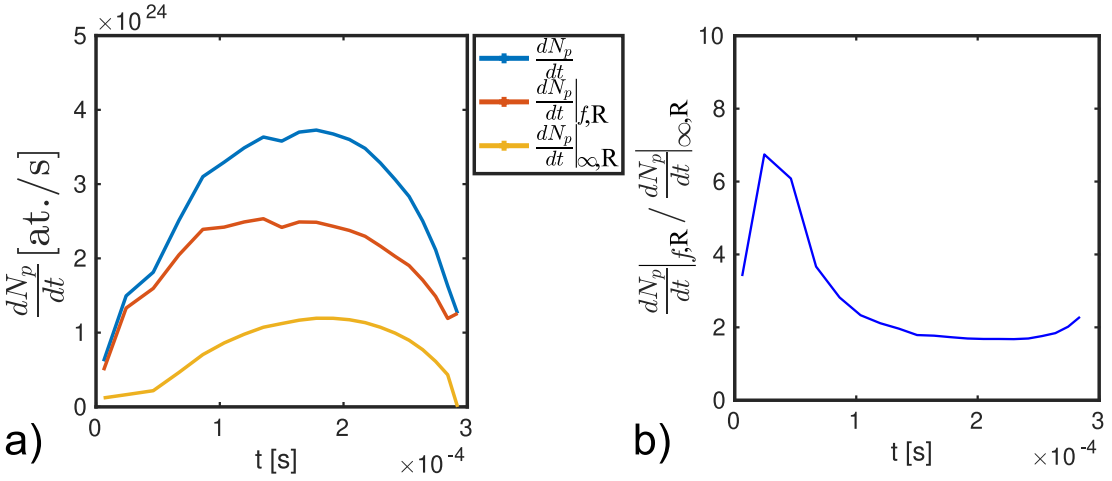


Figure 3.41. – (a) Contributions of fast ions and bulk electrons to the pellet ablation vs. time, (b) ratio between the fast ion and bulk electron contributions to pellet ablation.

3.8.5. Relation between ablation rate and cloud emission

Finally, the relation between the ablation rate and the power in the $H_{\beta 05}$, $H_{\beta 20}$ and C_{576nm} wavelength bands is shown in Fig. 3.42. Unsurprisingly, the curves exhibit the same shape as those displayed in Fig. 3.33b. Differences in the global level come from the superposition of the emission of several clouds at the beginning of the pellet lifetime and width and transmission of the filters. In this case again, no univocal relation can be established between the cloud emission and the local ablation rate.

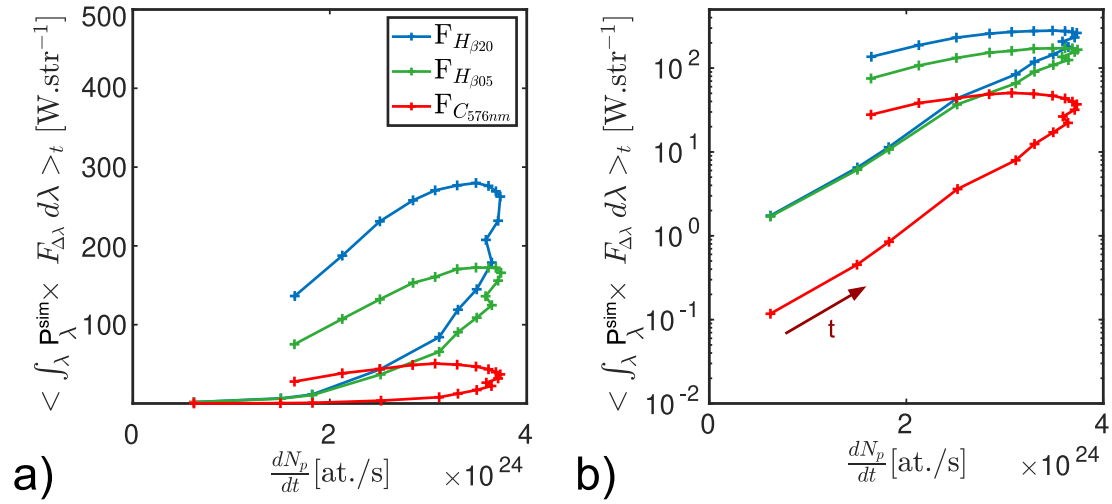


Figure 3.42. – Cloud emission vs. ablation rate in the $H_{\beta 05}$, $H_{\beta 20}$ and C_{576nm} wavelength bands. a) in linear scale and b) in log scale.

3.9. Discussion and conclusion

This Chapter presents a comparison of the measured and simulated ablation pattern of a well-documented pellet injected in a Neutral Beam Heated discharge of the Large Helical Device, for which a set of images in different wavelength domains and corresponding spectra are available. The simulated quantities result from the combination of an emission model with time dependent cloud characteristics calculated with the ablation module of the HPI2 code. Synthetic images and spectra are built and compared with measurements.
Global quantities and main trends are well reproduced by the simulation. Namely:

— The striation frequency.
— The decrease of the radius and length of the emitting zone of the cloud with pellet penetration.
— The main structure of the cloud emission, including the marked peak at the beginning of the latter.

This good agreement strongly supports the assumptions and calculations of the HPI2 ablation model:

— The magnitude of the striation frequency and its increase with penetration confirms that striations originate from the relative motion of the pellet with respect to the partly ionized cloud, due to the drift of the latter in the inhomogeneous magnetic field. It validates also the cross-field dimension of the ablation clouds calculated by HPI2, since the striation frequency is equal to the ratio of the drift velocity by the cloud radius (measurements on the tokamak ASDEX of the drift velocity confirms the values calculated by HPI2 [117]). Nevertheless, if this good agreement likely explicates the striation origin, it does not explains why one observes a quasi-periodic ejection of clouds, and not a continuous drift of the ionized material with respect to the pellet: the instability that triggers the cloud ejection remains to be formally identified [10].
— The rate of decrease of the cloud length and radius with pellet penetration (also predicted in [127]) validates the calculated dynamics of ionization and parallel expansion. The fact that absolute values are not reproduced comes likely from the fact that only volume averaged densities and temperatures are calculated in HPI2 when highly peaked distributions are expected, as pointed out by more sophisticated cloud models ([128–130]).
— The main structure of the emission pattern, including the prominent peak at the beginning of ablation and the power ratios between the different wavelength domains investigated are a further confirmation that the ionization dynamics - and therefore those of the density and temperature - are correctly calculated, since the time variation of the emission results from the partial superposition of the emission of several clouds. It validates also the way the over ablation by a

10. Although it is at this stage pure speculation, it is noticeable that a time-varying ablation rate when the pellet is inside a cloud could trigger a striation if its variation is large enough. But such a process results from a complex interplay between the neutral shielding and the time and space variation of the density in the partly ionized cloud, and is by far out of the capabilities of a code as HPI2.

fast population is included in the model, since time, intensity and duration of the above mentioned peaks result from the balance between the contributions to ablation of the fast ions and bulk electrons.

Despite these positive points, some important discrepancies remain: essentially the shape of the spectra and the total energy radiated in the different wavelength bands - and their ratio, which do not reproduce the experiments. No quantitative calculation can be yet done for explaining these discrepancies, but it is suspected that the simplifications used in the HPI2 calculation are responsible for a part of them. More specifically:

— HPI2 calculates the time evolution of the average cloud characteristics (density, temperature, ionized fraction) when, in actual ablation clouds, these quantities exhibit strongly inhomogeneous distributions. As explained above, this changes significantly the line self-absorption and the ratio of the different wavelength bands.

— In HPI2 the ablation rate, i.e. the particle source in the cloud, is constant for the whole time where the pellet stays inside the cloud when, in actual ablation clouds, the particle source is likely maximum at the beginning of the cloud building and decreases with time, before vanishing when the pellet exits the cloud.

These two points, by changing the shape of the spectra and their time evolution, are likely to explain - at least for a part - the discrepancies between the measured and calculated total radiated energy and power ratios in the different wavelength bands.

If this study constitutes a step in the validation of the physics captured in the ablation module of the HPI2 code, it cannot be considered as definitive, and additional work would be necessary. An obvious point is that it would be important to repeat this study with data obtained in different plasma conditions for confirming the results. Then, from the simulation point of view, it could be interesting to introduce the possibility of calculating a new cloud only when the pellet leaves the previously deposited one and to calculate a time-varying ablation rate depending on the parallel line integrated density of the cloud. However, it would not be appropriate to calculate consistent space varying distributions of the density and temperature in the cloud, because this would be a huge complication that would increase dramatically the computational time and, moreover, would be inconsistent with the simple description of the central neutral cloud. As far as experiment is concerned, the main cloud characteristics that limit the accuracy of the observations are the time- and space-scales of the cloud, i.e. $\sim 1\ \mu$s for the characteristic evolution time, and ~ 1 mm / ~ 1 cm for the gradient lengths in the cross-field / parallel directions. Such coupled time and space resolutions are, to our knowledge, out of the possibilities of present day diagnostics. This has for consequence that it seems extremely difficult to extract, without a priori assumptions, the density and temperature distributions in the cloud from the measurements [11], and that it seems more appropriate to build synthetic

11. Several attempts were performed for extracting the cloud density and temperature from the

signals from code predictions and to compare them with the measurements. Finally, the relation between the ablation rate and light emission is not univocal, whatever the wavelength domain considered, which implies that it is not possible to build a scaling low linking the light emitted by the ablation cloud to the local ablation rate.

spectra and camera images, using uniform or simple space distributions, but they systematically failed and it was not possible

SUMMARY

Pellet injection is mandatory for the core fueling of future magnetic fusion devices, but it is not possible to mimic in present day machines the conditions expected in a future reactor. Consequently, every prediction or fueling scenario relies only on simulation, and it is therefore necessary to dispose of a reliable chain of codes describing the different steps of pellet injection. They are:

— The pellet acceleration in the injector,
— The pellet path in the guide tube between the injector and the vacuum chamber,
— The pellet ablation in the plasma,
— The homogenization of the deposited material in the discharge.

Concerning the two first steps, if a number of models are available for describing the pellet acceleration in gas-gun or centrifugal injectors (see e.g. [131, 132]), nothing exists for modeling the pellet path in a guide tube. However, the necessity to use bended guide tubes for injecting pellets from the High Field Side can induce strong constraints on the ice, questioning the pellet integrity at the tube exit. Concerning the ablation / homogenization phases, if a number of models are available ([18] and references therein), only the homogenization phase was diagnosed in detail [27], the ablation models being only validated by checking the total pellet penetration, which integrates all the pellet lifetime in the plasma. From this situation, two voids clearly appear (1) the modeling of the pellet path in a guide tube and (2) a closer validation of ablation calculations, if possible focusing on the local ablation rate. This work aims at filling up these gaps.

Chapter 2 describes a model of pellet propagation in a guide tube of arbitrary geometry. Bended guide tubes limit the maximum pellet velocity due to the forces on the pellet when it bounces or slips on the guide tube wall, up to destroy the pellet when the induced constraint becomes larger than the ice yield strength. The forces taken into account are (1) that resultant from the pellet deformation during a bounce, (2) the centrifugal and Coriolis forces, (3) the slipping friction force, (4) the gravitation force and (5) the viscous friction with the residual gas filling up the guide tube. The model aims at estimating quantitatively the time evolution of the mass, temperature, velocity and forces experienced by the pellet along its path between the injector and the vacuum chamber. Main results are the pellet mass and velocity (in magnitude and direction) at the exit of the guide tube. The probability that the pellet has to be intact when delivered in the plasma is estimated from the stored elastic energy in the ice. Evaluating the ability of a guide tube of given geometry to deliver safely pellets in the vacuum chamber requires a statistic analysis using a large number of pellets launched with a dispersion in mass and velocity representative to what is expected at the injector exit. However, the model uses a number of coefficients governing the

magnitude of the different effects and forces (the contact heat transfer, the fluid and friction braking) or of the ice reaction to efforts (elasticity, dissipation, heat capacity) that are unknown for most of them. Only the behavior with temperature of the static strain-stress curve and heat capacity for Deuterium ice are known from literature. This cannot be used in confidence because the visco-elastic properties of a medium depend generally on the speed of deformation. Unfortunately, the code cannot yet be used practically for estimating the capacity of a given guide tube geometry to deliver safely pellets with some specified characteristics, due to the lack of an independent determination of the above mentioned coefficients. Even the satisfactory reproduction of measurements already obtained on guide tube models in different laboratories could not be considered as a valid code validation, because of the interplay between the different physical processes. Dedicated experiments are therefore a necessary complement, using test beds with guide tubes of e.g. constant curvature and varying length and pipe diameter, or different ice quality by manufacturing the pellets by in-situ condensation or extrusion.

Assuming Local Thermodynamic Equilibrium, Chapter 3 presents an emission model that calculates the H_α, H_β and H_γ lines, and the continuum emitted by a cold and dense, partially ionized Hydrogen cloud [115]. Starting from the results of the ablation module of the HPI2 code ([37, 38]), this model simulates the time evolution of the spectrum and images emitted by the ablation cloud. In a practical point of view, it is shown that there is no univocal relation between light emission and the local ablation rate, whatever the wavelength domain considered, and that it is therefore not possible to determine experimentally the ablation profile from H_α or H_β emission. In an attempt for validating in more details the predictions of the HPI2 ablation module, the simulated images and spectra are compared to similar measurements on a well-documented pellet injected in the Large Helical Device. Global trends and cloud characteristics (time behavior of the emitted power, average cloud particle content) are well reproduced, but significant discrepancies are observed when comparing in detail the measured and predicted spectra and images. If some of them originates from the approximations in HPI2, particularly the assumption that ablation clouds are homogenous in density and temperature, the largest part comes from the difficulty for measuring ablation clouds with a high enough space and time resolutions. Indeed, gradient lengths in clouds are ~ 1 mm perpendicularly to the magnetic field and ~ 1 cm in the parallel direction, with more than two orders of magnitude of difference in the density and temperature between the center and the periphery. Analogously, the cloud characteristic evolution times are a few μs. Present day technology does not allow to measure objects of such time and space scales with a high enough accuracy in a fusion device environment. In the present case, spectra have an integration time of several 10 ms and collect the light emitted by the whole cloud and, if the images are taken with a good enough integration time (2 μs), their space resolution is ~ 1 cm and their dynamics allows only to detect the brightest part of the clouds. It results from these limitations that it seems extremely difficult to extract cloud densities and temperatures from the measurements, even average values, and that the most efficient method of comparison consists in building synthetic diagnostics from the simulations,

with the same time as space resolutions as the measurements, and to compare them with the available data.
It follows that this work does not fill up completely the two gaps mentioned above. If the tool described in Chapter 2 is available for calculating the path of a pellet in a guide tube, it should be improved by allowing the possibility of tubes of a rectangular section (and not only circular) and of a curvature varying continuously. In addition, before the code is really operational, an important experimental work is required for determining relevant ice characteristics and coefficients governing the different forces experienced by the pellet. In what concerns the validation of ablation models, if the present study is more accurate than the simple comparison of the calculated and measured pellet penetrations, it suffers from the relative simplicity of HPI2. Progresses could be done by coupling the emission model described in Chapter 3 to more sophisticated ablation codes calculating realistic distributions of density and temperature in the clouds, and by building synthetic diagnostics adapted in each case to the available measurements.

A. APPENDICES - Chapter 2

A.1. CALCULATION OF THE MATRIX P AND VECTORS C_x, C_y AND C_z

The function $\tan^{-1}$ giving images in the interval $\left[-\frac{\pi}{2}, \frac{\pi}{2}\right]$, the values for $(\alpha_x, \alpha_y, \alpha_z)$ obtained from the first term of the r.h.s. of eq. 2.2 must be corrected by a number of times π to be correctly defined in the interval $[0, 2\pi]$. The exact value is determined from the 5-tuple ([M(1,1)], [M(1,2)],[M(1,3)],[M(2,3)],[M(3,3)]), whose sign of the elements change whether one of the angles α_x, α_y or, α_z is in the interval $\left[0, \frac{\pi}{2}\right], \left[\frac{\pi}{2}, \pi\right], \left[\pi, \frac{3\pi}{2}\right]$ or $\left[\frac{3\pi}{2}, 2\pi\right]$. This leads to:

$$
P = \begin{bmatrix}
+1 & -1 & +1 & -1 & +1 \\
-1 & -1 & +1 & -1 & +1 \\
-1 & +1 & +1 & -1 & +1 \\
+1 & +1 & +1 & -1 & +1 \\
-1 & +1 & +1 & +1 & -1 \\
+1 & +1 & +1 & +1 & -1 \\
+1 & -1 & +1 & +1 & -1 \\
-1 & -1 & +1 & +1 & -1 \\
-1 & +1 & -1 & +1 & -1 \\
+1 & +1 & -1 & +1 & -1 \\
+1 & -1 & -1 & +1 & -1 \\
-1 & -1 & -1 & +1 & -1 \\
+1 & -1 & -1 & -1 & +1 \\
-1 & -1 & -1 & -1 & +1 \\
-1 & +1 & -1 & -1 & +1 \\
+1 & +1 & -1 & -1 & +1 \\
+1 & -1 & +1 & -1 & -1 \\
-1 & -1 & +1 & -1 & -1 \\
-1 & +1 & +1 & -1 & -1 \\
+1 & +1 & +1 & -1 & -1 \\
-1 & +1 & +1 & +1 & +1 \\
+1 & +1 & +1 & +1 & +1 \\
+1 & -1 & +1 & +1 & +1 \\
-1 & -1 & +1 & +1 & +1 \\
-1 & +1 & -1 & +1 & +1 \\
+1 & +1 & -1 & +1 & +1 \\
+1 & -1 & -1 & +1 & +1 \\
-1 & -1 & -1 & +1 & +1 \\
+1 & -1 & -1 & -1 & -1 \\
-1 & -1 & -1 & -1 & -1 \\
-1 & +1 & -1 & -1 & -1 \\
+1 & +1 & -1 & -1 & -1
\end{bmatrix}, \quad
C_x = \begin{bmatrix}
0 \\ 0 \\ 0 \\ 0 \\ 0 \\ 0 \\ 0 \\ 0 \\ 0 \\ 0 \\ 0 \\ 0 \\ 0 \\ 0 \\ 0 \\ 0 \\ 1 \\ 1 \\ 1 \\ 1 \\ 1 \\ 1 \\ 1 \\ 1 \\ 1 \\ 1 \\ 1 \\ 1 \\ 1 \\ 1 \\ 1 \\ 1 \\ 1 \\ 1 \\ 1
\end{bmatrix}, \quad
C_y = \begin{bmatrix}
0 \\ 0 \\ 0 \\ 0 \\ 1 \\ 1 \\ 1 \\ 1 \\ 1 \\ 1 \\ 1 \\ 1 \\ 2 \\ 2 \\ 2 \\ 2 \\ 0 \\ 0 \\ 0 \\ 0 \\ 1 \\ 1 \\ 1 \\ 1 \\ 1 \\ 1 \\ 1 \\ 1 \\ 2 \\ 2 \\ 2 \\ 2
\end{bmatrix}, \quad
C_z = \begin{bmatrix}
0 \\ 1 \\ 1 \\ 2 \\ 0 \\ 1 \\ 1 \\ 2 \\ 0 \\ 1 \\ 1 \\ 2 \\ 0 \\ 1 \\ 1 \\ 2 \\ 0 \\ 1 \\ 1 \\ 2 \\ 0 \\ 1 \\ 1 \\ 2 \\ 0 \\ 1 \\ 1 \\ 2 \\ 0 \\ 1 \\ 1 \\ 2
\end{bmatrix}
$$

A.2. PELLET BREAKING LIMIT AND BOUNCE DYNAMICS FROM THE $[\sigma(T),\varepsilon(T)]$ DIAGRAM

In a general way, the mechanical characteristics of a viscoelastic material under deformation depend on the speed of this deformation. In the case of a high speed, the most adapted rheological models for describing this behavior are combinations of parallel Maxwell-Wiechert elements (a purely viscous damper, with viscousc coefficient θ and a purely elastic spring, with restoring coefficient κ, connected in series, Figure A.1a) and Kelvin-Voigt elements (a purely viscous damper, with viscous coefficient θ, and a purely elastic spring, with restoring coefficient κ, connected in parallel, Fig A.1b).

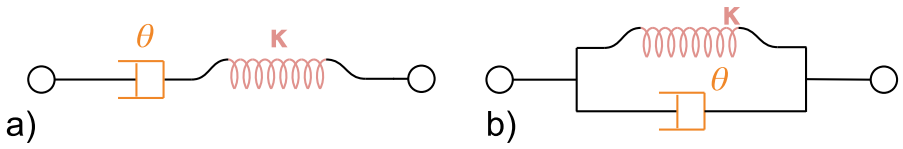


Figure A.1. – a) Maxwell-Wiechert element, b) Voigt-Kelvin element.

These models take into account that, under a dynamical constrain, the deformation and relaxation do not occur at a single time τ, but in a set of times $\tau_i = \kappa_i/\theta_i$, each of them corresponding to one of the elementary elements of the model. A reasonable knowledge of the varying time constant τ, allowing to determine the set of τ_i's, is therefore mandatory for an accurate modelling. In the present case, the mechanical properties of Hydrogen ice available [[133], [134]] result from static measurements, that take into account neither the speed of the constrain applied to the ice, nor the degradation of these properties due to the accumulation of defaults when the constrain is cycled. In such conditions, it is not possible to use the models introduced above. One can 1/ or directly use the $[\sigma(T),\varepsilon(T)]$ diagram from [133, 134] (Fig A.2a) as it is done in [132], 2/ or use a simple Maxwell-Wiechert or Kelvin-Voigt model, with a single element, where the parameters of the model, κ and θ, are adapted for fitting the experimental results. This is the choice done in the present work, essentially because it allows an analytical solution, which saves computational time when compared to the first one, which requires a numerical integration.

A.2.1. Available D_2 ice mechanical and thermal properties

In a general way, during a bounce, a proportion γ_1 of the perpendicular kinetic energy is stored as elastic energy in the pellet, and a proportion $(1-\gamma_1)(1-\gamma_2)$ for heating the ice in volume (the remaining part, $(1-\gamma_1)\gamma_2$, being consumed in the ice vaporization). The coupled evolution of stored the elastic energy and ice temperature can then be calculated from the variation with temperature of the $[\sigma(T),\varepsilon(T)]$ diagram and ice heat capacity [135], Fig A.2a).

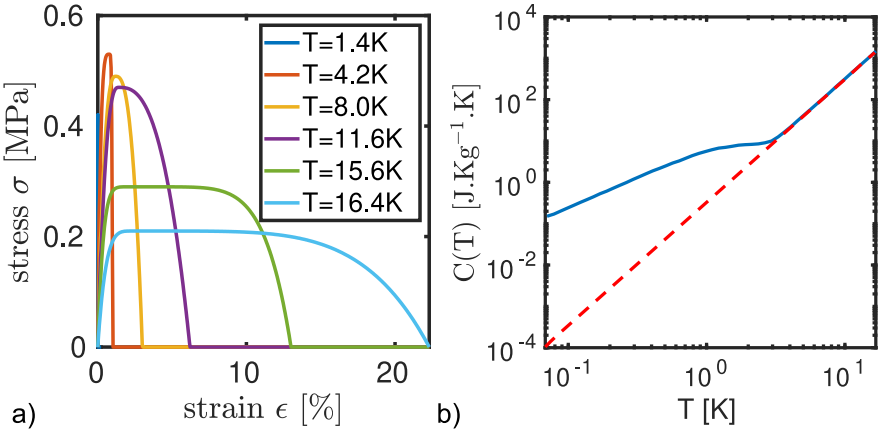


Figure A.2. – (a) $[\sigma(T),\varepsilon(T)]$ diagram for 6 temperature values, (b) Hydrogen heat capacity C(T) as a function of the temperature.

Practically, these parameters can be fitted by the following expressions:
Starting from a strain ε_i (in Fig A.2a, $\varepsilon_i = 0$)

$$\sigma(\varepsilon,\varepsilon_i,T) = \min\left\{\sigma_e(\varepsilon,\varepsilon_i,T);\sigma_p(\varepsilon,T)\right\} \tag{A.1}$$

with

$$\sigma_e(\varepsilon,\varepsilon_i,T) = E_Y(T)(\varepsilon-\varepsilon_i) \tag{A.2a}$$

$$\sigma_p(\varepsilon,T) = \begin{cases} \sigma_v(T)\left[1-\left(\frac{\varepsilon_v(T)-\varepsilon}{\varepsilon_v(T)}\right)^{\alpha(T)}\right] & \text{if} \quad \varepsilon \le \varepsilon_v(T) \\ \sigma_v(T)\left[1-\left(\frac{\varepsilon_v(T)-\varepsilon}{\varepsilon_v(T)-\varepsilon_m(T)}\right)^{\alpha(T)}\right] & \text{if} \quad \varepsilon > \varepsilon_v(T) \end{cases} \tag{A.2b}$$

where the values of $E_Y(T),\sigma_v(T),\varepsilon_v(T),\varepsilon_m(T)$, are given in Table A.1, and the specific heat:

$$C(T) = 7.5\times T^{1.5}\times\exp\left(-T^2/3\right)+0.33\times T^3\left[\,\mathrm{J/kg\cdot K}\right] \tag{A.3a}$$

$$\mathrm{C}(T) \approx 0.33\times T^3\left[\,\mathrm{J/kg\cdot K}\right] \quad \text{for T} \ge 3\ \mathrm{K} \tag{A.3b}$$

From these quantities, one can calculate the amount of stored elastic energy per unit volume (W(T)) above which the constrain on the ice exceeds the elastic limit, the failure outbreak limit and the first impact breaking limit, i.e. (see Fig A.3):

$$\mathrm{W}(T) = G\int_0^{\sigma_c}\sigma(\varepsilon,0,T)\,d\varepsilon \tag{A.4}$$

where $G = 3(1-2\nu)+6(1+\nu)$ and $\nu\sim 0.31$ is the Poisson's coefficient of the ice [136], and where $\sigma_c = \sigma_e^M(T),\sigma_v(T)$ and $\sigma_m(T)$, respectively.

T (k)	Elastic parameter			Necking point		ε_m (%)
	E_Y (MPa)	σ_e^m (MPa)	ε_c (%)	σ_v (MPa)	ε_v (%)	
1.4	420	0.42	0.10	0.42	0.5	0.6
4.2	270	0.29	0.11	0.53	0.8	1
8	110	0.22	0.20	0.49	1.2	3
11.6	90	0.16	0.18	0.47	1.4	6.2
15.6	80	0.08	0.13	0.29	2.3*	13
16.4	40	0.05	0.10	0.21	2.5*	22.3

Table A.1. – deuterium ice data used for calculation from [[133] [134]]. T is the temperature, E_Y the Young s' modulus, σ_e^M the stress at elastic limit, ε_c the strain at elastic limit (calculated), σ_v the stress at necking point, ε_v strain at necking point and ε_m strain at breaking point * = extrapolated data)

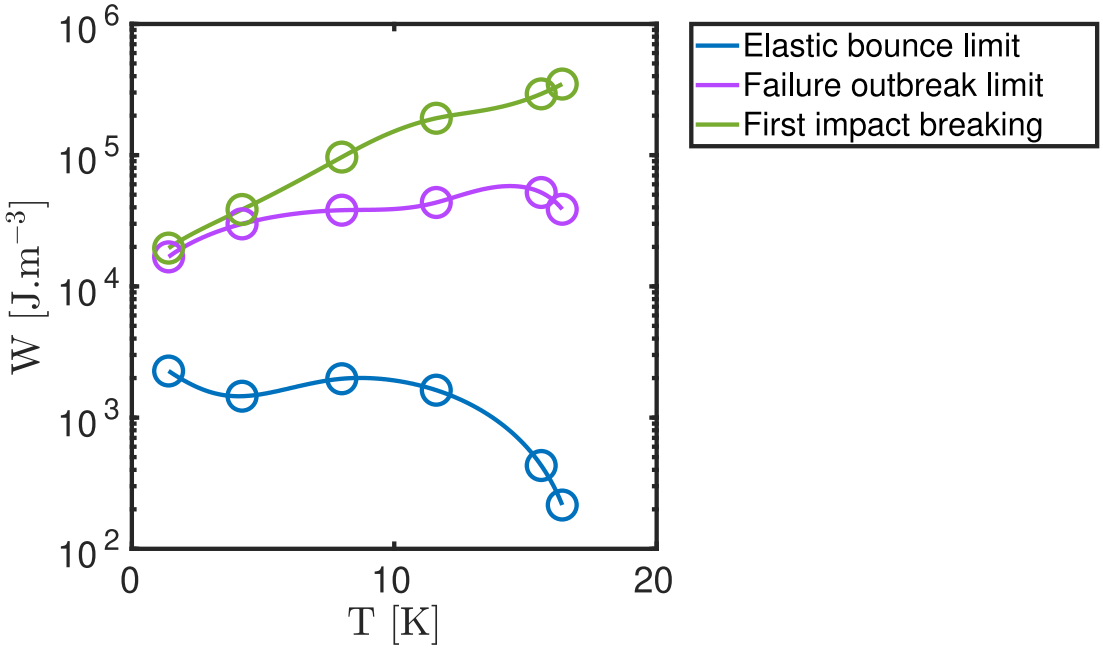


Figure A.3. – Energy density limits for elastic behavior, failure outbreak and first impact breaking vs. temperature.

A.2.2. Direct use of the $[\sigma(T), \varepsilon(T)]$ diagram

The procedure described in this section follows for a part that of ref. [132]. As soon as the elastic limit is exceeded, the pellet perpendicular velocity decreases during a bounce, from v_i^r to v_f^r $\left(v_i^r > v_f^r\right)$. The loss in kinetic energy, $\frac{m}{2}\left(v_i^{r^2} - v_f^{r^2}\right)$, is used for:

— Storage of elastic energy, in a proportion γ_1.
— Vaporization, in a proportion $(1-\gamma_1)\gamma_2$.
— Increase in temperature, in a proportion $(1-\gamma_1)(1-\gamma_2)$.

The trajectory followed in the $[\sigma(T), \varepsilon(T)]$ diagram is illustrated in Fig A.4.

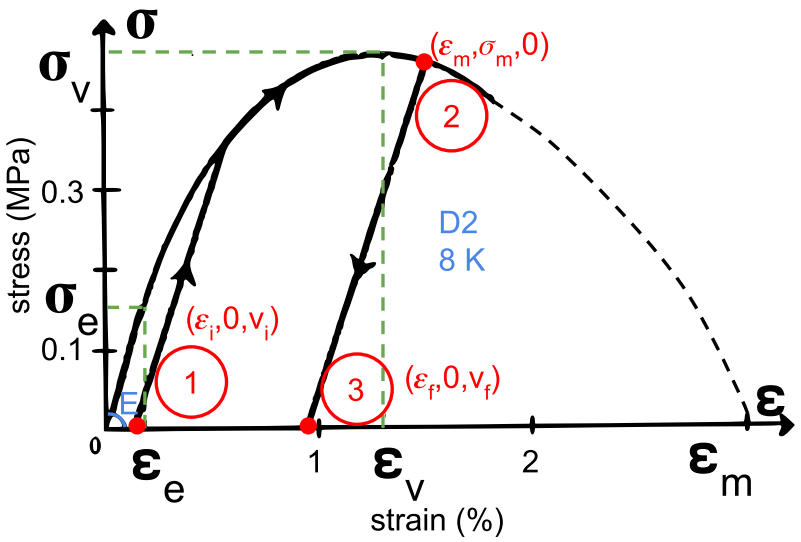


Figure A.4. – Stress-strain diagram for D_2 ice at $8K$, showing the general evolution of the ice state during a bounce. The stress and strain at the elastic limit $(\varepsilon_e, \sigma_e)$, necking $(\varepsilon_v, \sigma_v)$, and breaking (ε_m) points are also indicated. Their values are given in Table A.1.

During the first phase, from $(\varepsilon_i, 0, v_i)$ to $(\varepsilon_M, \sigma_M, 0)$, a proportion γ_1 of the perpendicular kinetic energy is absorbed, following:

$$\frac{dv^r}{d\varepsilon} = -\frac{1}{\gamma_1 v^r}\frac{G}{Mn_s}\sigma(\varepsilon, \varepsilon_i, T) \tag{A.5a}$$

and

$$\frac{dT}{d\varepsilon} = \frac{(1-\gamma_1)(1-\gamma_2)}{\gamma_1}\frac{G}{C(T)}\sigma(\varepsilon, \varepsilon_i, T) \tag{A.5b}$$

It is noticeable that the behavior of v^r and T only depends on volume quantities, and is there independent on the pellet radius. The evolution of the latter is given by:

$$\frac{dR_p}{d\varepsilon} = -\frac{(1-\gamma_1)\gamma_2}{\gamma_1}\frac{R_p G}{n_S(\varepsilon_s - 3k_B T/2)}\sigma(\varepsilon, \varepsilon_i, T) \tag{A.5c}$$

During the second phase of the bounce, from $(\varepsilon_M, \sigma_M, 0)$ to $(\varepsilon_f, 0, v_f)$, one has:

$$\frac{dv}{d\varepsilon} = -\frac{\gamma_1}{v^r}\frac{G}{Mn_s}(E_Y(T)[\varepsilon - \varepsilon_M] + \sigma_M) \tag{A.6a}$$

$$\frac{dT}{d\varepsilon} = -\left(1-\gamma_1\right)\left(1-\gamma_2\right)\frac{G}{C(T)}\sigma\left(\varepsilon, \varepsilon_i, T\right) \tag{A.6b}$$

$$\frac{dR_p}{d\varepsilon} = \left(1-\gamma_1\right)\gamma_2\frac{R_p G}{n_s\left(\varepsilon_s - 3k_B T/2\right)}\sigma\left(\varepsilon, \varepsilon_i, T\right) \tag{A.6c}$$

At the end of the bounce, the elastic energy stored in the ice per unit volume is:

$$\delta E_p = G\left[\int_{\varepsilon_i}^{\varepsilon_M} \sigma\left(\varepsilon, \varepsilon_i, T\right) d\varepsilon - \int_{\varepsilon_f}^{\varepsilon_M} \left(E_Y(T)\left[\varepsilon - \varepsilon_M\right] + \sigma_M\right) d\varepsilon\right] \tag{A.7}$$

This value is to be compared to the limits displayed in Fig A.3 Using

$$\varepsilon(t) = \frac{\left[R_p(t+dt) - R_p(t)\right]}{R_p(t)} = \frac{dR_p}{R_p(t)},$$

it comes $\dot{\varepsilon} = v^r / R_p(t)$, and one can reconstruct the time history of the pellet compression by imposing:

$$t = \int_{\varepsilon_i}^{\varepsilon} \frac{R_p(x)}{v^r(x)} dx$$

A.3. TRANSCIENT CHANGE IN μ IN CASE OF FORCED SLIPPING

For any realistic values of κ, θ and μ, the decrease in v^r is larger than that in $v^{\|}$ during a bounce. This has for consequence that, along a trajectory of constant curvature, the distance covered between two successive bounces, d, decreases continuously. This can lead to a huge accumulation of bounces on a very short distance before the condition $\alpha < \delta\alpha$ is verified, allowing the pellet to slip. This accumulation of bounces has no physical significance and leads to an unacceptable calculation time. Solution is to impose that the pellet slips as soon as the angle of the velocity with the wall at the end of the bounce, $(\alpha - \delta\alpha)$, is smaller than a critical value $\delta\alpha_{lim}$ chosen by the user (this procedure does not prevent from an accumulation of bounces for $(\alpha - \delta\alpha) \gtrsim \delta\alpha_{lim}$, but it allows controlling the distance δ covered between two successive bounces). The phase of forced slipping that follows is only an approximation for a series of bounces and the value of μ must be adapted for ensuring that the braking of the pellet due to the friction with the wall during this phase is equal to that resulting from the bounces. This value, μ', can thus be different to that used during the other phases of slipping and, for consistency, it must be applied on a distance d about that which would be covered by the succession of bounds until the condition $\alpha < \delta\alpha$ is verified, see Fig A.5. (This approximation is nevertheless not perfect because the series of bounces can lead to an accumulation of energy in the ice if the elastic limit is exceeded, which will not be the case for an equivalent slipping.)
The principle of the calculation is explicated below, starting from an initial pellet velocity $v_2 = \sqrt{v_2^{r^2} + v_2^{\|^2}}$. For simplicity, external forces are neglected.

A.3.1. Braking during a bounce

The time evolution of the pellet perpendicular velocity during a bounce writes:
$v^r(t) = v_2^r e^{-t/\tau}\left\{\cos(\omega t) - \frac{1}{\omega\tau}\sin(\omega t)\right\}$
with $\omega = \sqrt{\frac{\kappa}{m_2} - \frac{\theta^2}{4m_2{}^2}}$ and $\tau = 2m_2/\theta$.
The end of the bounce occurs at time $t_B = \frac{\pi}{\omega}$, for which: $v^r(t_B) = v_2^r e^{-t_B/\tau}$
The pellet velocity at the end of the bounce is then:

$$v_2^B = \sqrt{v_2^{r^2} e^{-2t_B/\tau} + v_2^{\|^2}} \tag{A.8}$$

corresponding to a change in the magnitude of the angle between the pellet velocity and the wall by a factor:

$$\xi = \frac{\tan^{-1}\left(v_2^r e^{-t_B/\tau}/v_2^{\|}\right)}{\tan^{-1}\left(v_2^r/v_2^{\|}\right)} \tag{A.9}$$

A.3.2. Braking during a slipping

At the critical angle $\delta\alpha_{\lim}$, the free flight of the pellet between two bounces corresponds to a distance $\langle R\rangle\delta\alpha_{\lim}$ along the wall surface. A pellet slipping along this distance will be braked by the friction force $-\mu' m_2 v^2/\langle R\rangle$, following the equation :

$$\frac{dv}{dt} = -\frac{\mu' v^2}{\langle R\rangle}$$

which, after integration, leads to:

$$v(t) = \frac{v_2\langle R\rangle}{v_2\mu' t + \langle R\rangle}$$

The time required for covering the distance $\langle R\rangle\delta\alpha_{lim}$ is given by:

$$\int_0^{t_F} v(t)dt = \langle R\rangle\delta\alpha_{\lim}$$

i.e. : $t_F = \frac{\langle R\rangle}{v_2\mu'}\left(e^{\mu'\delta\alpha_{\lim}} - 1\right)$
yielding to :

$$v_2^F = v_2 e^{-\mu'\delta\alpha_{\lim}} \tag{A.10}$$

A.3.3. Calculation of μ'

The condition to be satisfied for the braking to be the same for the bounce and the free flight is $v_2^B = v_2^F$, i.e.:

$$v_2^{r^2} e^{\left(-\frac{2\pi m_2}{\sqrt{4\kappa m_2 - \theta^2}}\right)} + v_2^{\|^2} = \left(v_2^{r^2} + v_2^{\|^2}\right) e^{-2\mu'\delta\alpha_{\lim}}$$

yielding:

$$\mu' = \frac{1}{2\delta\alpha_{\lim}} \log\left[\frac{v_2^{r^2} + v_2^{\|^2}}{v_2^{r2} e^{-\left(\frac{2\pi m_2}{\sqrt{4\kappa m_2 - \theta^2}}\right)} + v_2^{\|^2}}\right] \tag{A.11}$$

A.3.4. Calculation of d

Due to the different braking of the perpendicular and parallel components of the velocity during a bounce, the angle of the velocity with respect to the wall decreases by a factor ξ (eq.A.9)) between the beginning and the end of the bounce. Starting at the point where $\alpha \lesssim \delta\alpha_{lim}$, the left hand term of the inequality becomes $((((\alpha - \delta\alpha)\xi - \delta\alpha)\xi - \delta\alpha)\ldots)\xi - \delta\alpha = \alpha\xi^n - \delta\alpha\left(\frac{1-\xi^{n-2}}{1-\xi}\right)$ after n bounces. Then, the slipping condition

is verified for $\alpha\xi^n \leq \delta\alpha\left(1+\frac{1-\xi^{n-2}}{1-\xi}\right) \sim \delta\alpha\left(\frac{2-\xi}{1-\xi}\right)$, i.e.:

$$n = \mathrm{E}\left[\log\left(\frac{\delta\alpha}{\alpha}\left(\frac{2-\xi}{1-\xi}\right)\right)^{\frac{1}{\xi}}\right]$$

The distance covered during these n bounces is:

$$d = \langle R\rangle \sum_1^n \left[\delta\alpha_{lim}\xi^k - \delta\alpha\left(\frac{1-\xi^{k-2}}{1-\xi}\right)\right]$$

$$d = \langle R\rangle \left\{\delta\alpha_{lim}\left(\frac{1-\xi^{n-1}}{1-\xi}\right) - \frac{\delta\alpha}{1-\xi}\left[n - \frac{1}{\xi^2}\left(\frac{1-\xi^{n-1}}{1-\xi}\right)\right]\right\} \tag{A.12a}$$

$$\sim \frac{\langle R\rangle\left(\delta\alpha_{lim} - n\delta\alpha\right)}{1-\xi} \quad \text{for } \xi \to 1 \tag{A.12b}$$

In the succession of bounds, v^r decreases faster than $v^{\|\prime}$, leading to a decrease in μ' from eq. A.11. This decrease stops when the slipping condition $\alpha\xi^n \leq \delta\delta\alpha\left(\frac{2-\xi}{1-\xi}\right)$ is verified, for which $\mu' \to \mu$. Calculating the exact variation of μ' with s is possible but cumbersome and does not make the approximation more accurate. Practically, a simple linear decrease $\sim \mu' - \left(\frac{\mu-\mu'}{d}\right)s$ is enough.

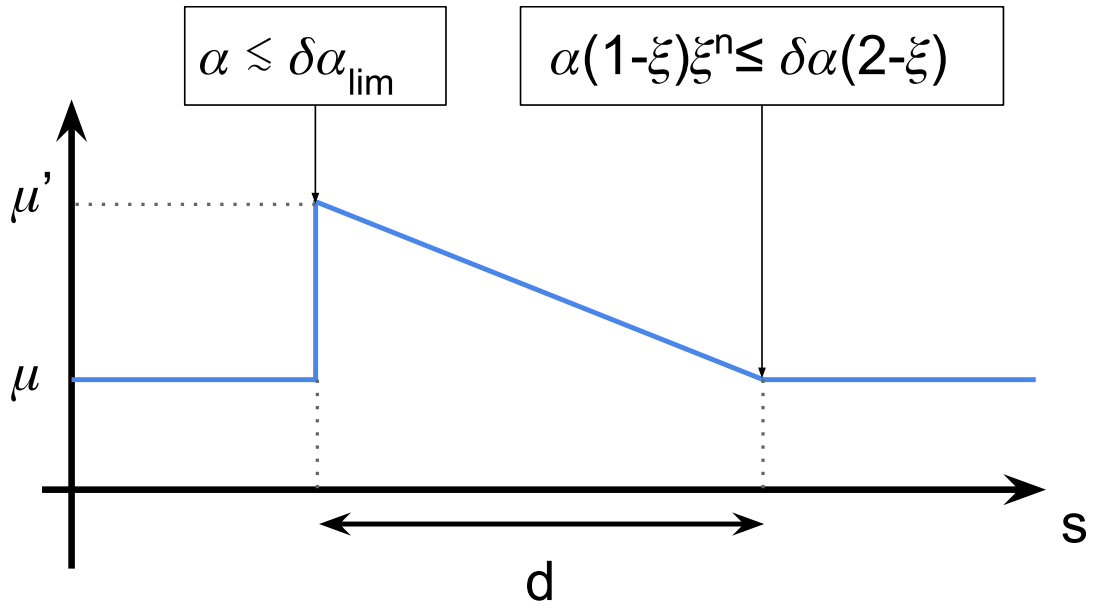


Figure A.5. – Variation of the friction coefficient after a forced slipping.

A.4. SET OF RECORDED PARAMETERS

The simulation of the pellet trajectory is performed by successive steps, every free-flight, bounce or slip phase being calculated independently. For ensuring the communication between the output of a step and the input of the following - and also for allowing a detailed post-analysis of the pellet trajectory - a set of parameters in the laboratory frame, listed in Table A.2, is systematically recorded at the end of each step.

Matrix_of_inputs(1)	1	2
Matrix_of_inputs(2)	R_0	NaN
Matrix_of_inputs(3)	$R_\delta(t_f)$	
Matrix_of_inputs(4)	$\varphi_{\max}$	L
Matrix_of_inputs(5)	$m(t_f)$	
Matrix_of_inputs(6)	$T(t_f)$	
Matrix_of_inputs(7)	$V^x(t_f)$	
Matrix_of_inputs(8)	$V^y(t_f)$	
Matrix_of_inputs(9)	$V^z(t_f)$	
Matrix_of_inputs(10)	$V^r(t_f)$	
Matrix_of_inputs(11)	$V^\psi(t_f)$	
Matrix_of_inputs(12)	$V^z(t_f)$	$V^\varphi(t_f)$
Matrix_of_inputs(13)	$x(t_f)$	
Matrix_of_inputs(14)	$y(t_f)$	
Matrix_of_inputs(15)	$z(t_f)$	
Matrix_of_inputs(16)	$r(t_f)$	
Matrix_of_inputs(17)	$\psi(t_f)$	
Matrix_of_inputs(18)	$\varphi(t_f)$	$z(t_f)$
Matrix_of_inputs(19)	G^x	
Matrix_of_inputs(20)	G^y	
Matrix_of_inputs(21)	G^z	
Matrix_of_inputs(22)	$G^r(t_f)$	
Matrix_of_inputs(23)	$G^\psi(t_f)$	
Matrix_of_inputs(24)	$G^\varphi(t_f)$	$G^z(t_f)$

Table A.2. – Set of parameters in the laboratory frame recorded at the end of every simulation step. In the first line 1 refers to a toric section & 2 for a cylindrical section.

B. APPENDICES - Chapter 3

B.1. NAMES OF THE QUANTITIES CHARACTERIZING THE RADIATION

Sections 3.3, 3.4 and 3.8 use numerous quantities characterizing the intensity of radiation. For the sake of clarity, the procedure used for building the corresponding symbols is explicated below.
The general form is $X^{\text{Superscript}}_{\text{Subscript}}$.
The main letter, X, defines the quantity: P for the power [W/.../str] and E for the energy [J/.../str].
A horizontal bar is added above the letter if the quantity, before calibration, is yet in arbitrary units: $\bar{X}$, and a star is added is the quantity is extrapolated to the whole space assuming that emission is isotropic: X^*, [W/...] or [J/...].
The subscript characterizes the domain of wavelength considered: λ for a particular wavelength [W or J/nm/...], $\Delta\lambda$ when multiplied by a filter [J], Σ for the whole spectrum [J].
The superscript indicates how the quantity is measured or calculated: S if measured by the spectrometer, D by the photodiodes and I by the fast camera in Section 3.3, 3.4 and 3.8, where the differentiation between the methods of measurement has no matter after cross-calibration, exp for the measurements and sim for the simulation.

B.2. INTERPOLATION PROCEDURE OF HPI2 SIMULATION

In HPI2, the ablation rate and corresponding cloud evolutions are calculated at constant space and time intervals $\delta R = \delta t V_{\text{inj}}$. However, for reconstructing the ablation pattern, one must take into account that each cloud begins developing at the time where the pellet exits the cloud just deposited previously. HPI2 outputs must therefore be adapted. This is done through an interpolation procedure that is described in this appendix.

Let us define two sets of clouds: the HPI2-clouds, whose all characteristics are known from the HPI2 outputs, and the time interpolated clouds - hereafter referred to as sim-clouds because they can be directly compared with the measurements. The deposition time of the sim-clouds follow the above schedule. The birth time of each cloud is built iteratively (Fig B.1):

- The deposition times of the first HPI2-cloud and sim-cloud coincide at $t = 0$.
- The time intervals necessary to the pellet for exciting every HPI2-cloud, t^i_{exit}, is interpolated with a continuous curve $t_{\text{exit}}(t)$.
- The deposition time of the sim-cloud #2 is equal to t^1_{exit}.
- The time at which the pellet exits the sim-cloud #2 is ${t'^2}_{\text{exit}} = t_{\text{exit}}\left(t^1_{\text{exit}}\right)$.
- The deposition time of the sim-cloud #3 is then equal to $t^1_{\text{exit}} + {t'^2}_{\text{exit}}$.
- etc...

The general term of the series giving the deposition time of the sim-clouds # j is:

$$t^j_{\text{dep}} = \sum_{j=1}^{j-1} {t'^i}_{\text{exit}} + t_{\text{exit}}\left(\sum_{j=1}^{j-1} t'^i_{\text{exit}}\right) = \sum_{j=1}^{j} {t'^i}_{\text{exit}} \text{ with } {t'^1}_{\text{exit}} = t^1_{\text{exit}} \tag{B.1}$$

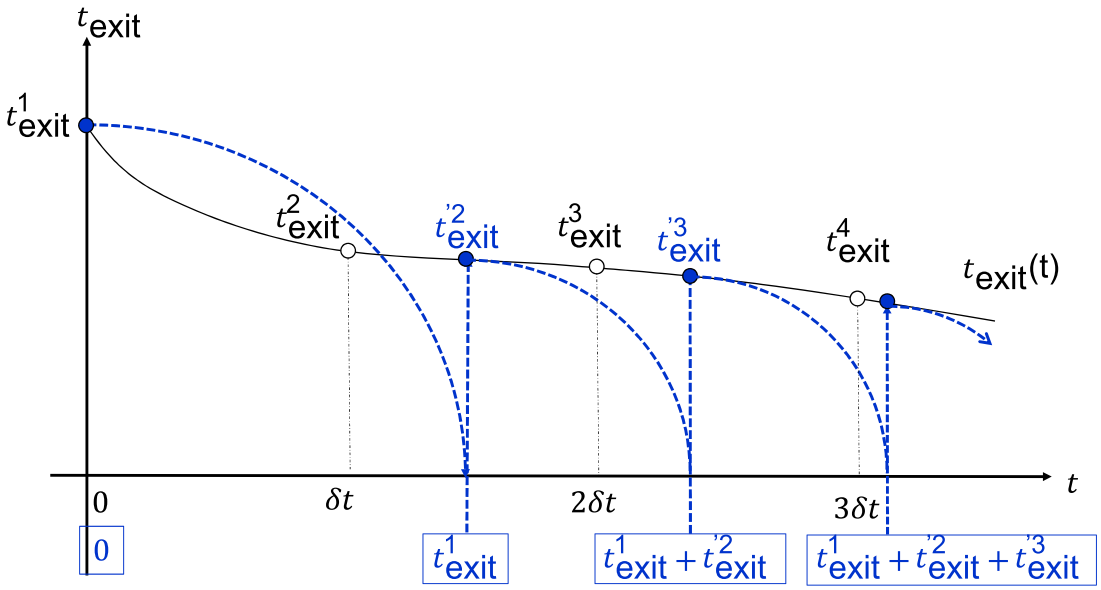


Figure B.1. – Interpolation procedure for calculating the deposition time of the set of sim-clouds.

It is then necessary to interpolate all the characteristics of the set of HPI2-clouds at times in agreement with the time schedule of the sim-clouds (the latter being deposited at times t^j_{dep}, and not at $(i-1)\delta t$). Practically, for every HPI2-cloud, the emission model described in Section 3.5 is applied 19 times, for $f_i = 5\%$ to $f_i = 95\%$, by step of 5%. The same interpolation procedure, explicated in Fig B.2, must be applied to any quantity hereafter referred to as U for commodity (it can be the radius, length, density, temperature, emission at any wavelength...).

— The value of U for the set of HPI2-clouds at the considered ionized fraction f_i, noted $U^n_{\%}$, and the time at which the clouds reach f_i, noted $\tau^n_{\%,}$, are interpolated with continuous curves $U_{\%}(t)$ and $\tau_{\%}(t)$ - The value $U^j_{\%}$ and time $\tau^j_{\%}$ are determined as $U_{\%}\left(t^j_{dep}\right)$ and $\tau_{\%}\left(t^j_{dep}\right)$, with $t^j_{dep} = \sum^j_{j=1} t'^i_{\text{exit}}$.

— In the reconstruction of global signal, the contribution to U of the sim-cloud " j " begins at time t^j_{dep} and reaches the value $U^j_{\%}$ at time $t^j_{dep} + \tau^j_{\%}$.

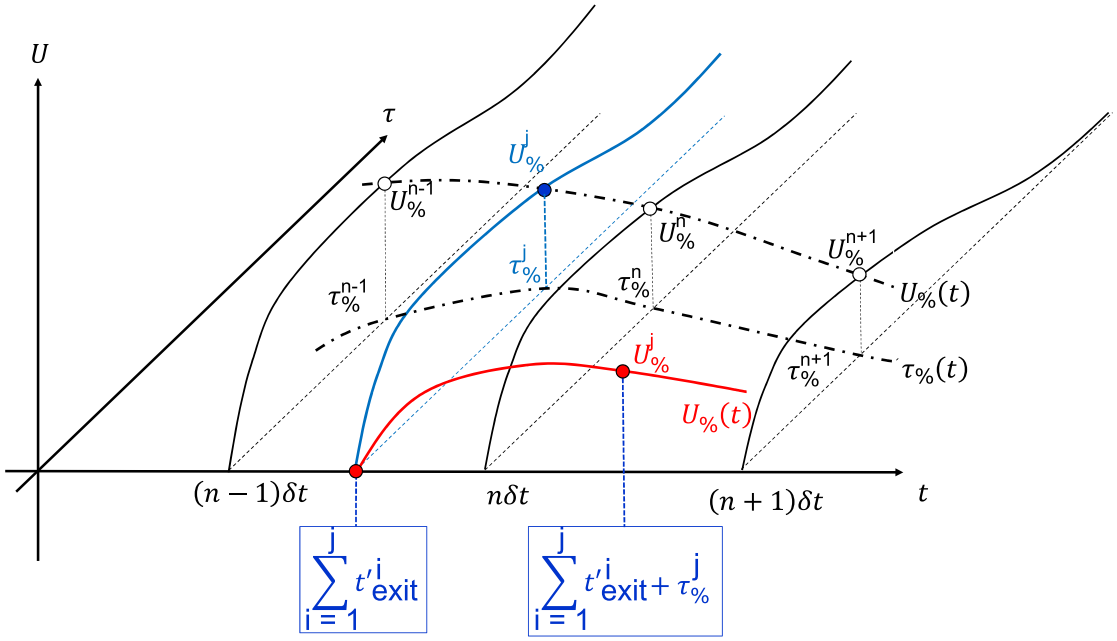


Figure B.2. – Interpolation procedure for calculating the characteristics of the set of sim-clouds.

Bibliography

[1] J.D. Lawson. In: *Proc. Phys. Soc.* B70 (1957), p. 6 (cit. on p. 19).

[2] D. J. Rose and M. Clark. In: *Plasma and Controlled Fusion (MIT and Wiley, New-York* 16 (1961) (cit. on p. 20).

[3] L. A. Artsimovitch. In: *Controlled Thermo-Nuclear Reactions (Oliver Boyd, Edimburg)* 286 (1964) (cit. on p. 20).

[4] K. Miyamoto. In: *Nucl, Fusion* 18 (1978), p. 243 (cit. on p. 20).

[5] D. C. Robinson King R.E. In: *Proc. 3rd Int. Conf. on Plasma Physics and Controlled Nuclear Fusion Research (I.A.E.A., Vienna)* 1 (1969), p. 263 (cit. on p. 21).

[6] J. B. Taylor. In: *Phys. Rev. Lett.* 33 (1974), p. 1139 (cit. on p. 21).

[7] L.A. Artsimovich. In: *Nucl. Fus.* 12 (1972), p. 215 (cit. on p. 21).

[8] P. Martin et al. In: *Nucl, Fusion* 51 (2011), p. 094023 (cit. on p. 21).

[9] J. G. Cordey. in Applied atomic and collision physics (Academic Press, Orlando), 1984 (cit. on p. 22).

[10] M. Porkolab. Vol. 339. Review of RF Heating, in Theory of Magnetically confined Plasmas, (Varenna, Proc. of the Int. School of Plasma Physics), 1979 (cit. on p. 22).

[11] Y. Peysson. In: *in Radio Frequency Power in Plasmas, Proc. 13th Top. Conf. on Radio Frequency Power in Plasmas (AIP Conference Proceedings)* 485 (1969), p. 183 (cit. on p. 22).

[12] A.S. Kukushkin et al. In: *J. Nucl. Mat.* 415 (2011), S497 (cit. on pp. 22, 41).

[13] M. Chatelier. In: *Vacuum* 47 (1996), p. 963 (cit. on p. 22).

[14] C. S. Pitcher P. C. Stangeby. In: *Plasma Phys. Control. Fusion* 39 (1997), p. 779 (cit. on p. 22).

[15] F. Engelmann. In: *Com. Plasma Phys. Contr. Fus.* 12 (1989), p. 293 (cit. on p. 22).

[16] B. Pégourié et al. In: *J. Nucl. Mater.* 313-316 (2003), p. 539 (cit. on pp. 23, 36).

[17] S.L. Milora et al. In: *Nucl. Fus.* 35 (1995), p. 657 (cit. on pp. 23–25).

[18] B. Pégourié et al. In: *Plasma Phys. Control. Fusion* 49 (2007), R87 (cit. on pp. 23–25, 28, 31, 32, 35, 36, 38, 137).

[19] B. Pégourié et al. In: *Plasma Phys. Control. Fusion* 51 (2009), p. 124023 (cit. on pp. 23, 25, 28, 31, 34, 35).

[20] H.W. Müller et al. In: *Phys. Rev. Lett.* 83 (1999), p. 2199 (cit. on pp. 23, 107).

[21] P.T. Lang et al. In: *Nucl, Fusion.* 52 (2012), p. 023017 (cit. on pp. 23, 38).

[22] P.T. Lang et al. In: *Nucl. Fus.* 51 (2011), p. 033010 (cit. on p. 23).

[23] S. Jachmich et al. In: *Nucl. Fus.* 62 (2022), p. 026012 (cit. on p. 23).

[24] B. Pégourié et al. In: *Proc. 43th Eur. Conf. on Plasmas Physics, Leuven (Eur. Phys. Soc., ECA)* 40A (2016), pp. 4–076 (cit. on pp. 24, 50).

[25] P.T. Lang et al. In: *Fusion Eng. Des.* 96-97 (2015), p. 123 (cit. on pp. 24, 41).

[26] N. Commaux et al. In: *Nucl, Fusion.* 50 (2010), p. 025011 (cit. on pp. 24, 35, 91).

[27] R. Sakamoto et al. In: *Nucl, Fusion.* 53 (2013), p. 063007 (cit. on pp. 24, 35, 91, 137).

[28] M. Romanelli et al. In: *Nucl, Fusion* 55 (2015), p. 093008 (cit. on p. 28).

[29] S.K. Combs and L.R. Baylor. In: *Fusion Sci. Technol.* 73 (2018), p. 493 (cit. on pp. 28, 50).

[30] R. Raman. In: *Fus. Eng. Des.* 83 (2008), p. 1368 (cit. on p. 28).

[31] W.A. Houlberg et al. In: *Nucl, Fusion.* 28 (1988), p. 595 (cit. on pp. 30, 31, 91).

[32] P. B. Parks et al. In: *Nucl, Fusion* 17 (1977), pp. 5539–556 (cit. on pp. 30, 31).

[33] N. Bosviel et al. In: *Phys.plasma* 28 (2021), p. 012506 (cit. on p. 31).

[34] R. Samulyak et al. In: *Nucl, Fusion.* 61 (2021), p. 046007 (cit. on pp. 31, 91).

[35] V.A. Rozhansky and I.Yu. Senichenkov. In: *Plasma Phys. Rep.* 31 (2005), p. 993 (cit. on p. 31).

[36] Y. Nakamura et al. In: *Nucl, Fusion.* 32 (1992), p. 2229 (cit. on p. 31).

[37] B. Pégourié et al. In: *Plasma Phys. Control. Fusion* 47 (2005), p. 17 (cit. on pp. 31, 91, 117, 138).

[38] A. Matsuyama et al. In: *Plasma Phys. Control. Fusion* 54 (2012), p. 035007 (cit. on pp. 31, 91, 117, 132, 138).

[39] A. Bortolon et al. In: *Nucl, Fusion.* 59 (2019), p. 084003 (cit. on p. 31).

[40] K.J. McCarthy et al. In: *Plasma Phys. Control. Fusion* 61 (2019), p. 014013 (cit. on p. 31).

[41] A.M. Arnold et al. In: *Plasma Phys. Control. Fusion* 63 (2021), p. 095008 (cit. on p. 32).

[42] V.A. Rozhansky et al. In: *Plasma Phys. Control. Fusion* 37 (1995), p. 399 (cit. on p. 32).

[43] P.B. Parks and L.R. Baylor. In: *Phys. Rev. Lett.* 94 (2005), p. 125002 (cit. on p. 32).

[44] P.B. Parks et al. In: *Phys.plasma* 7 (2000), p. 1968 (cit. on pp. 33, 91).

[45] B. Pégourié et al. In: *Nucl, Fusion* 47 (2007), p. 44 (cit. on p. 33).

[46] V.A. Rozhansky et al. In: *Plasma Phys. Control. Fusion* 46 (2004), p. 575 (cit. on p. 34).

[47] A. Matsuyama et al. In: *Nucl, Fusion.* 52 (2012), p. 123017 (cit. on pp. 34, 35).

[48] R. Ishizaki and N. Nakajima. In: *Plasma Phys. Control. Fusion* 53 (2011), p. 054009 (cit. on p. 34).

[49] A. Canton et al. In: *Plasma Phys. Control. Fusion* 43 (2001), p. 225 (cit. on pp. 35, 36).

[50] A. R. Polevoi and M. Shimada. In: *Plasma Phys. Control. Fusion* 43 (2001), p. 1525 (cit. on p. 35).

[51] F. Köchl et al. In: *Prepr. EFDA-JET-PR(12)* 57 (2012), p. 82 (cit. on p. 35).

[52] N. Panadero et al. In: *ECA-43C* (2019), P1.1077 (cit. on p. 35).

[53] L. Garzotti et al. In: *Nucl, Fusion.* 50 (2010), p. 100502 (cit. on p. 35).

[54] N. Hayashi et al. In: *Nucl, Fusion.* 51 (2011), p. 103030 (cit. on p. 35).

[55] N. Panadero et al. In: *Nucl, Fusion.* 58 (2018), p. 026025 (cit. on p. 35).

[56] L.R. Baylor et al. In: *Nucl, Fusion.* 47 (2007), p. 1598 (cit. on pp. 36, 37).

[57] A. Géraud et al. In: *J. Nucl. Mater.* 337-339 (2005), p. 485 (cit. on p. 36).

[58] M. Valovic et al. In: *Nucl, Fusion.* 52 (2012), p. 114022 (cit. on p. 38).

[59] M. Valovic et al. In: *Nucl, Fusion.* 55 (2015), p. 013011 (cit. on p. 38).

[60] P.T. Lang et al. In: *Nucl, Fusion.* 52 (2012), p. 023017 (cit. on p. 38).

[61] M. Valovic et al. In: *Plasma Phys. Control. Fusion* 60 (2018), p. 085013 (cit. on p. 38).

[62] M. Valovic et al. In: *Nucl, Fusion.* 60 (2020), p. 054006 (cit. on p. 38).

[63] P.T. Lang et al. In: *Nucl, Fusion.* 54 (2014), p. 083009 (cit. on p. 38).

[64] R. Sakamoto et al. In: *Nucl, Fusion.* 41 (2001), p. 381 (cit. on p. 38).

[65] C.D. Beidler et al. In: *Plasma Phys. Control. Fusion* 60 (2018), p. 105008 (cit. on p. 38).

[66] J. Baldzuhn al. In: *Plasma Phys. Control. Fusion* 60 (2018), p. 035006 (cit. on p. 38).

[67] J. Baldzuhn al. In: *Plasma Phys. Control. Fusion* 61 (2019), p. 095012 (cit. on p. 38).

[68] J. Baldzuhn al. In: *Plasma Phys. Control. Fusion* 62 (2020), p. 055012 (cit. on p. 38).

[69] S.A. Bozhenkov et al. In: *Nucl, Fusion.* 60 (2020), p. 066011 (cit. on pp. 38, 39).

[70] H. Yamada et al. In: *Nucl, Fusion.* 45 (2005), p. 1684 (cit. on pp. 38, 39).

[71] T. Morisaki et al. In: *Phys. Plasmas* 14 (2007), p. 056113 (cit. on pp. 39, 40, 45).

[72] S. Ohdachi et al. In: *Nucl, Fusion.* 57 (2017), p. 066042 (cit. on p. 39).

[73] K.J. McCarthy et al. In: *Nucl. Fusion* 57 (2017), p. 056039 (cit. on p. 39).

[74] J.L. Velasco et al. In: *Plasma Phys. Control. Fusion* 58 (2016), p. 084004 (cit. on p. 39).

[75] G. Motojima et al. In: *Plasma Phys. Control. Fusion* 61 (2019), p. 075014 (cit. on pp. 39, 40).

[76] R. Lorenzini et al. In: *Plasma Phys. Control. Fusion* 44 (2002), p. 233 (cit. on p. 39).

[77] M. D. Wyman et al. In: *Nucl. Fusion* 49 (2009), p. 015003 (cit. on p. 39).

[78] B. Pégourié et al. In: *ECA-40A* (2017), p. 4.076 (cit. on p. 41).

[79] F. Janky et al. In: *DEMO Control Challenges* 31st SOFT (2020) (cit. on pp. 41, 43).

[80] B. Ploeckl et al. In: *Fusion Sci. Technol.* 77 (2021), p. 266 (cit. on pp. 41, 43, 44, 50).

[81] G. Giruzzi et al. In: *Plasma Phys. Control. Fusion* 62 (2020), p. 014009 (cit. on p. 41).

[82] M. Shimada et al. In: *Nucl. Fusion* 47 (2007), S1 (cit. on p. 41).

[83] K. Tobita et al. In: *Fusion Sci. Technol.* 75 (2019), p. 372 (cit. on pp. 41, 42).

[84] G. Federici et al. In: *Nucl. Fusion* 59 (2019), p. 066013 (cit. on pp. 41, 42).

[85] A. Sagara et al. In: *Fusion Eng. Des.* 87 (2012), p. 594 (cit. on p. 41).

[86] P. T. Lang et al. In: *Fusion Sci. Technol.* 75 (2019), p. 178 (cit. on pp. 41, 42, 75).

[87] L. Garzotti et al. In: *Nucl, Fusion.* 52 (2012), p. 013002 (cit. on p. 41).

[88] F. Koechl et al. In: *Nucl, Fusion.* 60 (2020), p. 066015 (cit. on p. 41).

[89] S. K. Combs et al. In: *Fusion Eng. Des.* 87 (2012), p. 634 (cit. on pp. 42, 43).

[90] S. Tokugana et al. In: *Fusion Eng. Des.* 123 (2017), p. 620 (cit. on pp. 42, 44).

[91] P. Vincenzi et al. In: *Nucl. Fusion* 55 (2015), p. 113028 (cit. on p. 43).

[92] A. Frattolillo et al. In: *Fusion Eng. Des.* 162 (2021), p. 112138 (cit. on pp. 43, 50).

[93] R. Sakamoto and H. Yamada. In: *IEEE Transactions on Plasma Science* 44 (2016), p. 2915 (cit. on p. 43).

[94] T. Goto et al. In: *Fusion Eng. Des.* 89 (2014), p. 2451 (cit. on p. 43).

[95] R. Sakamoto and H. Yamada. In: *Fusion Eng. Des.* 89 (2014), p. 812 (cit. on p. 45).

[96] B. Ploeckl et al. In: *Fusion Eng. Des.* 123 (2017), p. 186 (cit. on p. 50).

[97] A. Frattolillo et al. In: *Fusion Eng. Des.* 124 (2017), pp. 846–849 (cit. on p. 50).

[98] Wikipedia article : Drag (physics) (cit. on p. 55).

[99] MA. Meyers and K.K. Chawla. Cambridge University Press, New York, 1999, pp. 98–103 (cit. on p. 58).

[100] P. T. Lang et al. In: *Fus. Eng. Design* 123 (2017), pp. 167–170 (cit. on p. 75).

[101] L.R. Baylor et al. In: *Nucl, Fusion.* 32 (1992), p. 2177 (cit. on p. 91).

[102] W.A. Houlberg et al. In: *Nucl, Fusion.* 32 (1992), p. 1951 (cit. on p. 91).

[103] LHD. In: *https://www.nifs.ac.jp/report/annrep18/pdf/001.pdf* () (cit. on pp. 91–94).

[104] G. Veres et al. In: *Proc. 32 nd EPS Conf. on Plasma Phys* ECA 29C (2005), p. 4.113 (cit. on p. 91).

[105] Y. Ogawa. In: *Phys.: Conf. Ser.* 717 (2016), p. 012003 (cit. on p. 92).

[106] K. Uo. In: *J. Phys. Soc. Jpn.* 16 (1961), p. 1380 (cit. on p. 92).

[107] A. Sagara et al. In: *Fusion Eng. Des.* 85 (2010), p. 1336 (cit. on p. 92).

[108] A. liyoshi et al. In: *Nucl. Fusion* 39 (1999), p. 1245 (cit. on p. 92).

[109] K. Ida et al. In: *Nucl, Fusion.* 55 (2015), p. 104018 (cit. on pp. 93, 94).

[110] Y. Takeiri. In: *Atoms* 6 (2018), p. 69 (cit. on pp. 93, 94).

[111] N. Ohyabu et al. In: *Plasma Phys. Control. Fusion* 48 (2006), B383 (cit. on pp. 93, 94).

[112] I. Vinyar et al. In: *Instrum. Exp. Tech.* 49 (2006), p. 732 (cit. on p. 95).

[113] R. Sakamoto et al. In: *Rev. Sci. Instrum.* 84 (2013), p. 083504 (cit. on p. 95).

[114] G. Motojima et al. In: *Rev. Sci. Instrum.* 83 (2012), p. 093506 (cit. on p. 95).

[115] M. Goto et al. In: *Plasma Phys. Control. Fusion* 49 (2007), p. 1163 (cit. on pp. 96, 101, 109, 111–114, 138).

[116] J. Kloe et al. In: *Phys. Rev. Lett.* 82 (1999), p. 2685 (cit. on pp. 98, 122).

[117] H.W. Müller et al. In: *Nucl. Fusion* 42 (2002), p. 301 (cit. on pp. 107, 134).

[118] B.V. Kuteev et al. In: *Technical Physics* 47 (2002), p. 935 (cit. on p. 107).

[119] C. Stehlé Hutcheon R. In: *Astron. Astrophys. SuppL. Ser.* 140 (1999), p. 93 (cit. on pp. 111, 115).

[120] A.W. Wishart. In: *Mon. Not. R. astr. Soc.* 187 (1979), p. 59 (cit. on p. 111).

[121] P.J. Storey Hummer D.G. In: *Comput. Phys. Commun.* 66 (1991), p. 129 (cit. on p. 112).

[122] M. Goto et al. In: *J-stage* 14 (2019), p. 3402053 (cit. on p. 113).

[123] G. Seguineaud et al. In: *Atoms* 6 (2018), p. 34 (cit. on p. 113).

[124] B. Pégourié et al. In: *Nucl. Fus.* 29 (1989), p. 745 (cit. on pp. 127, 132).

[125] P. B. Parks et al. In: *Phys. Fluids* 21 (1978), p. 1735 (cit. on p. 132).

[126] L. Garzotti et al. In: *Nucl, Fusion.* 37 (1997), p. 1167 (cit. on p. 132).

[127] L.L. Lengyel et al. In: *Nucl, Fusion* 34 (1994), p. 675 (cit. on p. 134).

[128] L.L. Lengyel et al. In: *Nucl, Fusion* 31 (1991), p. 1107 (cit. on p. 134).

[129] G. Kristof at al. In: *Physics of Plasmas* 5 (1998), p. 315 (cit. on p. 134).

[130] R. Samulyak et al. In: *Nucl, Fusion.* 47 (2007), p. 103 (cit. on p. 134).

[131] J. Mishra et al. In: *Fusion Sci. Technol.* 78 (2022), p. 211 (cit. on p. 137).

[132] J.-F Artaud and A. Géraud. "Proc". In: *20th SOFT Marseille (France)* (1998) (cit. on pp. 137, 142, 144).

[133] P. Clark Souers. *Hydrogen Properties for Fusion Energy*. University of California press, 1979 (cit. on pp. 142, 144).

[134] D.N. Bold'shutkin et al. In: *Solid State* 12 (1970) (cit. on pp. 142, 144).

[135] J.G. Daunt R.J. Roberts. In: *J. Low Temp. Phys* 6 (1972), p. 97 (cit. on p. 142).

[136] S. Laroze. *Résistance des matériaux et structures*. Vol. 1. Eyrolles, Paris, 1974. Chap. 4 (cit. on p. 143).